Advances in Mechanics and Mathematics 30

Jan Awrejcewicz
Zbigniew Koruba

Classical Mechanics

Applied Mechanics and Mechatronics

Springer

Advances in Mechanics and Mathematics

Volume 30

For further volumes:
http://www.springer.com/series/5613

Jan Awrejcewicz • Zbigniew Koruba

Classical Mechanics

Applied Mechanics and Mechatronics

Springer

Jan Awrejcewicz
Department of Automation
and Biomechanics
Łódź University of Technology
Łódź, Poland

Zbigniew Koruba
Department of Computer-based Technologies
and Armament Engineering
Kielce University of Technology
Kielce, Poland

ISSN 1571-8689 ISSN 1876-9896 (electronic)
ISBN 978-1-4614-3977-6 ISBN 978-1-4614-3978-3 (eBook)
DOI 10.1007/978-1-4614-3978-3
Springer New York Heidelberg Dordrecht London

Library of Congress Control Number: 2012940871

© Springer Science+Business Media, LLC 2012
This work is subject to copyright. All rights are reserved by the Publisher, whether the whole or part of the material is concerned, specifically the rights of translation, reprinting, reuse of illustrations, recitation, broadcasting, reproduction on microfilms or in any other physical way, and transmission or information storage and retrieval, electronic adaptation, computer software, or by similar or dissimilar methodology now known or hereafter developed. Exempted from this legal reservation are brief excerpts in connection with reviews or scholarly analysis or material supplied specifically for the purpose of being entered and executed on a computer system, for exclusive use by the purchaser of the work. Duplication of this publication or parts thereof is permitted only under the provisions of the Copyright Law of the Publisher's location, in its current version, and permission for use must always be obtained from Springer. Permissions for use may be obtained through RightsLink at the Copyright Clearance Center. Violations are liable to prosecution under the respective Copyright Law.
The use of general descriptive names, registered names, trademarks, service marks, etc. in this publication does not imply, even in the absence of a specific statement, that such names are exempt from the relevant protective laws and regulations and therefore free for general use.
While the advice and information in this book are believed to be true and accurate at the date of publication, neither the authors nor the editors nor the publisher can accept any legal responsibility for any errors or omissions that may be made. The publisher makes no warranty, express or implied, with respect to the material contained herein.

Printed on acid-free paper

Springer is part of Springer Science+Business Media (www.springer.com)

Preface

This is the third and final volume of a triad of books devoted to classical mechanics; it uses the theoretical background presented in *Classical Mechanics: Kinematics and Statics* and *Classical Mechanics: Dynamics*. It is focused on presenting a unique approach, rooted in classical mechanics, to studying mechanical and electromagnetic processes occurring in applied mechanics and mechatronics. In contrast to the majority of books devoted to applied mechanics, this volume places particular emphasis on theory, modeling, and analysis and control of gyroscopic devices, including military applications. This book provides practicing mechanical/mechatronic engineers and designers, researchers, and graduate and postgraduate students with a knowledge of mechanics focused directly on advanced applications.

Chapter 1 deals with dynamics in mechatronic systems. A unified approach based on mechanics and variational calculus is applied first to the study of dynamical processes in electromechanical systems, henceforth referred to as mechatronic systems. In Sect. 1.1, the constitutive relations of elements of electric circuits such as resistors, coils, capacitors, and inductors are introduced, and two of Kirchhoff's laws are presented in the form of two theorems. Then, the application of Hamilton's principle and the Lagrange equations to electrical (electromagnetic) systems is described. An illustrative example is also presented. In Sect. 1.2, dynamical processes in mechatronic systems are studied. The Lagrange equations for mechatronic systems are derived. Then various mechatronic transducers are described, including resistive-displacement transducers, resistance-based sensors, inductive transducers, capacitive and angular velocity transducers, temperature transducers, thermocouples, pressure transducers, magnetoelectric sensors and piezoelectric transducers. A single mechatronic system is also studied, and the magnetic force magnitude is derived. In Sect. 1.3, magnetic levitation is analyzed. A levitating cylindrically shaped rigid body is studied experimentally, and the governing equations of the body levitating in magnetic and gravitational fields are derived. Two cases of the numerical control are studied, and the numerical examples are presented. In Sect. 1.4, dynamics of the string-type generator is studied. Governing equations consist of a PDE and ODE with time delay, and they are analyzed using the averaging approach and numerical simulation. Lastly, Sect. 1.5 studies the dynamics of a rotor supported by a magnetohydrodynamic bearing. Both resonance and nonresonance cases, as well as rotor chaotic dynamics are analyzed

In Chap. 2, the dynamics of a rigid spherical body is studied with emphasis put on applications. In Sect. 2.1, the kinematics of a rigid body is revisited including the Euler and Cardan angles. In Sect. 2.2, the kinematic energy of a rigid body is defined and equations of the spherical motion of a rigid body are given. Here the Euler and Lagrange cases are studied more extensively in comparison to the book *Classical Mechanics: Dynamics*. The same applies to the Kovalevskaya case, and the essence of the gyroscopic effect is outlined.

Chapter 3 is devoted to the theory of gyroscopes. In Sect. 3.1, an historical outline of the theory of gyroscopes is given. In Sect. 3.2, elements of gyroscope classification are introduced, and then the evolution of the gyroscope concept is presented. Milestones in gyroscope development are highlighted in Sect. 3.4. In Sects. 3.5–3.9, the following gyroscope-type devices are considered: the directional gyroscope, the gyroscopic vertical, the stabilized gyroscopic platform, the laser gyroscope, the fiber-optic gyroscope, the piezoelectric gyroscope, the fork gyroscope, and the microgyroscope with a spinning disk and with a vibrating ring. Section 3.10 contains examples of devices for gyroscopic navigation. An example of an observation device with a built-in gyroscope is provided in Sect. 3.10. In Sect. 3.11, new challenges for the gyroscope are briefly summarized.

Chapter 4 is devoted to the dynamics and control of gyroscopes. In Sect. 4.1, the dynamics of the gyroscope on a movable platform is described. Then the equations of motion of the gyroscope axis and the gyroscope rotor are derived. The particular case of a static gyroscope placed on a fixed platform with the axis fixed to the rotor is studied. Finally, a technical equation of gyroscope motion and some remarks regarding the modeling of gyroscope dynamics are outlined. Gyroscope control is presented in Sect. 4.2. First, an inverse problem of gyroscope dynamics, i.e., motion control of the gyroscope axis in an open-loop system is studied and a numerical example is provided. Then, control with constant programmable moments is discussed and clarified through an illustrative numerical example. Section 4.3 deals with motion control of the gyroscope axis in a closed-loop system. First, a gyroscopic system with a PID controller is considered, and its stability is analyzed. Then, a regulator whose role is to minimize errors between the prescribed and actual motions is introduced into the gyroscope control system. In Sect. 4.4, selection of optimal parameters of a gyroscopic system in an elastic suspension is carried out and its optimal control is studied. Section 4.5 focuses on the selection of the optimal parameters of a gyroscope system with an axis fixed to the rotor; this section also includes the optimization of a classically controlled gyroscope.

In Chap. 5, gyroscopic control in self-guidance systems of flying objects is presented. In Sect. 5.1, a gyroscope control in an unmanned aerial vehicle is studied. First, the navigation kinematics of an unmanned aerial vehicle is analyzed, and then the control of a gyroscope fixed on its board as well as its full control are discussed. A gyroscope in a guided aerial bomb is studied in Sect. 5.2, which includes an analysis of the kinematics of a bomb self-guided motion to a ground target, the equations of motion of a guided bomb, and a description of a gyroscopic system devoted to bomb control including automatic pilot control.

The authors wish to express their thanks to Mr. P. Dąbek and Mr. M. Kaźmierczak for their help in the book's preparation. J. Awrejcewicz acknowledges also the hospitality of the Fraunhofer Institute of the Technical University of Darmstadt during his research, made possible by the Alexander von Humboldt Award.

Kielce, Poland — Zbigniew Koruba
Łódź, Poland — Jan Awrejcewicz

Contents

List of Symbols

The list contains major uses of symbol throughout the book. Minor uses are defined in the text of sections.

a_g,b_g,v_s	Parameters of the Archimedes spiral
a_γ,a_χ	Coefficients of proportional navigation
b_m,b_n	Coefficients of stabilising controls
c	Viscous damping coefficient; velocity of propagation of ultrasound in the fluid
c^*	Bearing clearance
d	Distance between rotor plates of the capacitor
$d(H_\mathrm{s})$	Air density at the pre-set UAV flight altitude H_s
d_b,d_c	Diameters of the bearing pins
$\mathbf{g}$	Acceleration due to gravity
e_b,e_c	Partial deviations
h	Displacement of the levitating mass
$h_b, h_c, h_{b1}, h_{c1}, k_b, k_c$	Parameters of the regulator PID
$h_{b1}(t), h_{c1}(t), h_{b2}(t), h_{c2}(t),$ $k_{b1}(t), k_{c1}(t), k_{b2}(t), k_{c2}(t)$	Part-time controller parameters
h_m,h_n	Coefficients of autopilot regulator damping
h_{ms},h_{ns}	Coefficients of control surfaces drive damping
k	Bellows stiffness
k_b,k_c,h_g	Correction regulator parameters
k_m,k_n	Coefficients of autopilot regulator amplifications
k_{ms},k_{ns}	Coefficients of control surfaces drive amplifications
l	Length of the conductor or length of the string
l_s	Distance between the centre of mass of the basis and the centre of the gyroscope motion
l_O	Distance between the centre of mass of system: rotor—internal frame and the centre of motion
m	Mass of the rigid body

m_s	UAV mass
m_n	Mass of the n-th material point
m_1,m_2,m_3	Masses of the external, internal (along with the axis) and rotor of the gyroscope, respectively
n_g	Rotation angular velocity of the gyroscope rotor
p	Pressure
p_s,q_s,r_s	Components of vector of UAV flight angular velocity
t	Time
t_0	Instant of the start of area penetration
t_w	Instant of target detection
t_s	Instant of the start of target tracking and illumination
t_k	Instant of target tracking completion (mission completion)
$\mathbf{u_g}$	Vector controls of gyroscope system
u_b,u_c	Correcting controls of gyroscope system
u_m,u_n	Stabilising controls worked out by UAV autopilot
u_s,v_s,w_s	Components of vector of UAV flight linear velocity
$u(t, x)$	String displacement in the (t, x) point
x	Distance between capacitor plates
$\mathbf{x_g}$	State variables of gyroscope system
(x, y)	Cartesian coordinates
x_O, y_O, z_O	Coefficients of UAV mass centre location in the terrestrial co-ordinate system
(x_O, y_O)	Coordinates of the rotor static equilibrium
x_1''', x_2''', x_3'''	Components of the radius vector $\boldsymbol{\rho}_\mathbf{e}$ in the coordinate system $OX_1'''X_2'''X_3'''$
$\mathbf{y_g}$	State variables of modified gyroscope system
z_1, z_2	Hysteretic forces
A	Cross section of the conductor or the active area of a capacitor
$\mathbf{A_g}$	Matrix of state of gyroscope system
$\mathbf{A_g^*}$	Matrix of state of optimal gyroscope system
A_x, A_y	Characteristic vibration amplitudes of the rotor in the horizontal and vertical direction respectively
B	Magnetic conduction
$\mathbf{B_g}$	Matrix controls of gyroscope system
$\mathbf{B_g^*}$	Modified matrix of state of gyroscope system
B_s	Saturation induction
B_s^p	Saturation polarization
$B(x)$	Magnetic induction
C	Capacitance

C_l,C_m,C_n	Aerodynamic coefficients of rolling moment L_s, pitching moment M_s and yawing moment N_s, respectively
C_x,C_y,C_z	Coefficients of components of aerodynamic resultant force
$Cx_cy_cz_c$	Coordinate system connected with target velocity vector
D	Dissipation function
E	Young's modulus of the resistive material
ET	Thermoelectric force of a thermoelement
E^{e}	Electric energy
E^{m}	Magnetic energy
E_c^{e}	Complementary energy
E_k	Kinetic energy of gyroscope (sum of the kinetic energy of the external and internal frame, the rotor and the axis)
E_p	Potential energy of gyroscope
E_1''', E_2''', E_3'''	Versors of the vector $\mathbf{K_0}$ in the coordinate system $OX_1'''X_2'''X_3'''$
F	Tensile (compressive) force or desired force
$\mathbf{F_g}(F_{gX_1}, F_{gX_2}, F_{gX_3})$	Components of the force acting on the centre of mass of the rotor in the frame fixed to the platform $O_{g1}X_1X_2X_3$
F_x, F_y	Magnetic control forces
(F_x, F_y, F_z)	Components of the resultant of the vector of external forces affecting UAV
$\mathbf{G}$	Gravity force
$Gx_gy_gz_g$	Coordinate system connected with point G velocity vector
$G_{x_1'''}, G_{x_2'''}, G_{x_3'''}$	Components of the vector of gravity force $\mathbf{G}$ in the coordinate system $OX_1'''X_2'''X_3'''$
H	Magnetic field
H_0	Uniform magnetic field strength
H_{s}	Saturation magnetic field strength or UAV flight altitude
I	Current
I_{gO}	Moment of inertia of the rotor relative to the main axis OX_3'''
I_{gk}	Transverse moment of inertia of the gyroscope rotor
I_n	Generalised current intensity
$I_{x_1'}, I_{x_2'}, I_{x_3'}$	Moments of inertia of the external frame about axes $O_{g1}X_1'$, $O_{g1}X_2'$, $O_{g1}X_3'$, respectively

$I_{x_1''}, I_{x_2''}, I_{x_3''}$	Moments of inertia of the internal frame about axes: $O_{g2}X_1''$, $O_{g2}X_2''$, $O_{g2}X_3''$, respectively
$I_{x_1'''}, I_{x_2'''}, I_{x_3'''}$	Moments of inertia about axis OX_1''', OX_2''', OX_3''', respectively
$I_{x_1'''}, I_{x_2'''}, I_{x_3'''}$	Moments of inertia of the rotor about axes $O_{g3}X_1'''$,$O_{g3}X_2'''$, $O_{g3}X_3'''$, respectively
$I^0_{x_1''}, I^0_{x_2''}$	Moments of inertia of the gyroscope axis about axes: $O_{g2}X_{10}''$, $O_{g2}X_{20}''$, respectively
$I_{x_1x_2}, I_{x_2x_3}, I_{x_1x_3}$	Moments of deviation of the body
I_*	Ideal current intensity generator
J_x, J_y, J_z	Moments of inertia in relation to UAV individual axes
J_{xy}, J_{yz}, J_{zx}	Moments of UAV deviation
$\mathbf{K_g}$	Coupling matrix of gyroscope system
K_n	Line of nodes (axis of nutation)
$\mathbf{K_O}$	Angular momentum in spherical motion of a body about a fixed point O (centre of the spherical motion)
$K_{x_1'''}, K_{x_2'''}, K_{x_3'''}$	Components of the angular momentum vector $\mathbf{K_O}$ in the coordinate system $OX_1'''X_2'''X_3'''$
$K_{x_{30}}$	Angular momentum projection of a rigid body onto the axis OX_{30}
Q	Charge
Q_n	Generalised charge
Q_*	Current of ideal generator
Q^*	Amplitude of the external excitation
$\mathbf{Q_g}, \mathbf{R_g}$	Weight matrices of state of gyroscope system
L	Inductance or Lagrangian function
L_c	Total bearing length
L_s, M_s, N_s	Components of resultant vector of moment of forces of UAV
M	Mass of moving parts of the sensor
$\mathbf{M_g}$	Moments of external forces acting on the gyroscope
M_b^p, M_c^p	Programme controls of the gyroscope
$\mathbf{M_c}(M_{bX_1'}, M_{bX_2'}, M_{bX_3'})$	Moment of force interactions of the external frame on the internal frame
$\mathbf{M_c}(M_{cX_1}, M_{cX_2}, M_{cX_3})$	Moment of force of interactions of the base on the external frame
$\mathbf{M_k}(M_{kX_1''}, M_{kX_2''}, M_{kX_3''})$	Moment of force of interactions of the internal frame on the rotor
$\mathbf{M_O}$	Torque acting on a rigid body (main moment of external forces acting on a body)

M_{rk}	Moment of friction forces in bearing of the rotor in the internal frame and aerodynamic resistance
M_{rc}^{T}	Moment of dry friction force in the bearings of the internal and external frames
M_{rk}^{V}	Moment of viscous friction force in the bearings of the internal frames
M_{zb},M_{zc}	Disturbing signals in a form of torques acting on the rotor directly
$M_{pz},M_{zw},M_{wr},M_{pw}$	Transformation matrices for the gyroscope on a rigid suspension
$M_{pz}^{O},M_{zw}^{O},M_{pw}^{O}$	Transformation matrices for the gyroscope on elastic suspension
$M_{x_1'''},M_{x_2'''},M_{x_3'''}$	Components of the main moment $\mathbf{M_O}$ in the coordinate system $OX_1'''X_2'''X_3'''$
$M_{\chi},M_{\gamma},M_{\chi\gamma},M_{\chi\gamma}^{s}$	Matrices of transformation
$\mathbf{M}_{\Gamma}$	Gyroscopic moment (moment of inertial forces generated by rotational motion about the symmetry axis OX_3''')
N	Circuit elements
N_b,N_c	Normal reactions in the bearings
N^{e}	Power
N^*	Number of independent coordinates of magnetic fluxes
O_{g1}	Centre of mass of the external frame of a gyroscope
O_{g2}	Centre of mass of the internal frame of a gyroscope
O_{g2}	Centre of mass of the rotor of a gyroscope
$O_O x_O' y_O' z_O'$	Motionless reference system connected with the Earth
$O_s x_O y_O z_O$	Normal (movable) co-ordinate system connected with moving UAV
$O_s xyz$	Co-ordinate system connected with UAV
$O_O x_{es} y_{es} z_{es}$	Co-ordinate system connected with radius vector $\overrightarrow{R}_{es}$
OX_1'	Nutation axis
OX_3'	Precession axis
OX_3'''	Eigenrotations axis
$O_{g1}X_1',O_{g1}X_2',O_{g1}X_3'$	Main, central axes of inertia of the external frame
$O_{g2}X_3''',O_{g3}X_3'''$	Main, central axes of inertia of the internal frame and the rotor, respectively
$OX_{10}'X_{20}'X_{30}'$	Reference frame (fixed coordinate system)
$OX_{10}'''X_{20}'''X_{30}'''$	Second frame stiffly connected with a body
$OX_1'''X_2'''X_3'''$	Coordinate system fixed to the rotor of a gyroscope
$\mathbf{P_g}$	Matrix solution of an algebraic Riccati equation

(P_r, P_τ)	Radial and tangential components of the dynamic oil-film action, respectively
R	Resistance
R_c	Journal radius
$\mathbf{R_{es}},\mathbf{R_{eg}},\mathbf{R_{ec}}$	Radius vectors of point S, point G and point C, respectively
R_L	Inductive resistance
S_x, S_y, S_z	Static moments in relation to UAV individual axes
$Sx_n y_n z_n$	Coordinate system connected with LWOC
$Sx_s y_s z_s$	Coordinate system connected with UAV velocity vector
T	Period of integration
T	Kinetic energy of the body
TEP_i	Peltier thermoelectric force at the junction Ai
TE	Thermoelectric force
$\mathrm{Tr}\mathbf{A_g}$	Trace of the matrix $\mathbf{A_g}$
$\mathrm{Tr}\mathbf{B_g}$	Trace of the matrix $\mathbf{B_g^*}$
TSOL	Target seeking and observation line
U	Voltage
UAV	Unmanned Aerial Vehicle
U_*	Voltage of an ideal generator
U_n	Generalised voltage
V_n	Velocity of the n-th material point
V	Potential energy
$\mathbf{V_e}$	Linear velocity of the body
$\mathbf{V_g}(V_{gX_1}, V_{gX_2}, V_{gX_3})$	Components of the linear velocity vector of the base displacement - coordinates of the point
$\mathbf{V_{g_2}}$	Linear velocity of the centre of mass of the rotor
$V_{gX_1''}, V_{gX_2''}, V_{gX_3''}$	Components of linear velocity vector $\mathbf{V_{g_2}}$
$V_{gX_1'}, V_{gX_2'}, V_{gX_3'}$	Linear velocity of the centre of mass of the external frame $\mathbf{V_{g_1}}$
$V^O_{gX_1''}, V^O_{gX_2''}, V^O_{gX_3''}$	Linear velocity of the centre of mass of a system: the external frame-axis
$\mathbf{V_O}$	Velocity of the body centre mass
$\mathbf{V_s}$	Vector of UAV flight velocity or drift velocity of the point O_s
W^{e}	Work
$X_{1C}''', X_{2C}''', X_{3C}'''$	Coordinates of the centre of masses in the coordinate system $OX_1'''X_2'''X_3'''$
α	Deformation sensitivity coefficient or proportionality factor
α_s, β_s	Angles of attack and slide
β	Proportionality factor

$\delta_l, \delta_m, \delta_n$	Angle of displacement of control surfaces of ailerons, a rudder and an elevator respectively, respectively
δ_s	Relative bearing clearance
δ_t	Angle of displacement of the drive control lever
ε	Dielectric constant or small parameter
$\eta_b, \eta_c, \mu_b, \mu_c$	Friction coefficients in the frame bearings
γ, λ	Control parameters
γ_s, χ_s	UAV flight angles
γ_s^*, χ_s^*	Desired UAV flight angles
γ_s^O, χ_s^O	UAV flight angles in target tracking and laser illumination
γ_s^p, χ_s^p	UAV flight angles in programme-run flight
γ_s^t, χ_s^t	UAV flight angles in transition from programme-run flight to target tracking flight
γ_n, χ_n	Angles of TSOL inclination and deflection, respectively
γ_g, χ_g	Angles of point G velocity vector inclination and deflection, respectively
γ_g, χ_g	Angles of target velocity vector inclination and deflection, respectively
$\gamma_1, \gamma_2, \gamma_3$	Direction cosines of angles between the axis OX_3''' and the axes OX_1, OX_2, OX_3
θ	Temperature
ϑ_e	Nutation angle
ϑ_g	Angle of rotation about the internal frame axis
κ	Stiffness coefficient of the elastic element connecting the axis with the rotor
μ	Magnetic permeability
μ_O	Vacuum permeability
μ_s	Oil viscosity
μ^*	Magnetic permeability of the core material
ν	Velocity of the fluid
ρ	Resistivity of the conductor material or density of the medium
(ρ, ϕ)	Polar coordinates
$\boldsymbol{\rho}_\mathbf{e}$	Radius vector of the body
$\boldsymbol{\rho}_\mathbf{n}$	Radius vector of the n-th material point
σ	Stress
τ	“Dimensionless” time
$\overrightarrow{\xi}_N$	Vector of point S distance from point G or C
$\varphi_\gamma^s, \varphi_\chi^s$	Angles of radius vector $\mathbf{R}_{\mathbf{es}}$ inclination and deflection, respectively
$\varphi_\gamma^g, \varphi_\chi^g$	Angles of radius vector $\mathbf{R}_{\mathbf{eg}}$ inclination and deflection, respectively

$\varphi_\gamma^c, \varphi_\chi^c$	Angles of radius vector $\mathbf{R_{ec}}$ inclination and deflection, respectively
$\psi_g, \vartheta_g, \Phi_g$	Angles determining the position of the rotor relative to the frame $O_{g1}X_1X_2X_3$
ψ_g^O, ϑ_g^O	Angles determining the position of the gyroscope axis relative to the frame $O_{g1}X_1X_2X_3$
ψ_e	Precession angle
ωL	Inductive reactance of the coil
$\boldsymbol{\omega}_\mathbf{e}$	Vector of angular velocity of the body
$\boldsymbol{\omega}_\mathbf{es}$	Vector of angular velocity of vector $\mathbf{R_{es}}$
$\omega_{ex_1'''}, \omega_{ex_2'''}, \omega_{ex_3'''}$	Velocity vector components in the coordinate system $OX_1'''X_2'''X_3'''$
$\boldsymbol{\omega}_\mathbf{g}$	Vector of angular velocity of the body in Cardan suspension
$\boldsymbol{\omega}_\mathbf{g}(p^*, q^*, r^*)$	Components of the angular velocity vector of the base (kinematic interaction)
$\omega_{gX_1'}, \omega_{gX_2'}, \omega_{gX_3'}$	Components of the angular velocity vector of the external frame in the coordinate system $O_{g1}X_1'X_2'X_3'$
$\omega_{gX_1''}, \omega_{gX_2''}, \omega_{gX_3''}$	Components of the angular velocity vector of the internal frame in the coordinate system $O_{g2}X_1''X_2''X_3''$
$\omega_{gX_1'''}, \omega_{gX_2'''}, \omega_{gX_3'''}$	Components of the angular velocity vector of the rotor in the coordinate system $O_{g3}X_1'''X_2'''X_3'''$
$\boldsymbol{\omega}_\mathbf{g}^*$	Vector of the angular velocity of the rotor
$\boldsymbol{\omega}_\mathbf{g}^O$	Angular velocity vector of the gyroscope
$\omega_{gX_1'}^O, \omega_{gX_2'}^O, \omega_{gX_3'}^O$	Components of the angular velocity vector of the gyroscope axis in the coordinate system $O_{g1}X_1'X_2'X_3'$
$\omega_{gX_1''}^O, \omega_{gX_2''}^O, \omega_{gX_3''}^O$	Components of the angular velocity vector of the gyroscope axis in the coordinate system $O_{g2}X_{10}''X_{20}''X_{30}''$
$\omega_1 = \dot{\psi}_e$	Precession speed (angular velocity of the forced rotation)
ω_O	Angular velocity of eigenrotations of a gyroscope
ω^*	Rotation speed
Δ_g	Deviation of the realised motion from the desired
$\Delta\overrightarrow{R}$	Vector of point G distance from point C
$\Delta\varphi$	Phase difference
Θ_k, ν_k	Parameters of the circular cone
Θ_r, ν_1, ν_2	Parameters of the n-flute rosette
Θ_s, Ψ_s, Φ_s	Angles of UAV longitudinal axis inclination, deflection and tilt, respectively
$\Pi(\cdot)$	Functions of square impulse

Φ	Magnetic flux
Φ_e	Eigenrotations angle
Φ_g	Angle of rotation about the axis of eigenrotations (fast)
Φ_n	Generalised magnetic flux
$\dot{\psi}_{e1}^{O}$	Angular velocity of precession of the first kind (slow precession)
$\dot{\psi}_{e2}^{O}$	Angular velocity of precession of the second kind (fast precession)
ψ_g	Angle of rotation about the external frame axis
$\psi_{gz}, \vartheta_{gz}$	Angles specifying motion of the gyroscope axis
Ω^*	Frequency of the external excitation

Chapter 1
Dynamics in Mechatronic Systems

Section 1.1 is devoted to the study of dynamical processes in electric circuits. It includes derivations of the constitutive relations of elements of electric circuits (capacitors, inductors) and describes current and voltage sources and Kirchhoff's law. Section 1.2 deals with dynamical processes in mechatronic systems (transducers) and the electromagnetomechanical circuit. In Sect. 1.3, the dynamics and control of a mass levitating in magnetic and gravitational fields is discussed. Two cases of numerical control are considered and verified experimentally. In Sect. 1.4, combined analytical and numerical analyses of vibrations in string-type generators is carried out. The vibrations of a string are governed by a PDE, whereas the dynamics of an amplifier is governed by an ODE with a time delay. The voltage generated on the string ends depends on both electromagnetic induction and string vibration speed. An averaged set of equations is derived and numerically studied. Finally, in Sect. 1.5, a 2-DOF nonlinear dynamics of a rotor supported by a magnetohydrodynamic bearing is investigated using perturbation analysis. Two modes corresponding to the vertical and horizontal vibrations of the rotor are coupled. The non-resonant case and the various resonant cases (with and without an internal resonance) are considered. Frequency-response curves are obtained. When the amplitude of the external harmonic excitation is near one of the natural frequencies of the vibrations and the system experiencing internal resonance, a saturation phenomenon occurs. When the amplitude of the external excitation increases, after some critical value the energy pumping between various submotions of the rotor occurs for each mode. Further, it is shown that in the case of rigid magnetic materials, hysteresis may be a cause of chaotic vibrations of the rotor. Chaotic regions and the amplitude level contours of the rotor vibrations are obtained in various control parameter planes.

J. Awrejcewicz and Z. Koruba, *Classical Mechanics*, Advances in Mechanics and Mathematics 30, DOI 10.1007/978-1-4614-3978-3_1,

1.1 Dynamical Processes in Electric Circuits

In Sect. 1.1, to write equations of dynamics in mechatronic systems, we will make use of the unified approach developed from mechanics and based on variational calculus [1, 2]. It should be emphasized that such an approach is based on the theory of the quasistatic electromagnetic field whose changes are slow enough to neglect the interactions occurring between magnetic and electric fields. Electric circuits consist of *passive elements* such as resistors, coils, and capacitors and *active elements* such as voltage and current sources.

1.1.1 Constitutive Relations of Elements of Electric Circuits

1.1.1.1 The Capacitor

Figure 1.1a shows a schematic of a capacitor to whose plates the voltage U was applied and an example of a constitutive function $U(Q)$ (Fig. 1.1b).

As the capacitor is charged, the charge Q is supplied to one of its plates and removed from another. The change in the charge on the plates separated by a dielectric produces the current flow

$$I = \frac{\mathrm{d}Q}{\mathrm{d}t} \equiv \dot{Q}. \tag{1.1}$$

During charging, a potential difference appears between the plates of the capacitor (voltage U). An example of measurements of the voltage U and the corresponding charge Q in static conditions leads to the construction of graph $U(Q)$ (Fig. 1.1b).

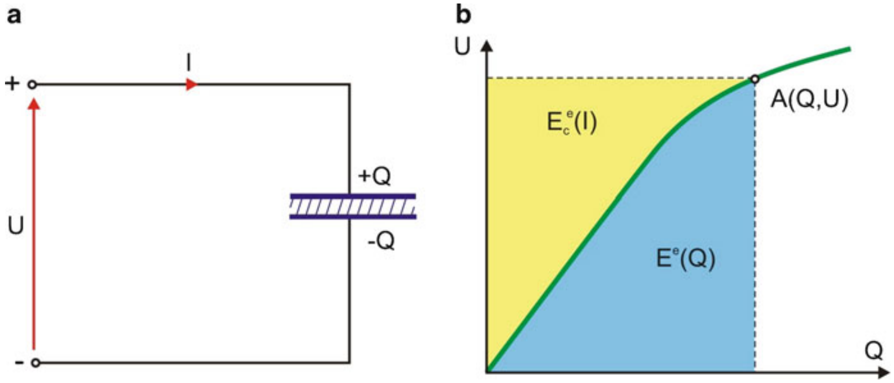

Fig. 1.1 Schematic diagram of a capacitor (**a**) and a constitutive function $U(Q)$ (**b**)

The electric energy gathered in the capacitor $E^{\mathrm{e}}(Q)$ is equivalent to the work done while charging it from value 0 to Q and is equal to

$$E^{\mathrm{e}}(Q) \equiv W^{\mathrm{e}}(Q) = \int_0^t N^{\mathrm{e}} \mathrm{d}t = \int_0^t UI \mathrm{d}t = \int_0^Q U \mathrm{d}Q, \tag{1.2}$$

where $N^{\mathrm{e}} = \dot{W}^{\mathrm{e}}$ is the power supplied to the system, and during transformations (1.1) was used. The value of integral (1.2) corresponds to the area under the curve $U(Q)$ in Fig. 1.1b. If in the neighborhood of the operating point A of the capacitor we conduct the linearization, we obtain

$$Q = CU = C\frac{\mathrm{d}E^{\mathrm{e}}}{\mathrm{d}Q}, \tag{1.3}$$

and integrating we have

$$E^{\mathrm{e}}(Q) = \frac{Q^2}{2C}. \tag{1.4}$$

A complementary state function may be easily determined on the basis of Fig. 1.1b, and it is equal to

$$E^{\mathrm{e}}(Q) + E^{\mathrm{e}}_{\mathrm{c}}(I) = UQ, \tag{1.5}$$

where $E^{\mathrm{e}}_{\mathrm{c}}(I)$ is the so-called *complementary energy*.

Making use of the method described earlier it is easy to notice that

$$E^{\mathrm{e}}_{\mathrm{c}}(U) = \frac{CU^2}{2}. \tag{1.6}$$

1.1.1.2 The Inductor

It is widely known that if the current of intensity I flows through a conductor, then around the conductor there is generated a magnetic field proportional to the intensity of the flowing current. In turn, if the conductor is situated in the changing magnetic field, then the voltage will be generated at its ends.

If the conductor is wound in turns so as to form a coil, then the generated magnetic flux Φ is proportional to the intensity of the current I flowing through the coil. If we now put a ferromagnetic core inside the coil, then the density of the magnetic flux is substantially increased.

According to Faraday's law of induction, the voltage induced in a conductor is equal to

$$U = \frac{\mathrm{d}\Phi}{\mathrm{d}t} \equiv \dot{\Phi}. \tag{1.7}$$

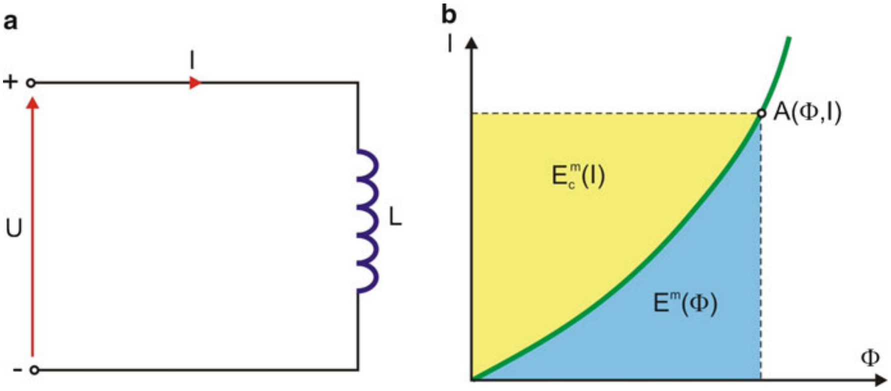

Fig. 1.2 Schematic diagram of an inductor (**a**) and the graph of the constitutive function (**b**)

If we have an ideal conductor, then $I = \text{const}$ (intensity of the current does not change in time) and a magnetic flux $\Phi = \text{const}$. In this case, from (1.7) it follows that $U = 0$ (the voltage in the conductor is not induced). If we perform the linearization of the function $I(\Phi)$ (Fig. 1.2b) in the neighborhood of operating point A, then

$$\Phi = LI, \tag{1.8}$$

where L is called the *inductance*.

As in the case of the capacitor, the magnetic energy stored in an ideal conductor is calculated based on the knowledge of the power supplied to the conductor (to the electric circuit) $N^{\mathrm{e}} = UI$, and it is equal to

$$E^{\mathrm{m}}(\Phi) = \int_0^t UI\,\mathrm{d}t = \int_0^{\Phi} I\,\mathrm{d}\Phi. \tag{1.9}$$

On the basis of the method described earlier we calculate the magnetic energy $E^{\mathrm{m}}(\Phi)$ and complementary magnetic energy $E_c^{\mathrm{m}}(I)$ of the forms

$$E^{\mathrm{m}}(\Phi) = \frac{\Phi^2}{2L}, \qquad E_c^m(I) = \frac{LI^2}{2}, \tag{1.10}$$

where

$$I = \frac{\mathrm{d}E^{\mathrm{m}}}{\mathrm{d}\Phi}. \tag{1.11}$$

It is easy to notice that

$$E^{\mathrm{m}}(\Phi) + E_c^m(I) = \Phi \mathrm{I}. \tag{1.12}$$

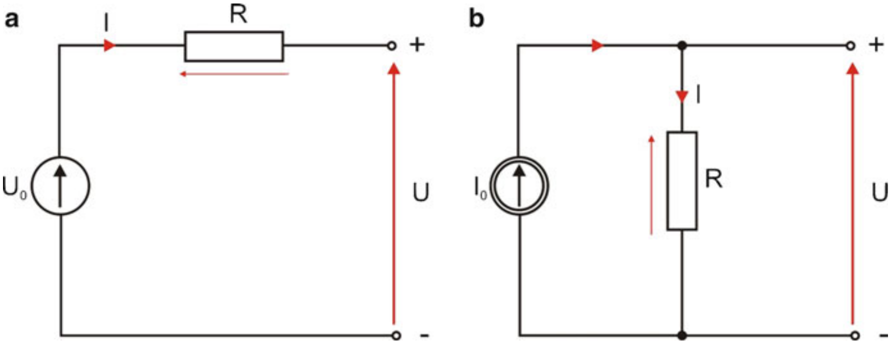

Fig. 1.3 Ideal voltage source (**a**) and ideal current source (**b**)

1.1.1.3 Current and Voltage Sources and Kirchhoff's Laws

An *ideal voltage source* is a source that produces the voltage $U = U(t)$ in a conductor (an electric circuit) and is not affected by the current flowing in the conductor (the circuit). During the composition of Lagrange's equations voltages will be treated as generalized forces.

In turn, a source that in a conductor produces the current intensity $I = I(t)$ and is not affected by the voltage in the conductor (the electric circuit) is called an *ideal current source*.

During composition of Lagrange's equations the current intensity $I(t) = \dot{Q}(t)$ in a dissipation function D is taken with a negative sign because it is the active element supplying the energy.

Figure 1.3a, b shows a schematic of the ideal voltage (current) source.

Voltage-current characteristics corresponding to Fig. 1.3a, b are respectively described by the equations

$$U_0 = U + RI, \tag{1.13}$$

$$RI_0 = U = RI. \tag{1.14}$$

It turns out that the development of contemporary electronics allows for the construction of almost ideal voltage and current sources.

If we now connect together the active elements (sources) and the passive ones (resistors, coils, and capacitors), then we will impose certain constraints on the variables describing the processes in the isolated, i.e., considered individually, elements (conductors or circuits). Such constraints imposed on electric systems are known as *Kirchhoff's laws*.

Theorem 1.1 (Kirchhoff's current law). *The sum of currents entering and leaving an arbitrary node of an electric circuit must be equal to zero (the conservation of electric charge).*

Theorem 1.2 (The Kirchhoff's voltage law). *The sum of voltage drops on each element along a closed subcircuit (loop) must be equal to zero (meaning that the electric potential at any point in the circuit is independent of the choice of the path leading to that point).*

There are many books (and other publications) devoted to the methods of composition of equations describing current processes in electric circuits based on Kirchhoff's law (the so-called *direct methods*), and they will not be described in this textbook. Mainly, the *indirect (variational) methods* originating in classical mechanics will be used here.

1.1.2 Application of Hamilton's Principle and Lagrange's Equations to Electrical Systems

There exist two possibilities for formulating Hamilton's principle for electromagnetic systems by different choices of generalized coordinates.

In the first case as generalized coordinates we will choose the charge Q_n and the current intensity I_n. The general equation of mechanics allows, by analogy, for a direct formulation of the general equation of electromagnetic systems of the form

$$\sum_{n=1}^{N}\left(U_n - \frac{\mathrm{d}\Phi_n}{\mathrm{d}t}\right)\delta Q_n = 0, \tag{1.15}$$

where now N denotes the number of elements of an electric circuit. In turn, the first component of (1.15) will be represented in the form

$$\sum_{n=1}^{N} U_n \delta Q_n = -\delta E^{\mathrm{e}} + \sum_{n*=1}^{N*} U_{n*}\delta Q_{n*}, \tag{1.16}$$

where U_{n^*} denotes generalized voltages associated with the n^*th non-conservative element.

In the preceding equation there is a distinction made between the fraction of the work (the energy) done by an element of conservative electrical circuit E^{e} and that done by N^* non-conservative elements associated with the generalized coordinates Q_{n^*}.

The minus sign in front of δE^{e} means that the application of voltage to a conservative element results in a decrease of electrical energy inside this element. In turn, the second component of (1.15) will be transformed in the following way:

$$-\sum_{n=1}^{N}\frac{\mathrm{d}\Phi_n}{\mathrm{d}t}\delta Q_n = -\sum_{n=1}^{N}\frac{\mathrm{d}}{\mathrm{d}t}\left(\Phi_n \delta Q_n\right) + \sum_{n=1}^{N}\Phi_n \frac{\mathrm{d}\left(\delta Q_n\right)}{\mathrm{d}t}. \tag{1.17}$$

Since according to (1.1) and (1.11) we have

$$\sum_{n=1}^{N} \Phi_n \frac{\mathrm{d}}{\mathrm{d}t}\delta Q_n = \sum_{n=1}^{N} \Phi_n \delta I_n = \delta E^{\mathrm{m}}, \tag{1.18}$$

taking into account the obtained result in the integrated (1.15) we have

$$\begin{aligned} S &= \int_{t_1}^{t_2} \left[-\delta E^{\mathrm{m}} - \delta E^{\mathrm{e}} + \sum_{n^*=1}^{N^*} U_{n^*}\delta Q_{n^*} - \sum_{n=1}^{N} \frac{\mathrm{d}}{\mathrm{d}t}\left(\Phi_n \delta Q_n\right) \right] \mathrm{d}t \\ &= \int_{t_1}^{t_2} \left[-\delta\left(E^{\mathrm{m}} + E^{\mathrm{e}}\right) + \sum_{n^*=1}^{N^*} U_{n^*}\delta Q_{n^*} \right] \mathrm{d}t - \underline{\sum_{n=1}^{N} \left[\Phi_n \delta Q_n\right]_{t_1}^{t_2}} \\ &= \int_{t_1}^{t_2} \left[-\delta\left(E^{\mathrm{m}} + E^{\mathrm{e}}\right) + \sum_{n^*=1}^{N^*} U_{n^*}\delta Q_{n^*} \right] \mathrm{d}t \\ &= \int_{t_1}^{t_2} \left[-\delta L + \sum_{n^*=1}^{N^*} U_{n^*}\delta Q_{n^*} \right] \mathrm{d}t = 0, \end{aligned} \tag{1.19}$$

because, according to Hamilton's principle, the underlined term is equal to zero, since $\delta Q_n(t_1) = \delta Q_n(t_2) = 0$. In (1.19), $L = E^{\mathrm{m}} + E^{\mathrm{e}}$, and it denotes the Lagrangian function.

In other words, according to Hamilton's principle, the dynamic equilibrium of a physical system is realized by the system by means of the choice of the *extremal value of the action* between the states of the system at time instants t_1 and t_2. The extremal value of the action in an electric circuit according to Hamilton leads to (1.19) for all possible and permitted changes of the charge δQ_n during the transition between the states of the system determined at time instants t_1 and t_2 and such that $\delta Q_n(t_1) = \delta Q_n(t_2) = 0$.

According to the notation introduced earlier, E^{m} in the equation denotes the magnetic energy in the circuit, that is, it is the sum of all energies of the individual conductors in the circuit expressed in terms of the current intensity I. In turn, E^{e} denotes the electric energy of the circuit, which is the sum of electric energies of all individual conductors in the circuit related to the charge Q_n. The possible current and charge intensities are allowed if they satisfy Kirchhoff's law and additionally $I_n = \frac{\mathrm{d}Q_n}{\mathrm{d}t}$. The expression $\sum_{n^*=1}^{N^*} U_{n^*}\delta Q_{n^*}$ represents the virtual work of non-conservative elements of the circuit. Let us now proceed to the second way to formulate Hamilton's principle for electromagnetic systems, that is, now we will choose as generalized coordinates the magnetic flux Φ_n and the voltage U_n.

Similarly to the previous case, the general equation of mechanics allows for the formulation of equation dual to (1.15) of the form

$$\sum_{n=1}^{N}\left(I_n - \frac{\mathrm{d}Q_n}{\mathrm{d}t}\right)\delta\Phi_n = 0, \tag{1.20}$$

where N denotes the number of circuit elements.

The first component of (1.20) will be represented as

$$\sum_{n=1}^{N} I_n\delta\Phi_n = -\delta E^{\mathrm{m}} + \sum_{n^*=1}^{N^*} I_{n^*}\delta\Phi_{n^*}, \tag{1.21}$$

where E^{m} denotes the magnetic energy of all elements in the circuit, whereas the second term on the right-hand side of (1.21) denotes the work associated with non-conservative elements of the circuit related to the generalized current intensities I_{n^*} and magnetic fluxes Φ_{n^*}, and N^* denotes the number of independent coordinates of magnetic fluxes.

The second component of (1.20) has the form

$$-\sum_{n=1}^{N}\frac{\mathrm{d}Q_n}{\mathrm{d}t}\delta\Phi_n = -\sum_{n=1}^{N}\frac{\mathrm{d}}{\mathrm{d}t}\left(Q_n\delta\Phi_n\right) + \sum_{n=1}^{N} Q_n\frac{\mathrm{d}}{\mathrm{d}t}\left(\delta\Phi_n\right). \tag{1.22}$$

Because according to (1.7) and (1.2) we have

$$\sum_{n=1}^{N} Q_n\frac{\mathrm{d}}{\mathrm{d}t}\delta\Phi_n = \sum_{n=1}^{N} Q_n\delta\left(\frac{\mathrm{d}\Phi_n}{\mathrm{d}t}\right) = \sum_{n=1}^{N} Q_n\delta U_n = \delta E^{\mathrm{e}}, \tag{1.23}$$

taking into account (1.23) in integrated (1.20) and taking into account (1.21) and (1.22) we obtain

$$\begin{aligned} S &= \int_{t_1}^{t_2}\left[-\delta L + \sum_{n^*=1}^{N^*} I_{n^*}\delta Q_{n^*} - \underline{\sum_{n=1}^{N}\frac{\mathrm{d}}{\mathrm{d}t}\left(Q_n\delta\Phi_n\right)}\right]\mathrm{d}t \\ &= \int_{t_1}^{t_2}\left[-\delta L + \sum_{n^*=1}^{N^*} I_{n*}\delta Q_{n^*}\right]\mathrm{d}t = 0, \end{aligned} \tag{1.24}$$

because, according to Hamilton's principle, the underlined term becomes zero (since we have $\delta\Phi_{n^*}(t_1) = \delta\Phi_{n^*}(t_2) = 0$).

In (1.24), E^{e} is the electric energy of the circuit that is the sum of all energies of the individual elements (the conductors) and expressed in terms of the voltage U_n. In turn, E^{m} is the function of magnetic energy of the circuit that is the sum of the magnetic energies of all its conductors. The Lagrangian function $L = E^{\mathrm{m}} - E^{\mathrm{e}}$ and the adopted generalized coordinates, that is, the voltage U_n and the magnetic flux Φ_n, will be allowed if they satisfy Kirchhoff's law $U_n = \frac{\mathrm{d}\Phi_n}{\mathrm{d}t}$.

From Hamilton's principle follow directly Lagrange's equations (see Chap. 3 of [3]). We will derive two elementary forms of Lagrange's equations of the second kind in relation to generalized coordinates Q_n (the charge) and Φ_n (the magnetic flux).

In the first case, according to (1.19), the Lagrangian of the electrical system is equal to

$$L = E^{\mathrm{m}}(\dot{Q}_n) + E^{\mathrm{e}}(Q_n), \qquad n = 1, \ldots, N, \tag{1.25}$$

where N denotes the number of generalized coordinates. Work done by non-conservative elements can be expressed by independent generalized coordinates Q_{n*} in the following way:

$$\sum_{n*=1}^{N*} U^*_{n*} \delta Q_{n*} = \sum_{n=1}^{N} U_n \delta Q_n, \tag{1.26}$$

and Lagrange's equations of the second kind in this case take the forms

$$\frac{\mathrm{d}}{\mathrm{d}t}\left(\frac{\partial L}{\partial \dot{Q}_n}\right) - \frac{\partial L}{\partial Q_n} = U_n, \qquad n = 1, \ldots, N, \tag{1.27}$$

where U_n is the generalized voltage corresponding to the generalized charge Q_n. Non-homogeneous Lagrange (1.27) after the introduction of a dissipation function

$$D(\dot{Q}) = \frac{R\dot{Q}^2}{2} \tag{1.28}$$

will take the form of homogeneous equations

$$\frac{\mathrm{d}}{\mathrm{d}t}\left(\frac{\partial L}{\partial \dot{Q}_n}\right) + \frac{\partial D}{\partial \dot{Q}_n} - \frac{\partial L}{\partial Q_n} = 0 \tag{1.29}$$

because

$$U_n = -\frac{\partial D}{\partial \dot{Q}_n}. \tag{1.30}$$

In the second case, according to (1.24), the Lagrangian of the electrical system is equal to

$$L = E^{\mathrm{m}}(\dot{\Phi}_n) - E^{\mathrm{e}}(\Phi_n), \qquad n = 1, \ldots, N, \tag{1.31}$$

Fig. 1.4 A resistor R as an example of a non-conservative conductor

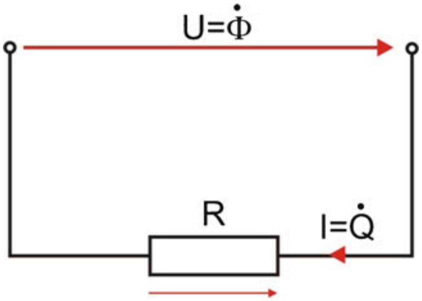

where $n = 1, \ldots, N$ denotes independent generalized coordinates of magnetic fluxes. In this case the work done by non-conservative elements is expressed by

$$\sum_{n^*=1}^{N^*} I_{n^*}^{*} \delta \Phi_{n^*} = \sum_{n=1}^{N} I_n \delta \Phi_n, \tag{1.32}$$

where I_n is the generalized current intensity corresponding to the generalized magnetic flux Φ_{n^*}, or by the dissipation function D, which will be shown on examples. Lagrange's equations for this case take the form

$$\frac{\mathrm{d}}{\mathrm{d}t}\left(\frac{\partial L}{\partial \dot{\Phi}_n}\right) + \frac{\partial L}{\partial \Phi_n} = I_n, \quad n = 1, \ldots, N. \tag{1.33}$$

Non-homogeneous Lagrange (1.33), following the introduction of a dissipation function

$$D(\dot{\Phi}) = \frac{\dot{\Phi}^2}{2R}, \tag{1.34}$$

will take the homogeneous form

$$\frac{\mathrm{d}}{\mathrm{d}t}\left(\frac{\partial L}{\partial \dot{\Phi}_n}\right) + \frac{\partial D}{\partial \dot{\Phi}} - \frac{\partial L}{\partial \Phi_n} = 0, \tag{1.35}$$

because

$$I_n = -\frac{\partial D}{\partial \dot{\Phi}}. \tag{1.36}$$

Finally, let us consider virtual work done on a non-conservative element (a resistor R) with the application of two different generalized coordinates, that is, the charge Q and the magnetic flux Φ (Fig. 1.4).

Work done on the non-conservative element can be positive (supplied energy) or negative (removed energy). In the case of the resistor shown in Fig. 1.4, the virtual work can be expressed in two ways:

(a) By the generalized charge

$$U\delta Q = -RI\delta Q = -R\dot{Q}\delta Q; \tag{1.37}$$

(b) By the generalized magnetic flux

$$I\delta\Phi = -\frac{U}{R}\delta\Phi = -\frac{\dot{\Phi}}{R}\delta\Phi, \tag{1.38}$$

where in both cases the minus sign denotes energy losses.

In the case of an ideal voltage generator, the voltage variation and, consequently, the variation of the flux change in time is equal to zero, and in this case virtual work can be expressed only in one way, that is, in terms of the variation of generalized charge of the form

$$U\delta Q = U_*\delta Q_*, \tag{1.39}$$

where the voltage of an ideal generator is denoted by U_*.

In turn, in the case of an ideal current intensity generator, the virtual work can be expressed only by changes in the generalized magnetic flux Φ, and it is equal to

$$I(t)\delta\Phi = I_*(t)\delta\Phi, \tag{1.40}$$

because in this case $\delta I = 0$.

Example 1.1. Derive equations of dynamics of electromagnetic processes in the circuit presented in Fig. 1.5 by means of the two methods described earlier.

(a) We choose charges Q_1 and Q_2 as generalized coordinates. The circuit is divided into two loops in which flow the currents $I_n(t) = \dot{Q}_n(t)$, $n = 1, 2$. However, these two generalized coordinates are dependent since

$$\dot{Q}_2 = \dot{Q}_1 + \dot{Q}_0,$$

where $\dot{Q}_0 = I(t)$.

Lagrange's (1.29) in this case takes the form

$$\frac{\mathrm{d}}{\mathrm{d}t}\left(\frac{\partial E^{\mathrm{m}}}{\partial \dot{Q}_1}\right) + \frac{\partial D}{\partial \dot{Q}_1} - \frac{\partial E^{\mathrm{e}}}{\partial Q_1} = 0,$$

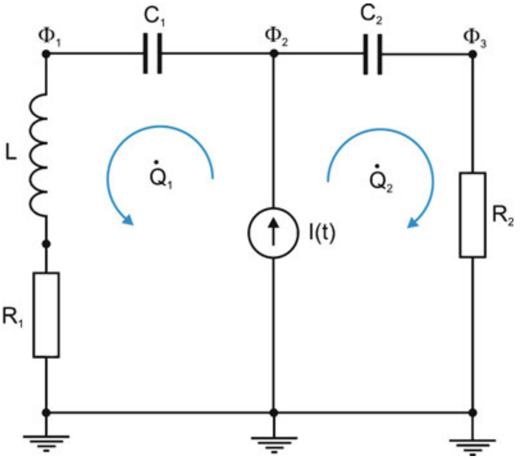

Fig. 1.5 Electric circuit constructed from two capacitors C_1 and C_2, resistors R_1 and R_2, an inductor L, and ideal current generator $I(t)$

where

$$E^{\mathrm{m}} = \frac{1}{2} L \dot{Q}_1^2, \quad E^{\mathrm{e}} = \frac{Q_1^2}{2C_1} + \frac{Q_2^2}{2C_2}, \quad D = \frac{1}{2} R_1 \dot{Q}_2^2 + \frac{1}{2} R_2 \dot{Q}_1^2.$$

We successively calculate

$$\begin{aligned}
\frac{\partial E^{\mathrm{m}}}{\partial \dot{Q}_1} &= L\dot{Q}_1, \qquad \frac{\mathrm{d}}{\mathrm{d}t}\left(\frac{\partial E^{\mathrm{m}}}{\partial \dot{Q}_1}\right) = L\ddot{Q}_1, \\
\frac{\partial E^{\mathrm{e}}}{\partial Q_1} &= \frac{Q_1}{C_1} + \frac{Q_1 + Q_0}{C_2} = Q_1\left(\frac{C_1 + C_2}{C_1 C_2}\right) + \frac{Q_0}{C_2}, \\
\frac{\partial D}{\partial \dot{Q}_1} &= (R_1 + R_2)\,\dot{Q}_1 + R_1 \dot{Q}_0,
\end{aligned}$$

and eventually obtain

$$L\ddot{Q}_1 + (R_1 + R_2)\,\dot{Q}_1 + \frac{C_1 + C_2}{C_1 C_2} Q_1 = -RI(t) - \frac{1}{C_2}\int_0^t I(t)\mathrm{d}t.$$

(b) We choose magnetic fluxes Φ_n for $n = 1, 2, 3$ as generalized coordinates. Lagrange's equations (1.35) in this case take the form

$$\frac{\mathrm{d}}{\mathrm{d}t}\left(\frac{\partial E^{\mathrm{e}}}{\partial \dot{\Phi}_n}\right) + \frac{\partial D}{\partial \dot{\Phi}_n} - \frac{\partial E^{\mathrm{m}}}{\partial \Phi_n} = 0, \qquad n = 1,\ 2,\ 3,$$

where

$$
\begin{aligned}
E^{\mathrm{e}} &= \frac{C_1}{2}\left(\dot{\Phi}_2 - \dot{\Phi}_1\right)^2 + \frac{C_2}{2}\left(\dot{\Phi}_3 - \dot{\Phi}_2\right)^2, \qquad E^{\mathrm{m}} = \frac{\Phi_1^2}{2L}. \\
D &= \frac{\dot{\Phi}_1^2}{2R} + \frac{\dot{\Phi}_3^2}{2R_2} - \frac{\dot{\Phi}_2^2}{2} \\
\dot{\Phi}_2 &= I(t)
\end{aligned}
$$

We successively calculate

$$
\begin{aligned}
&\frac{\partial E^{\mathrm{e}}}{\partial \dot{\Phi}_1} = -C_1\left(\dot{\Phi}_2 - \dot{\Phi}_1\right), \qquad \frac{\partial E^{\mathrm{e}}}{\partial \dot{\Phi}_2} = \left(C_1 + C_2\right)\dot{\Phi}_2 - C_1\dot{\Phi}_1 - C_2\dot{\Phi}_3, \\
&\frac{\partial E^{\mathrm{e}}}{\partial \dot{\Phi}_3} = C_2\left(\dot{\Phi}_3 - \dot{\Phi}_2\right), \qquad \frac{\partial E^{\mathrm{m}}}{\partial \Phi_1} = \frac{\Phi_1}{L}, \qquad \frac{\partial D}{\partial \dot{\Phi}_1} = \frac{\dot{\Phi}_1}{R}, \\
&\frac{\partial D}{\partial \dot{\Phi}_2} = -I(t), \qquad \frac{\partial D}{\partial \dot{\Phi}_3} = \frac{\dot{\Phi}_3}{R_2}.
\end{aligned}
$$

Eventually, from Lagrange's equations we obtain the following differential equations:

$$
\begin{aligned}
\ddot{\Phi}_1 - \ddot{\Phi}_2 + \frac{\dot{\Phi}_1}{R_1C_1} + \frac{\Phi_2}{C_1L} &= 0, \\
-C_1\ddot{\Phi}_1 + \left(C_1 + C_2\right)\ddot{\Phi}_2 - C_2\ddot{\Phi}_3 &= I(t), \\
-\ddot{\Phi}_2 + \ddot{\Phi}_3 + \frac{\dot{\Phi}_3}{R_2C_2} &= 0.
\end{aligned}
$$

As results we obtained the system of three non-autonomous linear differential equations, so the problem is more complex than it was in (a).

1.2 Dynamical Processes in Mechatronic Systems

Differential equations describing dynamical processes in mechatronic systems can be derived from one of Hamilton's principles, which for cases of mechanical and electrical systems was described respectively in Chaps. 3 and 4 of [3].

If we number independent mechanical generalized coordinates q_k using index k (K in total) and independent electrical generalized coordinates Q_n or Φ_n using index n (N in total), and if for the description of the electrical system as generalized coordinates we take charges Q_n, then the Lagrangian of a mechatronic system (mechanical and electrical) will take the form

$$L\left(q_k, \dot{q}_k, Q_n, \dot{Q}_n\right) = T_c + E^{\mathrm{m}} - V - E^{\mathrm{e}}. \tag{1.41}$$

The preceding equation describes the energy of conservative mechatronic systems, and the energy of non-conservative mechatronic systems is equal to

$$\delta W = \sum_{k=1}^{K} Q_k^F \delta q_k + \sum_{n=1}^{N} U_n \delta Q_n, \tag{1.42}$$

where Q_k^F denote generalized forces in the mechanical part of a mechatronic system.

Lagrange's equations in this case take the form

$$\frac{\mathrm{d}}{\mathrm{d}t}\left(\frac{\partial L}{\partial q_k}\right) + \frac{\partial D}{\partial \dot{q}_k} - \frac{\partial L}{\partial q_k} = Q_k, \qquad k = 1, \ldots, K, \tag{1.43}$$

$$\frac{\mathrm{d}}{\mathrm{d}t}\left(\frac{\partial L}{\partial \dot{Q}_n}\right) - \frac{\partial L}{\partial Q_n} = U_n, \qquad n = 1, \ldots, N, \tag{1.44}$$

where Q_k in (1.43) denotes the generalized force (moment of force), Q_n in (1.44) the generalized charge as a generalized coordinate, and D the mechanical dissipation function.

If for the description of the electrical part we take as generalized coordinates the magnetic fluxes Φ_n, then the Lagrangian of conservative elements of a conservative mechatronic system is equal to

$$L\left(q_k, \dot{q}_k, \Phi_n, \dot{\Phi}_n\right) = T_c + E^{\mathrm{e}} - V - E^{\mathrm{m}}. \tag{1.45}$$

Variation in the work of non-conservative elements of a mechatronic system is equal to

$$\delta W = \sum_{k=1}^{K} Q_k \delta q_k + \sum_{n=1}^{N} I_n \delta \Phi_n. \tag{1.46}$$

In this case, Lagrange's equations have the form

$$\frac{\mathrm{d}}{\mathrm{d}t}\left(\frac{\partial L}{\partial \dot{q}_k}\right) + \frac{\partial D}{\partial \dot{q}_k} - \frac{\partial L}{\partial q_k} = Q_k, \qquad k = 1, \ldots, K, \tag{1.47}$$

$$\frac{\mathrm{d}}{\mathrm{d}t}\left(\frac{\partial L}{\partial \dot{\Phi}_n}\right) - \frac{\partial L}{\partial \Phi_n} = I_n, \qquad n = 1, \ldots N. \tag{1.48}$$

In Lagrange's equations associated with the mechanical part of the system described by (1.43) and (1.47), particular components of the Lagrangian were already described earlier in Chap. 3 of [3], whereas particular components associated only with the electrical part are described subsequently in this chapter.

1.2.1 Mechatronic Transducers

Important components of mechatronic systems are transducers of different types that transform electrical energy into mechanical energy and vice versa.

In applications, we deal with various transducers transforming one kind of energy into completely other kinds. This takes place especially in the metrology of mechanical quantities, where various dynamical processes are measured with electrical methods. Then the mechatronic transducer plays the role of a sensor; it is possible to distinguish two types of sensors.

Changes in mechanical processes generate in *modulating sensors (passive sensors)* changes in electrical quantities such as voltage, resistance, capacitance, inductance, current intensity, frequency of current, or phase shift.

One may distinguish the following *modulating sensors*:

(a) Resistive (resistance of the sensor depends on its geometry).
(b) Thermometric (resistance of the sensor depends on its temperature).
(c) Photoelectric (energy of radiation changes the sensor's resistance).
(d) Inductive (induction of the sensor depends on its geometry).
(e) Magnetoelastic (magnetic permeability of a ferromagnetic material depends on mechanical stress).
(f) Capacitive (capacitance of the sensor depends on its geometry, configuration of electrodes, and permittivity of the medium).

The second type of sensor includes *self-generating sensors (active sensors)* such as

(a) Dynamic (here the phenomenon of electromagnetic induction is used).
(b) Thermoelectric (here the phenomenon of generation of a thermoelectric force resulting from temperature difference is used).
(c) Piezoelectric (here the piezoelectric effect is used).

Later we will describe briefly some sensors that transform mechanical energy into electrical energy and vice versa, all the while focusing on the derivation of approximate mathematical models of such simple mechatronic systems.

1. *Resistive Displacement Transducers*
   Resistive displacement transducers transform linear or rotational displacement into constant or variable voltage of the current as a result of changes in resistance caused by the displacement. Figure 1.6 shows a schematic of such a transducer with linear displacement.

   According to Fig. 1.6 we have

$$\begin{gathered} I = I_1 + I_2, \quad R_1 + R_2 = R_0, \quad R_1/R_0 = x/l_0, \\ I_1 R_1 = I_2 R_3, \quad U_3 = R_3 I_2, \quad U_0 = I_1 R_2 + I_2 R_3. \end{gathered} \tag{1.49}$$

Fig. 1.6 Schematic diagram of a resistive linear displacement transducer

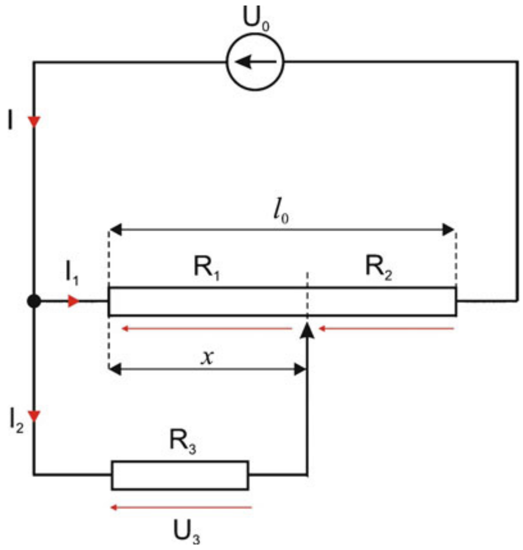

From the preceding equation we determine

$$U_3 = U_0 \frac{R_1}{R_0} \tag{1.50}$$

or, in equivalent form,

$$U_3 = U_0 \frac{x}{l_0}. \tag{1.51}$$

This means that the input signal x is proportional to the voltage U_3 measured on the resistor R_3.

2. *Resistance-based Sensors*
Resistance of a sensor is described by the equation

$$R = \frac{\rho l}{A}, \tag{1.52}$$

where ρ is the resistivity of the conductor material, l its length, and A its cross section. Resistance-based sensors include carbon sensors, fluid sensors, strain gauges, and others.

In the mechanics of deformable bodies for the measurement of stresses and displacements, strain gauges are commonly applied. If we glue a strain gauge onto the mechanical element being loaded, then, under the influence of stress, it changes its geometrical dimensions, and thus its resistance R changes according to (1.52).

Applying the logarithm function to both sides of (1.52), and then differentiating, we obtain

$$\frac{\mathrm{d}R}{R} = \frac{\mathrm{d}\rho}{\rho} + \frac{\mathrm{d}l}{l} - \frac{\mathrm{d}A}{A}. \tag{1.53}$$

Introducing a deformation sensitivity coefficient

$$\alpha = \frac{\mathrm{d}R}{R} \bigg/ \frac{\mathrm{d}l}{l}, \tag{1.54}$$

from (1.53) we obtain

$$\alpha = 1 + 2\nu + \frac{\rho_r}{\varepsilon}, \tag{1.55}$$

where

$$\nu = -\frac{1}{2}\left(\frac{\mathrm{d}A}{A}\right) \bigg/ \left(\frac{\mathrm{d}l}{l}\right), \quad \rho_r = \frac{\mathrm{d}\rho}{\rho}, \quad \varepsilon = \frac{\Delta l}{l}. \tag{1.56}$$

According to Hooke's law for a unidirectional state of deformation we have

$$\varepsilon = \frac{F}{EA}, \tag{1.57}$$

where E is Young's modulus of the resistive material and F is a tensile (compressive) force.

From (1.55), taking into account (1.54), (1.56), and (1.57), and replacing the differential operator with increment Δ, we obtain

$$\frac{\Delta R}{R} = \frac{F}{A}\frac{\alpha}{E} = C\sigma, \tag{1.58}$$

where $\sigma = F/A$ is the stress and $C = \alpha/E$ is constant for the given tensometer.

From (1.58) it follows that the relative change in resistance of the strain gauge is proportional to the change of stress existing in the sensor (the resistance wire).

3. *Inductive Transducers*

The operation of inductive transducers relies on changes in inductive resistance during the displacement of an armature Z outside the ferromagnetic core R, which is shown in Fig. 1.7.

If we take the displacement x for the input quantity, then through the coils of inductance L (according to Ohm's law) in the electric circuit will flow the current of intensity

$$I = \frac{U}{R_L} = \frac{U}{\sqrt{R^2 + (\omega L)^2}}, \tag{1.59}$$

where R_L is the inductive resistance and ωL the inductive reactance of the coil.

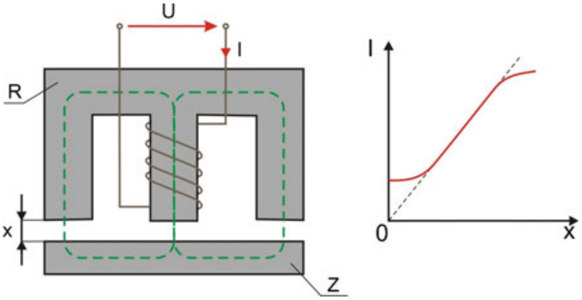

Fig. 1.7 Schematic diagram of an inductive transducer (**a**) and function $I(x)$ (**b**)

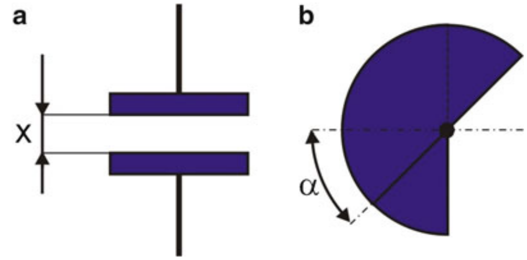

Fig. 1.8 Schematic diagram of a capacitive transducer of linear displacement (**a**) and angular displacement (**b**)

The inductance of the coil is equal to

$$L \cong \frac{0.2\pi N^2 A}{X} 10^{-8}, \tag{1.60}$$

where A denotes the cross-section area of the magnetic field and N is the number of turns of the coil winding. In practice $R \ll \omega L$, and in view of that $R_L \cong \omega L$. According to (1.59) we obtain

$$I(t) = \frac{Ux}{0.2\pi N^2 A\omega} 10^8 \equiv Cx(t), \tag{1.61}$$

where C is a constant characteristic for the given inductive sensor.

From (1.61) it follows that the current flowing in the coil winding is proportional to the air gap, and the ammeter measuring current intensity I can be calibrated directly in the units of gap length.

4. *Capacitive Transducers*

In a capacitive transducer, the input quantity is linear or angular displacement, and the output quantity is electrical capacitance (Fig. 1.8)

In the case of the schematic in Fig. 1.8a, the relationship $C(x)$ is described by the following equation:

$$C = \frac{\varepsilon A}{4\pi x}, \tag{1.62}$$

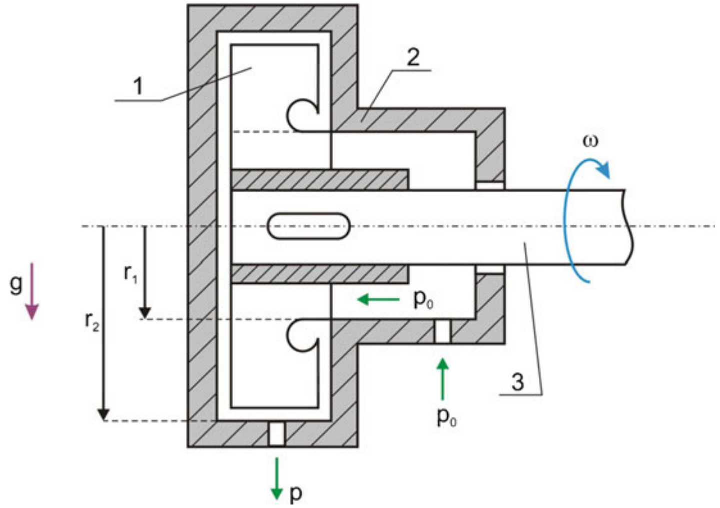

Fig. 1.9 Transducer for measurement of angular velocity ω

where ϵ is a dielectric constant, A denotes the active area of the capacitor, and x is the distance between capacitor plates.

In the case of the schematic from Fig. 1.8b we have

$$C = \frac{\varepsilon A}{4\pi d}\left(1 - \frac{\alpha}{\pi}\right), \tag{1.63}$$

where d is the distance between the rotor plates of the capacitor.

Capacitive sensors allow for a change in the capacitance not only by changes in the distance between plates (Fig. 1.8a) but also by changes in the active area of the capacitor plates or by the application of different dielectrics, e.g., air, or a layer of material of a different dielectric constant between the plates of the capacitor. Changes in mechanical quantities are registered through changes in the capacitance and then measured in an electrical measuring system. Capacitive sensors are characterized by a small force required for the displacement of the moving electrode of the sensor. Moreover, they enable contactless measurement and possess a small moving-electrode mass and large sensitivity.

5. *Angular Velocity Transducers*

An angular velocity transducer (Fig. 1.9) can be a mechanical part of a system, but, as distinct from the problems of the mechanics of a rigid body described so far, here we address the mechanics of fluid flow (a hydraulic transducer or gas flow transducer).

The measured angular velocity of shaft 3 is transmitted onto a paddle mixer 1 connected to casing 2. The pressure of a gas or liquid p_0 entering the working

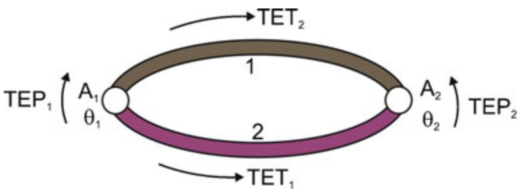

Fig. 1.10 Two conductors joined together (the thermocouple) and four thermoelectric forces

part of the angular velocity sensor passes through the paddle mixer, and at a hole in the casing the pressure p is seen, described by the equation

$$p = p_0 + \frac{\rho}{2g}\omega^2\left(r_2^2 - r_1^2\right), \tag{1.64}$$

where ρ is the density of the medium

6. *Temperature Transducers*
In this case, the change in resistance of a conductor R_Θ is associated with a change in temperature Θ according to the equation

$$R_\theta = R_0\left(1 + \alpha\left(\theta - \theta_0\right)\right), \tag{1.65}$$

where R_0 is the resistance of the conductor at temperature Θ_0. The coefficient $\alpha[°\mathrm{C}^{-1}]$ for iron is equal to 0.002–0.006, for aluminium 0.0045, and for carbon 0.0007.

Such a direct temperature measurement using temperature sensors called thermometers can span a range from -170°C to 700°C.

Also in use are *thermistors*, that is, semiconductors of large temperature coefficients of resistance. The dependency of resistivity (a specific resistance) of a thermistor on temperature is described by the equation

$$\rho_\theta = \rho_0 e^{(\alpha/\theta - \alpha/\theta_0)}, \tag{1.66}$$

where ρ_0 and ρ_Θ are the resistivities of a resistor corresponding to temperatures Θ_0 and Θ measured in degrees Kelvin, and α is a constant ($\sim 4,000$). Thermistors are used to measure temperature in a range of 60°C–120°C with an accuracy of up to 0.0005°C.

7. *Thermocouples*
Thermocouples are used in various kinds of automatic control systems for the measurement of temperature. A thermocouple consists of two conductors, welded together, of different properties of resistance change vs. the measured temperature, e.g., one electrode is made of pure platinum and the other is an alloy of platinum (90%) and rhodium (10%). Such thermocouples can be used to measure temperatures reaching up to 1,600°C.

If two metals 1 and 2 are joined together (Fig. 1.10) and their points of contact A_1 and A_2 are at different temperatures Θ_1 and Θ_2, then four thermoelectric

Fig. 1.11 A thermocouple (1, 2) forming a circuit with metal 3

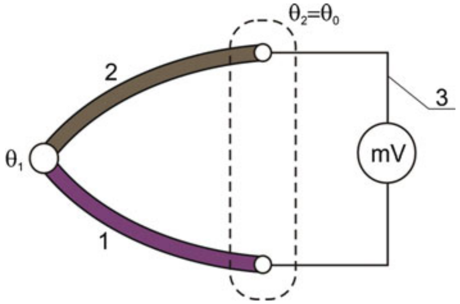

forces e will appear in the closed circuit. “Cold” ends of the thermocouple are connected to the system of potentiometers, and the “hot” end is in contact with a medium (an element) whose temperature is to be measured.

Undesirable changes in ambient temperature affecting the cold ends of a thermocouple are compensated by introducing a bridge with a thermometer R_t that measures the temperature of the cold ends.

The force TEP_i is the *Peltier thermoelectric force* at the junction A_i and the force TET_i is the *Thomson thermoelectric force* in the wire i $(i = 1, 2)$. The net thermoelectric force is equal to

$$TE = TEP_1 - TEP_2 + TET_2 - TET_1. \tag{1.67}$$

Because of difficulties in the identification of particular Peltier and Thomson thermoelectric forces, the following equation is used:

$$TE = TE\left(\theta_1\right) - TE\left(\theta_2\right), \tag{1.68}$$

where $TE(\varTheta_1)$ is the thermoelectric force at point A_1 (temperature $\varTheta_1$) and $TE(\varTheta_2)$ is the thermoelectric force at point A_2 (temperature $\varTheta_2$).

In practice two metals 1 and 2 are used for temperature measurement by means of their connection to a meter (e.g., a millivoltmeter). In this way, an additional metal 3 is introduced into the circuit, and the measuring wires and internal circuit of the meter are made of this third metal (Fig. 1.11).

The thermoelectric force in the circuit shown in Fig. 1.11 is equal to

$$TE = TE_{12}\left(\theta_1\right) + TE_{23}\left(\theta_0\right) + TE_{31}\left(\theta_0\right). \tag{1.69}$$

Because for $\varTheta = \varTheta_0$ we have $TE(\varTheta_0) = 0$, from (1.69) we obtain

$$TE_{23}\left(\theta_0\right) + TE_{31}\left(\theta_0\right) = -TE_{12}\left(\theta_0\right). \tag{1.70}$$

Substituting (1.70) into (1.69) we obtain

$$TE = TE_{12}\left(\theta_1\right) - TE_{12}\left(\theta_0\right). \tag{1.71}$$

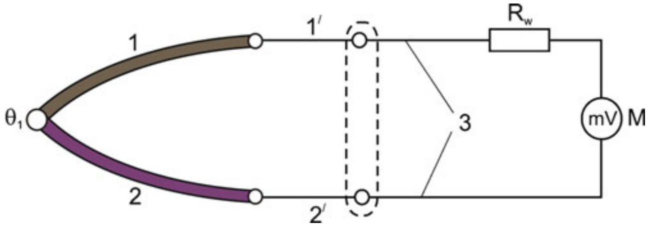

Fig. 1.12 Swing system applied to temperature measurement

The preceding equation holds on the condition that the introduction of a third metal into the system composed of metals 1 and 2 does not affect the value of the net thermoelectric force and both ends of metal 3 are at the same temperature.

The oldest, simplest, and the most commonly used system of thermoelectric thermometer in industry is the schematic of the so-called swing thermometer shown in Fig. 1.12.

In the schematic in Fig. 1.12, 1 and 2 denote thermoelements, 1′ and 2′ are compensating wires, R_w is the compensating resistor (selected in such a way that the external resistance of the meter $R_z = R_{zn}$, where R_{zn} is the nominal resistance of the meter, calibrated in degrees Celsius), and M is a millivoltmeter. The millivoltmeter M measures the voltage U, which is equal to

$$U = ET\frac{R_m}{R_z + R_m}, \tag{1.72}$$

$$R_z = R_{12} + R_{1'2'} + R_3 + R_w, \tag{1.73}$$

where R_{12} is the resistance of thermoelements 1 and 2, $R_{1'2'}$ is the resistance of compensating wires 1′ and 2′, R_3 is the resistance of connecting wires 3, and ET denotes the thermoelectric force of a thermoelement at the measured temperature Θ_1 and reference temperature Θ_0.

8. *Pressure Transducers*

Transducers for pressure measurement can be divided into two types. The first type includes transducers whose principal working elements are mechanical elastic elements, the deformations of which are transformed into electrical signals using capacitive elements, inductive elements, or strain gauges.

The second type includes transducers where the main working elements are magnetoelastic cylinders.

Figure 1.13 shows examples of sensors of the first type for measurement of pressure of a flowing gas (a) and liquid (b).

The bellows sensor for pressure measurement of a gas consists of a tube of undulating shape (a bellows) 1, a rack 2, and a pinion 3 connected to the terminal of the potentiometer 4. The pressure p causes stretching of the bellows 1 and displacement of the rack 2, and consequently a change in position

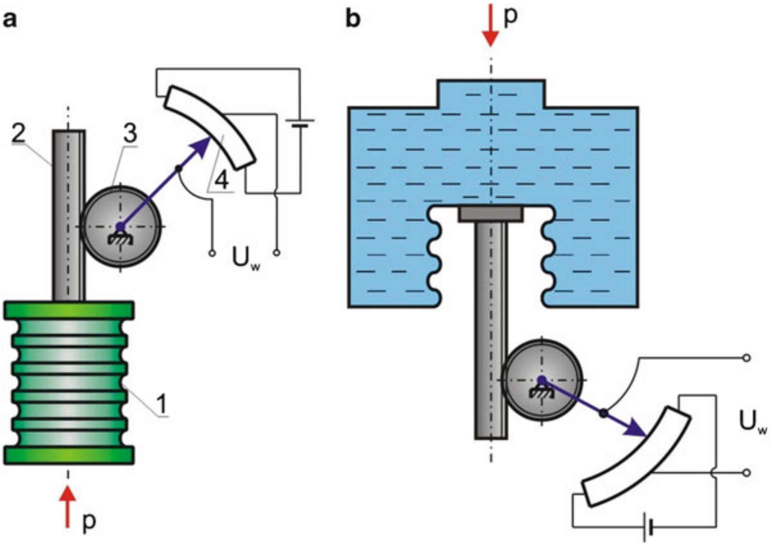

Fig. 1.13 Schematic diagram of pressure sensor of a flowing gas (**a**) and flowing liquid (**b**)

of the potentiometer terminal, which leads to a change in output voltage U_w. On the assumption that the relationship $U_w(p)$ is linear, the equation connecting the output voltage and the pressure has the form

$$U_w = \alpha p, \tag{1.74}$$

where α is a proportionality factor. Displacement of the rack x can be determined after solution of the following second-order differential equation:

$$M\ddot{x} + c\dot{x} + kx = Ap, \tag{1.75}$$

where M denotes the mass of moving parts of the sensor, c is the viscous damping coefficient, k denotes bellows stiffness, and A is the cross-section area of the bellows. The problem can be reduced to a model of second-order inertial elements of the form (see Chap. 6 of [3])

$$T^2\ddot{x} + 2\xi T\dot{x} + x = \alpha p, \tag{1.76}$$

where $T = \sqrt{\frac{M}{k}}$, $\xi = \frac{c}{2\sqrt{kM}}$, $\alpha = \frac{A}{k}$, and the right-hand side of this equation is equal to U_w [see (1.74)].

Equation (1.76) describes also the dynamics of the meter from Fig. 1.11b, and in this case the bellows is filled up with a liquid.

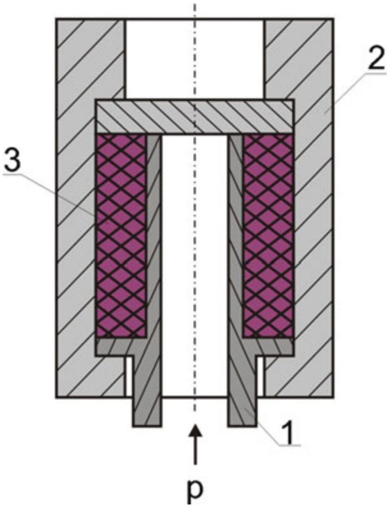

Fig. 1.14 Magnetoelastic element of a pressure sensor

9. *Magnetoelastic Sensors*

   In Fig. 1.14 the schematic of a magnetoelastic element of a (second type) transducer for pressure measurement is shown.

   Axial forces acting on a ferromagnetic element cause a change in the magnetic permeability of this element. The steel pipe 1 was covered with a pipe made of invar alloy. Inside was placed a choking coil 3. The pressure p causes expansion of the pipe 2, which leads to a change in the magnetic permeability of invar μ, which in turn affects the value of self-inductance of the coil according to the equation

   $$L = 0.4\pi N^2 10^{-8} \frac{\mu A}{l}, \tag{1.77}$$

   where N is the number of coil turns, A denotes the cross-section area of the invar pipe, and l is its length. The coil is connected to a bridge, and the change in inductance of the coil results in a change in current intensity proportional to the pressure magnitude.

   The measuring ammeter can be directly calibrated in units of force. Magnetoelastic sensors are also used for the measurement of large static and dynamic forces. The magnetoelastic effect apart from the aforementioned invar is also characteristic of nickel, permalloy, and iron.

10. *Piezoelectric Transducers*

    The piezoelectric effect discovered in 1880 by Marie and Pierre Curie consists in the generation of electric charges on faces of crystals loaded with tensile or compressive forces (e.g., quartz, Seignette's salt, or barium titanate).

In Fig. 1.15 the frequency response of a piezoelectric sensor is shown.

Because the force acting on a sensor plate is usually produced by a moving element of mass m, the signal obtained from the sensor is proportional to the

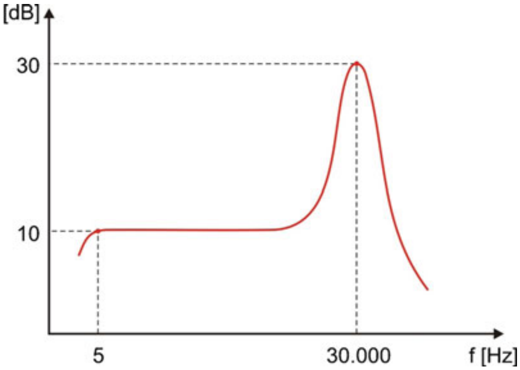

Fig. 1.15 Frequency response of a piezoelectric sensor

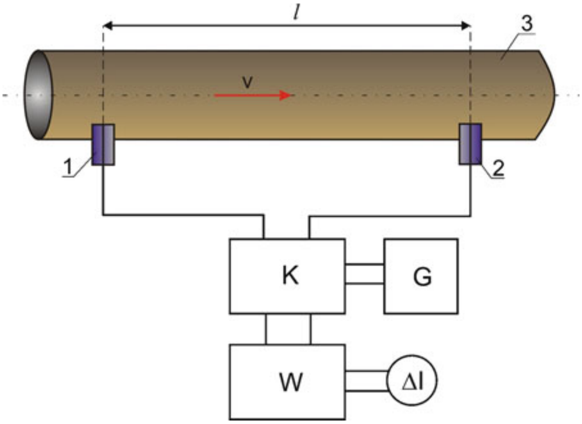

Fig. 1.16 Measurement of flow energy losses by means of piezoelements

acceleration of this element. The operating range of the sensor is 1–300 Hz, and the resonance frequency of this sensor is equal to about 30 kHz.

Piezoelectric sensors have a very wide range of application for the measurement of frequency and acceleration. Their disadvantage is the requirement of dynamic calibration.

The application of piezoelectric transducers is broad, but here we will limit ourselves to determining the loss of energy of fluid flow on the basis of determining the difference in propagation velocity of ultrasonic vibrations. Figure 1.16 shows a schematic of measurement of energy loss of the fluid flowing in pipe 3 with velocity v between two piezoelements 1 and 2 separated by distance l.

The generator G and the phase amplifier are alternately switched in by a commutator K in such a way that the piezoelements act at first as transmitters (radiators) and then as receivers of energy.

The instantaneous voltage of the radiating piezoelement

$$U_1 = U_{10} \sin \omega t, \tag{1.78}$$

and the instantaneous voltage on the receiving piezoelement is equal to

$$U_2 = U_{20} \sin \omega (t - T), \tag{1.79}$$

where T denotes the time it takes the ultrasonic wave to cover distance l.

The phase difference between a steady-state vibration regime (when the medium is stationary) and vibration of a fluid is equal to

$$\Delta\varphi_1 = \frac{l\omega}{c - v}, \tag{1.80}$$

and the difference between the standard vibration and a vibration whose sense is opposite to the velocity of the fluid v is equal to

$$\Delta\varphi_2 = \frac{l\omega}{c + v}, \tag{1.81}$$

where c is the velocity of propagation of ultrasound in the fluid and v is the velocity of the fluid.

The phase difference is equal to

$$\Delta = \Delta\varphi_1 - \Delta\varphi_2 = \frac{2\omega l v}{c^2 - v^2} \cong \frac{2\omega l v}{c^2} \tag{1.82}$$

for $c \gg v$. The voltage of the piezoelement will be inversely proportional to velocity, that is,

$$U_1 = \frac{\alpha}{c + v}, \qquad U_2 = \frac{\alpha}{c - v}, \tag{1.83}$$

where α is a proportionality factor. The values of current intensities in the amplifier are equal to

$$I_1 = \frac{\alpha_1 (c + v)}{\alpha}, \qquad I_2 = \frac{\alpha_1 (c - v)}{\alpha}, \tag{1.84}$$

hence we calculate

$$\Delta I = I_1 - I_2 = \beta v, \tag{1.85}$$

where $\beta = \frac{2\alpha_1}{\alpha}$ is a proportionality factor. From this the conclusion follows that for a constant volume of the pipe through which the fluid flows, losses of the flow will be proportional to the velocity of the flowing fluid.

1.2.2 Magnetic Force in a Single Mechatronic System

This problem was already partly considered in the section concerning inductive transducers. Let the single mechatronic system consist of a magnet core (1) with wounded coil of N turns (2), and armature (3), shown in Fig. 1.17.

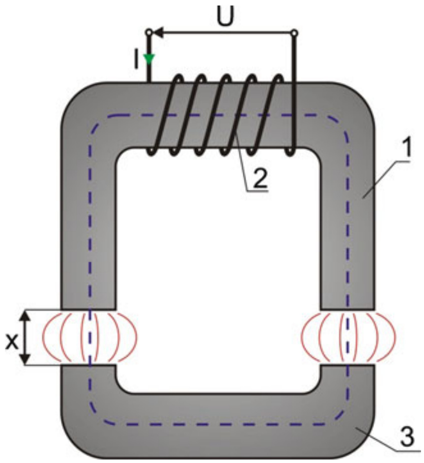

Fig. 1.17 Schematic diagram of a magnetic circuit in system of core (1), armature (3), and two air gaps

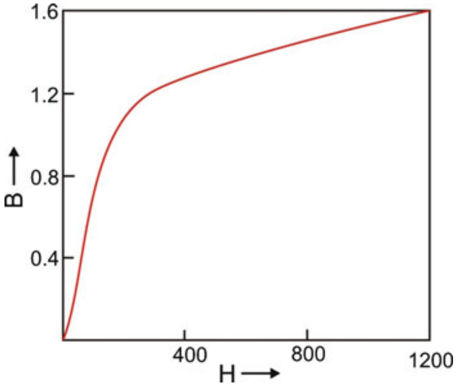

Fig. 1.18 $B(H)$ dependency for ARNON material used for transformer plates

The aim of these considerations is the determination of a magnetic force that attracts the armature (3) to the electromagnet (1) as a function of the current intensity I in the coil, the width of the air gap x, the cross-section area of core A, the length of the ferromagnetic part of the magnetic circuit l_r, and the number of turns of coil winding N. We will neglect the hysteresis phenomenon in the core and assume the magnetic permeability of the air to be equal to magnetic permeability of vacuum. The magnetic induction $B(T)$ generated in the circuit depends on the magnetic field H [A/m], for example, as presented in Fig. 1.18.

Let us note that the function $B(H)$ is bijective, making it is easy to build the inverse function $H(B)$. The aforementioned non-linear functions can be described after the introduction of relative permeability $\mu = \mu(B)$ or $\mu = \mu(H)$, and the function $B(H)$ takes the form

$$B = \mu(H)\mu_0 H, \tag{1.86}$$

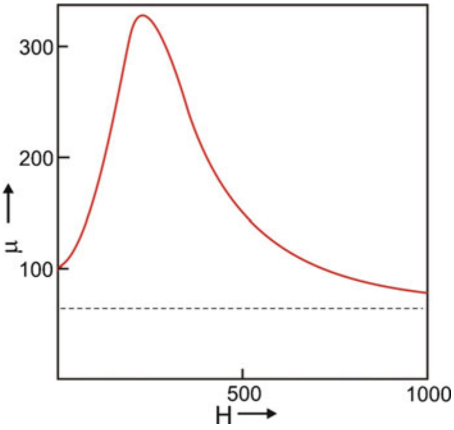

Fig. 1.19 Example of $\mu(H)$ dependency for ARNON material

where μ_0 is the vacuum permeability and is equal to $\mu_0 = 4\pi \cdot 10^{-7}\,[\frac{\mathrm{Vs}}{\mathrm{Am}}]$. A sample plot of the function $\mu(H)$ is shown in Fig. 1.19.

Let us note that $\lim_{H\to\infty} \mu(H) = 1$. From Kirchhoff's voltage law for a magnetic circuit from Fig. 1.18 we obtain

$$I(t) = \frac{(2R_{sz} + R_r)\,\Phi\,(t)}{N} \tag{1.87}$$

$$R_{sz} = \frac{x}{\mu_0 A}, \qquad R_c = \frac{l_r}{\mu_0 \mu A}, \tag{1.88}$$

where R_{sz} (R_r) denotes respectively the *reluctance* of two air gaps (reluctance of the ferromagnetic core and the armature) and $\Phi = \Phi[\mathrm{Tm}^2]$ is the magnetic flux, assumed to be uniform at each point of a magnetic circuit.

From (1.87) we obtain

$$I(t) = \frac{1}{\mu_0 A N}\left(2x + \frac{l_r}{\mu}\right)\Phi\,(t)\,, \tag{1.89}$$

hence

$$\frac{\Phi}{A} = \mu_0 N I \left(\frac{1}{2x + \frac{l_r}{\mu}}\right). \tag{1.90}$$

Because the magnetic flux

$$\Phi = BA, \tag{1.91}$$

from (1.91) and (1.90) we obtain

$$B = \frac{\Phi}{A} = \frac{\mu_0 I N}{2x + \frac{l_r}{\mu(B)}}. \tag{1.92}$$

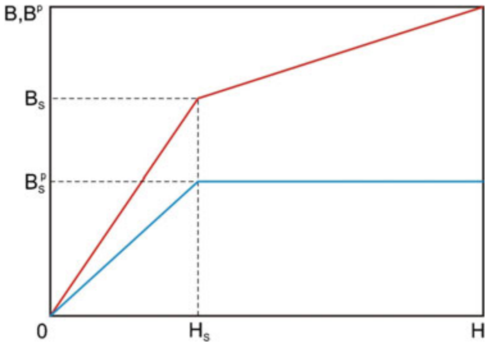

Fig. 1.20 Bilinear characteristics of $B^{\mathrm{p}}(H)$ and $B(H)$

Equation (1.92) is a non-linear algebraic equation, where for fixed parameters we determine function B by means of numerical calculations. From (1.92) and exploiting (1.86) we obtain

$$H = \frac{NI}{2x\mu(H) + l_r}. \tag{1.93}$$

Knowing function H [determined numerically from (1.93)] we determine its corresponding value of magnetic induction from (1.86).

Assuming a uniform magnetic field strength in the air gap, denoted H_0, the potential energy accumulated in the gap is equal to

$$V(x) = \frac{A}{2}\int_0^x BH_0 \mathrm{d}x. \tag{1.94}$$

The desired force acting on the armature is equal to

$$F = 2\frac{V(x)}{\partial x} = ABH_0 = \frac{AB^2}{\mu_0}, \tag{1.95}$$

where during transformations (1.86) and the value $\mu(H_0) = 1$ were used.

The relationship $B(H)$ presented in Fig. 1.18 and the so-called *phenomenon of magnetic polarization of the core* B^{p} as a function of H allow for the introduction of a bilinear magnetization curve. Since it turns out that with an increase of H polarization increases linearly and after passing the value H_{s}, the value of the polarization reaches a constant value $B^{\mathrm{p}} = B_{\mathrm{s}}^{\mathrm{p}}$ for $H \geq H_{\mathrm{s}}$ [1]. Assuming a simplified magnetization model, both $B(H)$ and $B^{\mathrm{p}}(H)$ have the bilinear characteristics shown in Fig. 1.20.

Piecewise linear changes in magnetic induction $B(H)$ and $B^{\mathrm{p}}(H)$ allow for the introduction of the following simplified equation:

$$B = \mu_0 H + B^{\mathrm{p}}. \tag{1.96}$$

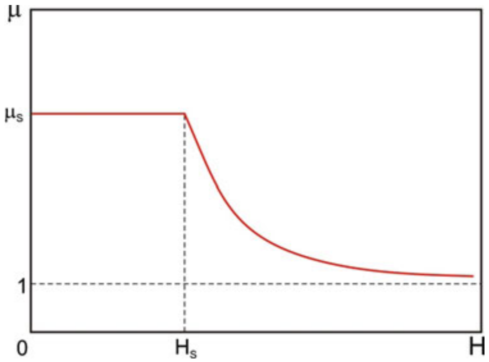

Fig. 1.21 Function of relative magnetic permeability $\mu(H)$ corresponding to the bilinear magnetization curve

The quantities H_s (saturation magnetic field strength), B_s^p (saturation polarization), and B_s (saturation induction), shown in Fig. 1.20, can be taken as material constants. Finally, the approximation of characteristics $B(H)$ can be conducted based on two material constants B_S and H_S, and its bilinear approximation has the form

$$\begin{aligned} B\left(H\right) &= \frac{B_\mathrm{s}}{H_\mathrm{s}} \quad \text{for} \quad 0 \le H \le H_\mathrm{s}, \\ B\left(H\right) &= B_\mathrm{s} + \mu_0\left(H - H_\mathrm{s}\right) \quad \text{for} \quad H > H_\mathrm{S}. \end{aligned} \tag{1.97}$$

To point $B_S(H_S)$ corresponds $\mu_S = \frac{B_S}{\mu_0 H_S}$, and the relative permeability $\mu = \mu(H)$ is described by the two equations

$$\begin{aligned} \mu\left(H\right) &= \mu_s \quad \text{for} \quad 0 \le H \le H_\mathrm{s}, \\ \mu\left(H\right) &= 1 + \frac{H_\mathrm{s}\left(\mu_s - 1\right)}{H} \quad \text{for} \quad H > H_\mathrm{S}, \end{aligned} \tag{1.98}$$

shown in Fig. 1.21.

Kirchhoff's voltage law when the bilinear approximation is used will take the following form:

$$NI = \frac{2x}{\mu_0}B + \begin{cases} l_r \frac{H_\mathrm{s}}{B_\mathrm{s}} B & \text{for} \quad B \le B_\mathrm{s}, \\ l_r\left[\frac{B}{\mu_0} + H_\mathrm{s} - \frac{B_\mathrm{s}}{\mu_0}\right] & \text{for} \quad B > B_\mathrm{s}. \end{cases} \tag{1.99}$$

The desired magnetic force is equal to

$$\begin{aligned} F &= \mu_0 A N^2 \frac{I^2}{\left(2x + \frac{l_r}{\mu_s}\right)^2} \quad \text{for} \quad \frac{\mu_0 N I}{2x + \frac{l_r}{\mu_s}} \le B_\mathrm{s}, \\ F &= \mu_0 A \frac{\left(NI + l_r\left(\frac{B_\mathrm{s}}{\mu_0} - H_\mathrm{s}\right)\right)^2}{\left(2x + l_r\right)^2} \quad \text{for} \quad \frac{\mu_0 N I}{2x + \frac{l_r}{\mu_s}} > B_\mathrm{s}. \end{aligned} \tag{1.100}$$

The simplification often used during the analysis of electromagnetic circuits is the assumption that $2x\mu \ll l_r$, which in many cases is justified, especially for small values of x. In this case from (1.93) we obtain

$$H = \frac{NI}{l_r}, \tag{1.101}$$

and in turn from (1.92) we get

$$B = \frac{\mu_0 NI}{2x + \frac{l_r}{\mu(I)}}. \tag{1.102}$$

The force acting on the armature, according to (1.95), is equal to

$$F = A\frac{\mu_0 N^2 I^2}{\left(2x + \frac{l_r}{\mu(B)}\right)^2}. \tag{1.103}$$

According to Kirchhoff's voltage law, the relationship between the voltage supplying the circuit U and the current intensity in circuit I has the form

$$U = IR - N\frac{\mathrm{d}\Phi}{\mathrm{d}t}, \tag{1.104}$$

where R is the resistance of the winding.

However, in the case under consideration, now changes in the magnetic flux Φ are the result of changes in both the current intensity and the width of the air gap x. Differentiating (1.91) we have

$$\dot{\Phi} = A\dot{B}, \tag{1.105}$$

where, according to (1.102), we have

$$\dot{B} = \mu_0 N\left[\frac{\dot{I}}{2x + \frac{l_r}{\mu(B)}} - \frac{2I\dot{x}}{\left(2x + \frac{l_r}{\mu(B)}\right)^2} + \frac{\dot{B}\frac{\mathrm{d}\mu}{\mathrm{d}B}\frac{l_r}{\mu^2(B)}}{\left(2x + \frac{l_r}{\mu(B)}\right)^2}\right]. \tag{1.106}$$

Complete coupled non-linear algebraic-differential equations describing the electromagnetomechanical (mechatronic) circuit from Fig. 1.17 have the form

$$\begin{aligned} U &= IR - NA\dot{B}, \\ B &= \frac{\mu_0 NI}{2x + \frac{l_r}{\mu(B)}}, \end{aligned} \tag{1.107}$$

and the force F acting on the armature is described by (1.95). If the field strength H is proportional to the current intensity I, then the preceding (1.107) are reduced to one equation of the form

$$U = IR - \frac{\mu_0 NA}{\left(2x + \frac{l_r}{\mu(I)}\right)^2}\left[2x + \frac{l_r}{\mu(I)} + \frac{I l_r}{\mu^2(I)}\frac{\mathrm{d}\mu}{\mathrm{d}t}\dot{I} - 2I\dot{x}\right], \tag{1.108}$$

where $U = U(t)$ is the voltage applied to the mechatronic system. The force F exerted by the electromagnet on the armature is described by (1.103), where the function $\mu = \mu(I)$ occurs in the denominator.

1.3 Magnetic Levitation

Magnetic levitation is a known topic and can be realized in several ways [4–6], but the most spectacular effects can be observed when an electromagnet made of superconductor is used. A simpler way to create a system for the investigation of the levitation phenomenon is to use a system with an infrared light sensor (barrier) that traces the position of the levitating mass placed in the magnetic field generated by the electromagnet.

For the purpose of the experiment presented here the role of sensor is played by the infrared light barrier, which traces the actual position of the cylindrical mass (Fig. 1.22).

The development toward future applications of fast and accurate position control systems used in optoelectronics, computer hardware, precision machining, robotics, and automotive has stimulated high-level engagement in the creation of non-conventional implementations [6,7]. In this section, a numerical analysis devoted to that domain concerning non-contact (frictionless) fixing of some cylindrical mass

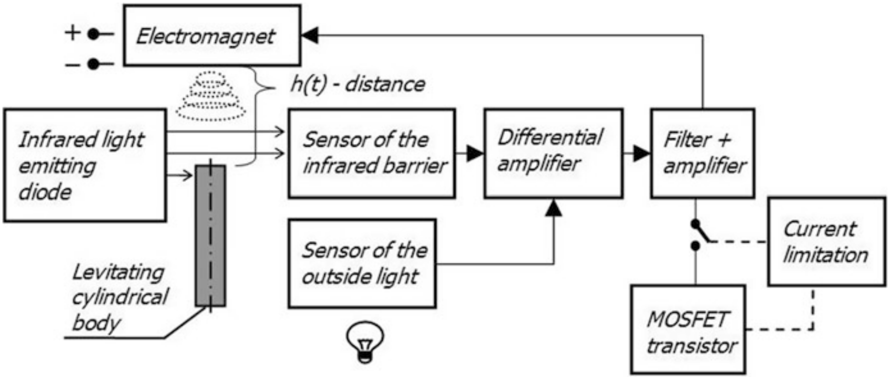

Fig. 1.22 Schematic block diagram of hardware, signal connections, and levitating solid body

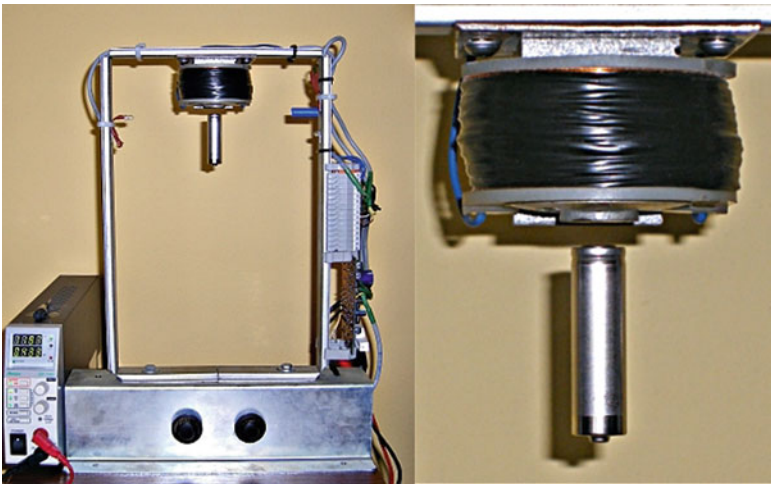

Fig. 1.23 Experimental setup of control system of levitating cylindrical light mass (constructed by Piotr Jędrzejczyk, student of second-degree studies at the Faculty of Mechanical Engineering of the Technical University of Lodz, Poland)

in an alternating magnetic field is carried out [8]. The calculations given are an introductory step to the identification of electromagnet parameters and magnetic fields in the experimental realization of the problem, shown in Fig. 1.22. The mass levitates in the field generated by the electromagnet system supplied by a voltage of 12 V. Next to the numerical algorithm of voltage feedback there a modified PID control [7] of transient oscillations of the levitating light mass was also used. These were recorded until it reached a stable equilibrium position. The results of the experiments are presented on time plots of displacement $h(t)$ measured between the opposite facing surfaces of the electromagnet core and the top surface of the levitating mass.

1.3.1 The Analyzed System

The electronic part of the system uses two light-sensitive resistors, the first one of which acts together with an infrared-light-emitting diode as a simple barrier tracing the cylindrical solid body position. Due to the existence in the surrounding space of many infrared-light-emitting sources such as the sun or lightbulbs (producing disturbance signals to the barrier), the second resistor measures the amount of light coming into the system from the surrounding space. If the barrier sensor is only partially illuminated (the result of being obstructed by the levitating body), the voltage difference appears and is input to the differential amplifier for the generation of the updated value of voltage supplying the electromagnet circuit. Experimental realization of the schematic diagram presented in Fig. 1.22 is shown in Fig. 1.23.

The system shown in Fig. 1.23 can be modeled by a dynamical system of three first-order differential (1.109) describing the motion of the mass levitating in magnetic and gravitational fields and the voltage equation for the electric circuit with alternating current. The meaning of the elements of the system-state vector $\mathbf{x}$ is as follows: $x_1 \rightarrow h$ is the displacement of the levitating mass measured downward from the electromagnet surface, $x_2 \rightarrow \mathrm{d}h/\mathrm{d}t$ the corresponding velocity of the displacement, and $x_3 \rightarrow i$ the electric current in the electromagnet electric circuit.

The governing equations follow:

$$\begin{aligned}
\dot{x}_1(t) &= x_2(t), \\
\dot{x}_2(t) &= g - \frac{k}{m}\left(\frac{x_3(t)}{x_1(t)}\right)^2 + u(t)\,\big|_{1\,\mathrm{case}}, \\
\dot{x}_3(t) &= \frac{1}{L}\left(v(t)\,\big|_{2\,\mathrm{case}} - Rx_3(t)\right),
\end{aligned} \tag{1.109}$$

where the electrical and physical constants are as follows: $L = 0.002\,H$ is the coefficient of inductance, $R = 0.29\,\Omega$ the coefficient of resistance, $k = 10^{-4}\,\mathrm{kg}\cdot\mathrm{m}^2/\mathrm{C}^2$, C the magnetic flux, $m = 0.0226\,\mathrm{kg}$ the mass of the levitating body.

1.3.2 Two Cases of Numerical Control

Voltage $v(t)$ and force excitation $u(t)$ are the two control signals. They are considered in two separate cases, namely: (1) $u(t)$ is feedback from position h in the system with a *PID* controller having the transfer function $\mathrm{PID}(s) = k_P + (s + k_I)/s + k_D s$ inserted into the first axis of the block diagram shown in Fig. 1.24, while $v(t)$ is a constant voltage source of 12 V; (2) a time-dependent control input voltage having the Laplace representation $V(s) = -((k_1 + k_2 s + k_3 s^2)H(s) - k_1 h_0)$ to the analyzed dynamical system working as the plant in the closed-loop control system with feedback from the full state vector (a numerical model of the control strategy is shown in Fig. 1.25). Disturbances coming from any external light sources have been neglected.

Both of the numerical models presented contain characteristics of the operation of an infrared light barrier $\mathrm{IRR}(t) = 1 - b_{\mathrm{IRR}} h(t)^{-2}$. This approximation with damping (sensitivity) constant b_{IRR} measures the amount of infrared light transferred from the emitting diode to the light-sensitive resistor with the levitating body serving as the barrier.

Figure 1.26 shows the well-studied effect of introducing an infrared light barrier. The case for a short range of values of the IRR factor was described as the correct one, being more realistic in relation to the motion of mass m observed on the experimental rig. During this experiment one tries to fix the mass at height $h_f = 1$ cm with the initial condition $h_0 = 3$ cm. It is clear that the mass is quickly attracted to the steady-state position but is achieved in a different manner.

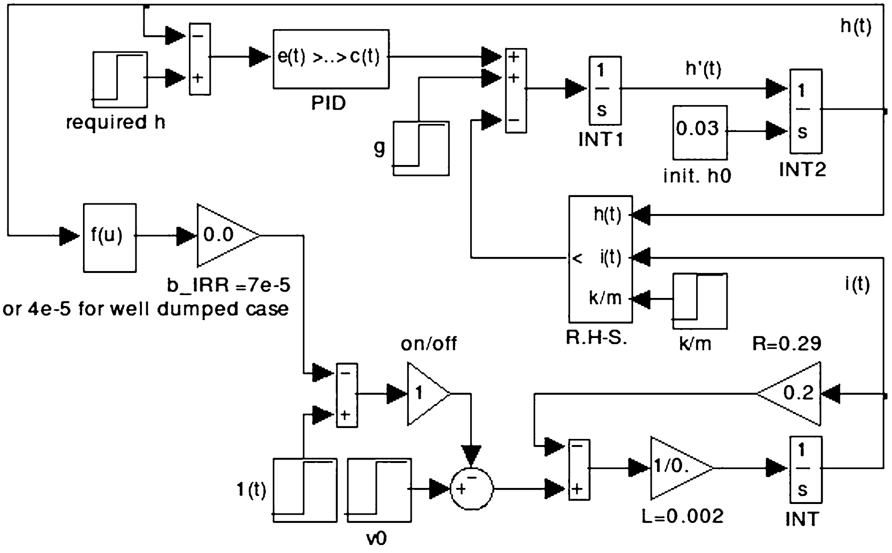

Fig. 1.24 Feedback from displacement of levitating mass in *PID* control for $k_P = 250, k_I = 800, k_D = 13$

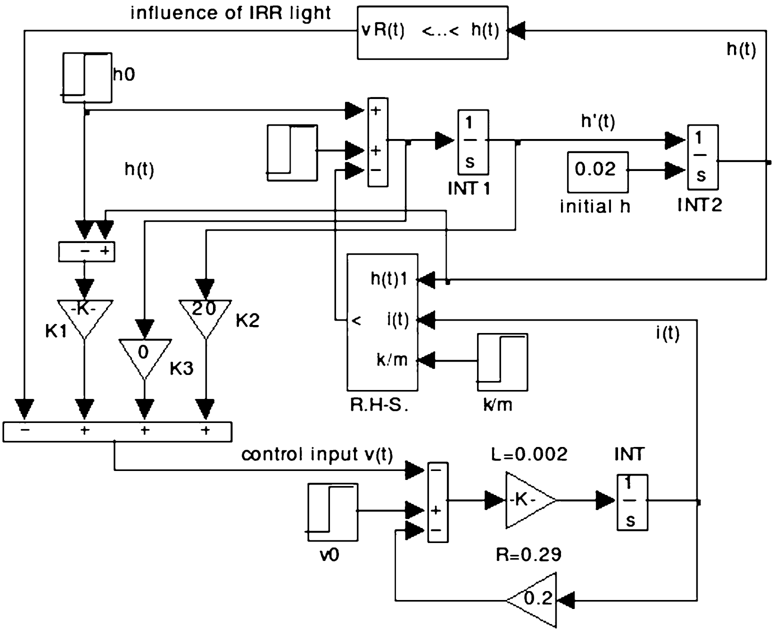

Fig. 1.25 Closed-loop input voltage control with use of full state-vector feedback for $k_1 = 10^3$, $k_2 = 20$, $k_3 = \{0.0, 0.2\}$ in a model made in Simulink

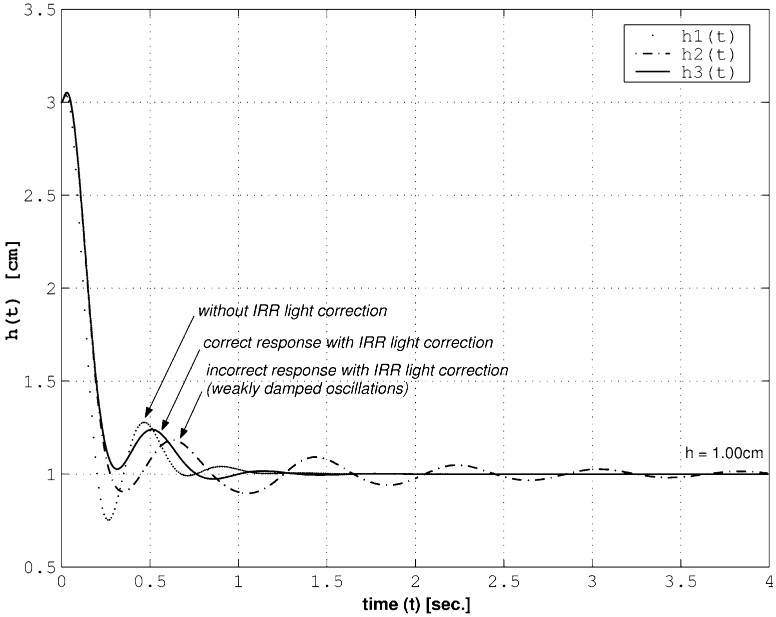

Fig. 1.26 Time plots of $h(t)$ obtained from diagram shown in Fig. 1.24 for different values of the infrared light barrier factor $b_{\mathrm{IRR}\{1,2,3\}} = \{\mathrm{IRR\ off},\ 0.7 \cdot 10^{-4},\ 0.4 \cdot 10^{-4}\}$ in the closed-loop position feedback control and for $h_0 = 3\,\mathrm{cm}$

Frictionless oscillations in the transition to a stable position can be damped very well (Fig. 1.27) with the use of the second case of the control strategy based on feedback from the full state vector, as shown in Fig. 1.25. For a different initial position ($h_0 = 2\,\mathrm{cm}$) of mass m there is visible a quicker (because of the voltage, not external force feedback, as examined in the first approach) and better damped attraction of the mass to the steady-state position. With respect to application of a different method of control (with a control with feedback to the voltage time variable input v), the whole system is characterized by a slightly different dynamics, so the position of convergence changes with the use of larger values of $b_{\mathrm{IRR}\{1,2,3\}} = \{7,\ 0.7,\ 22.2\} \cdot 10^{-4}$. Factor $b_{\mathrm{IRR}\{3\}}$ is the highest available here, and the control nicely fixes the levitating mass at $h_3 = 1.67\,\mathrm{cm}$. At this position the stabilized voltage supplying the electromagnet equals 13.66 V. The time plot of h_4 in Fig. 1.27 is an unnatural effect of a non-zero coefficient of feedback from acceleration ($k_3 = 0.2$; see Fig. 1.25). The desired position is achieved in about 1.2 s, and it confirms that the vector component of feedback from acceleration is not necessary in this application.

Depending on the presence of an IRR light barrier and the values of its sensitivity factor (b_{IRR}), various shapes of the step response can be distinguished. The convergence is quite fast and well damped when the IRR light correction exists and, additionally, takes a correct value of its significance. The choice of incorrect value of b_{IRR} results in the mass being brought into small-amplitude, weakly damped

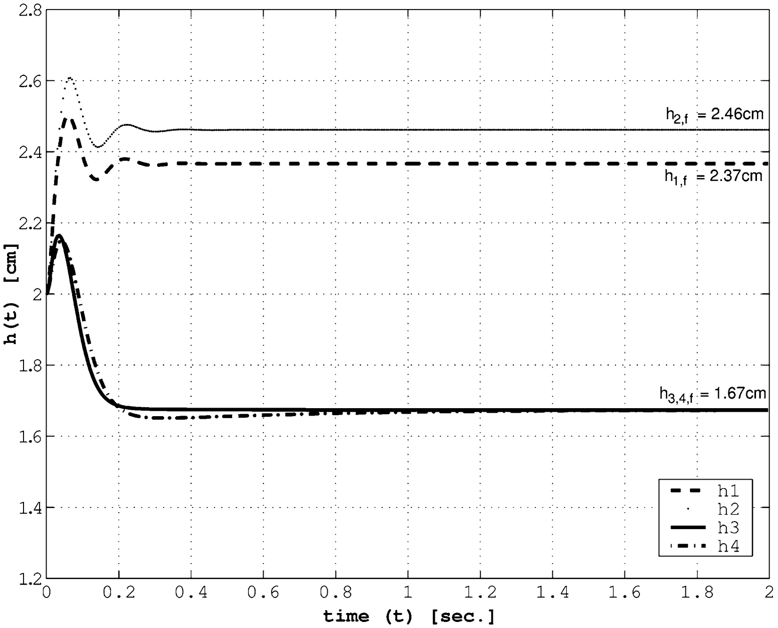

Fig. 1.27 Time plots of $h(t)$ evaluated from diagram shown in Fig. 1.25 for different values $b_{\mathrm{IRR}\{1,2,3\}} = \{7, 0.7, 22.2\} \cdot 10^{-4}$ corresponding to $h_{\{1,2,3\}}$ (for $k_3 = 0$), respectively. Infrared light sensitivity factor $b_{\mathrm{IRR}\{4\}} = b_{\mathrm{IRR}\{3\}}$ (for $k_3 = 0.2$), and $h_0 = 2\,\mathrm{cm}$

oscillations about its desired steady-state position. In some conditions, such an effect is observable also at a real laboratory rig and is undesirable if we need to fix the levitating mass at a constant height. Therefore, the introduced feedback from the infrared light barrier with mass m working as the armature of the electromagnet is justified. Better shapes of characteristics of the transition to steady-state responses were confirmed by the second control strategy. They are faster and more stable, and no oscillations are reported after examination of system parameters. The magnetic field allowed for elimination of any kinds of friction that are usually required in various realizations of fixings. Our experimental investigations will turn to the identification of electromagnetic parameters of the complete mechatronic system and the associated magnetic field. This is expected to help improve both the numerical adequacy of the presented approach and the tested strategy of control.

1.4 String-Type Generator

The dynamics of non-linear discrete-continuous systems governed by ordinary differential equations and partial differential equation often causes difficulties in numerical analysis. The reason lies not only in non-linear terms but mainly in time-consuming numerical techniques used to find the solution of the partial

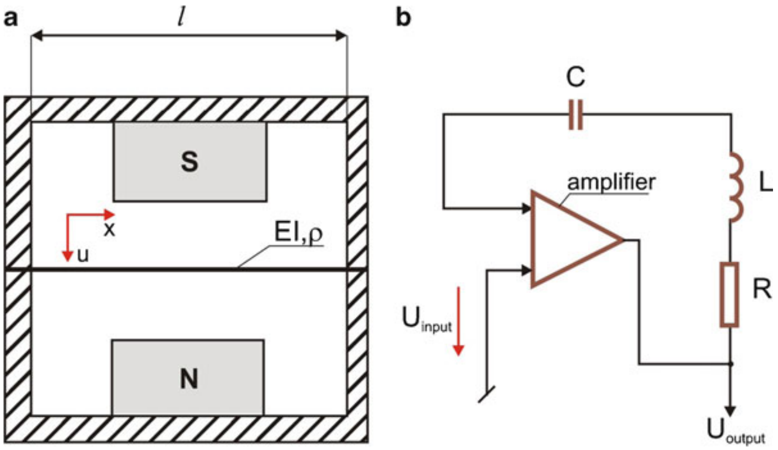

Fig. 1.28 Scheme of string embedded in magnetic field (**a**) and electrical model (**b**)

differential equations. Furthermore, usually real physical systems possess many parameters that can be changed over wide regions, and in practice direct simulation of the governing equations is costly and very tedious. Sometimes it does not provide physical insight into the obtained results. A deeper understanding of the dynamical behavior of the system under consideration can be discovered by the application of appropriate scaling and the proper use of averaging techniques [9–11]. In this section the electromechanical system under consideration serves as an example for a systematic strategy for solving many other related problems encountered in non-linear mechanical, biological, or chemical dynamical systems. First, an averaging method is proposed that is supported by a program for symbolic computation, and then further systematical study of the obtained ordinary differential equations is developed.

1.4.1 Analyzed System

The electromechanical model under consideration consists of a distributed mass system (string) whose oscillations are governed by a PDE (a detailed discussion of the model is given in [12–14]). The string is embedded in the magnetic field and crosses a magnetic flux perpendicularly (Fig. 1.28a). On the other hand, the string is made of steel and has its own inductance L, resistance R, and capacitance C. It appears that the equilibrium position of the string is unstable. The existence of the magnet induction and movement of the string causes the occurrence of voltage and then of a current in the string. The amplitude of the current undergoes change controlled by the amplifier with a time delay. Figure 1.28b shows the schematic of the electric system. The output and input voltages are governed by a non-linear cubic-type relation.

The magnetic induction $B(x)$ acting along the string generates voltage at the ends of the string according to the following equation:

$$U_{\mathrm{input}}(t) = \int_0^l B(x) \frac{\partial u(t,x)}{\partial t} \mathrm{d}x, \tag{1.110}$$

where x is the spatial coordinate, t denotes time, $u(t,x)$ is the string displacement in the point (t,x), and l is the length of the string. The amplifier gives the output voltage

$$\widetilde{U}_{\mathrm{output}} = \widetilde{h}_1 U_{\mathrm{input}}(t) - \widetilde{h}_2 U_{\mathrm{input}}^3(t), \tag{1.111}$$

where $\widetilde{h}_i$ $(i = 1,2)$ are constant coefficients.

The current oscillations, including a time delay τ in the amplifier, are governed by the equation

$$\ddot{I}(t) + 2\lambda \dot{I}(t) + kI(t) = \dot{U}_{\mathrm{output}}(t-\tau), \tag{1.112}$$

where

$$2\lambda = RL^{-1}, \qquad k = (LC)^{-1}, \qquad h_1 = L^{-1}\widetilde{h}_1, \qquad h_2 = L^{-1}\widetilde{h}_2,$$

$$U_{\mathrm{output}}(t) = h_1 U_{\mathrm{input}}(t) - h_2 U_{\mathrm{input}}^3(t),$$

and the dot denotes differentiation with respect to t and $I(t)$ denotes the changes of the current. The changes in time of $I(t)$ and the changes in x of $B(x)$ play the role of force acting on the string whose oscillations are governed by the equation

$$\frac{\partial^2 u(t,x)}{\partial t^2} - c^2 \frac{\partial^2 u(t,x)}{\partial x^2} = -\frac{\varepsilon}{\rho}\left(2h_0 \frac{\partial u(t,x)}{\partial t} - B(x)I(t)\right), \tag{1.113}$$

where h_0 is the external damping coefficient, ρ is the mass density along the unit length, and ε is the small positive parameter.

The frequencies of free oscillations of the string are given by $\omega_s = \pi cs/l$, and the homogeneous boundary conditions are as follows:

$$u(t,0) = u(t,l) = 0. \tag{1.114}$$

1.4.2 Averaging Method

Our consideration is limited to first-order averaging. For $\varepsilon = 0$ the solution to (1.113) can be approximated by

$$u_0 = a_1 \cos(\omega_1 t + \theta_1) \sin\left(\frac{\pi x}{l}\right) + a_3 \cos(3\omega_1 t + \theta_3) \sin\left(\frac{3\pi x}{l}\right), \tag{1.115}$$

where a_1, a_3 are the amplitudes, and θ_1, θ_3 the phases.

Only two modes are taken into account because the others are quickly damped during the string dynamics and their influence on the results can be neglected.

For a small enough $\varepsilon \neq 0$ the solution to (1.113) is expected to be of the form

$$u = u_0 + \varepsilon u_1(x, a_1, a_3, \theta_1, \theta_3) + O(\varepsilon^2). \tag{1.116}$$

Supposing that $B(x)$ is symmetric with respect to the ends of the string, i.e., $B(x) = B(l - x)$, we take

$$B = B_1 \sin(\pi x/l) + B_3 \sin(3\pi x/l). \tag{1.117}$$

This assumption clarifies the selection of modes in (1.115). From (1.110) we obtain

$$U_{\text{input}} = -\frac{1}{2}B_1 a_1 \omega_1 l \sin(\omega_1 t + \theta_1) - \frac{3}{2}B_3 a_3 \omega_1 l \sin(3\omega_1 t + \theta_3), \tag{1.118}$$

and the right-hand side of (1.112) is calculated using a symbolic calculation (in *Mathematica*)

$$\begin{aligned}
\dot{U}_{\text{output}}(t-\tau) = & -\frac{1}{2}B_1 a_1 h_1 l \omega_1^2 \cos\psi_{10} - \frac{9}{2}B_3 a_3 h_1 l \omega_1^2 \cos\psi_{30} \\
& + \frac{3}{8}B_1^3 a_1^3 h_2 l^3 \omega_1^4 \cos\psi_{10} \sin^2\psi_{30} \\
& + \frac{27}{8}B_1^2 B_3 a_1^2 a_3 h_2 l^3 \omega_1^4 \cos\psi_{30} \sin^2\psi_{10} \\
& + \frac{9}{8}B_1^2 B_3 a_1^2 a_3 h_2 l^3 \omega_1^4 \sin 2\psi_{10} \sin\psi_{30} \\
& + \frac{81}{8}B_1 B_3^2 a_1 a_3^2 h_2 l^3 \omega_1^4 \sin 2\psi_{30} \sin\psi_{10} \\
& + \frac{27}{8}B_1 B_3^2 a_1 a_3^2 h_2 l^3 \omega_1^4 \cos\psi_{10} \sin^2\psi_{30} \\
& + \frac{243}{8}B_3^3 a_3 h_2 l^3 \omega_1^4 \cos\psi_{30} \sin^2\psi_{30},
\end{aligned} \tag{1.119}$$

where

$$\psi_{10} = \omega t + \theta_1 - \mu t, \qquad \psi_{30} = 3\omega t + \theta_3 - 3\mu t, \qquad \mu = \frac{\tau\omega}{t}. \tag{1.120}$$

From (1.119) we take only the harmonics $\sin \mathrm{i}\omega_1 t$, $\cos \mathrm{i}\omega_1 t$ $(i = 1, 3)$, and therefore

$$\dot{U}_{\text{output}}(t-\tau) = b_{1c}\cos\omega_1 t + b_{1s}\sin\omega_1 t + b_{3c}\cos 3\omega_1 t + b_{3s}\sin 3\omega_1 t, \tag{1.121}$$

where

$$
\begin{aligned}
b_{1c} &= A\cos\theta_1^* - \frac{9}{32}B_1^2B_3a_1^2a_3h_2l^3\omega_1^4\cos(2\theta_1^*-\theta_3^*),\\
b_{1s} &= -A\sin\theta_1^* + \frac{45}{64}B_1^2B_3a_1^2a_3h_2l^3\omega_1^4\sin(2\theta_1^*-\theta_3^*),\\
b_{3c} &= C\cos\theta_3^* - \frac{3}{32}B_1^3B_3a_1^3a_3h_2l^3\omega_1^4\cos(3\theta_1^*),\\
b_{3s} &= -C\sin\theta_3^* + \frac{3}{32}B_1^3a_1^3h_2l^3\omega_1^4\sin(3\theta_1^*),\\
A &= -\frac{1}{2}B_1a_1h_1l\omega_1^2 + \frac{3}{12}B_1^3a_1^3h_2l^3\omega_1^4 + \frac{27}{16}B_1B_3^2a_1a_3^2h_2l^3\omega_1^4,\\
C &= -\frac{9}{2}B_3a_3h_1l\omega_1^2 + \frac{27}{16}B_1^2a_1^2a_3h_2l^3\omega_1^4 + \frac{243}{32}B_3^3a_3^3h_2l^3\omega_1^4,\\
\theta_1^* &= \theta_1 - \mu t, \qquad \theta_3^* = \theta_3 - 3\mu t.
\end{aligned}
\tag{1.122}
$$

A solution to the linear (1.112) has the form

$$
I_0(t) = \sum_{i=1,3}\{(b_{ic}M_i - b_{is}N_i)\cos \mathrm{i}\omega_1 t + (b_{ic}N_i - b_{is}M_i)\sin \mathrm{i}\omega_1 t\} + h.h.,
\tag{1.123}
$$

where M_i, N_i are given below:

$$
M_i = \frac{k - i^2\omega_1^2}{(k-i^2\omega_1^2)^2 + 4i^2\lambda^2\omega_1^2}, \qquad N_i = \frac{2\lambda \mathrm{i}\omega_1}{(k-i^2\omega_1^2)^2 + 4i^2\lambda^2\omega_1^2}
\tag{1.124}
$$

and the abbreviation $h.h.$ denotes higher harmonics that are not taken into account.

Further analysis is straightforward for the perturbation technique, and the details can be found elsewhere [9, 15]. Because $B(x)$ and $I(t)$ are defined, (1.113) can be solved using a classical perturbation approach. (It is assumed that $u_1(x, a_1, a_3, \theta_1, \theta_3)$ is a limited and periodic function).

Substituting (1.116) into (1.113) and taking into account that $a_i = a_i(t)$ and $\theta_i = \theta_i(t)$ $(i = 1, 3)$ are slowly changing in time, from the right-hand side of (1.113) (henceforth referred to as R) the following resonance terms are computed:

$$
\begin{aligned}
R_{ic} &= \frac{2}{\pi l}\int_0^l\int_0^{2\pi} R\sin\frac{\pi i x}{l}\cos\psi_{i0}\mathrm{d}\psi_{i0},\\
R_{is} &= \frac{2}{\pi l}\int_0^l\int_0^{2\pi} R\sin\frac{\pi i x}{l}\sin\psi_{i0}\mathrm{d}\psi_{i0},\\
\psi_{i0} &= \mathrm{i}\omega_1 + \theta_i, \qquad i = 1, 3,
\end{aligned}
\tag{1.125}
$$

where R_{ic}, R_{is} correspond to the terms by $\cos\psi_{i0}$ and $\sin\psi_{i0}$, respectively. The comparison of the terms by $\cos\psi_{i0}$ and $\sin\psi_{i0}$ and generated by the left-hand side of (1.113) to those defined by (1.125) leads to the following average-amplitude equations:

$$\begin{aligned}
\dot{a}_1 &= -\frac{\varepsilon h_0 a_1}{\rho} - \frac{\varepsilon B_1}{2\rho\omega_1}\{(b_{1c}M_1 - b_{1s}N_1)\sin\theta_1 \\
&\qquad + (b_{1c}N_1 + b_{1s}M_1)\cos\theta_1\}, \\
\dot{a}_3 &= -\frac{\varepsilon h_0 a_3}{\rho} - \frac{\varepsilon B_3}{6\rho\omega_1}\{(b_{3c}M_3 - b_{3s}N_3)\sin\theta_3 \\
&\qquad + (b_{3c}N_3 + b_{3s}M_3)\cos\theta_3\}, \\
\dot{\theta}_1 &= -\frac{\varepsilon B_1}{2a_1\rho\omega_1}\{(b_{1c}M_1 - b_{1s}N_1)\cos\theta_1 \\
&\qquad - (b_{1c}N_1 + b_{1s}M_1)\sin\theta_1\}, \\
\dot{\theta}_3 &= -\frac{\varepsilon B_3}{6a_3\rho\omega_1}\{(b_{3c}M_3 - b_{3s}N_3)\cos\theta_3 \\
&\qquad - (b_{3c}N_3 + b_{3s}M_3)\sin\theta_3\}.
\end{aligned} \tag{1.126}$$

The preceding equations are coupled via (1.122). The first attempt to derive an averaged set of equations was made by Rubanik [12]. However, neither qualitative nor quantitative analysis or predictions of the possible behavior of the solutions to the equations obtained have been given.

The analyzed set of equations has some properties that can cause difficulties during numerical analysis. First of all, this is a stiff set of equations [note the occurrence of a_i $(i = 1, 3)$ in the denominator of the last two equations of (1.126)]. As is assumed by the averaging procedure, amplitudes a_i and θ_i change in time very slowly, and a long integration to trace the behavior of the system is required.

For the further analysis of the time-dependent solutions we transform (1.126) into amplitude equations. For this purpose we assume

$$u_0 = (Y_1\cos\omega_1 t + Y_2\sin\omega_1 t)\sin\frac{\pi x}{l} + (Y_3\cos 3\omega_1 t + Y_4\sin 3\omega_1 t)\sin\frac{3\pi x}{l}. \tag{1.127}$$

The comparison with (1.115) yields the following relations:

$$\begin{aligned}
Y_1(t) &= a_1(t)\cos\theta_1(t), & Y_2(t) &= -a_1(t)\sin\theta_1(t), \\
Y_3(t) &= a_3(t)\cos\theta_3(t), & Y_4(t) &= -a_3(t)\sin\theta_3(t).
\end{aligned} \tag{1.128}$$

In what follows the set of amplitude differential equations has the form

$$\begin{aligned}\dot{Y}_1(t) &= \dot{a}_1(t)\cos\theta_1(t) - a_1(t)\dot{\theta}_1(t)\sin\theta_1(t),\\ \dot{Y}_2(t) &= -\dot{a}_1(t)\sin\theta_1(t) - a_1(t)\dot{\theta}_1(t)\cos\theta_1(t),\\ \dot{Y}_3(t) &= a_3(t)\cos\theta_3(t) - a_3(t)\dot{\theta}_3(t)\sin\theta_3(t),\\ \dot{Y}_4(t) &= -\dot{a}_3(t)\sin\theta_3(t) - a_3(t)\dot{\theta}_3(t)\cos\theta_3(t),\end{aligned} \tag{1.129}$$

where $\dot{a}_i$ and $\dot{\theta}_i$ are given by (1.126) and

$$\begin{aligned}\theta_1 &= \arctan(-Y_2/Y_1), & \theta_3 &= \arctan(-Y_4/Y_3),\\ a_1 &= (Y_1^2 + Y_2^2)^{1/2}, & a_3 &= (Y_3^2 + Y_4^2)^{1/2}.\end{aligned} \tag{1.130}$$

1.4.3 Numerical Analysis and Results

In a standard approach to non-linear dynamical system analysis, time-dependent solutions are first considered and examined. For this purpose we consider a non-linear set of algebraic equations obtained from (1.126), where the left-hand sides are equal to zero. To solve the problem, a Powell hybrid method and a variation of Newton's method were used. They require a finite-difference approximation to the Jacobian with high-precision arithmetic. The root was accepted if the relative error between two successive approximations was less than 0.0001.

In a general case it can happen that the system of equations under consideration has one isolated solution or has a family of coexisting solutions for a fixed set of parameters. The system always possesses the trivial solution $a_1 = a_3 = \theta_1 = \theta_3 = 0$, which corresponds to the equilibrium position of the original system. Non-trivial solutions correspond to the periodic oscillations of the string described by the assumed solution (1.116). The stability of periodic oscillations corresponds to the stability of fixed points, i.e., to the stability of roots of the non-linear algebraic equations. To define the stability of the time-independent solutions obtained from the algebraic non-linear set of equations, we perturb them and then substitute for (1.116). Taking into account only the first powers of perturbations we get from (1.116) a linear set of differential equations. Based on these equations, a matrix corresponding to the analyzed fixed point is defined. In our case, because of the complicated equations, that matrix is obtained numerically. The eigenvalues of the matrix obtained determine the stability and bifurcation of the analyzed solutions (see monographs [16, 17]).

We present below two examples of such a computation. The following parameters were treated as fixed: $l = 0.1$, $\omega = 4.1$, $\lambda = 0.01$, $k = 25$, $h_1 = 0.01$, $h_2 = 0.6$, $\varepsilon/\rho = 1$, $h_0 = 0$, $B_3 = 0.4$. The coefficient μ and the amplitude B_1 served as the control parameters. In Fig. 1.29 one can observe that for $\mu = 0.001$ with an increase in the first amplitude of the electromagnetic induction, the amplitude a_1

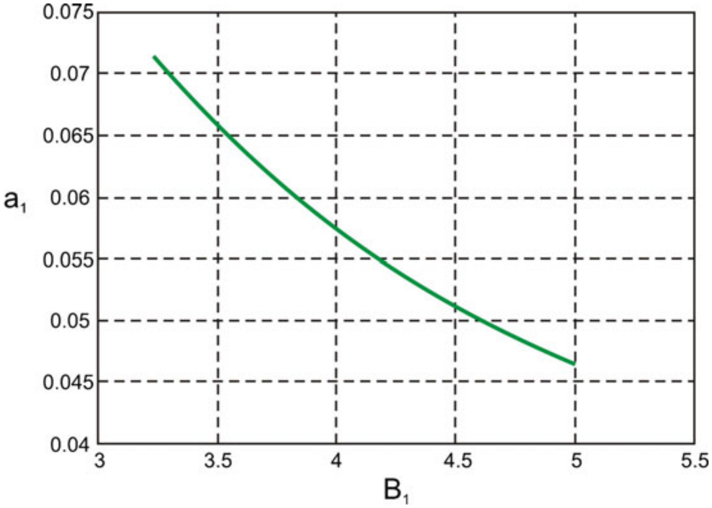

Fig. 1.29 First harmonic amplitude against B_1

decreases (the amplitude a_3 and the phases θ_1 and θ_3 remain almost constant). A similar situation is observed for $\mu = 0.01$ and $\mu = 0.1$. This means that for the considered set of fixed parameters, an increase in B_1 damps the magnitude of oscillations.

A question arises as to whether there is only one isolated solution that corresponds to the fixed value of B_1. We have found that in an interval $B_1 \in (3.0, 5.0)$ for each value of B_1 there exist two solutions for a_1 (marked with triangles) and one for a_3 (marked with crosses), as shown in Fig. 1.30. In both figures the obtained solutions are stable.

It is a difficult task to prove the existence of time-dependent solutions in the system of averaged (1.129). The most expected situation (confirmed by numerical computations) is to find stable fixed points that correspond to the oscillations with constant amplitudes in the original system. However, we have also found periodic orbits in the analyzed averaged differential equations. On the basis of this example, it is proper to describe the benefits obtained from the averaging technique applied. Instead of examining of a complicated system of non-linear partial and ordinary differential equations, we reduce the problem to the analysis of the four ordinary differential equations. Inserting the results obtained numerically into (1.127) we obtain an averaged solution corresponding to the original system.

We now briefly describe a numerical method for tracking down changes in periodic orbits, their stability, and potential bifurcations [16, 17]. For this purpose, let us consider an approximate position of the fixed point $Y_0^{(k)}$ close to the unknown exact one and perform numerical integration over the estimated period $T^{(k)}$. Actually, we have rescaled the equations according to the rule $\bar{t} = \Omega t$, where Ω serves as an unknown to be determined and the period is equal to 2π.

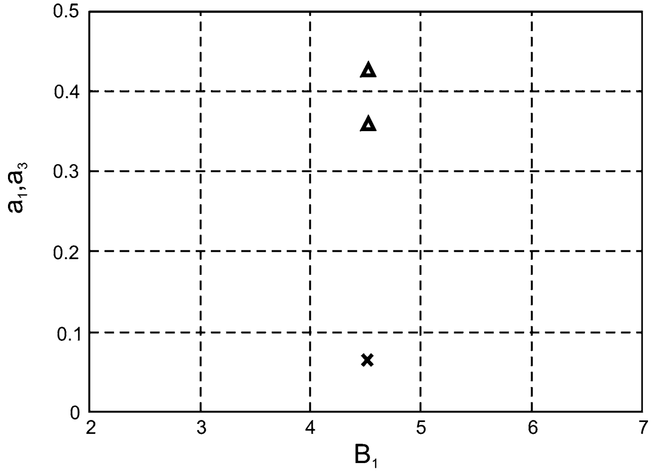

Fig. 1.30 Example of multiple set of solutions corresponding to $B_1 = 4.5$

The error $E = Y_0^{(k)} - G_0^{(k)}$ (where $G_0^{(k)} = G(Y_0^{(k)})$ is a point mapping) shows the accuracy of the calculations. Then, after a perturbation of the fixed point, its stability is determined based on the eigenvalues of a monodromy matrix. The results of calculation of the fixed points of the map (periodic orbits) as functions of B_1 for $l = 0.1$, $\mu = 0.1$, $\omega = 2.9$, $\lambda = 0.1$, $k = 9.0$, $h_1 = 0.05$, $h_2 = 0.01$, $\rho/\varepsilon = 1.0$, $h_0 = 0.02$, $B_3 = 0.8$ are presented in Fig. 1.31a, b. In this figure, Y_3 and Y_4 are much smaller than Y_1 and Y_2 and are assumed to be zero. Variation of the period following the change of B_1 is evident (Fig. 1.31b, where $Z = 1/\Omega$). The observed periodic orbit is "strongly" stable because the corresponding multipliers lie close to the origin. As an example, one of the periodic orbits is presented in Fig. 1.32a, b. One revolution of the variables $Y_{1,2}$ corresponds to two revolutions of $Y_{3,4}$ during the period 2π.

Special attention is focused on detecting the time-dependent aperiodic solutions to the averaged equations. Some interesting non-linear phenomena will be discussed subsequently and illustrated based on the gear simulation of the averaged equations.

Let us first consider the following fixed parameters: $l = 0.1$, $\mu = 0.15$, $\omega_1 = 190$, $\lambda = 0.1$, $k = 25.0$, $h_1 = 0.58$, $h_2 = 0.05544$, $\rho = 1.0$, $\varepsilon = 0.05$, $h_0 = 0.001$, $B_3 = 0.08$. Here the coefficient μ serves as a control parameter. Figure 1.33a illustrates the oscillations of $Y_{1,2}$ and the exponential decay of $Y_{3,4}$. The variables $Y_{1,3}$ and $Y_{2,4}$ correspond to the time evolution of the first two modes of the string arid their derivatives, respectively.

The amplitudes of the first mode oscillate, but those corresponding to the third mode decrease in time in a non-oscillatory (exponential) manner. The decrease in μ damps the oscillatory effects, which is shown in Fig. 1.33b for $\mu = 0.125$.

Figure 1.34 ($l = 0.1$, $\mu = 0.0$, $\omega_1 = 900.0$, $\lambda = 0.1515$, $k = 2750.0$, $h_1 = 5.48$, $h_2 = 70.0$, $\rho = 1.0$, $\varepsilon = 0.009$, $h_0 = 0.00001$, $B_1 = 0.65$, $B_3 = 0.89$)

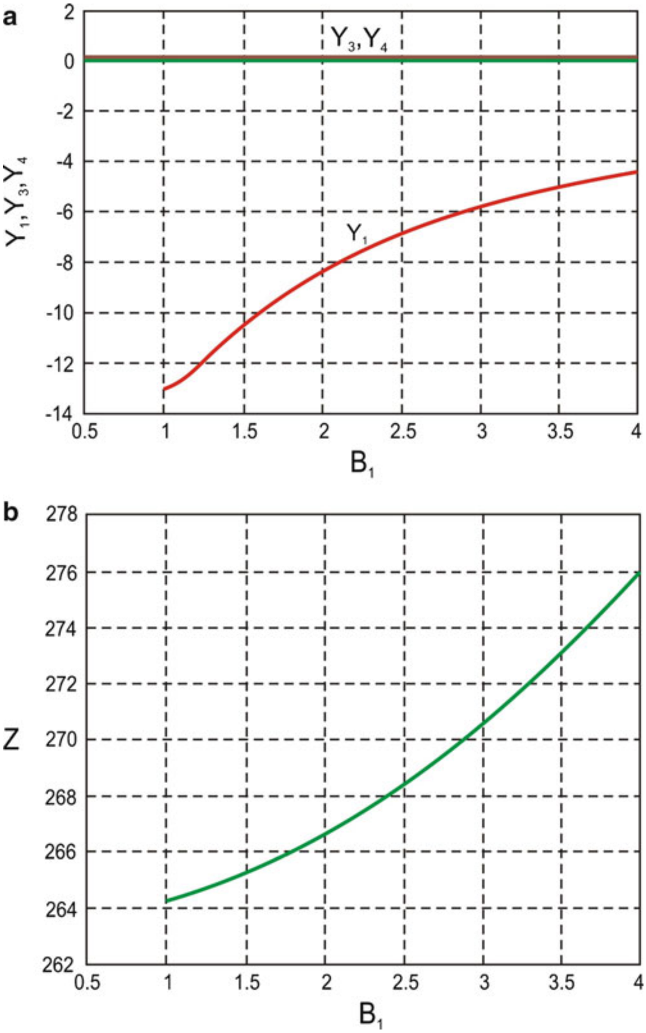

Fig. 1.31 Fixed points of Y_1, Y_3, Y_4 (**a**) and $Z = 1/\Omega$ (**b**) against control parameter B_1

illustrates an unexpected non-linear phenomenon. A long time-transitional process has been interrupted by the sudden occurrence of the strong nonlinear $Y_{1,2}$ oscillations.

In Fig. 1.35 the coexistence of the periodic oscillations $Y_{1,2}(t)$ with the exponential decay of $Y_{3,4}(t)$ is shown. The simulation was performed for the following fixed parameters: $l = 0.1$, $\mu = 0.1$, $\omega_1 = 0.1$, $\lambda = 0.1$, $k = 7250.0$, $h_1 = 0.1$, $h_2 = 0.1$, $\rho = 1.0$, $\varepsilon = 0.05$, $h_0 = 0.001$, $B_1 = 6.3$, $B_3 = 0.08$. Because $Y_{1,2}$ and $Y_{3,4}$ correspond to the first and third modes of the string, respectively, this result can be interpreted as the independent mode behavior.

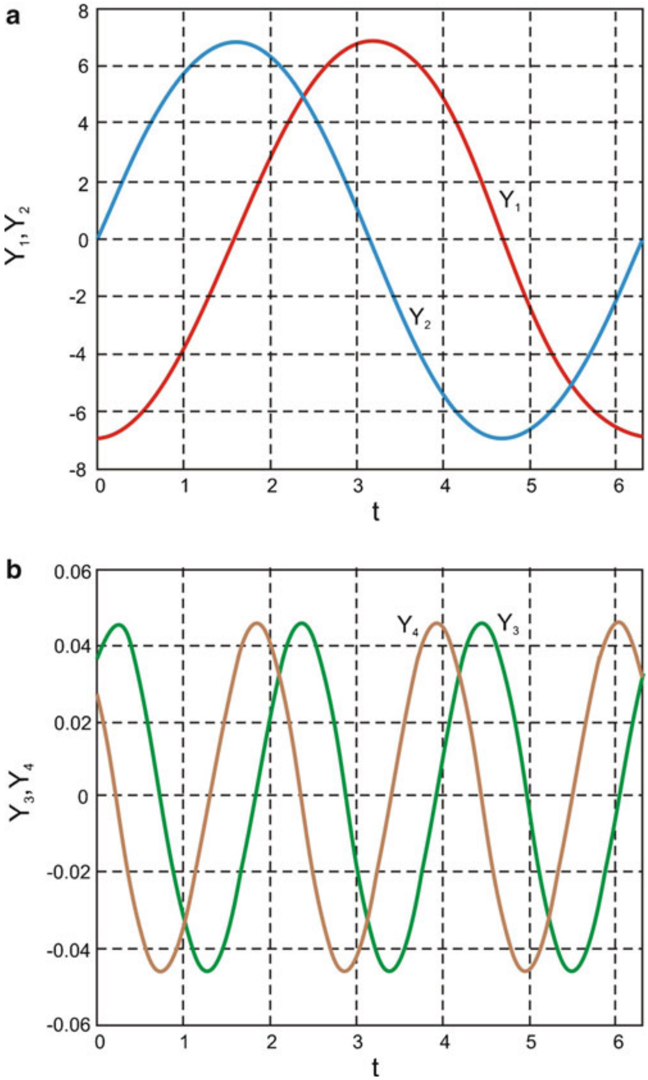

Fig. 1.32 Periodic orbits $Y_{1,2}$ (**a**) and $Y_{3,4}$ (**b**) with normalized 2π period

The result obtained also illustrates another interesting non-linear behavior. The solution to the averaged non-linear differential equations can be assumed analytically in a different form: an exponential decay function and an oscillatory function with a constant amplitude.

Figure 1.36 ($l = 0.1$, $\mu = 0.1$, $\omega_1 = 190.0$, $\lambda = 0.1$, $k = 25.0$, $h_1 = 0.58$, $h_2 = 0.05544$, $\rho = 1.0$, $\varepsilon = 0.005$, $h_0 = 0.00999$, $B_1 = 6.3$, $B_3 = 0.08$) presents a strange time evolution leading to instability. Here also $Y_{1,2}(t)$ increases

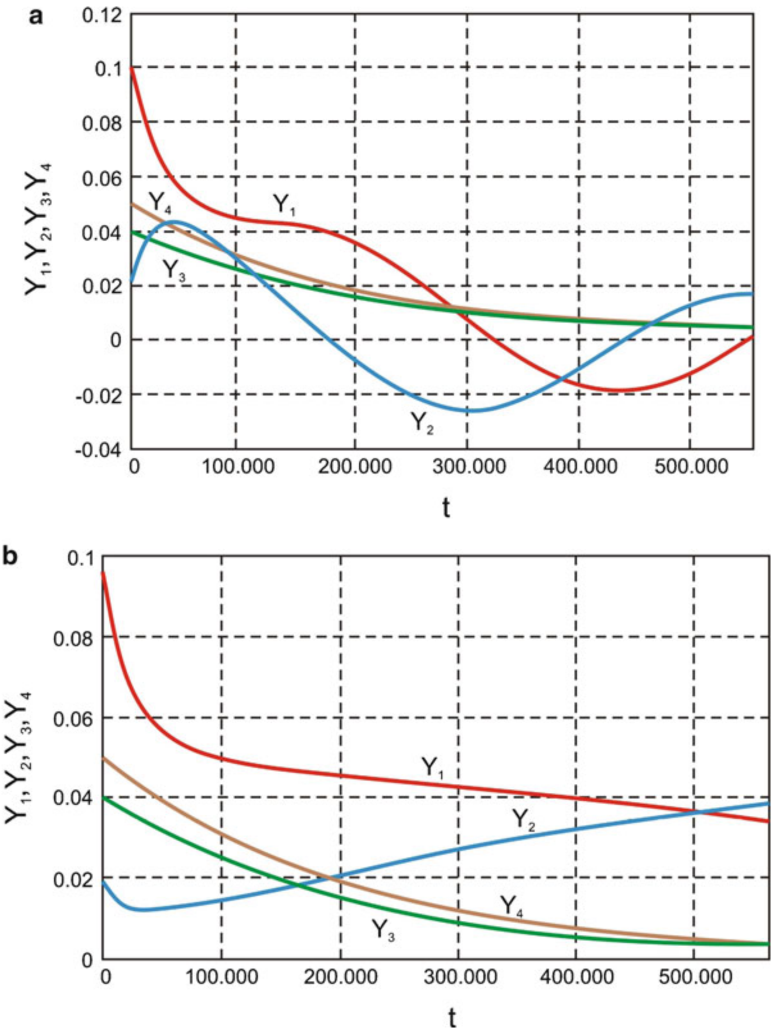

Fig. 1.33 Time evolutions of amplitudes: (**a**) $\mu = 0.15$, (**b**) $\mu = 0.125$

with oscillations, while $Y_{3,4}(t)$ slightly decreases almost linearly. After a long transitional state, barrierlike phenomena appear. Finally, strong nonlinear pressing effects, leading to the vertical unlimited increase in $Y_{1,2}(t)$, are observed.

This behavior can be explained as follows. An almost linear decrease in $Y_{3,4}(t)$ leading asymptotically to zero causes the occurrence of a sudden increase in $Y_{1,2}(t)$ due to the existence of a_3 in the denominator of the last equation of (1.126). However, typically the system does not exhibit such instability effects.

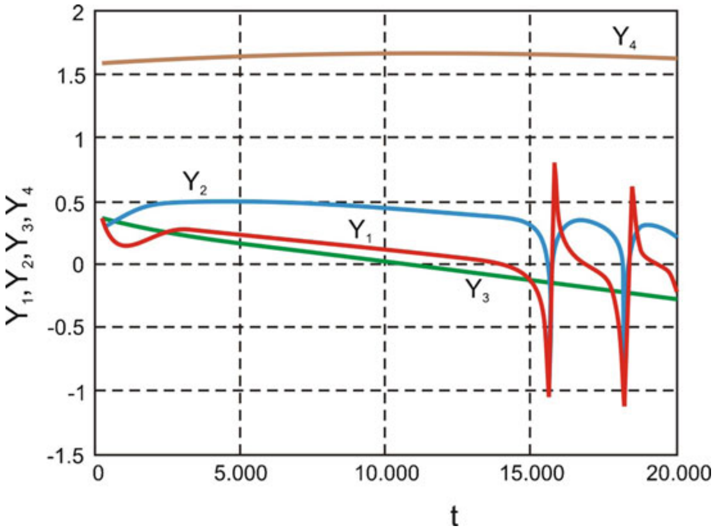

Fig. 1.34 Strong non-linear oscillations of amplitudes

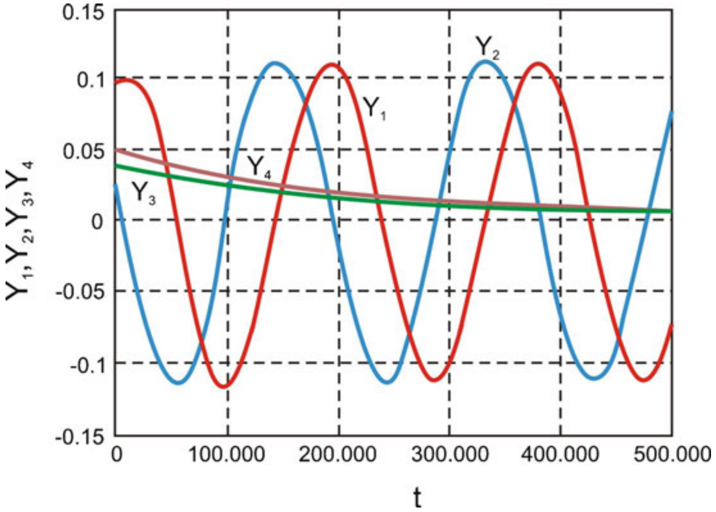

Fig. 1.35 Amplitude versus time

Finally, consider the following set of fixed parameters: $l = 0.1$, $\mu = 0.00001$, $\omega_1 = 900.0$, $\lambda = 0.1515$, $k = 7250.0$, $h_1 = 5.48$, $h_2 = 65.0$, $\rho = 1.0$, $\varepsilon = 0.009$, $h_0 = 0.00001$, $B_1 = 0.65$, $B_3 = 0.23$. A strong non-linear transitional oscillation of $Y_1(t)$ is shown in Fig. 1.37. The variables $Y_{3,4}(t)$ again change in a non-oscillatory manner quite independently in comparison with the first oscillation mode.

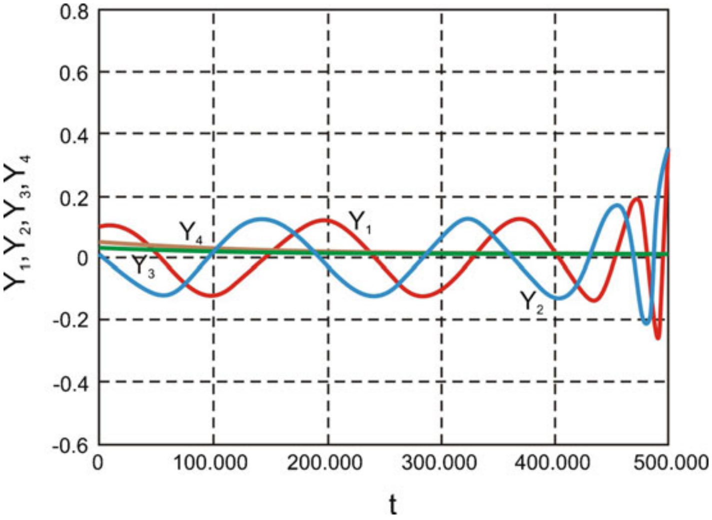

Fig. 1.36 Independent transitional time evolution of amplitudes leading to instability

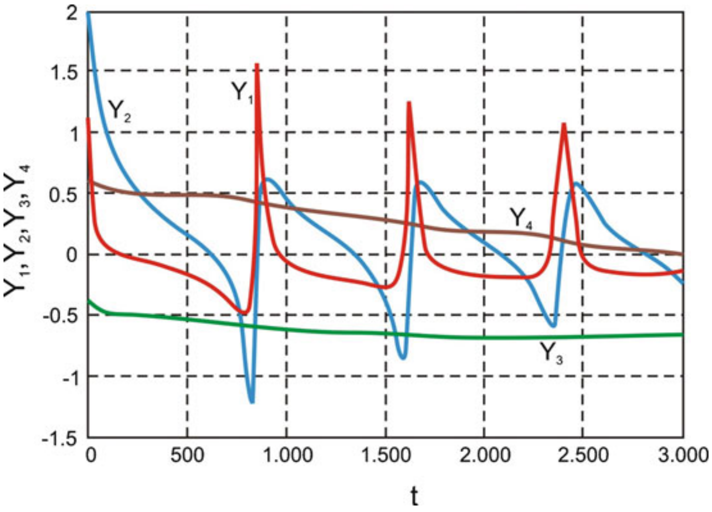

Fig. 1.37 Strong non-linear transitional oscillations

1.5 Rotor Supported by Magnetohydrodynamic Bearing

In general, rotating machinery elements are frequently encountered in mechanical/mechatronic engineering, and in numerous cases their non-linear dynamics causes many harmful effects, i.e., noise and vibrations. In particular, non-linear rotordynamics plays a crucial role in understanding various non-linear phenomena and despite its long research history (see, e.g., [18–22] and references therein), it continues to attract the attention of many researchers and engineers. Since the topics related to non-linear rotordynamics are broad ranging and cover many interesting aspects related to both theory and practice, in this section we aim only at the analysis of some problems related to a rotor suspended in a magnetohydrodynamic field in the case of soft and rigid magnetic materials.

Magnetic, magnetohydrodynamic, and piezoelectric bearings are used in many mechanical engineering applications to support a high-speed rotor, provide vibration control, minimize rotating friction losses, and potentially avoid flutter instability. Many publications are dedicated to the dynamic analysis and control of a rotor supported on various bearing systems. The conditions for active closed-/open-loop control of a rigid rotor supported on hydrodynamic bearings and subjected to harmonic kinematical excitation are presented in [23, 24]. The methodology for modeling lubricated revolute joints in constrained rigid multibody systems is described in [25]. The hydrodynamic forces used in the dynamic analysis of journal bearings, including both squeeze and wedge effects, are evaluated from the system-state variables and included in the equations of motion of multibody systems. To analyze the dynamic behavior of a rub-impact rotor supported by turbulent journal bearings and lubricated with couple stress fluid under quadratic damping, the authors of reference [26] used system-state trajectory, Poincar maps, power spectrum, bifurcation diagrams, and Lyapunov exponents. Dynamic motion was detected to be periodic, quasiperiodic, and chaotic.

Rotor-active magnetic bearing (AMB) systems with time-varying stiffness are considered in [27]. Using the method of multiple scales, a governing non-linear equation of motion for the rotor-AMB system with one degree of freedom is transformed into an averaged equation, and then bifurcation theory and a bifurcation method of the detection function are used to analyze the bifurcations of multiple limit cycles of the averaged equation.

Rotors supported by floating ring bearings may exhibit instabilities due to self-excited vibrations [28]. The authors applied linear stability analysis to reveal a sign change of real parts of the conjugated eigenvalue pairs, and a center manifold reduction approach allowed them to explain the rotor destabilization via Hopf bifurcation. Owing to the analytical predictions that were applied, both sub- and supercritical bifurcations were found, and the analytical results were compared with numerical ones using a continuation method. Observe that rotors supported by a simple fluid film bearing the so-called oil whirl and oil whip dynamics ad been studied analytically in [18, 20–23]. Additionally, this problem was reconsidered recently with respect to inner and outer oil films and synchronization [29]. The full annular rub motion of a flexible rotor induced by mass unbalance and contact rub force with rigid and flexible stators, taking into account dry friction between the stator and rotor, is studied in [30]. Stability and synchronous problems of full annular rub motions are discussed, and a simplified formula for the dynamic stability of the system being investigated is derived.

Ishida et al. [31] investigate the vibrations of a flexible rotor system with radial clearance between an outer ring of the bearing and a casing using numerical and experimental studies. The following non-linear behavior was detected, illustrated, and discussed: (a) sub-, super-sub, and combined resonances; (b) self-excited vibrations of forward whirling mode; and (c) transitions from self-excited to forced system vibrations. In particular, the influence of static force and bearing damping was analyzed using the harmonic balance method.

Quinn [32] studied the non-linear output of a damped Jeffcott rotor with anisotropic stiffness and imbalance. It was shown that for sufficiently small external torque (or large imbalance), resonance capture may occur whereby the rotational shaft velocity cannot increase beyond the fundamental resonance between the rotational and translational motion providing a mechanism for energy transfer. Prediction of the system behavior on the basis of the reduced-order averaged model is verified and validated against numerical studies of the original ODE-governed model.

In this section, the two-degree-of-freedom non-linear dynamics of a rotor supported on a magnetohydrodynamic bearing system (MHDB) is analyzed in the cases of soft and rigid magnetic materials. In the case of soft magnetic materials, the analytical solutions were obtained using the method of multiple scales [9, 15]. Rigid magnetic materials possess hysteretic properties that are realized in the present work by means of the Bouc–Wen hysteretic model [33, 34]. This model enables simulation of hysteretic loops of various forms for systems from very different fields such as mechanics, biology, electronics, ferroelectricity, and magnetism [35]. In particular, in mechanical/civil and mechatronic engineering, hysteresis occurs as the natural inclination of materials to yield to restoring forces against motion and dissipate energy, and it often deals with the memory nature of inelastic material properties, where the restoring forces (torques) depend on the deformation process history. In general, the classic Bouc–Wen model is described by the first-order non-linear ODE governing the input (displacement rotations) and output (restoring force/torque) signals in a hysteretic way. Furthermore, a proper choice of the Bouc–Wen parameters allows one to control their behavior so that it is similar to that of real hysteresis looplike processes. Observe that despite the simplicity of the Bouc–Wen model, its behavior and possible application still attract many researchers, in particular regarding the following topics:

(a) Ways of tuning the Bouc–Wen control parameters to match application-oriented hysteretic material properties (identifications process).
(b) Numerical analysis of a given full mathematical model including its control.
(c) Rigorous mathematical background devoted to proofs of the convergence between the Bouc–Wen-like models and their real application-oriented counterpart dynamic objects.

An extensive list of references related to the Bouc–Wen model and beyond, together with results of the researches associated with the analysis, identification, and control of the Bouc–Wen-like models, are reported in the monograph by Ikhouave and Rodellar [36], where the following topics are illustrated and discussed:

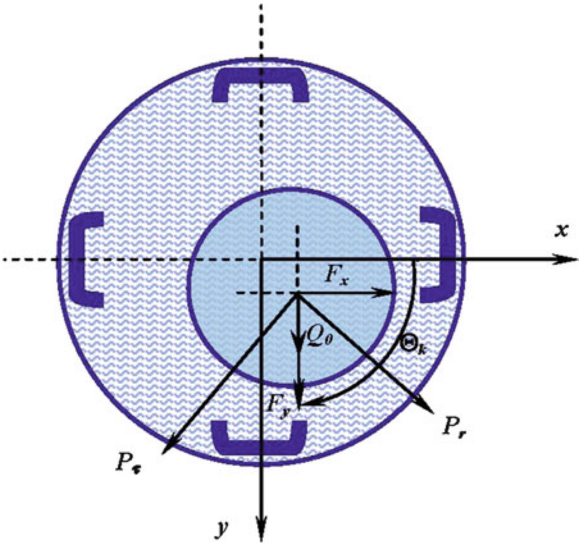

Fig. 1.38 Cross-section diagram of a rotor symmetrically supported on magnetohydrodynamic bearing

compatibility of the model versus physical laws, model parameters and hysteresis loops, identification and control of dynamic systems with Bouc–Wen models. Finally, various mathematical approaches to the hysteresis phenomenon are given in a survey reference [37].

As was demonstrated by investigations in [35], systems with hysteresis may reveal an unexpected behavior. On the one hand, hysteresis, like any dissipation, promotes the stabilization of motion and may restrain the occurrence of chaos. On the other hand, it may cause chaotic vibrations in a system. This last property is confirmed by the results of this section. In the absence of hysteresis, chaos is not observed. Taking into account hysteretic properties leads to chaotic vibrations of a rotor under certain conditions. The effect of hysteretic dissipation on the emergence of chaos is investigated using a methodology based on an analysis of wandering trajectories [33, 38]. Chaotic regions were obtained in parametric planes characterized by dynamic oil film action, magnetic control parameters, hysteretic dissipation, and the amplitude and frequency of external excitation.

1.5.1 Mathematical Model

Let us consider a uniform symmetric rigid rotor (Fig. 1.38) supported by a magnetohydrodynamic bearing system. The four-pole legs are symmetrically placed in the stator. F_k is the electromagnetic force produced by the kth opposed pair of electromagnet coils. This force is controlled by electric currents

$$i_k = i_0 \pm \Delta i_k \tag{1.131}$$

and can be expressed in the form

$$F_k = -\frac{2\mu_0 A N^2 i_0}{(2\delta + l/\mu^*)^2} \Delta i_k, \tag{1.132}$$

where i_0 denotes the bias current in the actuators' electric circuits, μ_0 is the magnetic permeability of vacuum, A is the core cross-section area, N is the number of windings of the electromagnet, δ is the air gap in the central position of the rotor with reference to the bearing sleeve, l is the total length of the magnetic path, the constant value $\mu^* = B_S/(\mu_0 H_S)$ denotes the magnetic permeability of the core material; the values of the magnetic induction B_S and magnetizing force H_S define the magnetic saturation level [23, 24]. θ_k is the angle between axis x and the kth magnetic actuator, Q_0 is the vertical rotor load identified with its weight, and (P_r, P_τ) are the radial and tangential components of the dynamic oil-film action, respectively. The equations of motion of the rotor are represented in the following form [23, 24, 39]:

$$\begin{aligned}
m^* \ddot{x}^* &= P_r^*\left(\rho, \dot{\rho}^*, \dot{\phi}^*\right) \cos\phi - P_\tau^*\left(\rho, \dot{\phi}^*\right) \sin\phi \\
&\quad + \sum_{k=1}^{K} F_k^* \cos\theta_k + Q_x^*(t), \\
m^* \ddot{y}^* &= P_r^*\left(\rho, \dot{\rho}^*, \dot{\phi}^*\right) \sin\phi + P_\tau^*\left(\rho, \dot{\phi}^*\right) \cos\phi \\
&\quad + \sum_{k=1}^{K} F_k^* \sin\theta_k + Q_0^* + Q_y^*(t), \\
P_r^*\left(\rho, \dot{\rho}^*, \dot{\phi}^*\right) &= -2C^* \left\{ \frac{\rho^2\left(\omega^* - 2\dot{\phi}^*\right)}{p(\rho)\, q(\rho)} + \frac{\rho\dot{\rho}^*}{p(\rho)} + \frac{2\dot{\rho}^*}{\sqrt{p(\rho)}} \arctan\sqrt{\frac{1+\rho}{1-\rho}} \right\}, \\
P_\tau^*\left(\rho, \dot{\phi}^*\right) &= \pi C^* \frac{\rho\left(\omega^* - 2\dot{\phi}^*\right)}{q(\rho)\sqrt{p(\rho)}}.
\end{aligned} \tag{1.133}$$

Here m^* denotes the rigid rotor mass, (x^*, y^*) are the Cartesian coordinates of the rotor center, $Q_x^*(t)$, $Q_y^*(t)$ are the external excitation characterizing bearing movements. We consider the vibrations of the rotor excited by the harmonic movements of the bearing foundation in the vertical direction:

$$Q_x^*(t) = 0, \qquad Q_y^*(t) = Q^* \sin\Omega^* t^*, \tag{1.134}$$

where Q^* and Ω^* are the amplitude and frequency of the external excitation, respectively. The constant C^* is defined as

$$C^* = \frac{6\mu_s R_c L_c}{\delta_s^2}. \tag{1.135}$$

The parameters μ_s, δ_s, R_c, and L_c denote the oil viscosity, relative bearing clearance, journal radius, and total bearing length, respectively. (ρ, ϕ) are the polar coordinates, and $p(\rho) = 1 - \rho^2, q(\rho) = 2 + \rho^2$.

To represent the equations of motion in a dimensionless form, the following changes in variables and parameters are introduced:

$$\begin{aligned}
&t = \omega^* t^*, \quad \dot{\phi} = \frac{\dot{\phi}^*}{\omega^*}, \quad \dot{\rho} = \frac{\dot{\rho}^*}{\omega^*},\\
&x = \frac{x^*}{c^*}, \quad \dot{x} = \frac{\dot{x}^*}{\omega^* c^*}, \quad \ddot{x} = \frac{\ddot{x}^*}{\omega^{*2} c^*},\\
&y = \frac{y^*}{c^*}, \quad \dot{y} = \frac{\dot{y}^*}{\omega^* c^*}, \quad \ddot{y} = \frac{\ddot{y}^*}{\omega^{*2} c^*},\\
&C = \frac{C^*}{m^* \omega^* c^*}, \quad \Omega = \frac{\Omega^*}{\omega^*}, \quad Q = \frac{Q^*}{m^* \omega^{*2} c^*}, \quad Q_0 = \frac{Q_0^*}{m^* \omega^{*2} c^*},\\
&F_k = \frac{F_k^*}{m^* \omega^{*2} c^*}, \quad P_r = \frac{P_r^*}{m^* \omega^{*2} c^*}, \quad P_\tau = \frac{P_\tau^*}{m^* \omega^{*2} c^*},
\end{aligned} \tag{1.136}$$

where ω^* is the rotation speed of the rotor and c^* is the bearing clearance.

Thus the dimensionless equations of motion take the form

$$\begin{aligned}
\ddot{x} &= P_r\left(\rho, \dot{\rho}, \dot{\phi}\right)\cos\phi - P_\tau\left(\rho, \dot{\phi}\right)\sin\phi + F_x,\\
\ddot{y} &= P_r\left(\rho, \dot{\rho}, \dot{\phi}\right)\sin\phi + P_\tau\left(\rho, \dot{\phi}\right)\cos\phi + F_y + Q_0 + Q\sin\Omega t,\\
P_r\left(\rho, \dot{\rho}, \dot{\phi}\right) &= -2C\left\{\frac{\rho^2\left(1 - 2\dot{\phi}\right)}{p(\rho)\, q(\rho)} + \frac{\rho\dot{\rho}}{p(\rho)} + \frac{2\dot{\rho}}{\sqrt{p(\rho)}}\arctan\sqrt{\frac{1+\rho}{1-\rho}}\right\},\\
P_\tau\left(\rho, \dot{\phi}\right) &= \pi C \frac{\rho\left(1 - 2\dot{\phi}\right)}{q(\rho)\sqrt{p(\rho)}}.
\end{aligned} \tag{1.137}$$

Here

$$\begin{aligned}
&x = \rho\cos\phi, \quad y = \rho\sin\phi,\\
&\dot{\phi} = \frac{\dot{y}x - \dot{x}y}{\rho^2}, \quad \dot{\rho} = \frac{x\dot{x} + y\dot{y}}{\rho}, \quad \rho = \sqrt{x^2 + y^2},\\
&\cos\phi = \frac{x}{\sqrt{x^2 + y^2}}, \quad \sin\phi = \frac{y}{\sqrt{x^2 + y^2}},
\end{aligned} \tag{1.138}$$

and the magnetic control forces are expressed as follows

$$F_x = -\gamma\dot{x} - \lambda\left(x - x_0\right), \qquad F_y = -\gamma\dot{y} - \lambda\left(y - y_0\right), \tag{1.139}$$

where (x_0, y_0) are the coordinates of the rotor static equilibrium and γ and λ are the control parameters.

1.5.2 Soft Magnetic Materials

In this section, we consider the two-degree-of-freedom dynamics of the rotor in the MHDB system without taking hysteresis into account.

1.5.2.1 Non-resonant case

The right-hand sides of (1.137) were expanded into Taylor series, and the origin was shifted to the location of the static equilibrium (x_0, y_0) for the convenience of investigation. The linear and quadratic terms were retained, so the reformed equations of motion are as follows:

$$\begin{aligned}
\ddot{x} + \alpha x - \beta \dot{y} &= -2\hat{\mu}_1 \dot{x} + \alpha_1 x^2 + \alpha_2 y^2 + \alpha_3 x\dot{x} \\
&\quad + \alpha_4 xy + \alpha_5 x\dot{y} + \alpha_6 \dot{x} y + \alpha_7 y\dot{y}, \\
\ddot{y} + \alpha y + \beta \dot{x} &= -2\hat{\mu}_2 \dot{y} + \beta_1 x^2 + \beta_2 y^2 + \beta_3 x\dot{x} \\
&\quad + \beta_4 xy + \beta_5 x\dot{y} + \beta_6 \dot{x} y + \beta_7 y\dot{y} + F\cos(\Omega t + \tau)\,. \qquad (1.140)
\end{aligned}$$

We seek the first-order solution for small but finite amplitudes in the form

$$\begin{aligned}
x &= \varepsilon x_1 (T_0, T_1) + \varepsilon^2 x_2 (T_0, T_1) + \cdots, \\
y &= \varepsilon y_1 (T_0, T_1) + \varepsilon^2 y_2 (T_0, T_1) + \cdots, \qquad (1.141)
\end{aligned}$$

where ε is the small, dimensionless parameter related to the amplitudes and $T_n = \varepsilon^n t$ $(n = 0, 1)$ are the independent variables; T_0 is the "fast" time, whereas T_1 is the "slow" time. It follows that the derivatives with respect to t become expansions in terms of the partial derivatives with respect to T_n according to

$$\begin{aligned}
\frac{\mathrm{d}}{\mathrm{d}t} &= \frac{\partial}{\partial T_0}\frac{\partial T_0}{\partial t} + \frac{\partial}{\partial T_1}\frac{\partial T_1}{\partial t} + \frac{\partial}{\partial T_2}\frac{\partial T_2}{\partial t} + \cdots \\
&= D_0 + \varepsilon D_1 + \varepsilon^2 D_2 + \cdots, \\
\frac{\mathrm{d}^2}{\mathrm{d}t^2} &= \left(D_0 + \varepsilon D_1 + \varepsilon^2 D_2 + \ldots\right)^2 \\
&= D_0^2 + 2\varepsilon D_0 D_1 + \varepsilon^2 \left(D_1^2 + 2D_0 D_2\right) + \cdots, \qquad (1.142)
\end{aligned}$$

where $D_k = \frac{\partial}{\partial T_k}$.

To analyze the *non-resonant case* the forcing term is ordered so that it appears at order ε. Thus, we recall in (1.140) $F = \varepsilon f$, $\hat{\mu}_n = \varepsilon \mu_n$. Substituting (1.141) into (1.140) and equating the coefficients of similar powers of ε we obtain

Order ε

$$\begin{aligned} D_0^2 x_1 + \alpha x_1 - \beta D_0 y_1 &= 0, \\ D_0^2 y_1 + \alpha y_1 + \beta D_0 x_1 &= f \cos\left(\Omega T_0 + \tau\right). \end{aligned} \tag{1.143}$$

Order ε^2

$$\begin{aligned} D_0^2 x_2 + \alpha x_2 - \beta D_0 y_2 &= -2D_0\left(D_1 x_1 + \mu_1 x_1\right) \\ &\quad + \beta D_1 y_1 + \alpha_1 x_1^2 + \alpha_2 y_1^2 + \alpha_3 x_1 D_0 x_1 \\ &\quad + \alpha_4 x_1 y_1 + \alpha_5 x_1 D_0 y_1 + \alpha_6 y_1 D_0 x_1 + \alpha_7 y_1 D_0 y_1, \\ D_0^2 y_2 + \alpha y_2 + \beta D_0 x_2 &= -2D_0\left(D_1 y_1 + \mu_2 y_1\right) \\ &\quad - \beta D_1 x_1 + \beta_1 x_1^2 + \beta_2 y_1^2 + \beta_3 x_1 D_0 x_1 \\ &\quad + \beta_4 x_1 y_1 + \beta_5 x_1 D_0 y_1 + \beta_6 y_1 D_0 x_1 + \beta_7 y_1 D_0 y_1. \end{aligned} \tag{1.144}$$

The solution of (1.143) is expressed in the form

$$\begin{aligned} x_1 &= A_1\left(T_1\right) \exp\left(\mathrm{i}\omega_1 T_0\right) + A_2\left(T_1\right) \exp\left(\mathrm{i}\omega_2 T_0\right) \\ &\quad + \Phi_1 \exp\left[\mathrm{i}\left(\Omega T_0 + \tau\right)\right] + CC, \\ y_1 &= \Lambda_1 A_1\left(T_1\right) \exp\left(\mathrm{i}\omega_1 T_0\right) + \Lambda_2 A_2\left(T_1\right) \exp\left(\mathrm{i}\omega_2 T_0\right) \\ &\quad + \Phi_2 \exp\left[\mathrm{i}\left(\Omega T_0 + \tau\right)\right] + CC, \end{aligned} \tag{1.145}$$

where CC denotes the complex conjugate of the preceding terms, A_1 and A_2 are the arbitrary functions of T_1 at this level of approximation,

$$\begin{aligned} \Lambda_n &= \frac{\omega_n^2 - \alpha}{\omega_n \beta} i, \qquad \Phi_1 = \frac{i}{2} \frac{\beta \Omega f}{\left(\alpha - \Omega^2\right)^2 - \beta^2 \Omega^2}, \\ \Phi_2 &= \frac{1}{2} \frac{f\left(\alpha - \Omega^2\right)}{\left(\alpha - \Omega^2\right)^2 - \beta^2 \Omega^2}, \qquad (n = 1,\ 2), \end{aligned} \tag{1.146}$$

ω_n are assumed to be distinct, and ω_n^2 are the roots of the characteristic equation

$$\begin{aligned} \det \begin{pmatrix} -\lambda & 1 & 0 & 0 \\ -\alpha & -\lambda & 0 & \beta \\ 0 & 0 & -\lambda & 1 \\ 0 & -\beta & -\alpha & -\lambda \end{pmatrix} &= \lambda^4 + \left(2\alpha + \beta^2\right) \lambda^2 + \alpha^2 \\ &= \omega_n^4 - \left(2\alpha + \beta^2\right) \omega_n^2 + \alpha^2 = 0, \\ \lambda_{1,2} = \pm \mathrm{i}\omega_1, &\qquad \lambda_{3,4} = \pm \mathrm{i}\omega_2, \end{aligned}$$

$$\lambda_{1,2} = \pm\frac{1}{2}\sqrt{-4\alpha - 2\beta^2 + 2\beta\sqrt{\beta^2 + 4\alpha}},$$
$$\lambda_{3,4} = \pm\frac{1}{2}\sqrt{-4\alpha - 2\beta^2 - 2\beta\sqrt{\beta^2 + 4\alpha}}. \quad (1.147)$$

Substitution of (1.145) into (1.144) gives

$$\begin{aligned} D_0^2 x_2 + \alpha x_2 - \beta D_0 y_2 &= \left[-2\mathrm{i}\omega_1\left(A_1^{'} + \mu_1 A_1\right) + \beta\Lambda_1 A_1^{'}\right]\exp\left(\mathrm{i}\omega_1 T_0\right) \\ &+ \left[-2\mathrm{i}\omega_2\left(A_2^{'} + \mu_1 A_2\right) + \beta\Lambda_2 A_2^{'}\right]\exp\left(\mathrm{i}\omega_2 T_0\right) + \cdots + CC, \\ D_0^2 y_2 + \alpha y_2 + \beta D_0 x_2 &= \left[-2\mathrm{i}\omega_1\Lambda_1\left(A_1^{'} + \mu_2 A_1\right) - \beta A_1^{'}\right]\exp\left(\mathrm{i}\omega_1 T_0\right) \\ &+ \left[-2\mathrm{i}\omega_2\Lambda_2\left(A_2^{'} + \mu_2 A_2\right) - \beta A_2^{'}\right]\exp\left(\mathrm{i}\omega_2 T_0\right) + \cdots + CC. \quad (1.148) \end{aligned}$$

Terms that do not influence the solvability conditions are not presented in the last equations and were replaced by dots. To determine the solvability conditions of (1.144), following the method of undetermined coefficients we seek a particular solution in the form

$$\begin{aligned} x_2 &= P_{11}\exp\left(\mathrm{i}\omega_1 T_0\right) + P_{12}\exp\left(\mathrm{i}\omega_2 T_0\right), \\ y_2 &= P_{21}\exp\left(\mathrm{i}\omega_1 T_0\right) + P_{22}\exp\left(\mathrm{i}\omega_2 T_0\right), \quad (1.149) \end{aligned}$$

with unknowns P_{11}, P_{12}, P_{21}, and P_{22}. Substitution of expressions (1.149) into (1.148) and collecting the coefficients at $\exp(\mathrm{i}\omega_1 T_0)$ and $\exp(\mathrm{i}\omega_2 T_0)$ yield

$$\begin{aligned} \left(\alpha - \omega_n^2\right) P_{1n} - i\beta\omega_n P_{2n} &= R_{1n}, \\ i\beta\omega_n P_{1n} + \left(\alpha - \omega_n^2\right) P_{2n} &= R_{2n}, \quad n = 1, 2, \quad (1.150) \end{aligned}$$

where

$$\begin{aligned} R_{11} &= -2\mathrm{i}\omega_1\left(A_1^{'} + \mu_1 A_1\right) + \beta\Lambda_1 A_1^{'}, \\ R_{12} &= -2\mathrm{i}\omega_2\left(A_2^{'} + \mu_1 A_2\right) + \beta\Lambda_2 A_2^{'}, \\ R_{21} &= -2\mathrm{i}\omega_1\Lambda_1\left(A_1^{'} + \mu_2 A_1\right) - \beta A_1^{'}, \\ R_{22} &= -2\mathrm{i}\omega_2\Lambda_2\left(A_2^{'} + \mu_2 A_2\right) - \beta A_2^{'}. \quad (1.151) \end{aligned}$$

Taking into account the characteristic (1.147), the determinant Δ of the set of linear algebraic equations relative to P_{1n}, P_{2n} [(1.150)] is equal to zero:

$$\Delta = \begin{vmatrix} \alpha - \omega_n^2 & -\mathrm{i}\beta\omega_n \\ \mathrm{i}\beta\omega_n & \alpha - \omega_n^2 \end{vmatrix} = \left(\alpha - \omega_n^2\right)^2 - \beta^2\omega_n^2 = 0. \quad (1.152)$$

According to the Kronecker–Kapelly theorem, the set of linear algebraic equations is compatible if and only if the matrix rank of the linear set is equal to the extended matrix rank. Therefore, the solvability conditions are

$$\begin{vmatrix} R_{1n} & -\mathrm{i}\beta\omega_n \\ R_{2n} & \left(\alpha-\omega_n^2\right) \end{vmatrix} = 0, \qquad n = 1, 2; \tag{1.153}$$

otherwise the set of linear algebraic (1.150) has no solutions. So

$$R_{1n} = \frac{\mathrm{i}\beta\omega_n R_{2n}}{\omega_n^2-\alpha} \tag{1.154}$$

and the solvability conditions can be written in the form

$$R_{1n} = \frac{R_{2n}}{\bar{\Lambda}_n}, \quad n = 1, 2. \tag{1.155}$$

The differential equations to define $A_1(T_1)$ and $A_2(T_1)$ are the consequence of solvability conditions (1.155)

$$\begin{aligned} &\left(\beta\Lambda_1 - 2\mathrm{i}\omega_1 + \frac{2\mathrm{i}\omega_1\Lambda_1+\beta}{\bar{\Lambda}_1}\right)A_1' + \left(\frac{2\mathrm{i}\omega_1\Lambda_1\mu_2}{\bar{\Lambda}_1} - 2\mathrm{i}\omega_1\mu_1\right)A_1 = 0, \\ &\left(\beta\Lambda_2 - 2\mathrm{i}\omega_2 + \frac{2\mathrm{i}\omega_2\Lambda_2+\beta}{\bar{\Lambda}_2}\right)A_2' + \left(\frac{2\mathrm{i}\omega_2\Lambda_2\mu_2}{\bar{\Lambda}_2} - 2\mathrm{i}\omega_2\mu_1\right)A_2 = 0. \end{aligned} \tag{1.156}$$

It follows from (1.141), (1.145), and (1.156) that the complex solution of the differential set (1.140) is

$$\begin{aligned} x &= \varepsilon[\exp\left(-\varepsilon\nu_1 t\right)a_1\exp\left(\mathrm{i}\omega_1 t\right) + \exp\left(-\varepsilon\nu_2 t\right)a_2\exp\left(\mathrm{i}\omega_2 t\right) \\ &\quad +\Phi_1\exp\left[\mathrm{i}\left(\Omega t+\tau\right)\right] + CC] + O\left(\varepsilon^2\right), \\ y &= \varepsilon[\Lambda_1\exp\left(-\varepsilon\nu_1 t\right)a_1\exp\left(\mathrm{i}\omega_1 t\right) + \Lambda_2\exp\left(-\varepsilon\nu_2 t\right)a_2\exp\left(\mathrm{i}\omega_2 t\right) \\ &\quad +\Phi_2\exp\left[\mathrm{i}\left(\Omega t+\tau\right)\right] + CC] + O\left(\varepsilon^2\right). \end{aligned} \tag{1.157}$$

Then the real solution is as follows:

$$\begin{aligned} x &= \varepsilon[\exp\left(-\varepsilon\nu_1 t\right)a_1\cos\left(\omega_1 t+\Theta_1\right) + \exp\left(-\varepsilon\nu_2 t\right)a_2\cos\left(\omega_2 t+\Theta_2\right) \\ &\quad +2\mathrm{Im}\Phi_1\sin\left(\Omega t+\tau\right)] + O\left(\varepsilon^2\right), \\ y &= \varepsilon[\mathrm{Im}\Lambda_1\exp\left(-\varepsilon\nu_1 t\right)a_1\sin\left(\omega_1 t+\Theta_1\right) + \mathrm{Im}\Lambda_2\exp\left(-\varepsilon\nu_2 t\right)a_2\sin\left(\omega_2 t+\Theta_2\right) \\ &\quad +2\Phi_2\cos\left(\Omega t+\tau\right)] + O\left(\varepsilon^2\right), \end{aligned} \tag{1.158}$$

where

$$\nu_n = \frac{2\omega_n\left(\mu_1+\mu_2\right)}{4\omega_n-\beta\left(\mathrm{Im}\varLambda_n+\frac{1}{\mathrm{Im}\varLambda_n}\right)}, \tag{1.159}$$

and a_n and $\varTheta_n$ are the real constants.

Figures 1.39–1.41 show a comparison of the numerical integration of (1.140) and the perturbation solutions (1.158) for the following parameters of set (1.140): $\alpha = 1,500$, $\beta = 70$, $\alpha_1 = 9.985\times 10^2$, $\alpha_2 = 2\times 10^3$, $\alpha_3 = 7.9588\times 10^3$, $\alpha_4 = 0.002$, $\alpha_5 = -4.0794\times 10^3$, $\alpha_6 = 4.0002\times 10^3$, $\alpha_7 = 8.0005\times 10^3$, $\beta_1 = 29.9975$, $\beta_2 = -0.001$, $\beta_3 = -4.1594\times 10^3$, $\beta_4 = -1.9997\times 10^3$, $\beta_5 = -7.9188\times 10^3$, $\beta_6 = 0.7959$, $\beta_7 = -0.4083$; the initial conditions are $x(0) = 10^{-12}$, $y(0) = 10^{-10}$, $\dot{x}(0) = \dot{y}(0) = 0$.

In the case of non-resonant undamped vibrations of a rotor (Fig. 1.39), it is accepted for numerical integration that $\hat{\mu}_1 = 0$, $\hat{\mu}_2 = 0$, $F = 0$. According to (1.158), the perturbation solution is presented by the expressions

$$\begin{aligned} x &= 8.2686044\cdot 10^{-6}\cos(17.2015t) + 1.6313956\cdot 10^{-6}\cos(87.2015t),\\ y &= 8.2686044\cdot 10^{-6}\sin(17.2015t) - 1.6313956\cdot 10^{-6}\sin(87.2015t). \end{aligned} \tag{1.160}$$

Figure 1.40 corresponds to the non-resonant damped vibrations of a rotor. For this case, $\hat{\mu}_1 = 0.1$, $\hat{\mu}_2 = 0.15$, $F = 0$. The perturbation solution has the form

$$\begin{aligned} x &= 8.2686044\cdot 10^{-6}\exp(-0.0412t)\cos(17.2015t)\\ &\quad +1.6313956\cdot 10^{-6}\exp(-0.2088t)\cos(87.2015t),\\ y &= 8.2686044\cdot 10^{-6}\exp(-0.0412t)\sin(17.2015t)\\ &\quad -1.6313956\cdot 10^{-6}\exp(-0.2088t)\sin(87.2015t). \end{aligned} \tag{1.161}$$

For the non-resonant forced damped vibrations of a rotor (Fig. 1.41) it is accepted for numerical integration that $\hat{\mu}_1 = 0.1$, $\hat{\mu}_2 = 0.15$, $F = 0.005$, $\varOmega = 10$, $\tau = -\pi/2$. The perturbation solution is

$$\begin{aligned} x &= 5.8241\cdot 10^{-6}\exp(-0.0412t)\cos(17.2015t)\\ &\quad +1.69495\cdot 10^{-6}\exp(-0.2088t)\cos(87.2015t)\\ &\quad -2.38095\cdot 10^{-6}\sin(10t-\pi/2),\\ y &= 5.8241\cdot 10^{-6}\exp(-0.0412t)\sin(17.2015t)\\ &\quad -1.69495\cdot 10^{-6}\exp(-0.2088t)\sin(87.2015t)\\ &\quad +4.7619\cdot 10^{-6}\cos(10t-\pi/2). \end{aligned} \tag{1.162}$$

Figures 1.39–1.41 demonstrate good agreement of the numerical and analytical solutions.

Fig. 1.39 Comparison of numerical integration (1.140) and perturbation solutions (1.158) in the case of non-resonant undamped vibrations of a rotor

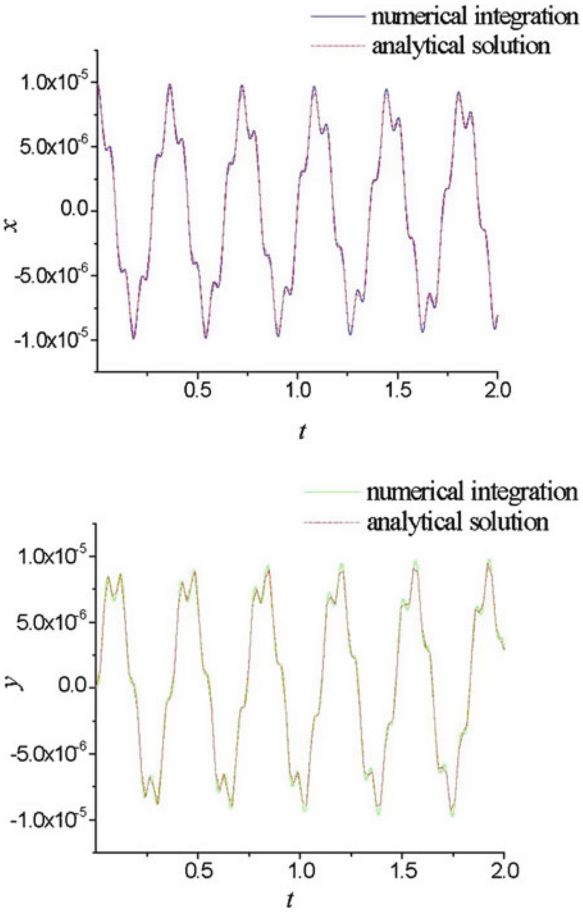

1.5.2.2 Primary Resonance: The Cases of no Internal Resonance and an Internal Resonance

To analyze primary resonances, the forcing term is ordered such that it appears at order ε^2 or in the same perturbation equation as the non-linear terms and damping. Thus, we recall in (1.140) $F = \varepsilon^2 f$, $\hat{\mu}_n = \varepsilon \mu_n$. Consider the case where $\Omega \approx \omega_2$. The case $\Omega \approx \omega_1$ is analogous. Let us introduce the detuning parameter σ_1 and set $\Omega = \omega_2 + \varepsilon \sigma_1$.

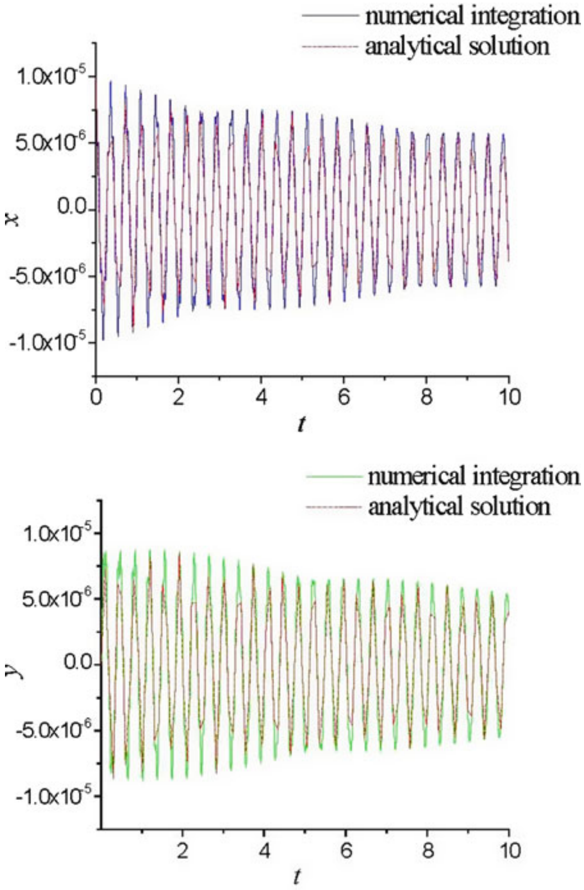

Fig. 1.40 Comparison of numerical integration (1.140) and perturbation solutions (1.158) in the case of non-resonant damped vibrations of a rotor

Substituting (1.141) into (1.140) and equating coefficients of similar powers of ε we obtain

Order ε

$$\begin{aligned} &D_0^2 x_1 + \alpha x_1 - \beta D_0 y_1 = 0, \\ &D_0^2 y_1 + \alpha y_1 + \beta D_0 x_1 = 0. \end{aligned} \tag{1.163}$$

Order ε^2

$$\begin{aligned} D_0^2 x_2 + \alpha x_2 - \beta D_0 y_2 = {} & -2D_0 \left(D_1 x_1 + \mu_1 x_1 \right) + \beta D_1 y_1 \\ & + \alpha_1 x_1^2 + \alpha_2 y_1^2 + \alpha_3 x_1 D_0 x_1 + \alpha_4 x_1 y_1 \\ & + \alpha_5 x_1 D_0 y_1 + \alpha_6 y_1 D_0 x_1 + \alpha_7 y_1 D_0 y_1, \end{aligned}$$

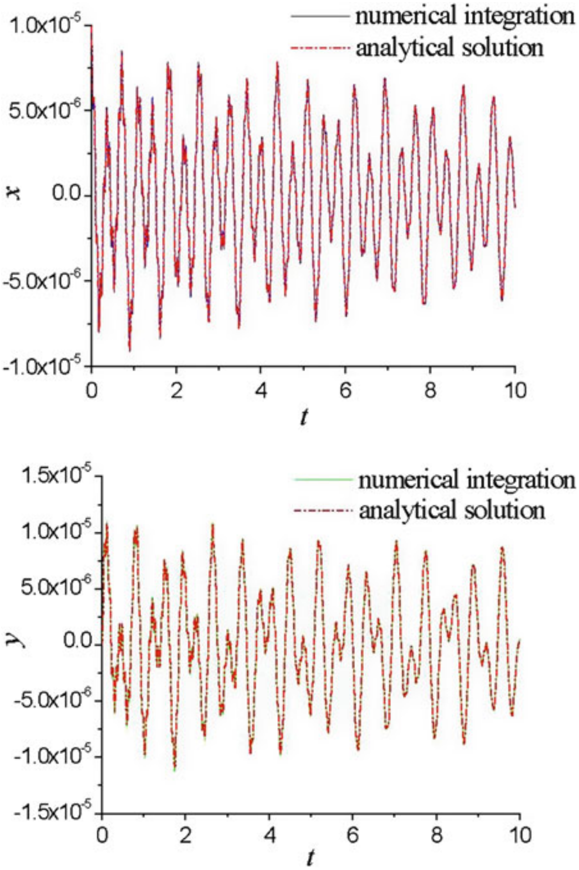

Fig. 1.41 Comparison of numerical integration (1.140) and perturbation solutions (1.158) in the case of non-resonant forced damped vibrations of a rotor

$$\begin{aligned} D_0^2 y_2 + \alpha y_2 + \beta D_0 x_2 = & -2D_0 \left(D_1 y_1 + \mu_2 y_1\right) - \beta D_1 x_1 \\ & + \beta_1 x_1^2 + \beta_2 y_1^2 + \beta_3 x_1 D_0 x_1 + \beta_4 x_1 y_1 \\ & + \beta_5 x_1 D_0 y_1 + \beta_6 y_1 D_0 x_1 + \beta_7 y_1 D_0 y_1 \\ & + f \cos\left(\Omega T_0 + \tau\right). \end{aligned} \tag{1.164}$$

The solution of (1.163) is given in the form

$$\begin{aligned} x_1 &= A_1\left(T_1\right)\exp\left(\mathrm{i}\omega_1 T_0\right) + A_2\left(T_1\right)\exp\left(\mathrm{i}\omega_2 T_0\right) + CC, \\ y_1 &= \Lambda_1 A_1\left(T_1\right)\exp\left(\mathrm{i}\omega_1 T_0\right) + \Lambda_2 A_2\left(T_1\right)\exp\left(\mathrm{i}\omega_2 T_0\right) + CC, \end{aligned} \tag{1.165}$$

where

$$\Lambda_n = \frac{\omega_n^2 - \alpha}{\omega_n \beta} i. \tag{1.166}$$

Substitution of (1.165) into (1.164) yields

$$\begin{aligned}
D_0^2 x_2 + \alpha x_2 - \beta D_0 y_2 &= \left[-2\mathrm{i}\omega_1 \left(A_1' + \mu_1 A_1\right)\right. \\
&\quad \left. + \beta \varLambda_1 A_1'\right] \exp\left(\mathrm{i}\omega_1 T_0\right) + \left[-2\mathrm{i}\omega_2 \left(A_2' + \mu_1 A_2\right)\right. \\
&\quad \left. + \beta \varLambda_2 A_2'\right] \exp\left(\mathrm{i}\omega_2 T_0\right) + A_1^2[\alpha_1 + \varLambda_1^2 \alpha_2 + \mathrm{i}\omega_1 \alpha_3 + \varLambda_1 \alpha_4 \\
&\quad + \mathrm{i}\omega_1 \varLambda_1 \alpha_5 + \mathrm{i}\omega_1 \varLambda_1 \alpha_6 + \mathrm{i}\omega_1 \varLambda_1^2 \alpha_7] \exp\left(2\mathrm{i}\omega_1 T_0\right) \\
&\quad + A_2^2[\alpha_1 + \varLambda_2^2 \alpha_2 + \mathrm{i}\omega_2 \alpha_3 + \varLambda_2 \alpha_4 + \mathrm{i}\omega_2 \varLambda_2 \alpha_5 + \mathrm{i}\omega_2 \varLambda_2 \alpha_6 \\
&\quad + \mathrm{i}\omega_2 \varLambda_2^2 \alpha_7] \exp\left(2\mathrm{i}\omega_2 T_0\right) + A_1 A_2[2\alpha_1 + 2\varLambda_1 \varLambda_2 \alpha_2 + \left(\mathrm{i}\omega_1 + \mathrm{i}\omega_2\right) \alpha_3 \\
&\quad + \left(\varLambda_1 + \varLambda_2\right) \alpha_4 + \left(\mathrm{i}\omega_2 \varLambda_2 - \mathrm{i}\omega_1 \varLambda_1\right) \alpha_5 + \left(\mathrm{i}\omega_2 \varLambda_1 + \mathrm{i}\omega_1 \varLambda_2\right) \alpha_6 \\
&\quad + \left(\mathrm{i}\omega_1 + \mathrm{i}\omega_2\right) \varLambda_1 \varLambda_2 \alpha_7] \exp\left(\mathrm{i}\left(\omega_1 + \omega_2\right) T_0\right) + \bar{A}_1 A_2[2\alpha_1 + 2\bar{\varLambda}_1 \varLambda_2 \alpha_2 \\
&\quad + \left(\mathrm{i}\omega_2 - \mathrm{i}\omega_1\right) \alpha_3 + \left(\varLambda_2 + \bar{\varLambda}_1\right) \alpha_4 + \left(\mathrm{i}\omega_2 \varLambda_2 - \mathrm{i}\omega_1 \bar{\varLambda}_1\right) \alpha_5 \\
&\quad + \left(\mathrm{i}\omega_2 \bar{\varLambda}_1 - \mathrm{i}\omega_1 \varLambda_2\right) \alpha_6 + \left(\mathrm{i}\omega_2 - \mathrm{i}\omega_1\right) \bar{\varLambda}_1 \varLambda_2 \alpha_7] \exp\left(\mathrm{i}\left(\omega_2 - \omega_1\right) T_0\right) \\
&\quad + A_1 \bar{A}_1 \left(\alpha_1 + \varLambda_1 \left(\bar{\varLambda}_1 \alpha_2 + \alpha_4 + \mathrm{i}\omega_1 \left(\alpha_5 - \alpha_6\right)\right)\right) \\
&\quad + A_2 \bar{A}_2 \left(\alpha_1 + \varLambda_2 \left(\bar{\varLambda}_2 \alpha_2 + \alpha_4 + \mathrm{i}\omega_2 \left(\alpha_5 - \alpha_6\right)\right)\right) + CC,
\end{aligned} \tag{1.167}$$

$$\begin{aligned}
D_0^2 y_2 + \alpha y_2 + \beta D_0 x_2 &= \left[-2\mathrm{i}\omega_1 \varLambda_1 \left(A_1' + \mu_2 A_1\right) - \beta A_1'\right] \exp\left(\mathrm{i}\omega_1 T_0\right) \\
&\quad + \left[-2\mathrm{i}\omega_2 \varLambda_2 \left(A_2' + \mu_2 A_2\right) - \beta A_2'\right] \exp\left(\mathrm{i}\omega_2 T_0\right) \\
&\quad + A_1^2[\beta_1 + \varLambda_1^2 \beta_2 + \mathrm{i}\omega_1 \beta_3 + \varLambda_1 \beta_4 + \mathrm{i}\omega_1 \varLambda_1 \beta_5 + \mathrm{i}\omega_1 \varLambda_1 \beta_6 \\
&\quad + \mathrm{i}\omega_1 \varLambda_1^2 \beta_7] \exp\left(2\mathrm{i}\omega_1 T_0\right) + A_2^2[\beta_1 + \varLambda_2^2 \beta_2 + \mathrm{i}\omega_2 \beta_3 + \varLambda_2 \beta_4 + \mathrm{i}\omega_2 \varLambda_2 \beta_5 \\
&\quad + \mathrm{i}\omega_2 \varLambda_2 \beta_6 + \mathrm{i}\omega_2 \varLambda_2^2 \beta_7] \exp\left(2\mathrm{i}\omega_2 T_0\right) + A_1 A_2[2\beta_1 + 2\varLambda_1 \varLambda_2 \beta_2 \\
&\quad + \left(\mathrm{i}\omega_1 + \mathrm{i}\omega_2\right) \beta_3 + \left(\varLambda_1 + \varLambda_2\right) \beta_4 + \left(\mathrm{i}\omega_2 \varLambda_2 - \mathrm{i}\omega_1 \varLambda_1\right) \beta_5 \\
&\quad + \left(\mathrm{i}\omega_2 \varLambda_1 + \mathrm{i}\omega_1 \varLambda_2\right) \beta_6 + \left(\mathrm{i}\omega_1 + \mathrm{i}\omega_2\right) \varLambda_1 \varLambda_2 \beta_7] \exp\left(\mathrm{i}\left(\omega_1 + \omega_2\right) T_0\right) \\
&\quad + \bar{A}_1 A_2[2\beta_1 + 2\bar{\varLambda}_1 \varLambda_2 \beta_2 + \left(\mathrm{i}\omega_2 - \mathrm{i}\omega_1\right) \beta_3 \\
&\quad + \left(\varLambda_2 + \bar{\varLambda}_1\right) \beta_4 + \left(\mathrm{i}\omega_2 \varLambda_2 - \mathrm{i}\omega_1 \bar{\varLambda}_1\right) \beta_5 \\
&\quad + \left(\mathrm{i}\omega_2 \bar{\varLambda}_1 - \mathrm{i}\omega_1 \varLambda_2\right) \beta_6 + \left(\mathrm{i}\omega_2 - \mathrm{i}\omega_1\right) \bar{\varLambda}_1 \varLambda_2 \beta_7] \exp\left(\mathrm{i}\left(\omega_2 - \omega_1\right) T_0\right) \\
&\quad + A_1 \bar{A}_1 \left(\beta_1 + \varLambda_1 \left(\bar{\varLambda}_1 \beta_2 + \beta_4 + \mathrm{i}\omega_1 \left(\beta_5 - \beta_6\right)\right)\right) \\
&\quad + A_2 \bar{A}_2 \left(\beta_1 + \varLambda_2 \left(\bar{\varLambda}_2 \beta_2 + \beta_4 + \mathrm{i}\omega_2 \left(\beta_5 - \beta_6\right)\right)\right) \\
&\quad + \frac{1}{2} f \exp\left(\mathrm{i}\left(\omega_2 T_0 + \sigma_1 T_1 + \tau\right)\right) + CC.
\end{aligned} \tag{1.168}$$

Let $\omega_2 > \omega_1$ for definiteness. We need to distinguish between the case of internal resonance $\omega_2 \approx 2\omega_1$ and the case of no internal resonance, i.e., ω_2 is away from $2\omega_1$. The case $\omega_1 > \omega_2$, $\omega_1 \approx 2\omega_2$ is analogous. When ω_2 is away from $2\omega_1$, the solvability conditions (1.155) are written in the form

$$
\begin{aligned}
&q_{\omega_1} + \frac{1}{\Lambda_1} p_{\omega_1} = 0,\\
&q_{\omega_2} + \frac{1}{\Lambda_2} p_{\omega_2} + \frac{1}{2\Lambda_2} f \exp\left(\mathrm{i}\left(\sigma_1 T_1 + \tau\right)\right) = 0,
\end{aligned}
\tag{1.169}
$$

where

$$
\begin{aligned}
q_{\omega_1} &= -2\mathrm{i}\omega_1 \left(A_1^{\prime} + \mu_1 A_1\right) + \beta \Lambda_1 A_1^{\prime},\\
q_{\omega_2} &= 2\mathrm{i}\omega_2 \left(A_2^{\prime} + \mu_1 A_2\right) + \beta \Lambda_2 A_2^{\prime},\\
p_{\omega_1} &= -2\mathrm{i}\omega_1 \Lambda_1 \left(A_1^{\prime} + \mu_2 A_1\right) - \beta A_1^{\prime},\\
p_{\omega_2} &= -2\mathrm{i}\omega_2 \Lambda_2 \left(A_2^{\prime} + \mu_2 A_2\right) - \beta A_2^{\prime}.
\end{aligned}
\tag{1.170}
$$

Thus, when there is no internal resonance, the first approximation is not influenced by the non-linear terms; it is essentially a solution of the corresponding linear problem.

Actually, the solutions of the differential equations below

$$
\begin{aligned}
&\left(\beta \Lambda_1 - 2\mathrm{i}\omega_1 + \frac{2\mathrm{i}\omega_1 \Lambda_1 + \beta}{\bar{\Lambda}_1}\right) A_1^{\prime} + \left(\frac{2\mathrm{i}\omega_1 \Lambda_1 \mu_2}{\bar{\Lambda}_1} - 2\mathrm{i}\omega_1 \mu_1\right) A_1 = 0,\\
&\left(\beta \Lambda_2 - 2\mathrm{i}\omega_2 + \frac{2\mathrm{i}\omega_2 \Lambda_2 + \beta}{\bar{\Lambda}_2}\right) A_2^{\prime} + \left(\frac{2\mathrm{i}\omega_2 \Lambda_2 \mu_2}{\bar{\Lambda}_2} - 2\mathrm{i}\omega_2 \mu_1\right) A_2\\
&\quad = -\frac{1}{2\Lambda_2} f \exp\left[\mathrm{i}\left(\sigma_1 T_1 + \tau\right)\right]
\end{aligned}
\tag{1.171}
$$

are

$$
\begin{aligned}
A_1\left(T_1\right) &= \frac{1}{2} a_1 \exp\left(-\nu_1 T_1 + \mathrm{i}\Theta_1\right),\\
A_2\left(T_1\right) &= \frac{1}{2} a_2 \exp\left(-\nu_2 T_1 + \mathrm{i}\Theta_2\right)\\
&\quad + \frac{f\left(\nu_2 - \mathrm{i}\sigma_1\right)}{2 \operatorname{Im}\Lambda_2 \operatorname{Im}\kappa_2 \left(\nu_2^2 + \sigma_1^2\right)} \exp\left[\mathrm{i}\left(\sigma_1 T_1 + \tau\right)\right],
\end{aligned}
\tag{1.172}
$$

where a_n and Θ_n are the real constants:

$$\nu_n = \frac{2\omega_n\left(\mu_1+\mu_2\right)}{4\omega_n-\beta\left(\mathrm{Im}\Lambda_n+\frac{1}{\mathrm{Im}\Lambda_n}\right)},$$

$$\kappa_2 = -4\omega_2 i+\beta\left(\mathrm{Im}\Lambda_2+\frac{1}{\mathrm{Im}\Lambda_2}\right)i. \tag{1.173}$$

As $t\to\infty$, $T_1\to\infty$, and

$$A_1\to 0,\quad A_2\to\frac{f\left(\nu_2-\mathrm{i}\sigma_1\right)}{2\mathrm{Im}\Lambda_2\mathrm{Im}\kappa_2\left(\nu_2^2+\sigma_1^2\right)}\exp\left[\mathrm{i}\left(\sigma_1T_1+\tau\right)\right], \tag{1.174}$$

and according to (1.165), we obtain the following steady-state response:

$$x_1 = \frac{f\left(\nu_2-\mathrm{i}\sigma_1\right)}{2\mathrm{Im}\Lambda_2\mathrm{Im}\kappa_2\left(\nu_2^2+\sigma_1^2\right)}\exp\left[\mathrm{i}\left(\omega_2T_0+\sigma_1T_1+\tau\right)\right]+CC,$$

$$y_1 = \Lambda_2\frac{f\left(\nu_2-\mathrm{i}\sigma_1\right)}{2\mathrm{Im}\Lambda_2\mathrm{Im}\kappa_2\left(\nu_2^2+\sigma_1^2\right)}\exp\left[\mathrm{i}\left(\omega_2T_0+\sigma_1T_1+\tau\right)\right]+CC. \tag{1.175}$$

Therefore, the real solution is

$$x = \frac{F}{\varepsilon}\frac{1}{\mathrm{Im}\Lambda_2\mathrm{Im}\kappa_2\left(\nu_2^2+\sigma_1^2\right)}\left[\nu_2\cos\left(\Omega t+\tau\right)+\sigma_1\sin\left(\Omega t+\tau\right)\right]+O\left(\varepsilon^2\right),$$

$$y = \frac{F}{\varepsilon}\frac{1}{\mathrm{Im}\kappa_2\left(\nu_2^2+\sigma_1^2\right)}\left[\sigma_1\cos\left(\Omega t+\tau\right)-\nu_2\sin\left(\Omega t+\tau\right)\right]+O\left(\varepsilon^2\right), \tag{1.176}$$

or it can be rewritten in the form

$$x = \frac{F}{\varepsilon}\frac{1}{\mathrm{Im}\Lambda_2\mathrm{Im}\kappa_2\left(\nu_2^2+\sigma_1^2\right)^{1/2}}\sin\left(\Omega t+\tau+\tilde{\gamma}_1\right)+O\left(\varepsilon^2\right),$$

$$y = \frac{F}{\varepsilon}\frac{1}{\mathrm{Im}\kappa_2\left(\nu_2^2+\sigma_1^2\right)^{1/2}}\sin\left(\Omega t+\tau+\tilde{\gamma}_2\right)+O\left(\varepsilon^2\right), \tag{1.177}$$

where $\tilde{\gamma}_1=\arctan(\nu_2/\sigma_1)$, $\tilde{\gamma}_2=-\arctan(\sigma_1/\nu_2)$.

Another situation occurs when the internal resonance $\omega_2\approx 2\omega_1$ exists. Let us introduce the detuning parameter σ_2 and set

$$\omega_2 = 2\omega_1-\varepsilon\sigma_2. \tag{1.178}$$

Taking into account (1.161), the solvability conditions for this case become

$$\begin{aligned} &q_{\omega_1} + \frac{1}{\Lambda_1} p_{\omega_1} + \left(q_{\omega_2-\omega_1} + \frac{1}{\Lambda_1} p_{\omega_2-\omega_1}\right) \bar{A}_1 A_2 \exp\left(-\mathrm{i}\sigma_2 T_1\right) = 0, \\ &q_{\omega_2} + \frac{1}{\Lambda_2} p_{\omega_2} + \left(q_{2\omega_1 + \frac{1}{\Lambda_2} p_{2\omega_1}}\right) A_1^2 \exp\left(\mathrm{i}\sigma_2 T_1\right) + \frac{1}{2\Lambda_2} f \exp\left(\mathrm{i}\left(\sigma_1 T_1 + \tau\right)\right) = 0. \end{aligned} \tag{1.179}$$

Here coefficients q_{ω_1}, q_{ω_2}, $q_{\omega_2-\omega_1}$, and $q_{2\omega_1}$ are the expressions in parentheses at the exponents with the corresponding powers (1.167) and p_{ω_1}, p_{ω_2}, $p_{\omega_2-\omega_1}$, and $p_{2\omega_1}$ are the expressions in brackets at the exponents with the corresponding powers (1.168):

$$\begin{aligned} q_{\omega_1} &= -2\mathrm{i}\omega_1 \left(A_1' + \mu_1 A_1\right) + \beta \Lambda_1 A_1', \\ q_{\omega_2} &= 2\mathrm{i}\omega_2 \left(A_2' + \mu_1 A_2\right) + \beta \Lambda_2 A_2', \\ q_{2\omega_1} &= \alpha_1 + \Lambda_1^2 \alpha_2 + \mathrm{i}\omega_1 \alpha_3 + \Lambda_1 \alpha_4 + \mathrm{i}\omega_1 \Lambda_1 \alpha_5 + \mathrm{i}\omega_1 \Lambda_1 \alpha_6 + \mathrm{i}\omega_1 \Lambda_1^2 \alpha_7, \\ q_{\omega_2-\omega_1} &= 2\alpha_1 + 2\bar{\Lambda}_1 \Lambda_2 \alpha_2 + \left(\mathrm{i}\omega_2 - \mathrm{i}\omega_1\right) \alpha_3 + \left(\Lambda_2 + \bar{\Lambda}_1\right) \alpha_4 \\ &\quad + \left(\mathrm{i}\omega_2 \Lambda_2 - \mathrm{i}\omega_1 \bar{\Lambda}_1\right) \alpha_5 + \left(\mathrm{i}\omega_2 \bar{\Lambda}_1 - \mathrm{i}\omega_1 \Lambda_2\right) \alpha_6 + \left(\mathrm{i}\omega_2 - \mathrm{i}\omega_1\right) \bar{\Lambda}_1 \Lambda_2 \alpha_7, \\ p_{\omega_1} &= -2\mathrm{i}\omega_1 \Lambda_1 \left(A_1' + \mu_2 A_1\right) - \beta A_1', \\ p_{\omega_2} &= -2\mathrm{i}\omega_2 \Lambda_2 \left(A_2' + \mu_2 A_2\right) - \beta A_2', \\ p_{2\omega_1} &= \beta_1 + \Lambda_1^2 \beta_2 + \mathrm{i}\omega_1 \beta_3 + \Lambda_1 \beta_4 + \mathrm{i}\omega_1 \Lambda_1 \beta_5 + \mathrm{i}\omega_1 \Lambda_1 \beta_6 + \mathrm{i}\omega_1 \Lambda_1^2 \beta_7, \\ p_{\omega_2-\omega_1} &= 2\beta_1 + 2\bar{\Lambda}_1 \Lambda_2 \beta_2 + \left(\mathrm{i}\omega_2 - \mathrm{i}\omega_1\right) \beta_3 + \left(\Lambda_2 + \bar{\Lambda}_1\right) \beta_4 \\ &\quad + \left(\mathrm{i}\omega_2 \Lambda_2 - \mathrm{i}\omega_1 \bar{\Lambda}_1\right) \beta_5 + \left(\mathrm{i}\omega_2 \bar{\Lambda}_1 - \mathrm{i}\omega_1 \Lambda_2\right) \beta_6 + \left(\mathrm{i}\omega_2 - \mathrm{i}\omega_1\right) \bar{\Lambda}_1 \Lambda_2 \beta_7. \end{aligned} \tag{1.180}$$

For convenience let us introduce the polar notation

$$A_m = \frac{1}{2} a_m \exp\left(\mathrm{i}\Theta_m\right), \qquad m = 1, 2, \tag{1.181}$$

where a_m and Θ_m are the real functions of T_1. Substitution of (1.181) into (1.179) yields

$$\begin{aligned} &\left(a_1' + \mathrm{i}a_1 \Theta_1'\right) + \nu_1 a_1 + \frac{1}{2\kappa_1} a_1 a_2 \left[\varphi + \mathrm{i}\psi\right] \exp\left(\mathrm{i}\gamma_2\right) = 0, \\ &\left(a_2' + \mathrm{i}a_2 \Theta_2'\right) + \nu_2 a_2 + \frac{1}{2\kappa_2} a_1^2 \left[\zeta + \mathrm{i}\eta\right] \exp\left(-\mathrm{i}\gamma_2\right) + \frac{f}{\kappa_2\ \Lambda_2} \exp\left(\mathrm{i}\gamma_1\right) = 0. \end{aligned} \tag{1.182}$$

In the preceding expressions the following notations were introduced:

$$\begin{aligned}
\varphi &= \mathrm{Re}\left(q_{\omega_2-\omega_1} + \frac{1}{\Lambda_1} p_{\omega_2-\omega_1}\right), \quad \psi = \mathrm{Im}\left(q_{\omega_2-\omega_1} + \frac{1}{\Lambda_1} p_{\omega_2-\omega_1}\right),\\
\zeta &= \mathrm{Re}\left(q_{2\omega_1} + \frac{1}{\Lambda_2} p_{2\omega_1}\right),\\
\eta &= \mathrm{Im}\left(q_{2\omega_1} + \frac{1}{\Lambda_2} p_{2\omega_1}\right),\\
\kappa_n &= -4\omega_n \mathrm{i} + \beta\left(\mathrm{Im}\Lambda_n + \frac{1}{\mathrm{Im}\Lambda_n}\right)\mathrm{i}, \qquad n = 1, 2,\\
\gamma_1 &= \sigma_1 T_1 + \tau - \Theta_2, \qquad \gamma_2 = \Theta_2 - 2\Theta_1 - \sigma_2 T_1,
\end{aligned} \tag{1.183}$$

and ν_1 and ν_2 are defined as in (1.158).

Separating (1.182) into real and imaginary parts and taking into account that according to (1.145) Λ_n $(n = 1, 2)$ is the imaginary value, we obtain

$$\begin{aligned}
a'_1 &= -\nu_1 a_1 - \frac{a_1 a_2}{2\mathrm{Im}\kappa_1}\left(\psi\cos\gamma_2 + \varphi\sin\gamma_2\right),\\
a_1\Theta'_1 &= \frac{a_1 a_2}{2\mathrm{Im}\kappa_1}\left(\varphi\cos\gamma_2 - \psi\sin\gamma_2\right),\\
a'_2 &= -\nu_2 a_2 - \frac{a_1^2}{2\mathrm{Im}\kappa_2}\left(\eta\cos\gamma_2 - \zeta\sin\gamma_2\right) + \frac{f}{\mathrm{Im}\kappa_2 \mathrm{Im}\Lambda_2}\cos\gamma_1,\\
a_2\Theta'_2 &= \frac{a_1^2}{2\mathrm{Im}\kappa_2}\left(\zeta\cos\gamma_2 + \eta\sin\gamma_2\right) + \frac{f}{\mathrm{Im}\kappa_2 \mathrm{Im}\Lambda_2}\sin\gamma_1.
\end{aligned} \tag{1.184}$$

For the steady-state response $a'_n = \gamma'_n = 0$, therefore,

$$\Theta'_1 = \frac{1}{2}\left(\sigma_1 - \sigma_2\right), \qquad \Theta'_2 = \sigma_1. \tag{1.185}$$

Two possibilities follow from (1.184). The first one is given by (1.174). It is the solution of the linear problem. Let us find functions a_1 and a_2 of T_1 according to the second possibility. It follows from the first two equations of (1.184) that

$$\begin{aligned}
\frac{4\omega_1\left(\mu_1 + \mu_2\right)}{a_2} &= -\psi\cos\gamma_2 - \varphi\sin\gamma_2,\\
\frac{\mathrm{Im}\kappa_1}{a_2}\left(\sigma_1 - \sigma_2\right) &= \varphi\cos\gamma_2 - \psi\sin\gamma_2.
\end{aligned} \tag{1.186}$$

So

$$a_2 = \left(\frac{16\omega_1^2\left(\mu_1 + \mu_2\right)^2 + \mathrm{Im}\kappa_1^2\left(\left(\sigma_1 - \sigma_2\right)^2\right)}{\varphi^2 + \psi^2}\right)^{1/2}. \tag{1.187}$$

Let us take $\sin\gamma_2$ and $\cos\gamma_2$ using, for example, the formulas by Cramer:

$$\cos\gamma_2 = \frac{\Delta_1}{\Delta}, \qquad \sin\gamma_2 = \frac{\Delta_2}{\Delta}, \tag{1.188}$$

where

$$\begin{aligned}
\Delta &= \begin{vmatrix} -\psi & -\phi \\ \varphi & -\psi \end{vmatrix} = \varphi^2 + \psi^2, \\
\Delta_1 &= -\frac{1}{a_2}\begin{vmatrix} 2\mathrm{Im}\kappa_1\nu_1 & \varphi \\ \mathrm{Im}\kappa_1\left(\sigma_1 - \sigma_2\right) & \psi \end{vmatrix} \\
&= \frac{1}{a_2}\left(4\omega_1\left(\mu_1 + \mu_2\right)\psi + \mathrm{Im}\kappa_1\left(\sigma_1 - \sigma_2\right)\varphi\right), \\
\Delta_2 &= \frac{1}{a_2}\begin{vmatrix} -\psi & 2\mathrm{Im}\kappa_1\nu_1 \\ \varphi & \mathrm{Im}\kappa_1\left(\sigma_1 - \sigma_2\right) \end{vmatrix} \\
&= \frac{1}{a_2}\left(-\mathrm{Im}\kappa_1\left(\sigma_1 - \sigma_2\right)\psi - 4\omega_1\left(\mu_1 + \mu_2\right)\varphi\right).
\end{aligned} \tag{1.189}$$

Then a biquadratic equation relative to a_1 follows from the last two equations of (1.184):

$$\begin{aligned}
& a_1^4(\zeta^2 + \eta^2) + 4a_1^2[-2\omega_2(\mu_1 + \mu_2)a_2(\eta\cos\gamma_2 - \zeta\sin\gamma_2) \\
& -\mathrm{Im}\kappa_2\sigma_1 a_2(\zeta\cos\gamma_2 + \eta\sin\gamma_2)] \\
& +4\left[4\omega_2^2(\mu_1 + \mu_2)^2 + \mathrm{Im}\kappa_2^2\sigma_1^2\right]a_2^2 - \frac{4f^2}{(\mathrm{Im}\Lambda_2)^2} = 0.
\end{aligned} \tag{1.190}$$

Finally, we obtain the expression for a_1:

$$a_1 = \left[-\frac{p}{2} \pm \left(\left(\frac{p}{2}\right)^2 - q\right)^{\frac{1}{2}}\right]^{\frac{1}{2}}, \tag{1.191}$$

where

$$\begin{aligned}
p &= \frac{4a_2}{\zeta^2 + \eta^2}\left[-2\omega_2\left(\mu_1 + \mu_2\right)\left(\eta\cos\gamma_2 - \zeta\sin\gamma_2\right) - \mathrm{Im}\kappa_2\sigma_1\left(\zeta\cos\gamma_2 + \eta\sin\gamma_2\right)\right], \\
q &= \frac{1}{\zeta^2 + \eta^2}\left\{4a_2^2\left[4\omega_2^2\left(\mu_1 + \mu_2\right)^2 + \mathrm{Im}\kappa_2^2\sigma_1^2\right] - \frac{4f^2}{\left(\mathrm{Im}\Lambda_2\right)^2}\right\}.
\end{aligned} \tag{1.192}$$

Thus, the unknown functions in (1.165) were defined. It follows from (1.141), (1.165), and (1.181) that

$$
\begin{aligned}
x &= \varepsilon\left[\frac{1}{2}a_1\exp\left[\mathrm{i}\left(\Theta_1+\omega_1 T_0\right)\right]+\frac{1}{2}a_2\exp\left[\mathrm{i}\left(\Theta_2+\omega_2 T_0\right)\right]+CC\right]+O\left(\varepsilon^2\right),\\
y &= \varepsilon\left[\frac{1}{2}\Lambda_1 a_1\exp\left[\mathrm{i}\left(\Theta_1+\omega_1 T_0\right)\right]+\frac{1}{2}\Lambda_2 a_2\exp\left[\mathrm{i}\left(\Theta_2+\omega_2 T_0\right)\right]+CC\right]+O\left(\varepsilon^2\right).
\end{aligned}
\tag{1.193}
$$

Then, the real solution is as follows:

$$
\begin{aligned}
x &= \varepsilon\left\{a_1\cos\left[\frac{1}{2}\left(\Omega t+\tau-\gamma_1-\gamma_2\right)\right]+a_2\cos\left(\Omega t+\tau-\gamma_1\right)\right\}+O\left(\varepsilon^2\right),\\
y &= -\varepsilon\left\{a_1\mathrm{Im}\Lambda_1\sin\left[\frac{1}{2}\left(\Omega t+\tau-\gamma_1-\gamma_2\right)\right]a_2\mathrm{Im}\Lambda_2\sin\left(\Omega t+\tau-\gamma_1\right)\right\}+O\left(\varepsilon^2\right).
\end{aligned}
\tag{1.194}
$$

Here a_1 and a_2 are defined by (1.187) and (1.191).

Let us consider the expression for a_1 (1.191). When

$$
\{[(p/2)>0]\wedge(q>0)\}\vee[(p/2)^2<q],
\tag{1.195}
$$

there are no real values of a_1 defined by (1.191) and the response must be given by (1.177). When

$$
[(p/2)^2>q]\wedge(q<0),
\tag{1.196}
$$

there is one real solution defined by (1.191). Therefore, the response is one of the two possibilities given by (1.177) and (1.194). When

$$
[(p/2)<0]\wedge[(p/2)^2>q]\wedge(q>0),
\tag{1.197}
$$

there are two real solutions defined by (1.191). Therefore, the response is one of the three possibilities given by (1.177) and (1.194).

Figure 1.42 depicts frequency-response curves. a_1 and a_2 are plotted as functions of σ_1 for $\sigma_2 = 0$. The dashed line with a peak at $\sigma_1 = 0$ corresponds to $a_1 = 0$ and is a solution of the corresponding linear problem. Arrows indicate the jump phenomenon associated with varying the frequency of external excitation Ω. The perturbation solution obtained is the superposition of two submotions with amplitudes a_1 and a_2 and frequencies ω_1 and ω_2, respectively. To compare the perturbation and numerical solutions, we performed an approximate harmonic analysis of solutions $x(t)$ and $y(t)$, obtained numerically. These functions are expanded in Fourier series formed from cosines

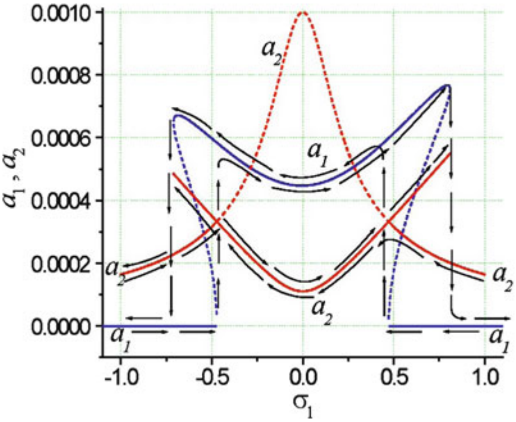

Fig. 1.42 Frequency-response curves; $\sigma_2 = 0$, $\Omega \approx \omega_2$

$$x(t) = \frac{a_0}{2} + \sum_{k=1}^{\infty} a_k \cos \frac{k\pi t}{T},$$

$$a_k = \frac{2}{T} \int_0^T x(t) \cos \frac{k\pi t}{T} \mathrm{d}t, \quad k = 0, 1, 2\ldots, \tag{1.198}$$

where T is the period of integration, $0 \le t \le T$. The coefficients of the Fourier series were calculated approximately. The following parameters of set (1.140) were accepted: $\alpha = 200$, $\beta = 10$, $\alpha_1 = 9.985 \times 10^2$, $\alpha_2 = 2 \times 10^3$, $\alpha_3 = 7.9588 \times 10^3$, $\alpha_4 = 0.002$, $\alpha_5 = -4.0794 \times 10^3$, $\alpha_6 = 4.0002 \times 10^3$, $\alpha_7 = 8.0005 \times 10^3$, $\beta_1 = 29.9975$, $\beta_2 = -0.001$, $\beta_3 = -4.1594 \times 10^3$, $\beta_4 = -1.9997 \times 10^3$, $\beta_5 = -7.9188 \times 10^3$, $\beta_6 = 0.7959$, $\beta_7 = -0.4083$.

Parameters $\alpha = 200$, $\beta = 10$ correspond to natural frequencies $\omega_1 = 10$, $\omega_2 = 20$, i.e., $\omega_2 = 2\omega_1$. The curves in Fig. 1.43 were plotted using points $(\frac{k\pi}{T}, \frac{a_0}{2} + a_k)$. Figure 1.43 demonstrates good agreement of the perturbation and numerical solutions: panel a characterizes $x(t)$ as harmonic motion with amplitude $a_2 \approx 1.5 \times 10^{-4}$ and frequency $\omega_2 = 20$; panel b characterizes $x(t)$ as a superposition of harmonic motions with amplitude $a_1 \approx 4 \times 10^{-4}$, frequency $\omega_1 = 10$, amplitude $a_2 \approx 1.5 \times 10^{-4}$, and frequency $\omega_2 = 20$.

In Figs. 1.45 and 1.46 one can see the saturation phenomenon. As f increases from zero, a_2 also increases until it reaches the value $a_2 = 3.5 \times 10^{-4}$. In Fig. 1.44 it reaches the value $a_2 = 1.125 \times 10^{-4}$, whereas in Fig. 1.46 a_1 is zero. This agrees with the solution of the corresponding linear problem. Then a_2 saves the constant value and a_1 starts to increase. Approximate harmonic analysis of Fig. 1.45 (Fig. 1.47) demonstrates good agreement of the theoretical prediction presented in Fig. 1.44 (Fig. 1.46) and the corresponding numerical solution of (1.140).

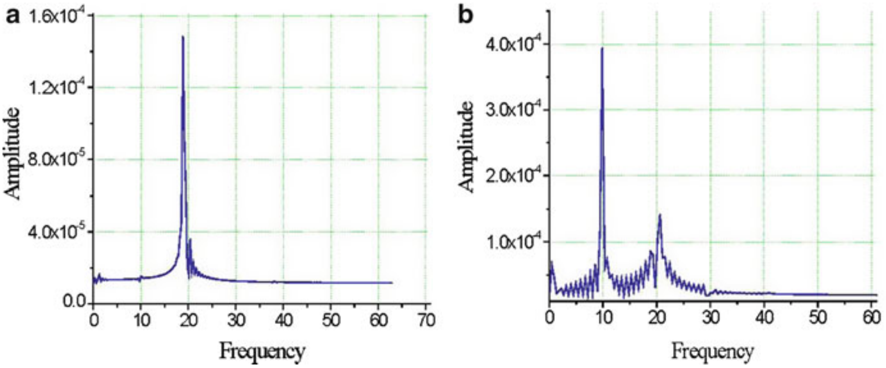

Fig. 1.43 Comparison of analytical results presented on the frequency-response curves (Fig. 1.42) with numerical integration of (2): (**a**) $\Omega = 19$ $(\delta_1 = -1, \delta_2 = 0)$, $f = 0.01$; (**b**) $\Omega = 20$ $(\delta_1 = 0, \delta_2 = 0)$, $f = 0.01$

Fig. 1.44 Amplitudes a_1, a_2 versus the amplitude of external excitation f; $\Omega \approx \omega_2, \sigma_1 = -0.5, \sigma_2 = 0$

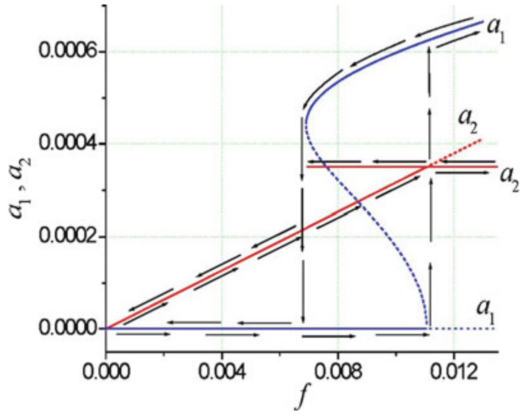

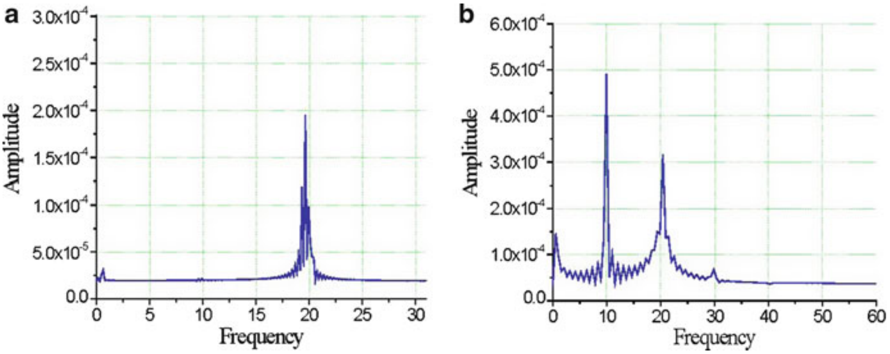

Fig. 1.45 Comparison of analytical results presented in Fig. 1.44 with numerical integration of (1.140): (**a**) $\Omega = 19.5$ $(\sigma_1 = -0.5, \sigma_2 = 0)$, $f = 0.0065$; (**b**) $\Omega = 19.5$ $(\sigma_1 = -0.5, \sigma_2 = 0)$, $f = 0.01$

Fig. 1.46 Amplitudes a_1, a_2 versus the amplitude of external excitation f; $\Omega \approx \omega_2, \sigma_1 = \sigma_2 = 0$

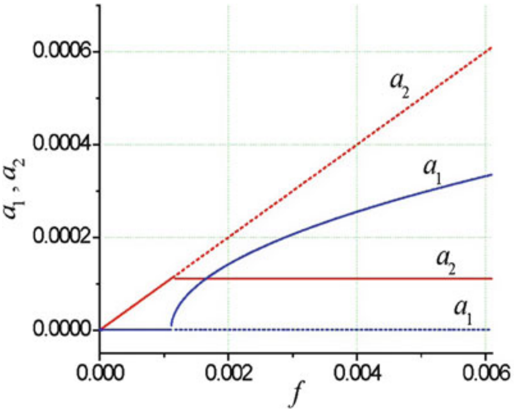

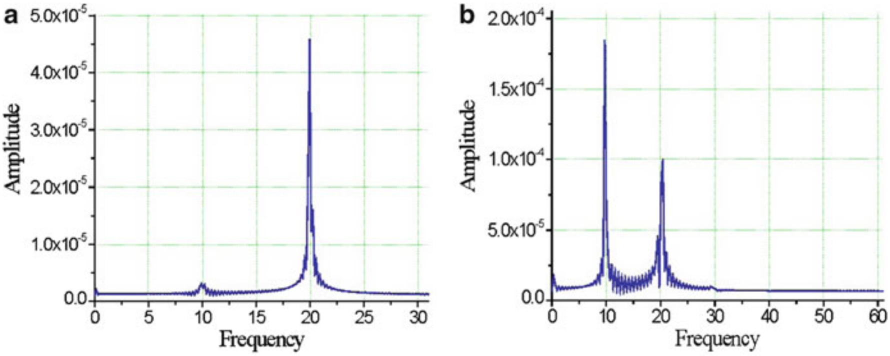

Fig. 1.47 Comparison of analytical results presented in Fig. 1.46 with numerical integration of (1.140): (**a**) $\Omega = 20$ ($\sigma_1 = \sigma_2 = 0$), $f = 0.0006$; (**b**) $\Omega = 20$ ($\sigma_1 = \sigma_2 = 0$), $f = 0.003$

1.5.2.3 Rigid Magnetic Materials: Conditions for Chaotic Vibrations of a Rotor in Various Control Parameter Planes

In the case of rigid magnetic materials, the hysteretic properties of system (1.137) can be considered using the Bouc–Wen hysteretic model. It was shown [35] that this modeling mechanism for energy dissipation was sufficiently accurate to model loops of various shapes in accordance with a real experiment, reflecting the behavior of hysteretic systems from very different fields. The hysteretic model of the rotor-MHDB system is as follows:

$$\begin{aligned}\ddot{x} = {} & P_r\left(\rho, \dot{\rho}, \dot{\phi}\right)\cos\phi - P_\tau\left(\rho, \dot{\phi}\right)\sin\phi - \gamma_m \dot{x} \\ & -\lambda_m\left[\delta\left(x - x_0\right) + (1-\delta)\, z_1\right],\end{aligned}$$

$$\begin{aligned} \ddot{y} &= P_r\left(\rho,\dot{\rho},\dot{\phi}\right)\sin\phi + P_\tau\left(\rho,\dot{\phi}\right)\cos\phi - \gamma_m\dot{y} \\ &\quad -\lambda_m\left[\delta\left(y-y_0\right)+\left(1-\delta\right)z_2\right] + Q_0 + Q\sin\Omega t, \\ \dot{z}_1 &= \left[k_z - \left(\gamma + \beta\operatorname{sgn}\left(\dot{x}\right)\ \operatorname{sgn}\left(z_1\right)\right)\ \left|z_1\right|^n\right]\dot{x}, \\ \dot{z}_2 &= \left[k_z - \left(\gamma + \beta\operatorname{sgn}\left(\dot{y}\right)\ \operatorname{sgn}\left(z_2\right)\right)\ \left|z_2\right|^n\right]\dot{y}. \end{aligned} \tag{1.199}$$

Here z_1 and z_2 are the hysteretic forces. The case $\delta = 0$ corresponds to maximal hysteretic dissipation and $\delta = 1$ to the absence of hysteretic forces in the system; parameters $(k_z, \beta, n) \in R^+$ and $\gamma \in R$ govern the shape of the hysteresis loops.

The conditions for chaotic vibrations of a rotor have been found using the approach based on an analysis of wandering trajectories. The description of the approach, its advantages over standard procedures, and a comparison with other approaches can be found, for example, in [35, 38, 40].

The stability of motion depends on all the parameters of system (1.199), including the initial conditions. We traced the irregular vibrations of a rotor to sufficient accuracy in the parametric planes of amplitude of external excitation versus hysteretic dissipation (δ, Q), the amplitude versus frequency of external excitation (Ω, Q), the amplitude versus dynamic oil-film action characteristics (C, Q), and the amplitude versus the magnetic control parameters (γ_m, Q) and (λ_m, Q).

Chaos is not found in the absence of hysteresis when $\delta = 1$. The chaotic vibrations of a rotor are caused by hysteresis and for all chaotic regions presented $\delta \neq 1$. Thus in system (1.199), chaos was quantified using the following conditions:

$$\exists t^* \in [t_1, T] : \{ \underbrace{(\,|x(t^*) - \tilde{x}(t^*)\,| > \alpha A_x)}_{\substack{\Downarrow \\ \text{chaotic vibrations} \\ \text{in the horizontal direction}}} \vee \underbrace{(|y(t^*) - \tilde{y}(t^*)\,| > \alpha A_y)}_{\substack{\Downarrow \\ \text{chaotic vibrations} \\ \text{in the vertical direction.}}} \} \tag{1.200}$$

Here $x(t)$, $\tilde{x}(t)$ and $y(t)$, $\tilde{y}(t)$ are nearby trajectories respectively, A_x and A_y are the characteristic vibration amplitudes of the rotor in the horizontal and vertical direction, respectively:

$$\begin{aligned} A_x &= \frac{1}{2}\left|\max_{t_1\le t\le T} x(t) - \min_{t_1\le t\le T} x(t)\right|, \\ A_y &= \frac{1}{2}\left|\max_{t_1\le t\le T} y(t) - \min_{t_1\le t\le T} y(t)\right|. \end{aligned} \tag{1.201}$$

$[t_1, T] \subset [t_0, T]$ and $[t_0, T]$ is the time interval over which the trajectories are considered. The interval $[t_0, t_1]$ is the time interval over which all transient processes are damped. The introduced parameter α is an auxiliary parameter such that $0 < \alpha < 1$. αA_x and αA_y are referred to as the divergence measures of the observable trajectories in the horizontal and vertical directions and, with the aid of the chosen parameter α, are *inadmissible* for the case of the *regularity* of motion.

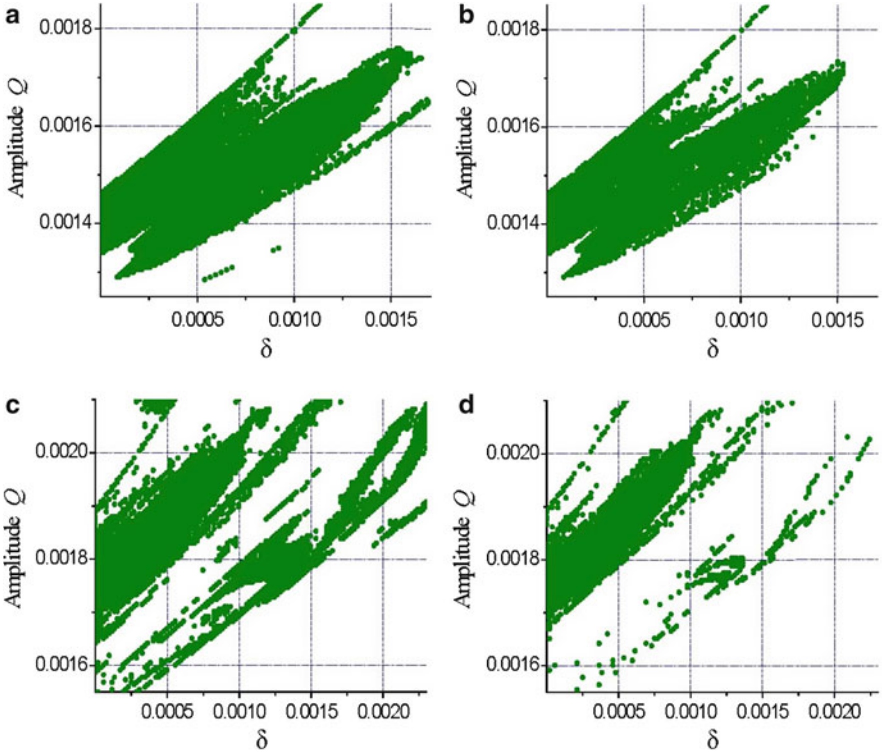

Fig. 1.48 Influence of hysteretic dissipation parameter δ on chaos in horizontal (**a, c**) and vertical (**b, d**) vibrations of rotor (1.199) in the case of rigid magnetic materials. The following parameters are fixed in (**a, b**): $C = 0.03$, $\gamma_m = 0.001$, $\lambda_m = 450$, $k_z = 0.000055$, $\gamma = 15$, $\beta = 0.25$, $n = 1.0$, $\Omega = 0.87$, $Q_0 = 0$, $x_0 = 0$, $y_0 = 0$, $x(0) = y(0) = 10^{-8}$, $\dot{x}(0) = \dot{y}(0) = 0$, $z_1(0) = z_2(0) = 0$; (c, d): $C = 0.2$, $\gamma_m = 0$, $\lambda_m = 500$, $k_z = 0.000055$, $\gamma = 15$, $\beta = 0.25$, $n = 1.0$, $\Omega = 0.87$, $Q_0 = 0$, $x_0 = 0$, $y_0 = 0$, $x(0) = y(0) = 10^{-8}$, $\dot{x}(0) = \dot{y}(0) = 0$, $z_1(0) = z_2(0) = 0$

If inequality (1.200) is satisfied in some nodal point of the sampled control parameter space, then the motion is chaotic (including transient and alternating chaos). The manifold of all such nodal points of the investigated control parameter space defines the domains of chaotic behavior for the considered system.

Figure 1.48 displays the regions of rotor chaotic vibrations in the (δ, Q) plane. Part of this plane ($10^{-7} < \delta \le 0.0017; 0.00125 < Q \le 0.00185$) (panels a and b) and ($10^{-7} < \delta \le 0.0023; 0.00155 < Q \le 0.0021$) (panels c and d) was sampled by means of a uniform rectangular grid. For this purpose two families of straight lines were drawn through dividing points of the axes

$$\begin{aligned} \delta^i &= i\Delta\delta, \quad i = 0, 1, \ldots, 120, \\ Q^j &= j\Delta Q, \quad j = 0, 1, \ldots, 120. \end{aligned} \tag{1.202}$$

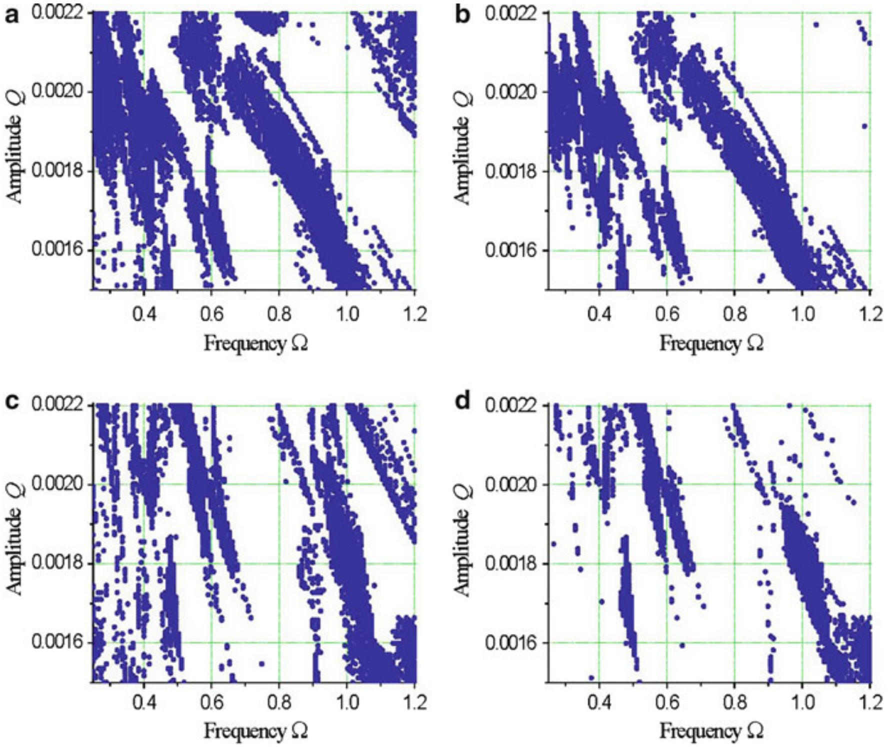

Fig. 1.49 Chaotic regions for horizontal (**a, c**) and vertical (**b, d**) vibrations of rotor (28) in (Ω, Q) parametric plane with decrease of the hysteretic dissipation value (**a, b**) $\delta = 0.0001$; (**c, d**) $\delta = 0.0013$ with other parameters of the system fixed: $C = 0.2$, $\gamma_m = 0$, $\lambda_m = 500$, $k_z = 0.000055$, $\gamma = 15$, $\beta = 0.25$, $n = 1.0$, $Q_0 = 0$, $x_0 = 0$, $y_0 = 0$, $x(0) = y(0) = 10^{-8}$, $\dot{x}(0) = \dot{y}(0) = 0$, $z_1(0) = z_2(0) = 0$

Here $\Delta\delta = 1.4165\times10^{-5}$, $\Delta Q = 5\times10^{-6}$ (panels a and b), $\Delta\delta = 1.91658\times10^{-5}$, $\Delta Q = 4.58333\times10^{-6}$ (panels c and d).

The time period for the simulation T is of $\frac{200\pi}{\Omega}$ in non-dimentional time units. During the computations, two-thirds of time period T corresponds to the time interval $[t_0, t_1]$, where transient processes are damped. The integration step size is $0.02\frac{\pi}{\Omega}$. The initial conditions of the nearby trajectories differ by less than 0.5% of characteristic vibration amplitudes, e.g., the starting points of these trajectories are in the rectangle $(|x(t_0) - \tilde{x}(t_0)| < 0.005A_x, |y(t_0) - \tilde{y}(t_0)| < 0.005A_y)$. The parameter α is chosen to be equal to $\frac{1}{3}$.

All domains have a complex structure. There are a number of scattered points, streaks, and islets here. Such a structure is characteristic of domains where chaotic vibrations are possible. For each aggregate of control parameters there is some critical value of the hysteretic dissipation $(1 - \delta_c r)$ that if $(1 - \delta) < (1 - \delta_c r)$, then chaos is not observed in the system under consideration.

In Fig. 1.49 chaotic regions for the horizontal and vertical vibrations of a rotor are depicted in the (Ω, Q) parametric plane $(0.25 < \Omega \leq 1.2; 0.0015 < Q \leq 0.0022)$.

The time period for the simulation T and other numerical integration characteristics are the same as for (δ, Q) parametric plane, $\Delta\Omega = 7.91667 \times 10^{-3}$, $\Delta Q = 5.83333e \times 10^{-6}$. One can observe that for the larger hysteretic dissipation $(1 - \delta)$, $\delta = 0.0001$ the chaotic regions areas are larger.

Figure 1.50 shows the phase portraits, hysteretic loops, and Poincar maps of chaotic motion of a rotor. The parameters of motion correspond to the parameters of the chaotic region depicted in Fig. 1.49a, b. The phase portraits, hysteretic loops, and Poincar maps of the periodic rotor motion that also agree well with the obtained regions of regular/irregular behavior of the rotor depicted in Fig. 1.49a, b are shown in Fig. 1.51.

The influence of the dynamic oil-film action characteristics on chaos occurring in the rotor motion can be observed in Fig. 1.52. One can see the restraining of chaotic regions with decreasing of hysteretic dissipation $(1 - \delta)$. The (C, Q) parametric plane was uniformly sampled by 120×120 nodal points in the rectangles $(0 < C \leq 1.5;\ 0.0015 < Q \leq 0.0021)$, $\Delta C = 0.0125$, $\Delta Q = 5 \times 10^{-6}$ (panels a and b) and $(0 < C \leq 1.5;\ 0.0015 < Q \leq 0.00225)$, $\Delta C = 0.0125$, $\Delta Q = 6.25 \times 10^{-6}$ (panels c and d).

The influence of the magnetic control parameters γ_m, λ_m on chaos occurring in the rotor vibrations can be observed in Figs. 1.53 and 1.54. The (γ_m, Q) and (λ_m, Q) parametric planes were uniformly sampled by 120×120 nodal points in the rectangles $(0 < \gamma_m \leq 0.09;\ 0.00165 < Q \leq 0.0019)$, $\gamma_m = 7.5 \times 10^{-4}$, $\Delta Q = 2.08333 \times 10^{-6}$, Fig. 1.44a, b; $(0 < \gamma_m \leq 0.15;\ 0.00155 < Q \leq 0.0023)$, $\gamma_m = 1.25 \times 10^{-3}$, $\Delta Q = 6.25 \times 10^{-6}$ Fig. 1.44c, d; $(450 < \lambda_m \leq 630;\ 0.00145 < Q \leq 0.0025)$, $\Delta\lambda_m = 1.5$, $\Delta Q = 8.75 \times 10^{-6}$, Fig. 1.54a and b; $(420 < \lambda_m \leq 800;\ 0.0015 < Q \leq 0.0043)$, $\Delta\lambda_m = 3.16667$, $\Delta Q = 2.33333 \times 10^{-5}$, Fig. 1.54c, d. The time period for simulation T and other numerical integration characteristics are the same as for the (δ, Q) parametric plane.

Impact phenomena are possible in the bearings for both chaotic and periodic rotor motion at large amplitudes of the external harmonic excitation. An analysis of the rotor behavior after a collision with the bearings is not considered in this paper because the model described does not have a physical meaning in this case. To see if the rotor chaotic motion is accompanied by an increase in the amplitude of vibration, the amplitude level contours of the horizontal and vertical vibrations of the rotor were obtained. In Fig. 1.55, the amplitude level contours are presented in the (γ_m, Q) parametric plane with the same parameters as in Fig. 1.53a, b. Some "consonance" between the chaotic vibrations regions and the amplitude level contours is observed. At that level the amplitudes of chaotic rotor vibrations are greater in comparison to the periodic vibrations.

In Fig. 1.56 the amplitude level contours are presented in the (C, Q) parametric plane with the same parameters as in Fig. 1.52a, b. Although some "consonance" between the chaotic regions of vibrations and the amplitude level contours is observed, it cannot be concluded that chaos leads to an essential increase in the rotor vibration amplitude [40].

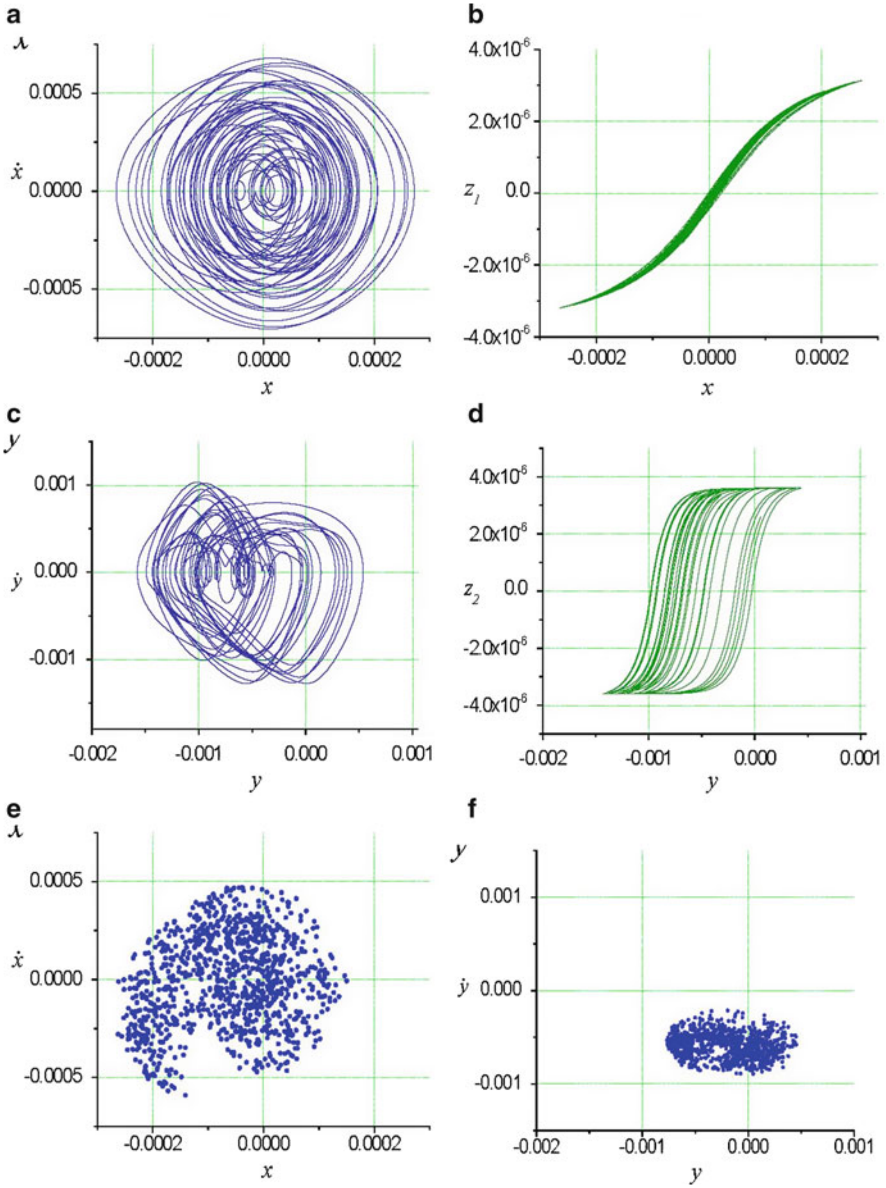

Fig. 1.50 Phase portraits (**a, c**), hysteresis loops (**b, d**), and Poincar maps (**e, f**) of rotor motion that agree with the chaotic regions in Fig. 1.49 (**a, b**). The parameters $\Omega = 0.87$, $Q = 0.00177$, $\delta = 0.0001$, $C = 0.2$, $\gamma_m = 0$, $\lambda_m = 500$, $k_z = 0.000055$, $\gamma = 15$, $\beta = 0.25$, $n = 1.0$, $Q_0 = 0$, $x_0 = 0$, $y_0 = 0$, $x(0) = y(0) = 10^{-8}$, $\dot{x}(0) = \dot{y}(0) = 0$, $z_1(0) = z_2(0) = 0$ are fixed

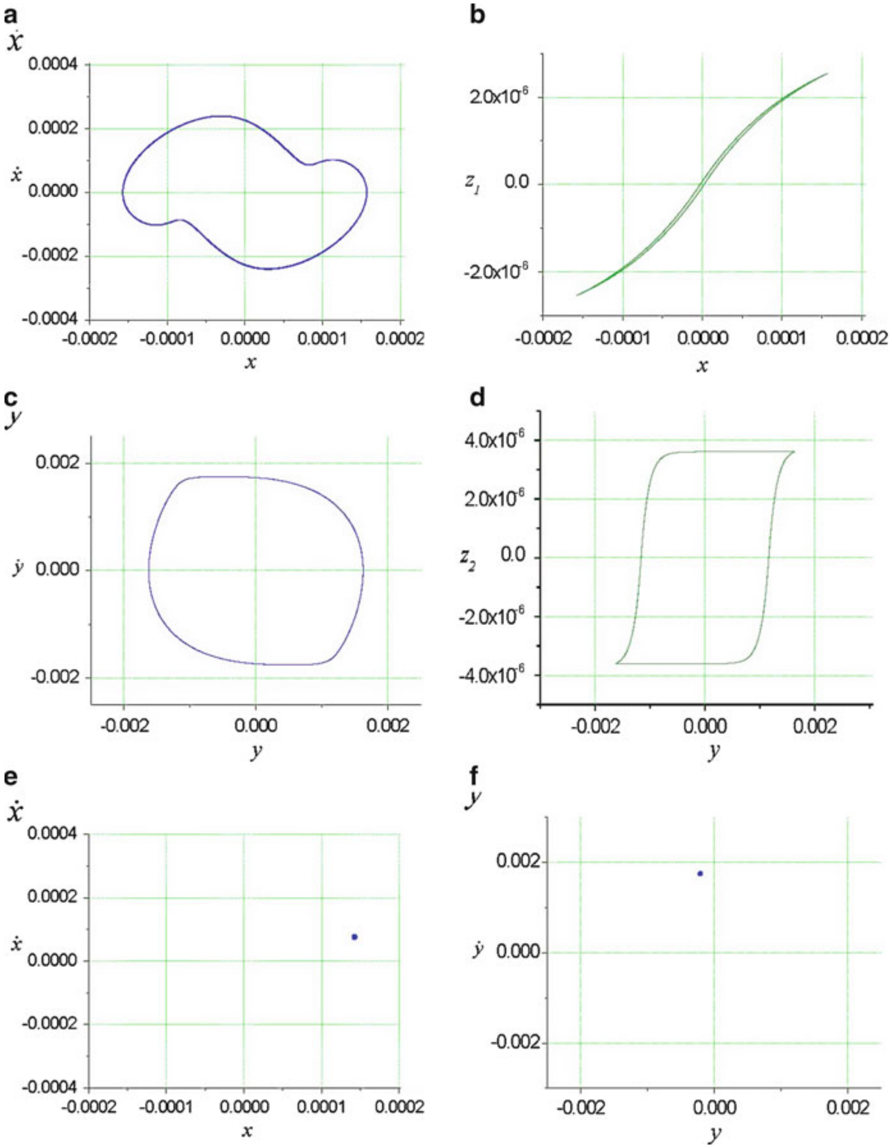

Fig. 1.51 Phase portraits (**a, c**), hysteresis loops (**b, d**), and Poincar maps (**e, f**) of periodic rotor motion that agree with regions of regular motion in Fig. 1.49a–d. The parameters $\Omega = 1.2$, $Q = 0.0017$, $\delta = 0.0001$, $C = 0.2$, $\gamma_m = 0$, $\lambda_m = 500$, $k_z = 0.000055$, $\gamma = 15$, $\beta = 0.25$, $n = 1.0$, $Q_0 = 0$, $x_0 = 0$, $y_0 = 0$, $x(0) = y(0) = 10^{-8}$, $\dot{x}(0) = \dot{y}(0) = 0$, $z_1(0) = z_2(0) = 0$ are fixed

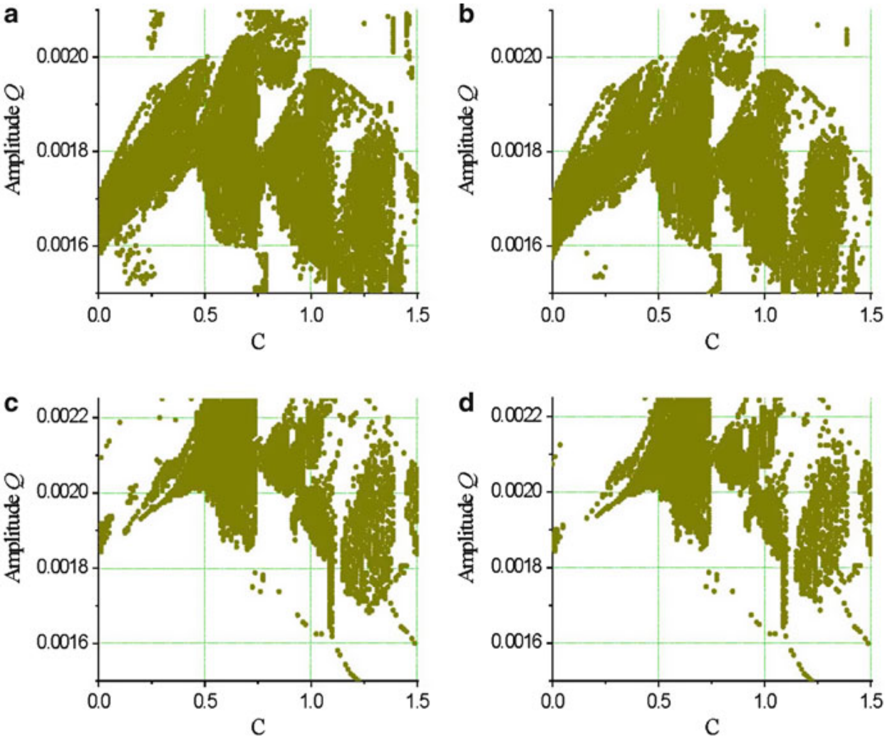

Fig. 1.52 Influence of dynamic oil-film action characteristics on chaos occurring in horizontal (**a, c**) and vertical (**b, d**) vibrations of rotor (1.199) in the case of rigid magnetic materials. The parametric planes (C,Q) are depicted at (**a**), (**b**) $\delta = 0.000001$, $\gamma_m = 0$ and (**c**), (**d**) $\delta = 0.001$, $\gamma_m = 0.03$ with other parameters of the system fixed: $\lambda_m = 500$, $k_z = 0.000055$, $\gamma = 15$, $\beta = 0.25$, $n = 1.0$, $Q_0 = 0$, $x_0 = 0$, $y_0 = 0$, $x(0) = y(0) = 10^{-8}$, $\dot{x}(0) = \dot{y}(0) = 0$, $z_1(0) = z_2(0) = 0$

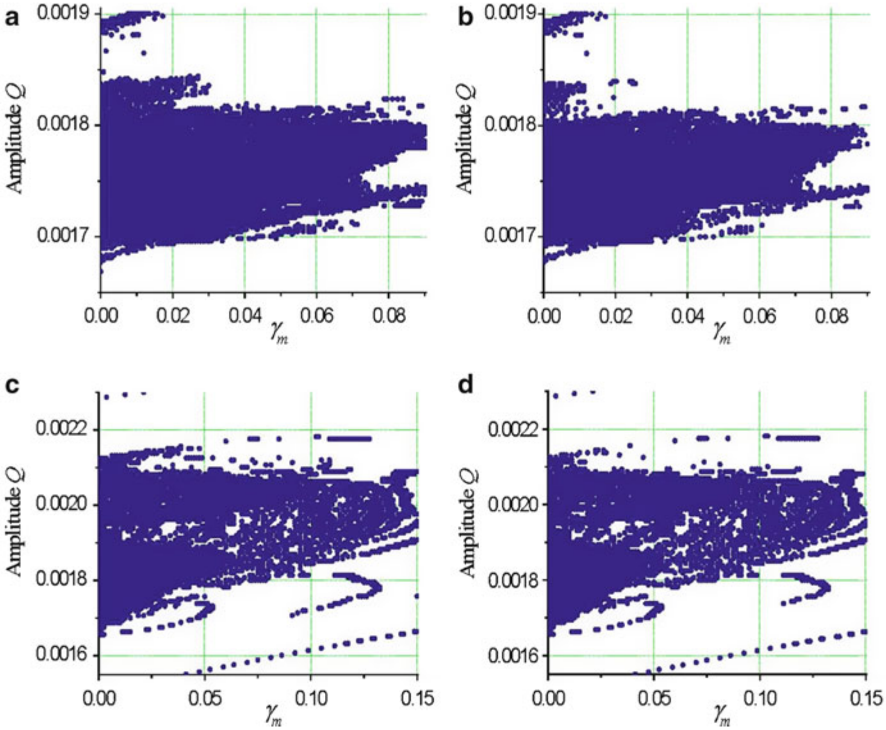

Fig. 1.53 Influence of magnetic control parameter γ_m on chaos occurring in horizontal (**a, c**) and vertical (**b, d**) vibrations of rotor (1.199) in the case of rigid magnetic materials. The parametric planes (γ_m, Q) are depicted at (**a, b**) $\delta = 0.000001$, $C = 0.2$ and (**c, d**) $\delta = 0.0005$, $C = 1$ with other parameters of the system fixed: $\lambda_m = 500$, $k_z = 0.000055$, $\gamma = 15$, $\beta = 0.25$, $n = 1.0$, $\Omega = 0.87$, $Q_0 = 0$, $x_0 = 0$, $y_0 = 0$, $x(0) = y(0) = 10^{-8}$, $\dot{x}(0) = \dot{y}(0) = 0$, $z_1(0) = z_2(0) = 0$

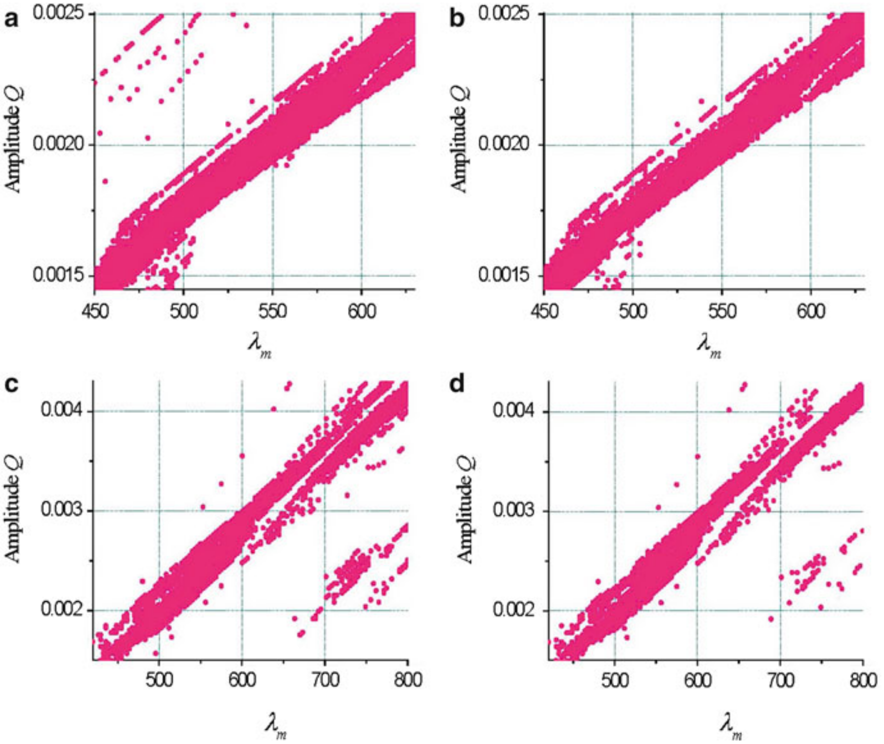

Fig. 1.54 Influence of magnetic control parameter γ_m on chaos occurring in horizontal (**a, c**) and vertical (**b, d**) vibrations of rotor (1.199) in the case of rigid magnetic materials. The parametric planes (γ_m, Q) are depicted at (**a, b**) $\delta = 0.000001$, $C = 0.2$, $\gamma_m = 0$ and (**c, d**) $\delta = 0.001$, $C = 1$, $\gamma_m = 0.005$ with other parameters of the system fixed: $k_z = 0.000055$, $\gamma = 15$, $\beta = 0.25$, $n = 1.0$, $\Omega = 0.87$, $Q_0 = 0$, $x_0 = 0$, $y_0 = 0$, $x(0) = y(0) = 10^{-8}$, $\dot{x}(0) = \dot{y}(0) = 0$, $z_1(0) = z_2(0) = 0$

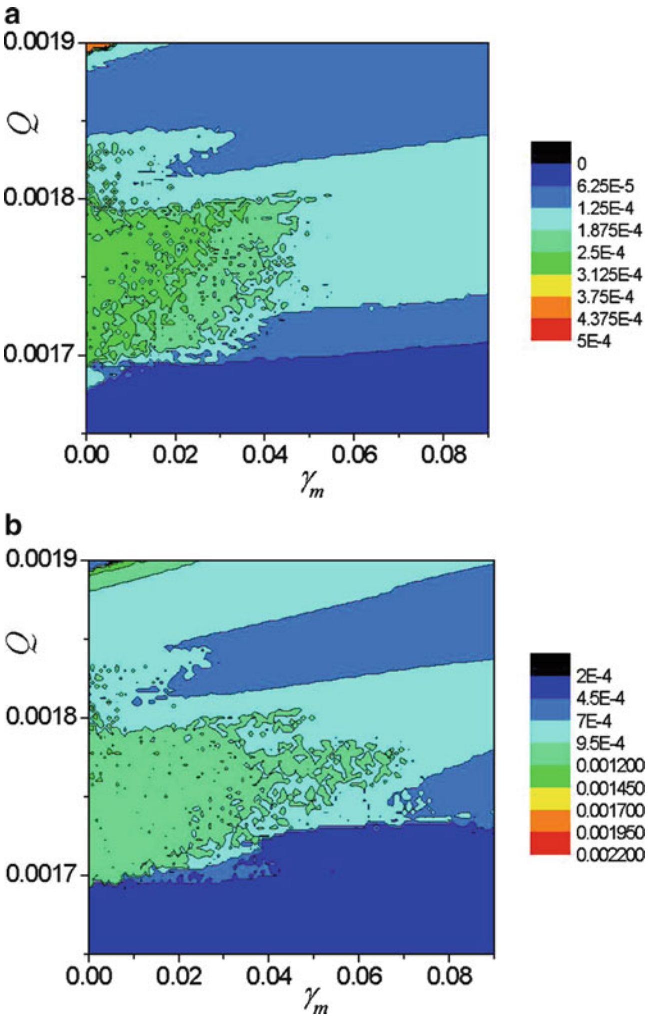

Fig. 1.55 Amplitude level contours (corresponding to Fig. 1.53a, b) of horizontal (**a**) and vertical (**b**) vibrations of rotor (1.199) in parametric plane (γ_m, Q) at $\delta = 0.000001$, $C = 0.2$, $\lambda_m = 500$, $k_z = 0.000055$, $\gamma = 15$, $\beta = 0.25$, $n = 1.0$, $\Omega = 0.87$, $Q_0 = 0$, $x_0 = 0$, $y_0 = 0$, $x(0) = y(0) = 10^{-8}$, $\dot{x}(0) = \dot{y}(0) = 0$, $z_1(0) = z_2(0) = 0$

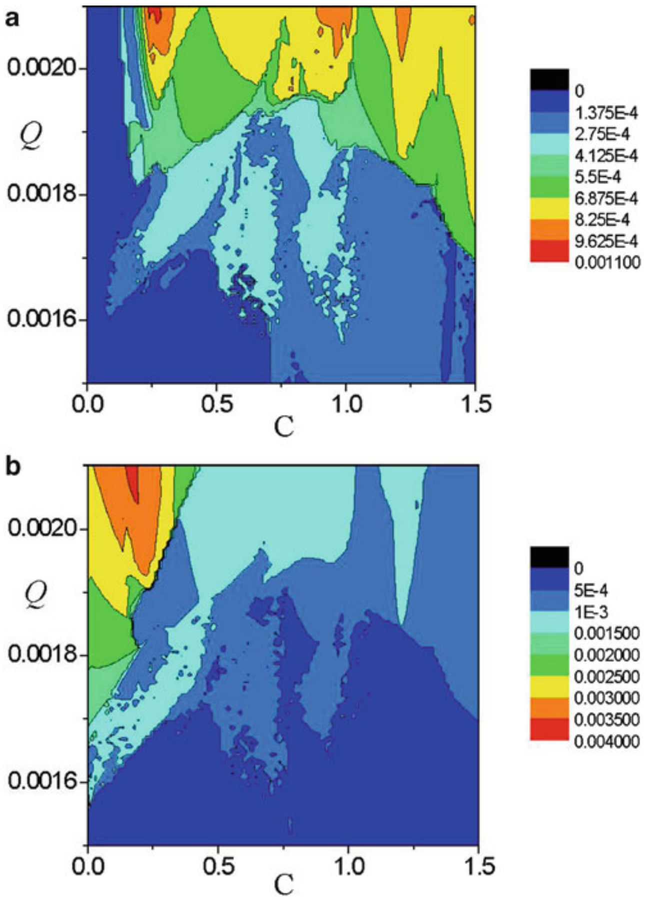

Fig. 1.56 Amplitude level contours (corresponding to Fig. 1.52a, b) of horizontal (**a**) and vertical (**b**) vibrations of rotor (1.199) in parametric plane (C, Q) at $\delta = 0.000001$, $\gamma_m = 0$, $\lambda_m = 500$, $k_z = 0.000055$, $\gamma = 15$, $\beta = 0.25$, $n = 1.0$, $\Omega = 0.87$, $Q_0 = 0$, $x_0 = 0$, $y_0 = 0$, $x(0) = y(0) = 10^{-8}$, $\dot{x}(0) = \dot{y}(0) = 0$, $z_1(0) = z_2(0) = 0$

References

1. S.H. Crandall, D.C. Karnogg, E.F. Kurtz, D.C. Pridmore-Brown, *Dynamics of Mechanical and Electromechanical Systems* (McGraw-Hill, New York, 1968)
2. A. Preumont, *Mechatronics: Dynamics of Electromechanical and Piezoelectric Systems* (Springer, Berlin, 2006)
3. J. Awrejcewicz, *Classical Mechanics: Dynamics* (Springer, Berlin, 2012)
4. A. Nicolaide, *Magnetism and Magnetic Materials: Theory, Properties, Modeling* (Transylvania University Press, Transylvania, 2001)
5. A. Green, K.C. Craig, Robust, design, nonlinear control of magnetic-levitation systems. J. Dyn. Meas. Contr. **120**(4), 488–495 (1998)
6. A. Piat, *Active Magnetic Suspension and Bearing. Modeling and Simulation* (InTech Education and Publishing, Vienna, 2008), pp. 453–470
7. M. Aliasghary, et al., *Sliding mode control of magnetic levitation system using radial basis function neural network.* IEE XPlore, RAM (2008), pp. 467–470
8. P. Olejnik, J. Awrejcewicz, in *Magnetic Levitation of a Light Cylindrical-Shape Mass with Control of Damping of the Transition-State Vibrations. Proceedings of the XXIV Symposium "Vibrations in Physical Systems,"* Pozna-Bedlewo, 12–15 May 2010
9. A.H. Nayfeh, D.T. Mook, *Nonlinear Oscillations* (Wiley Interscience, New York, 1979)
10. V.I. Arnold, *Geometrical Methods in Theory of Ordinary Differential Equations* (Springer, Berlin, 1983)
11. J. Guckenheimer, P. Holmes, *Nonlinear Oscillations: Dynamical Systems and Bifurcations of Vector Fields* (Springer, Berlin, 1983)
12. W.P. Rubanik, *Oscillations in Complex Quasilinear Systems with Dealy* (University Press, Minsk, 1985), in Russian
13. J. Awrejcewicz, Nonlinear oscillations of a string caused by the electromagnetic field. J. Tech. Phys. **35**, 1–2, 5–12 (1994)
14. J. Awrejcewicz, Strange nonlinear behaviour governed by a set of four averaged amplitude equations. Meccanica **31**, 347–361 (1996)
15. J. Awrejcewicz, V.A. Krysko, *Introduction to Asymptotic Methods* (Taylor and Francis Group, Boca Raton, FL, 2006)
16. J. Awrejcewicz, *Bifurcation and Chaos in Simple Dynamical Systems* (World Scientific, Singapore, 1989)
17. J. Awrejcewicz, *Bifurcation and Chaos in Coupled Oscillators* (World Scientific, Singapore, 1999)
18. A. Tondl, *Some Problems of Rotor Dynamics* (Chapman & Hall, London, 1965)
19. T. Someya, *Journal-Bearing Databook* (Springer, Berlin, 1998)
20. J.S. Rao, *Rotor Dynamics* (Wiley, New York, 1991)
21. R. Gasch, R. Nordmann, H. Pfützner, *Rotordynamik* (Springer, Berlin, 2002)
22. A. Muszyska, *Rotordynamics* (CRC Press, Boca Raton, FL, 2005)
23. W. Kurnik, Active magnetic antiwhirl control of a rigid rotor supported on hydrodynamic bearings. Mach. Dyn. Prob. **10**, 21–36 (1995)
24. K. Dziedzic, W. Kurnik, Stability of a rotor with hybrid magneto-hydrodynamic support. Mach. Dyn. Prob. **26**(4), 33–43 (2002)
25. P. Flores, J. Ambrosio, J.C. Claro, H.M. Lancarani, C.S. Koshy, Lubricated revolute joints in rigid multibody systems. Non-linear Dynm. **56**, 277–295 (2009)
26. C.W. Chang-Jian, C.K. Chen, Non-linear analysis of a rub-impact rotor supported by turbulent couple stress fluid film journal bearings under quadratic damping. Non-linear Dynam. **56**, 297–314 (2009)
27. W. Zhang, X.P. Zhan, Periodic and chaotic motions of a rotor-active magnetic bearing with quadratic and cubic terms and time-varying stiffness. Non-linear Dynam. **41**, 331–359 (2005)
28. A. Boyaci, H. Hetzler, W. Seeman, C. Proppe, J. Wauer, Analytical bifurcation analysis of a rotor supported by floating ring bearings. Non-linear Dynam. **57**, 497–507 (2009)

29. B. Schweizer, Oil whirl, oil whip and whirl/whip synchronization occurring in rotor systems with full-floating ring bearings. Non-linear Dynam. **57**, 509–532 (2009)
30. G.F. Zhang, W.N. Xu, B. Xu, W. Zhang, Analytical study of non-linear synchronous full annular rub motion of flexible rotor-stator system and its dynamic stability. Non-linear Dynam. **57**, 579–592 (2009)
31. Y. Ishida, M. Inagaki, R. Ejima, A. Hayashi, Non-linear resonances and self-excited oscillations of a rotor caused by radial clearance and collision. Non-linear Dynam. **57**, 593–605 (2009)
32. D.D. Quinn, Resonant dynamics in a rotordynamics system with non-linear inertial coupling and shaft anisotropy. Non-linear Dynam. **57**, 623–633 (2009)
33. R. Bouc, Modele mathmatique d'hystrsis (A mathematical model for hysteresis). Acustica **21**, 16–25 (1971)
34. Y.K. Wen, Method for random vibration of hysteretic system. J. Eng. Mech. Div. **102**(EMI), 246–263 (1976)
35. J. Awrejcewicz, L. Dzyubak, Hysteresis modelling and chaos prediction in one- and 2-DOF hysteretic models. Arch. Appl. Mech. **77**, 261–279 (2007)
36. F. Ikhouave, J. Rodellar, *Systems with Hysteresis* (Wiley, Chichester, 2007)
37. J.W. Mack, P. Nistri, P. Zecca, Mathematical models for hysteresis. SIAM Rev. **35**(1), 94–123 (1993)
38. J. Awrejcewicz, L. Dzyubak, C. Grebogi, Estimation of chaotic and regular (stick-slip and slip-slip) oscillations exhibited by coupled oscillators with dry friction. Non-linear Dynam. **42**(2), 383–394 (2005)
39. Z. Osinski (ed.), *Damping of Vibrations* (A.A. Balkema, Rotterdam, Brookfield, 1998)
40. J. Awrejcewicz, L. Dzyubak, Chaos caused by hysteresis and saturation phenomenon in 2-DOF vibrations of the rotor supported by the magneto-hydrodynamic bearing. Int. J. Bifurcation Chaos **21**(10), 2801–2823 (2011)

Chapter 2
Equations of Motion of a Rigid Spherical Body

In this chapter, we introduce basic equations of dynamics of a rigid body during motion about a fixed pivot point. On the basis of these equations, later in this work, we will describe gyroscopic phenomena.

2.1 Kinematics of Rigid-Body Motion

To describe the spherical motion of a rigid body, it is necessary to find angular coordinates that uniquely determine the position of a rigid body in the reference frame [1–3]. In what follows, we take two frames (Fig. 2.1).

The first frame, $OX'_{1O}X'_{2O}X'_{3O}$, is a reference frame. In the considered problem, we can think of it as a fixed coordinate system. The second frame, $OX'''_1X'''_2X'''_3$, is stiff-connected with the body so that it rotates. The origins O of both these frames are the same fixed point. The position of a body with respect to the fixed coordinate system $OX'_{1O}X'_{2O}X'_{3O}$ is described by means of three angles of rotation. This means that a rotation of the body about an arbitrarily oriented axis in space, originating from point O, can be composed of another three rotations. The angles of these rotations can be specified in various ways. There exist many ways of describing the same position of a body by means of three angles [1–3]. The most popular technique was proposed by Euler.

2.1.1 The Euler Angles

After Euler,the position of a fixed-body frame $OX_1X_2X_3$ relative to the fixed frame $OX'_{1O}X'_{2O}X'_{3O}$ can be specified by the three angles Ψ_e, ϑ_e, Φ_e depicted in Fig. 2.2.

J. Awrejcewicz and Z. Koruba, *Classical Mechanics*, Advances in Mechanics and Mathematics 30, DOI 10.1007/978-1-4614-3978-3_2,

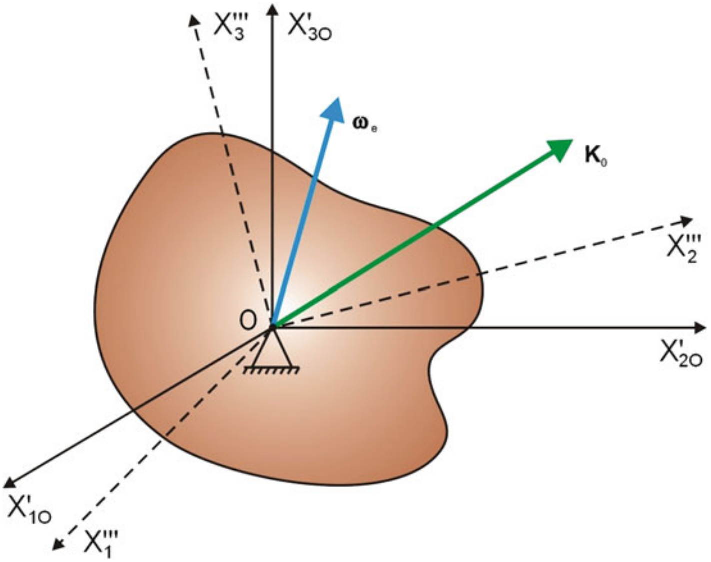

Fig. 2.1 Position of body in frames

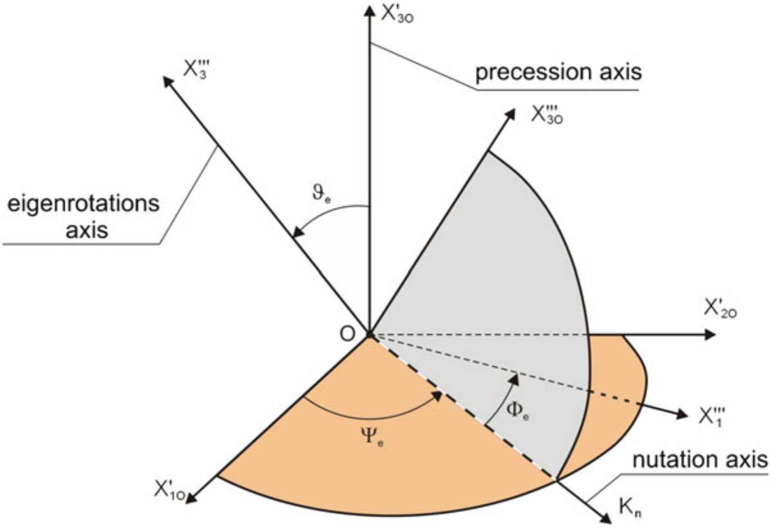

Fig. 2.2 Euler's angles

The angle ϑ_e is between two axes OX'_{3O} and OX_3. The two remaining angles are measured in the planes $OX'_{1O}X'_{2O}$ and $OX'''_1X'''_2$ (Fig. 2.2). Following the description given in [1–3], a line of intersection of these planes is called a *line of nodes* (K_n) or *axis of nutation*. The angle ψ_e is between a line of nodes and

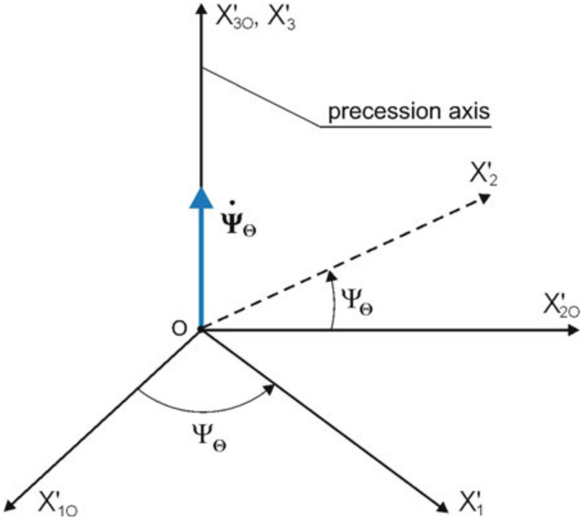

Fig. 2.3 Rotation about precession axis

the axis OX'_{1O}, and the angle Φ_e is between the line of nodes and the axis OX'''_1. In the theory of gyroscopes, angles ϑ_e, ψ_e, and ϕ_e are called *nutation*, *precession*, and *eigenrotations*, respectively. However, it should be emphasized that these terms are geometrical names and should not be confused with notions of nutation and precession, used in the rest of this work with a completely different meaning.

Thus, in the Euler approach an arbitrary position of a body can be specified as follows:

1. The first rotation is made about the OX'''_3 axis by a precession angle ψ_e (Fig. 2.3).
   This orthogonal transformation can be presented by means of a matrix of transformation:

$$m^{\psi} = \begin{bmatrix} \cos\psi_e & \sin\psi_e & 0 \\ -\sin\psi_e & \cos\psi_e & 0 \\ 0 & 0 & 1 \end{bmatrix}.$$

2. The second rotation is made about the OX'_1 axis by a nutation angle ϑ_e (Fig. 2.4).
   This operation is equivalent to the matrix

$$m^{\vartheta} = \begin{bmatrix} 1 & 0 & 0 \\ 0 & \cos\vartheta_e & \sin\vartheta_e \\ 0 & -\sin\vartheta_e & \cos\vartheta_e \end{bmatrix}.$$

3. The final rotation needs to be made about the axis of eigenrotations OX''_3 by an angle ϕ_e (Fig. 2.5).

Fig. 2.4 Rotation about nutation angle

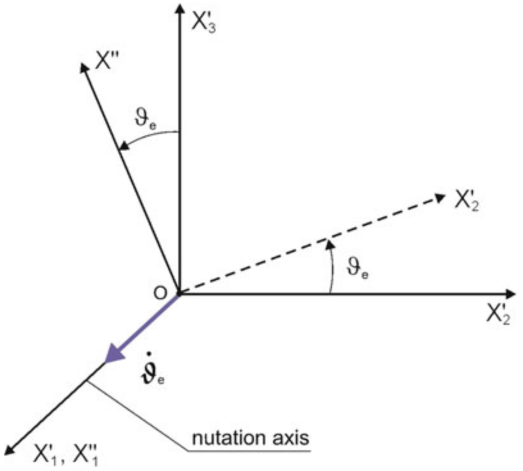

Fig. 2.5 Rotation about the axis of eigenrotations

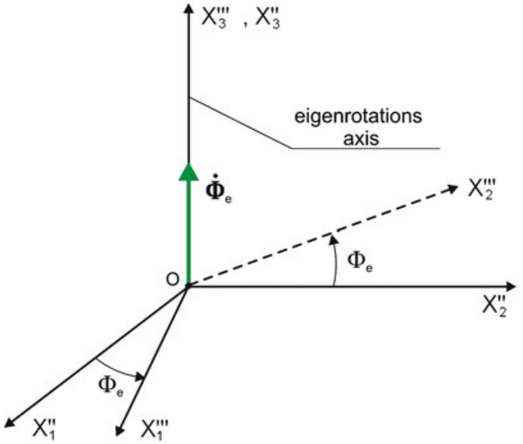

The corresponding transformation matrix has the following form:

$$m^{\Phi} = \begin{bmatrix} 0 & 0 & 0 \\ \cos \Phi_e & \sin \Phi_e & 0 \\ -\sin \Phi_e & \cos \Phi_e & 1 \end{bmatrix}.$$

Let us determine the cosines of the inclination angles of the axes $OX_1'''OX_2'''$ OX_3''' to $OX'_{1O}OX'_{2O}OX'_{3O}$ (observe that these angles are not equal to $\vartheta_e,\ \psi_e,\ \Phi_e$ except some particular cases). These direction cosines are elements of the matrix of transformation, which can be obtained by successive transformations. Then we have

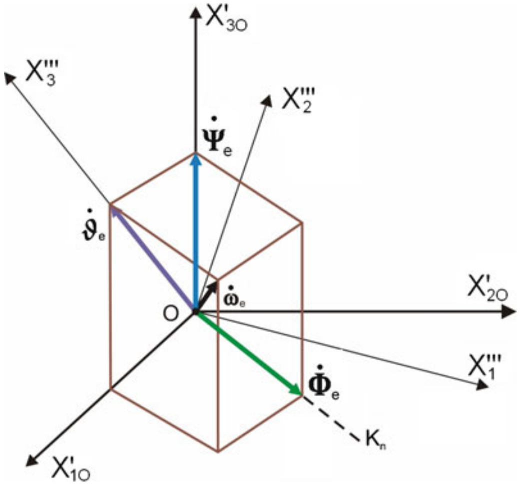

Fig. 2.6 Angular velocity vector of body [1]

$$
\begin{aligned}
m^E &= m^{\Phi}\, m^{\vartheta} m^{\psi} \\
&= \begin{bmatrix} \cos\psi_e & \sin\psi_e & 0 \\ -\sin\psi_e & \cos\psi_e & 0 \\ 0 & 0 & 1 \end{bmatrix}
\begin{bmatrix} 1 & 0 & 0 \\ 0 & \cos\vartheta_e & \sin\vartheta_e \\ 0 & -\sin\vartheta_e & \cos\vartheta_e \end{bmatrix}
\begin{bmatrix} 0 & 0 & 0 \\ \cos\Phi_e & \sin\Phi_e & 0 \\ -\sin\Phi_e & \cos\Phi_e & 1 \end{bmatrix} \\
&= \begin{bmatrix} \cos\psi_e\cos\Phi_e - \sin\Phi_e\cos\vartheta_e\sin\psi_e & \cos\Phi_e\sin\psi_e + \sin\Phi_e\cos\psi_e\cos\vartheta_e & \sin\Phi_e\sin\vartheta_e \\ -\sin\Phi_e\cos\psi_e - \cos\Phi_e\cos\vartheta_e\sin\psi_e & -\sin\Phi_e\sin\psi_e + \cos\Phi_e\cos\psi_e\cos\vartheta_e & \cos\psi_e\sin\vartheta_e \\ \sin\vartheta_e\sin\psi_e & -\sin\vartheta_e\cos\psi_e & \cos\vartheta_e \end{bmatrix}.
\end{aligned}
\tag{2.1}
$$

The vector $\boldsymbol{\omega}_e$ of the body's angular velocity is a vector sum of the component velocities (Fig. 2.6):

$$
\boldsymbol{\omega}_e = \dot{\boldsymbol{\vartheta}}_e + \boldsymbol{\psi}_e + \dot{\boldsymbol{\Phi}}_e, \tag{2.2}
$$

where

$$
\dot{\boldsymbol{\vartheta}}_e = \frac{d\boldsymbol{\vartheta}_e}{dt}, \quad \dot{\boldsymbol{\psi}}_e = \frac{\mathrm{d}\boldsymbol{\psi}}{\mathrm{d}t_e}, \quad \dot{\boldsymbol{\Phi}}_e = \frac{\mathrm{d}\boldsymbol{\Phi}}{\mathrm{d}t_e}.
$$

Projections of vector $\boldsymbol{\omega}_e$ onto the OX_1''', OX_2''', and OX_3''' axes are determined in such a way that each of the vectors $\dot{\boldsymbol{\vartheta}}_e$, $\dot{\boldsymbol{\psi}}_e$, and $\dot{\boldsymbol{\Phi}}_e$ is projected onto the aforementioned axes:

$$\boldsymbol{\omega}_e^{OX_1'''X_2'''X_3'''} = m^{\vartheta\Phi}\begin{bmatrix}0\\0\\\dot{\psi}_e\end{bmatrix} + m^{\Phi}\begin{bmatrix}\dot{\vartheta}_e\\0\\0\end{bmatrix} + \begin{bmatrix}0\\0\\\dot{\Phi}_e\end{bmatrix},$$

$$\begin{bmatrix}\omega_{eX_1'''}\\\omega_{eX_2''}\\\omega_{eX_3'''}\end{bmatrix} = \begin{bmatrix}\dot{\Psi}_e\sin\vartheta_e\sin\Phi_e + \dot{\vartheta}_e\cos\Phi_e\\\dot{\psi}_e\sin\vartheta\cos\phi_e - \dot{\vartheta}_e\sin\Phi_e\\\dot{\Phi}_e + \dot{\Phi}_e\cos\vartheta_e\end{bmatrix}. \tag{2.3}$$

The projections of vector $\boldsymbol{\omega}_e$ onto the axes of the fixed frame OX_{1O}', OX_{2O}', OX_{3O}' are as follows:

$$\boldsymbol{\omega}_e^{OX_{1O}'X_{2O}'X_{3O}'} = m^{\psi\vartheta}\begin{bmatrix}0\\0\\\dot{\Phi}_e\end{bmatrix} + m^{\Psi}\begin{bmatrix}\dot{\vartheta}_e\\0\\0\end{bmatrix} + \begin{bmatrix}0\\0\\\dot{\psi}_e\end{bmatrix},$$

$$\begin{bmatrix}\omega_{eX_{1O}'}\\\omega_{eX_{2O}'}\\\omega_{eX_{3O}'}\end{bmatrix} = \begin{bmatrix}\dot{\Phi}_e\sin\vartheta_e\sin\psi_e + \dot{\vartheta}_e\cos\psi_e\\\dot{\Phi}_e\sin\vartheta\cos\psi_e - \dot{\vartheta}_e\sin\psi_e\\\dot{\psi}_e + \dot{\Phi}_e\cos\vartheta_e\end{bmatrix}. \tag{2.4}$$

The preceding formulas (2.3) and (2.4) can be regarded as systems of equations of unknowns $\dot{\vartheta}_e$, $\dot{\psi}_e$, and $\dot{\Phi}_e$. Determining, e.g., on the basis of (2.3), projections of the angular velocities $\dot{\boldsymbol{\vartheta}}_e$, $\dot{\boldsymbol{\psi}}_e$, $\dot{\boldsymbol{\Phi}}_e$ onto the movable axes OX_1''', OX_2''', OX_3''', we have

$$\begin{aligned}
\dot{\vartheta}_e &= \omega_{eX_1'''}\cos\Phi_e - \omega_{eX_2'''}\sin\Phi_e,\\
\dot{\psi}_e &= \frac{\omega_{eX_1'''}\sin\Phi_e + \omega_{eX_1'''}\cos\Phi_e}{\sin\vartheta_e},\\
\dot{\Phi}_e &= \omega_{eX_3'''} - \frac{\omega_{eX_1'''}\sin\Phi_e + \omega_{eX_2'''}\cos\Phi_e}{tan\vartheta_e}.
\end{aligned} \tag{2.5}$$

Equations (2.5) imply the following conclusions:

(a) For $\vartheta_e = 0$ we have $\dot{\psi}_e$ and $\dot{\Phi}_e$ undetermined.

(b) For $\vartheta_e = \psi_e = \Phi_e = 0$ we have: $\omega_{eX_1'''} = \dot{\vartheta}_e$, $\omega_{eX_2}''' = 0$, $\omega_{eX_3}''' = \dot{\psi}_e + \dot{\Phi}_e$ [(2.3)] regardless of the fact that the values $\dot{\vartheta}_e$, $\dot{\psi}_e$, $\dot{\Phi}_e$ are non-zero, which is not true in a general case.

(c) When $\vartheta_e = 0$, then formulas (2.3) imply that $\omega_{eX_1'''} = -\omega_{eX_2}'''\tan\Phi_e$, which is not valid in a general case either. There are certain paradoxes. Thus, using the Euler angles one should avoid the position of the body at $\vartheta_e = 0$.

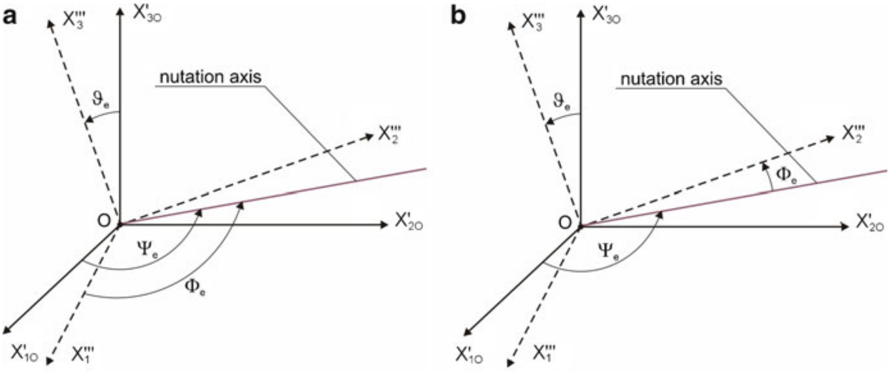

Fig. 2.7 Variants of Euler angles

There exist other variants in specifying angles ψ_e and Φ_e (Fig. 2.7a, b).

Using formulas (2.2), it is possible to determine both the value and direction of the angular velocity $\boldsymbol{\omega}_e$. For the value of the angular velocity ω_e we obtain the expression

$$\omega_e = \sqrt{\omega_{eX_1'''}^2 + \omega_{eX_2'''}^2 + \omega_{eX_3'''}^2} = \sqrt{\dot{\vartheta}_e^2 + \dot{\psi}_e^2 + \dot{\Phi}_e^2 + 2\dot{\psi}_e^2\dot{\Phi}_e^2 \cos\vartheta_e}. \tag{2.6}$$

The linear velocities of points of a body that rotates about a fixed point O are angular velocities about the instantaneous axis of rotation. This means that the linear velocity $\mathbf{V}_e$ is a cross product of the angular velocity $\boldsymbol{\omega}_e$ of the form [the radius vector $\boldsymbol{\rho}(X_1''',\ X_2''',\ X_3''')$ is going to a given point from the fixed point O]

$$\mathbf{V}_e = \boldsymbol{\omega}_e \times \boldsymbol{\rho}_e. \tag{2.7}$$

Projecting the velocity $\mathbf{V}_e$ onto the OX_1''', OX_2''', OX_3''' axes one obtains

$$\begin{aligned}
V_{eX_1'''} &= \omega_{eX_2'''}x_3''' - \omega_{eX_3'''}x_2''',\\
V_{eX_2'''} &= \omega_{eX_3'''}x_1''' - \omega_{eX_1'''}x_3''',\\
V_{eX_3'''} &= \omega_{eX_1'''}x_2''' - \omega_{eX_2'''}x_1'''.
\end{aligned} \tag{2.8}$$

2.1.2 *Cardan Angles*

The appearance of the Cardan angles is connected with the fact of a common spread of the Cardan suspension in gyroscopic devices. The Euler angles ψ_e, ϑ_e, and Φ_e in this kind of device are inconvenient for analysis. This refers to the fact that small movements of the rigid body axis cannot be related to the two small angles from

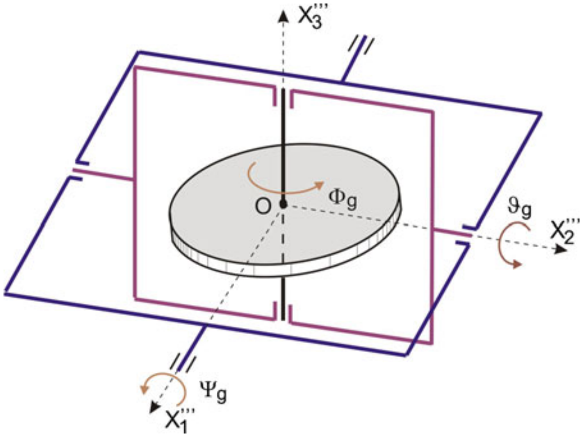

Fig. 2.8 Cardan angles

the following set: ψ_e, ϑ_e, and Φ_e. Moreover, the OX_1''', OX_2''', OX_3''' axes, which are fixed to the body, change their orientation very fast in space at high angular velocities of the body [4,5]. This causes some difficulties in exhibiting various kinds of correcting and control torques, usually about physical axes of the suspension, in the equations of motion of a rigid body. These defects can be eliminated by choosing another set of angles ψ_g, ϑ_g, Φ_g, i.e., the aforementioned Cardan angles compared to ψ_e, ϑ_e, Φ_e.

The Cardan angles can be specified in various ways as angles between particular elements of a suspension. One of the possible forms of a Cardan suspension, along with the assumed angles, is depicted in Fig. 2.8. The Cardan suspension is discussed in more detail subsequently.

Figure 2.8 shows a gyroscope in its initial position, at which the coordinate system $OX_1'''X_2'''X_3'''$, fixed to the rotor, coincides with the fixed system $OX_{1O}'X_{2O}'X_{3O}'$. By mutual rotations of these two bodies, we can specify an arbitrary position of the gyroscope in space, bearing in mind that the origin O remains at rest.

As in the case of the Euler angles, any position of the rotor of the gyroscope can be achieved in the following way (see also [3]):

4. The first rotation is made about the fixed axis (of the external frame) OX_{1O}', by an angle ψ_g (Fig. 2.9). This orthogonal transformation can be expressed by means of a matrix m_g^{ψ} [see (2.9)].
5. The second rotation is made about the internal frame axis OX_1' by an angle ϑ_g (Fig. 2.10). The respective transformation matrix is m_g^{ϑ} [see (2.9)].
6. The final rotation needs to be made about the eigenrotation axis OX_3'' at angle Φ_g (Fig. 2.11). The corresponding transformation matrix is m_g^{Φ} [see (2.9)].

The transformation matrix from the coordinate system OX_{1O}', OX_{2O}', OX_{3O}' to the system OX_1''', OX_2''', OX_3''' has the following form:

Fig. 2.9 Rotation about external frame axis

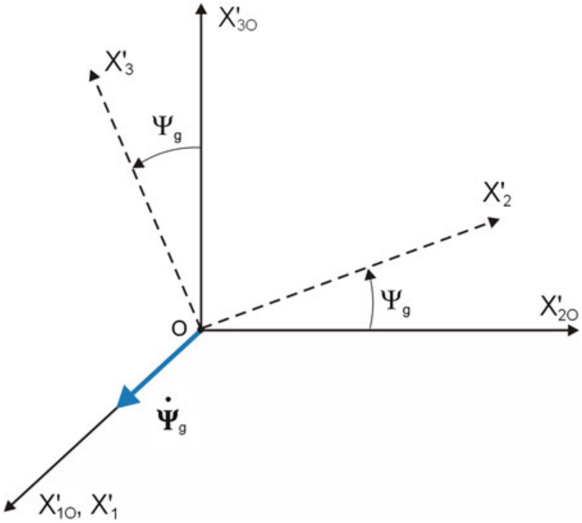

Fig. 2.10 Rotation about internal frame axis

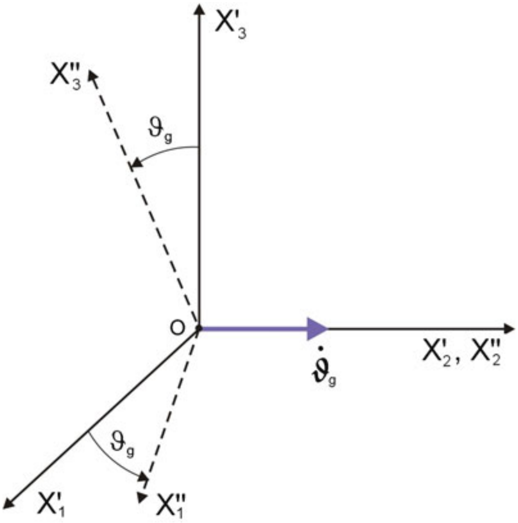

$$m^K = m_g^{\psi} m_g^{\vartheta} m_g^{\Phi}$$

$$= \begin{bmatrix} 1 & 0 & 0 \\ 0 & \cos\psi_g & \sin\psi_g \\ 0 & -\sin\psi_g & \cos\psi_g \end{bmatrix} \begin{bmatrix} \cos\vartheta_g & 0 & -\sin\vartheta_g \\ 0 & 1 & 0 \\ \sin\vartheta_g & 0 & \cos\vartheta_g \end{bmatrix} \begin{bmatrix} \cos\Phi_g & \sin\Phi_g & 0 \\ -\sin\Phi_g & \cos\Phi_g & 0 \\ 0 & 0 & 1 \end{bmatrix}$$

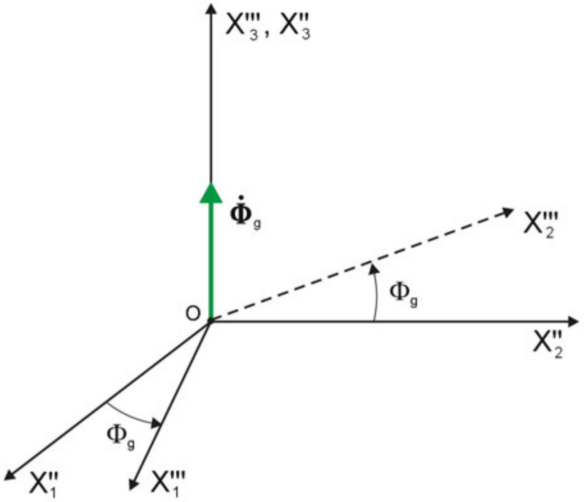

Fig. 2.11 Rotation about eigenrotation axis (fast)

$$= \begin{bmatrix} \cos\psi_g \cos\Phi_g; & \cos\psi_g \sin\Phi_g + \sin\vartheta_g \sin\psi_g \cos\Phi_g; & \sin\psi_g \sin\Phi_g - \cos\vartheta_g \sin\psi_g \cos\Phi_g \\ -\sin\psi_g \cos\Phi_g; & \cos\psi_g \cos\Phi_g - \sin\vartheta_g \sin\psi_g \sin\Phi_g; & \sin\psi_g \cos\Phi_g + \sin\vartheta_g \cos\psi_g \sin\Phi_g \\ \sin\psi_g; & -\cos\vartheta_g \sin\psi_g; & \cos\psi_g \cos\vartheta_g \end{bmatrix}. \tag{2.9}$$

Projections of $\boldsymbol{\omega}_g$ onto the OX_1''', OX_2''', OX_3''' axes are as follows:

$$\boldsymbol{\omega}_g{}^{OX_1'''X_2'''X_3'''} = m_g^{\vartheta\Phi} \begin{bmatrix} \dot{\psi}_g \\ 0 \\ 0 \end{bmatrix} + m_g^{\Phi} \begin{bmatrix} 0 \\ \dot{\vartheta}_g \\ 0 \end{bmatrix} + \begin{bmatrix} 0 \\ 0 \\ \dot{\Phi}_g \end{bmatrix},$$

$$\begin{bmatrix} \omega_{gX_1'''} \\ \omega_{gX_2'''} \\ \omega_{gX_3'''} \end{bmatrix} = \begin{bmatrix} \dot{\psi}_g \cos\vartheta_g \cos\Phi_g + \dot{\vartheta}_g \sin\Phi_g \\ -\dot{\psi}_g \cos\vartheta_g \sin\Phi_g + \dot{\vartheta}_g \cos\Phi_g \\ \dot{\Phi}_g + \dot{\psi}_g \sin\vartheta_g \end{bmatrix}. \tag{2.10}$$

By (2.9) we determine projections of the angular velocities $\dot{\boldsymbol{\vartheta}}_e$, $\dot{\boldsymbol{\psi}}_e$, $\dot{\boldsymbol{\Phi}}_e$ onto the movable axes OX_1''', OX_2''', OX_3''', i.e., we obtain

$$\begin{aligned} \dot{\vartheta}_g &= \omega_{gX_1'''} \sin\Phi_g - \omega_{gX_2'''} \cos\Phi_g, \\ \dot{\psi}_g &= \frac{\omega_{gX_1'''} \cos\Phi_g - \omega_{gX_2'''} \sin\Phi_g}{\cos\vartheta_g}, \\ \dot{\Phi}_g &= \omega_{gX_3'''} - \left(\omega_{gX_1'''} \cos\Phi_g - \omega_{gX_2'''} \sin\Phi_g\right) \tan\vartheta_g. \end{aligned} \tag{2.11}$$

Projections of the angular velocity $\boldsymbol{\omega}_g$ described by relations (2.10) [or projections of the angular velocity $\boldsymbol{\omega}_e$ described by relations (2.3)] are not holonomic coordinates in the sense of analytical mechanics. Thus it is not possible to obtain, by means of integration, the angles that could uniquely specify the position of a body in space. That is why one should not measure the components of the angular velocity of a moving object (airplane, missile, bomb, ship) with measurement instruments placed on this object to obtain the rotation angles, by means of direct integration, about the axis of the coordinate system fixed to the object. However, one should integrate a system of non-linear (2.11) [or (2.5)] to determine the aforementioned angles precisely.

In the case of the Cardan angles, we can also observe ambiguities in determining the angular velocities $\dot{\vartheta}_g$, $\dot{\psi}_g$, and $\dot{\Phi}_g$. In a given case it concerns the angle $\vartheta_g = \pi/2$. This corresponds to the case of the so-called frame folding of a Cardan suspension, when the gyroscope fails to operate as a gyroscope.

2.2 Kinetic Energy of a Rigid Body

Considering a body as a set of N material points moving at velocities V_n, we express the kinetic energy of the body as follows [6, 7]:

$$T = \frac{1}{2}\sum_{n=1}^{N} m_n V_n^2. \tag{2.12}$$

Using (2.8), the square of velocity of the nth material point reads

$$\begin{aligned} V_n^2 &= V^2_{nX_1'''} + V^2_{nX_2'''} + V^2_{nX_3'''} = \left(\omega_{eX_2'''} x_3^n - \omega_{eX_3'''} x_2^n\right)^2 \\ &\quad + \left(\omega_{eX_3'''} x_1^n - \omega_{eX_1'''} x_3^n\right)^2 + \left(\omega_{eX_1'''} x_2^n - \omega_{eX_2'''} x_1^n\right)^2 \\ &= \omega^2_{eX_1'''}\left(\left(x_2^n\right)^2 + \left(x_3^n\right)^2\right) + \omega^2_{eX_2'''}\left(\left(x_3^n\right)^2 + \left(x_1^n\right)^2\right) \\ &\quad + \omega^2_{eX_3'''}\left(\left(x_1^n\right)^2 + \left(x_2^n\right)^2\right) - 2\omega_{eX_2'''}\omega_{eX_3'''} x_2^n x_3^n \\ &\quad - 2\omega_{eX_3'''}\omega_{eX_1'''} x_3^n x_1^n - 2\omega_{eX_1'''}\omega_{eX_2'''} x_1^n x_2^n. \end{aligned} \tag{2.13}$$

Substituting the preceding expression into (2.12) we obtain

$$\begin{aligned} T = \frac{1}{2}\Big(& I_{X_1'''}\omega^2_{eX_1'''} + I_{X_2'''}\omega^2_{eX_2'''} + I_{X_3'''}\omega^2_{eX_3'''} - 2I_{yz}\omega_{eX_2'''}\omega_{eX_3'''} \\ & - 2I_{zx}\omega_{eX_3'''}\omega_{eX_1'''} - 2I_{xy}\omega_{eX_1'''}\omega_{eX_2'''}\Big). \end{aligned} \tag{2.14}$$

As was assumed in our considerations that the axes OX_1''', OX_2''', OX_3''' were fixed to the body and oriented along the main axes of inertia and with the origin at point O, so in this case the moments of inertia $I_{X_1'''}$, $I_{X_2'''}$, $I_{X_3'''}$ are constant and deviation moments equal zero, i.e., $I_{X_2X_3} = I_{X_3X_1} = I_{X_1X_2} = 0$.
Thus, the kinetic energy is expressed in the following form:

$$T = \frac{1}{2}\left(I_{X_1'''}\omega^2_{eX_1'''} + I_{X_2'''}\omega^2_{eX_2'''} + I_{X_3'''}\omega^2_{eX_3'''}\right). \tag{2.15}$$

The kinetic energy of a body—in cases where the body, besides spherical motion, moves in translational motion at the velocity $\mathbf{V}_o$ of its center of mass (by the König theorem)—can be written in the following form:

$$T = \frac{1}{2}m_3V_o^2 + \frac{1}{2}\left(I_{X_1'''}\omega^2_{eX_1'''} + I_{X_2'''}\omega^2_{eX_2'''} + I_{X_3'''}\omega^2_{eX_3'''}\right). \tag{2.16}$$

2.2.1 Equations of Spherical Motion of a Rigid Body

Let us write a theorem on the variation of the angular momentum in the spherical motion of a body about a fixed point O (center of spherical motion) in the following form (see [1,7] and Chap. 9 of [2]):

$$\frac{\mathrm{d}\mathbf{K}_o}{\mathrm{d}t} = \mathbf{M_o}. \tag{2.17}$$

We find the angular momentum $\mathbf{K}_o$ of the body by the following formula:

$$\begin{aligned}\mathbf{K}_o &= \sum_{n=1}^{N}\boldsymbol{\rho}_n \times m_n\mathbf{V}_n = \sum_{n=1}^{N}\boldsymbol{\rho}_n \times m_n\left(\boldsymbol{\omega}_e \times \boldsymbol{\rho}_n\right)\\ &= \sum_{n=1}^{N} m_n\left[\boldsymbol{\rho}_n \times (\boldsymbol{\omega}_e \times \boldsymbol{\rho}_n)\right].\end{aligned} \tag{2.18}$$

Using the properties of vector product, (2.18) takes the following form:

$$\begin{aligned}\mathbf{K}_o &= \sum_{n=1}^{N} m_n\left[\boldsymbol{\omega}_e\left(\boldsymbol{\rho}_n \circ \boldsymbol{\rho}_n\right) - \boldsymbol{\rho}_n\left(\boldsymbol{\omega}_e \circ \boldsymbol{\rho}_n\right)\right]\\ &= \sum_{n=1}^{N} m_i\left[\boldsymbol{\omega}_e \circ \rho_n^2 - \rho_n(\boldsymbol{\omega}_e \circ \boldsymbol{\rho}_n)\right]\\ &= \sum_{n=1}^{N} m_n\Big[\boldsymbol{\omega}_e\big((x_1^n)^2 + (x_2^n)^2 + (x_3^n)^2\big) - \boldsymbol{\rho}_n(\omega_{eX_1'''}x_1^n + \omega_{eX_2'''}x_2^n + \omega_{eX_3'''}x_3^n)\Big].\end{aligned} \tag{2.19}$$

In projections onto particular axes of the coordinate system $O_{g_3}X_1'''X_2'''X_3'''$, the components of the angular momentum vector read

$$\begin{aligned}
K_{X_1'''} &= I_{X_1'''}\omega_{eX_1'''} - I_{X_1X_2}\omega_{eX_2'''} - I_{X_1X_3}\omega_{eX_3'''},\\
K_{X_2'''} &= I_{X_2'''}\omega_{eX_2'''} - I_{X_2X_3}\omega_{eX_3'''} - I_{yx}\omega_{eX_1'''},\\
K_{X_3'''} &= I_{X_3'''}\omega_{eX_3'''} - I_{X_3X_1}\omega_{eX_1'''} - I_{X_3X_2}\omega_{eX_2'''},
\end{aligned} \tag{2.20}$$

where

$$\begin{aligned}
I_{X_1'''} &= \sum_{n=1}^{N} m_n\left(\left(x_2^n\right)^2 + \left(x_3^n\right)^2\right), & I_{X_2'''} &= \sum_{n=1}^{N} m_n\left(\left(x_3^n\right)^2 + \left(x_2^n\right)^2\right),\\
I_{X_3'''} &= \sum_{n=1}^{N} m_n\left(\left(x_1^n\right)^2 + \left(x_2^n\right)^2\right), & I_{X_1X_2} &= \sum_{n=1}^{N} m_n x_1^n x_2^n,\\
I_{X_2X_3} &= \sum_{n=1}^{N} m_n x_2^n x_3^n, & I_{X_3X_1} &= \sum_{n=1}^{N} m_n x_3^n x_1^n.
\end{aligned}$$

In cases where the axes OX_1''', OX_2''', OX_3''' are the main axes intersecting at point O, the moments of deviation of the body relative to these axes read $I_{X_1X_2} = I_{X_2X_3} = I_{X_1X_3} = 0$.

Finally, the components of the angular momentum take the form

$$K_{X_1'''} = I_{X_1'''}\omega_{eX_1'''}, \quad K_{X_2'''} = I_{X_2'''}\omega_{eX_2'''}, \quad K_{X_3'''} = I_{X_3'''}\omega_{eX_3'''}. \tag{2.21}$$

A derivative of the angular momentum $\mathbf{K}_o$ with respect to time has the following form:

$$\begin{aligned}
\frac{\mathrm{d}\mathbf{K}_o}{\mathrm{d}t} &= \mathbf{E}_1'''\frac{\mathrm{d}K_{X_1'''}}{\mathrm{d}t} + \mathbf{E}_2'''\frac{\mathrm{d}K_{X_2'''}}{\mathrm{d}t} + \mathbf{E}_3'''\frac{\mathrm{d}K_{X_3'''}}{\mathrm{d}t} + \boldsymbol{\omega}_e \times \mathbf{K}_o\\
&= \mathbf{E}_1'''\frac{\mathrm{d}K_{X_1'''}}{\mathrm{d}t} + \mathbf{E}_2'''\frac{\mathrm{d}K_{X_2'''}}{\mathrm{d}t} + \mathbf{E}_3'''\frac{\mathrm{d}K_{X_3'''}}{\mathrm{d}t}\\
&\quad + \begin{vmatrix} \mathbf{E}_1''' & \mathbf{E}_2''' & \mathbf{E}_3'''\\ \omega_{eX_1'''} & \omega_{eX_2'''} & \omega_{eX_3'''}\\ K_{X_1'''} & K_{X_2'''} & K_{X_3'''} \end{vmatrix}.
\end{aligned} \tag{2.22}$$

Equations (2.17), taking into account (2.22) in projections onto the axes of the movable coordinate system $OX_1'''X_2'''X_3'''$, will have the form

$$\begin{aligned}
&\frac{\mathrm{d}K_{X_1'''}}{\mathrm{d}t} + \omega_{eX_2'''}K_{X_3'''} - \omega_{eX_3'''}K_{X_2'''} = M_{X_1'''},\\
&\frac{\mathrm{d}K_{X_2'''}}{\mathrm{d}t} + \omega_{eX_3'''}K_{X_1'''} - \omega_{eX_1'''}K_{X_3'''} = M_{X_2'''},\\
&\frac{\mathrm{d}K_{X_3'''}}{\mathrm{d}t} + \omega_{eX_1'''}K_{X_2'''} - \omega_{eX_2'''}K_{X_1'''} = M_{X_3'''}. \qquad (2.23)
\end{aligned}$$

Assuming that the axes of the movable coordinate system are the main axes of inertia of the body at the point O_{g_3}, we substitute (2.21) into (2.23) and obtain

$$I_{X_1'''}\frac{\mathrm{d}\omega_{eX_1'''}}{\mathrm{d}t} + \left(I_{X_3'''} - I_{X_2'''}\right)\omega_{eX_2'''}\omega_{eX_3'''} = M_{X_1'''}, \qquad (2.24\text{a})$$

$$I_{X_2'''}\frac{\mathrm{d}\omega_{eX_2'''}}{\mathrm{d}t} + \left(I_{X_1'''} - I_{X_3'''}\right)\omega_{eX_2'''}\omega_{eX_3'''} = M_{X_2'''}, \qquad (2.24\text{b})$$

$$I_{X_3'''}\frac{\mathrm{d}\omega_{eX_3'''}}{\mathrm{d}t} + \left(I_{X_2'''} - I_{X_1'''}\right)\omega_{eX_1'''}\omega_{eX_2'''} = M_{X_3'''}. \qquad (2.24\text{c})$$

These are the Euler equations of a rigid body in spherical motion [1, 3, 7, 8]. By adding to the preceding (2.23) the relations among projections of the angular velocities $\omega_{eX_1'''}$, $\omega_{eX_2'''}$, $\omega_{eX_3'''}$, we will obtain six first-order ODEs, which (along with suitable initial conditions) fully govern the rotation of a rigid body about a fixed point. The solution of the non-linear differential (2.24) involves elliptic integrals.

Suppose that the torque $\mathbf{M_o}$ acting on a rigid body is caused by a single gravity force $\mathbf{G} = m\mathbf{g}$. It can thus be presented in the form

$$\mathbf{M_o} = \mathbf{r}_c \times m\mathbf{g} = \begin{vmatrix} \mathbf{E}_1''' & \mathbf{E}_2''' & \mathbf{E}_3''' \\ x_{1C}''' & x_{2C}''' & x_{3C}''' \\ G_{X_1'''} & G_{X_2'''} & G_{X_3'''} \end{vmatrix}, \qquad (2.25)$$

where X_{1C}''', X_{2C}'''', X_{3C}''' are coordinates of the center of mass in the coordinate system $OX_1'''X_2'''X_3'''$. Observe that $[G_{X_1'''},\quad G_{X_2'''},\quad G_{X_3'''}]^{\mathrm{T}} = m^E[0,\quad 0,\quad -G]^{\mathrm{T}} = -G[\sin\Phi_e \sin\vartheta_e,\quad \cos\Phi_e \sin\vartheta_e,\quad \cos\vartheta_e]^{\mathrm{T}}$, where m^E is matrix of transformation described by relation (2.1); $\gamma_1,\ \gamma_2,\ \gamma_3$ are direction cosines of the angles between the axis OX_3''' and the axes $OX_1,\ OX_2,\ OX_3$, where

$$\gamma_1 = \sin\Phi_e \sin\vartheta_e, \quad \gamma_2 = \cos\Phi_e \sin\vartheta_e, \quad \gamma_3 = \cos\vartheta_e. \qquad (2.26)$$

Taking into account (2.25), the dynamical Euler equations can be cast in the following form:

$$I_{X_1'''}\frac{\mathrm{d}\omega_{eX_1'''}}{\mathrm{d}t}+\left(I_{X_3'''}-I_{X_2'''}\right)\omega_{eX_2'''}\omega_{eX_3'''}=G\left(\gamma_2x_{3C}'''-\gamma_3x_{2C}'''\right), \tag{2.27a}$$

$$I_{X_2'''}\frac{\mathrm{d}\omega_{eX_3'''}}{\mathrm{d}t}+\left(I_{X_1'''}-I_{X_3'''}\right)\omega_{eX_1'''}\omega_{eX_3'''}=G\left(\gamma_3x_{1C}'''-\gamma_1x_{3C}'''\right), \tag{2.27b}$$

$$I_{X_3'''}\frac{\mathrm{d}\omega_{eX_3'''}}{\mathrm{d}t}+\left(I_{X_2'''}-I_{X_1'''}\right)\omega_{eX_1'''}\omega_{eX_2'''}=G\left(\gamma_1x_{2C}'''-\gamma_2x_{1C}'''\right). \tag{2.27c}$$

The derivative of versor $\mathbf{k}$ of OX_3 with respect to time is as follows:

$$\begin{aligned}\frac{\mathrm{d}\mathbf{k}}{\mathrm{d}t}&=\left.\frac{\mathrm{d}\mathbf{k}}{\mathrm{d}t}\right|_{OX_1'''X_2'''X_3'''}+\boldsymbol{\omega}_e\times\mathbf{k}=\frac{\mathrm{d}k_{X_1'''}}{\mathrm{d}t}\mathbf{E}_1'''+\frac{\mathrm{d}k_{X_2'''}}{\mathrm{d}t}\mathbf{E}_2'''+\frac{\mathrm{d}k_{X_3'''}}{\mathrm{d}t}\mathbf{E}_3'''\\&+\begin{vmatrix}\mathbf{E}_1''' & \mathbf{E}_2''' & \mathbf{E}_3'''\\ \omega_{eX_1'''} & \omega_{eX_2'''} & \omega_{eX_3'''}\\ k_{X_1'''} & k_{X_2'''} & k_{X_3'''}\end{vmatrix}=\left(\frac{\mathrm{d}\gamma_1}{\mathrm{d}t}+\omega_{eX_2'''}\gamma_3-\omega_{eX_3'''}\gamma_2\right)\mathbf{E}_1'''\\&+\left(\frac{\mathrm{d}\gamma_2}{\mathrm{d}t}+\omega_{eX_3'''}\gamma_1-\omega_{eX_1'''}\gamma_3\right)\mathbf{E}_2'''+\left(\frac{\mathrm{d}\gamma_3}{\mathrm{d}t}+\omega_{eX_1'''}\gamma_3-\omega_{eX_2'''}\gamma_1\right)\mathbf{E}_3''',\end{aligned}$$

and hence

$$\frac{\mathrm{d}\gamma_1}{\mathrm{d}t}=\omega_{eX_3'''}\gamma_2-\omega_{eX_2'''}\gamma_3, \tag{2.28a}$$

$$\frac{\mathrm{d}\gamma_2}{\mathrm{d}t}=\omega_{eX_1'''}\gamma_3-\omega_{eX_3'''}\gamma_1, \tag{2.28b}$$

$$\frac{\mathrm{d}\gamma_3}{\mathrm{d}t}=\omega_{eX_2'''}\gamma_1-\omega_{eX_1'''}\gamma_2. \tag{2.28c}$$

The obtained relations are called the *Poisson equations*. These equations, together with (2.27), form a basic mathematical model of motion of a heavy rigid body about a fixed point; they are called the *Euler–Poisson equations*. The angle ψ_e, which does not occur in (2.28), can be determined by means of quadratures of the *Euler kinematic equations* (2.3). Although one can determine as well the remaining angles Φ_e and ϑ_e from (2.3) knowing the angular velocities $\omega_{eX_1'''}$, $\omega_{eX_2'''}$, and $\omega_{eX_3'''}$, the relationships (2.28) are more advantageous since they require no redundant integrations.

One can show that [1, 3] when four first integrals are found, the problem of solving the system of (2.27) and (2.28) reduces to the quadratures. Three integrals can be determined directly.

Multiplying each equation of system (2.28) by $\gamma_1,\ \gamma_2,\ \gamma_3$, respectively, and adding the equations we obtain a trivial integral

$$\gamma_1^2 + \gamma_2^2 + \gamma_3^2 = 1. \tag{2.29}$$

We obtain the second integral from the obvious relation

$$\frac{\mathrm{d}K_{X_{3O}}}{\mathrm{d}t} = M_{X_{3O}} = 0, \tag{2.30}$$

where $K_{X_{3O}}$ is a projection of the angular momentum of a rigid body onto the OX_{3O} axis in a fixed frame and reads

$$K_{X_{3O}} = K_{X_1'''} \sin \Phi_e \sin \vartheta_e + K_{X_2'''} \cos \Phi_e \sin \vartheta_e + K_{X_3'''} \cos \vartheta_e. \tag{2.31}$$

Taking into account (2.26) and (2.21), we obtain the first integral of the form

$$I_{X_1'''}\omega_{X_1'''}\gamma_1 + I_{X_1'''}\omega_{X_2'''}\gamma_2 + I_{X_3'''}\omega_{X_3'''}\gamma_3 = \text{const.} \tag{2.32}$$

If each equation of system (2.27) is multiplied by $\omega_{eX_1'''}$, $\omega_{eX_2'''}$, and $\omega_{eX_3'''}$, respectively, and the equations are added to one another, then we will obtain the first integral of the kinetic energy:

$$T = \frac{1}{2}\left(I_{X_1'''}\omega_{X_1'''}^2 + I_{X_2'''}\omega_{X_2'''}^2 + I_{X_3'''}\omega_{X_3'''}^2\right). \tag{2.33}$$

It is easy to see that the potential energy of a rigid body in the considered case reads

$$V = Gx_{3O} = G\left(x_{1C}'''\gamma_1 + x_{2C}'''\gamma_1 + x_{3C}'''\gamma_1\right). \tag{2.34}$$

Thus, by the principle of conservation of energy for a heavy rigid body in spherical motion

$$T + V = \text{const}, \tag{2.35}$$

we obtain the third integral in the form

$$\frac{1}{2}\left(I_{X_1'''}\omega_{X_1'''}^2 + I_{X_2'''}\omega_{X_2'''}^2 + I_{X_3'''}\omega_{X_2'''}^2\right) + G\left(x_{1C}'''\gamma_1 + x_{2C}'''\gamma_1 + x_{3C}'''\gamma_1\right) = \text{const.} \tag{2.36}$$

A problem related to finding the fourth integral is the essence of solving the Euler–Poisson system of equations. It was precisely this problem that was investigated by Euler, Lagrange, Poinsot, Kovalevskaya, Poincaré, Lyapunov, and many other renowned scientists. Unfortunately, the problem remains unsolved. However, a general solution of these equations has been found only in three cases: Euler ($x_{1C}''' = 0,\ x_{2C}''' = 0,\ x_{3C}''' = 0$); Lagrange ($I_{X_1'''} = I_{X_2'''},\ x_{1C}''' = 0,\ x_{2C}''' = 0$); Kovalevskaya ($I_{X_1'''} = I_{X_2'''} = 2I_{X_3'''},\ x_{3C}''' = 0$); see also the related discussion in [3].

In subsequent subsections, we will consider the aforementioned cases of spherical motion of a rigid body in more detail from the point of view of applications.

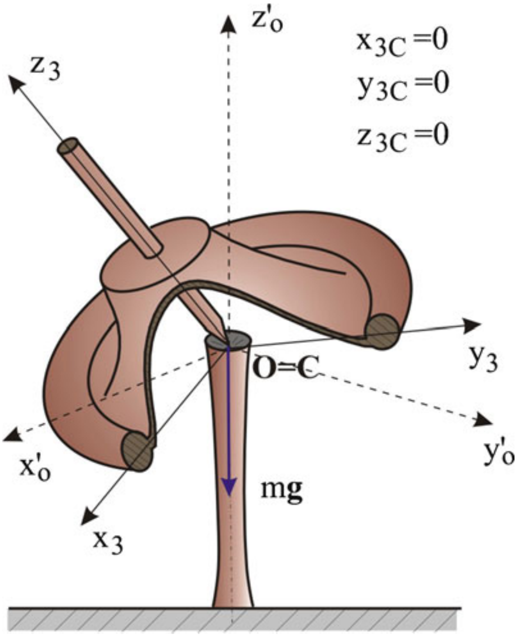

Fig. 2.12 The Euler case

2.2.2 The Euler Case and Geometric Interpretation of Motion of a Body by Poinsot

Consider the motion of a rigid body about a fixed supporting point O. Suppose that the center of mass of this body coincides with the center of rotation at the point O (Fig. 2.12).

If we ignore friction in the bearing, which supports the body and air resistance, then the moments of all external forces about the fixed center of mass O will equal zero. The system of the Euler dynamical equations (2.22) will take the form

$$I_{X_1'''}\frac{\mathrm{d}\omega_{eX_1'''}}{\mathrm{d}t}+\left(I_{X_3'''}-I_{X_2'''}\right)\omega_{eX_2'''}\omega_{eX_3'''}=0, \tag{2.37a}$$

$$I_{X_2'''}\frac{\mathrm{d}\omega_{eX_2'''}}{\mathrm{d}t}+\left(I_{X_1'''}-I_{X_3'''}\right)\omega_{eX_1'''}\omega_{eX_3'''}=0, \tag{2.37b}$$

$$I_{X_3'''}\frac{\mathrm{d}\omega_{eX_3'''}}{\mathrm{d}t}+\left(I_{X_2'''}-I_{X_1'''}\right)\omega_{eX_1'''}\omega_{eX_2'''}=0. \tag{2.37c}$$

Note that it is not difficult to find two integrals of (2.37). To find the first integral, let us multiply the first of these equations by $\omega_{eX_1'''}$, the second one by $\omega_{eX_2'''}$, and the third one by $\omega_{eX_3'''}$ and then add them all up. Then we obtain

$$I_{X_1'''}\omega_{eX_1'''}\dot{\omega}_{eX_1'''}+I_{X_2'''}\omega_{eX_2'''}\dot{\omega}_{eX_2'''}+I_{X_3'''}\omega_{eX_3'''}\dot{\omega}_{eX_3'''}=0. \tag{2.38}$$

The preceding equation is transformed into the form

$$\frac{1}{2}\frac{\mathrm{d}}{\mathrm{d}t}\left(I_{X_1'''}\omega^2_{eX_1'''} + I_{X_2'''}\omega^2_{eX_2'''} + I_{X_3'''}\omega^2_{eX_3'''}\right) = 0. \tag{2.39}$$

Hence we have

$$I_{X_1'''}\omega^2_{eX_1'''} + I_{X_2'''}\omega^2_{eX_2'''} + I_{X_3'''}\omega^2_{eX_3'''} = \text{const.} \tag{2.40}$$

The expression on the left-hand side of (2.40) is equal to a doubled kinetic energy of the considered body, governed by formula (2.35). Thus we have shown that in the given case, the kinetic energy is constant $T = T^o = \text{const}$. The latter observation is obviously consistent with the theorem on kinetic energy when external forces acting on the body do not undertake any work. Let us write (2.40) in the form

$$\begin{aligned} &I_{X_1'''}\omega^2_{eX_1'''} + I_{X_2'''}\omega^2_{eX_2'''} + I_{X_3'''}\omega^2_{eX_3'''} \\ &\quad = K_{X_1'''}\omega_{eX_1'''} + K_{X_2'''}\omega_{eX_2'''} + K_{X_3'''}\omega_{eX_3'''} = 2T^o. \end{aligned} \tag{2.41}$$

It follows from (2.41) that the end of vector $\boldsymbol{\omega}_e$ can move only in the plane perpendicular to $\mathbf{K}_o$.

We are left to find the second integral. This time, let us multiply (2.37a) by $K_{X_1'''} = I_{X_1'''}\omega_{eX_1'''}$, (2.37b) by $K_{X_2'''} = I_{X_2'''}\omega_{eX_2'''}$, and (2.37c) by $K_{X_3'''} = I_{X_3'''}\omega_{eX_3'''}$ and add them up. Then we obtain

$$I^2_{X_1'''}\omega_{eX_1'''}\frac{\mathrm{d}\omega_{eX_1'''}}{\mathrm{d}t} + I^2_{X_2'''}\omega_{eX_2'''}\frac{\mathrm{d}\omega_{eX_2'''}}{\mathrm{d}t} + I^2_{X_3'''}\omega_{eX_3'''}\frac{\mathrm{d}\omega_{eX_3'''}}{\mathrm{d}t} = 0. \tag{2.42}$$

Equation (2.42) is equivalent to

$$\frac{\mathrm{d}}{\mathrm{d}t}\left(I^2_{X_1'''}\omega^2_{eX_1'''} + I^2_{X_2'''}\omega^2_{eX_2'''} + I^2_{X_3'''}\omega^2_{eX_3'''}\right) = 0. \tag{2.43}$$

Note that the expression in parentheses in (2.43) is equal to the square of the absolute value of the angular momentum $\mathbf{K}_o$ relative to point O. Thus, we obtain the following integral of (2.43):

$$I^2_{X_1'''}\omega^2_{eX_1'''} + I^2_{X_2'''}\omega^2_{eX_2'''} + I^2_{X_3'''}\omega^2_{eX_3'''} = K_o^2 = \text{const.} \tag{2.44}$$

This time it was shown that the magnitude of the angular momentum relative to point O is constant.

Although the first two integrals (2.42) and (2.44) do not allow one to obtain the components of the angular velocity $\boldsymbol{\omega}_e$ as a function of time t, they provide a simple geometric interpretation that was first studied by Poinsot. Note that (2.41) describes the energy ellipsoid, which can be written in the form

$$\left(\frac{\omega_{eX_1'''}}{a_e}\right)^2 + \left(\frac{\omega_{eX_2'''}}{b_e}\right)^2 + \left(\frac{\omega_{eX_3'''}}{c_e}\right)^2 = 1, \tag{2.45}$$

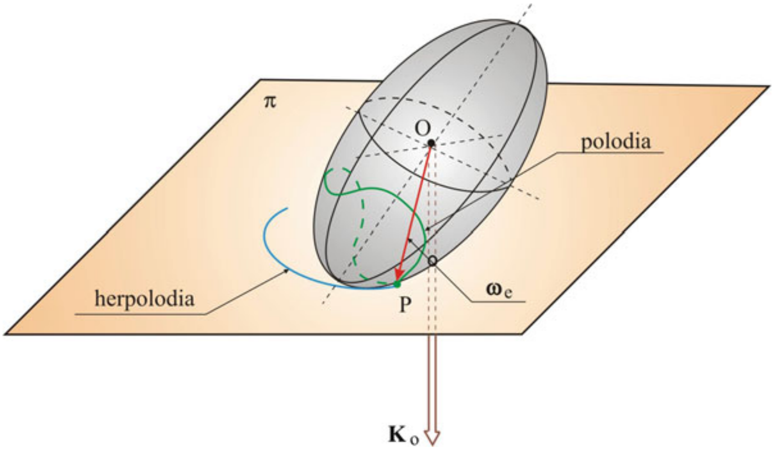

Fig. 2.13 Rolling of energy ellipsoid on a fixed plane

where the semiaxes are as follows:

$$a_e = \sqrt{\frac{2T^o}{I_{X_1'''}}}, \quad b_e = \sqrt{\frac{2T^o}{I_{X_2'''}}}, \quad c_e = \sqrt{\frac{2T^o}{I_{X_3'''}}}.$$

Ellipsoid (2.45) is a locus of ends of the vector $\boldsymbol{\omega}_e$ (it corresponds to the constant kinetic energy T^o). The main axes of the energy ellipsoid are simultaneously main axes of the body, whose center coincides with the supporting point O (Fig. 2.13). Equation (2.44) describes the kinetic ellipsoid, which is a locus of ends of vector $\boldsymbol{\omega}_e$ (it corresponds to the constant angular momentum).

The invariant plane π and ellipsoid (2.45) touch each other at point P, which is an end of vector $\boldsymbol{\omega}_e$. Since the angular momentum $\mathbf{K}_o$ is permanently perpendicular to the plane π, this plane is tangent to the energy ellipsoid at point P. The ellipsoid rolls without slip on the plane because point P lies on the instantaneous axis, which is why its velocity equals zero. During this rolling, pole P draws on the plane $\boldsymbol{\pi}$, a curve called a *herpolodia*, while on an energy ellipsoid a curve, it is known as a *polodia* (Fig. 2.13).

Polodias are closed curves on the surface of an energy ellipsoid. We can determine them as curves of intersection between the ellipsoid described by (2.41) and the kinetic ellipsoid described by (2.44). Shapes of polodias can be viewed by means of their projections onto the main planes $OX_1'''X_2'''$, $OX_1'''X_3'''$, and $OX_2'''X_3'''$. Making appropriate transformations of (2.41) and (2.44) we obtain

$$I_{X_2'''}\left(I_{X_1'''} - I_{X_2'''}\right)\omega_{eX_2'''}^2 + I_{X_3'''}\left(I_{X_1'''} - I_{X_3'''}\right)\omega_{eX_3'''}^2 = 2T^o I_{X_1'''} - K_o^2, \tag{2.46a}$$

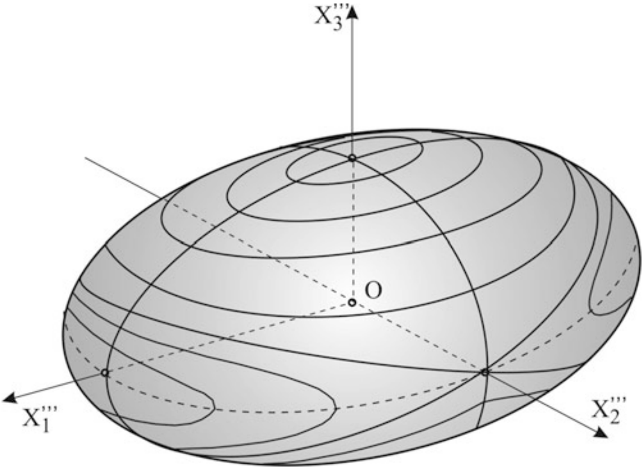

Fig. 2.14 Rolling of energy ellipsoid on invariant plane

$$-I_{X_1'''}\left(I_{X_1'''}-I_{X_2'''}\right)\omega_{eX_1'''}^2+I_{X_3'''}\left(I_{X_2'''}-I_{X_3'''}\right)\omega_{eX_3'''}^2=2T^oI_{X_2'''}-K_o^2, \tag{2.46b}$$

$$-I_{X_1'''}\left(I_{X_1'''}-I_{X_3'''}\right)\omega_{eX_1'''}^2-I_{X_3'''}\left(I_{X_2'''}-I_{X_3'''}\right)\omega_{eX_2'''}^2=2T^oI_{X_3'''}-K_o^2. \tag{2.46c}$$

If we choose the main axes so that $I_{X_1'''} > I_{X_2'''} > I_{X_3'''}$, then (2.46) imply that in the planes $OX_2'''X_3'''$ and $OX_1'''X_2'''$, projections of polodia are ellipses, whereas in the plane $OX_1'''X_3'''$ they are hiperbolas (Fig. 2.14). In a projection onto the plane $OX_1'''X_3'''$ the boundary curves reduce to straight lines, which are asymptotes of hyperbola families. From (2.46b) we easily determine equations of these asymptotes:

$$\omega_{eX_1'''}=\pm\sqrt{\frac{I_{X_3'''}\left(I_{X_2'''}-I_{X_3'''}\right)}{I_{X_1'''}\left(I_{X_1'''}-I_{X_2'''}\right)}}\omega_{eX_3'''}. \tag{2.47}$$

When $I_{X_2'''} = I_{X_3'''}$, then a direction coefficient of a straight line equals zero, and if $I_{X_1'''} = I_{X_2'''}$, then the coefficient tends to infinity, which corresponds to the inclination angle of the line, namely, $\pi/2$. In the former case we are dealing with a flatten rotational ellipsoid, whereas in the second case we are dealing with a lengthened rotational ellipsoid with respect to its symmetry axis.

Fig. 2.15 Rolling of energy ellipsoid on invariant plane

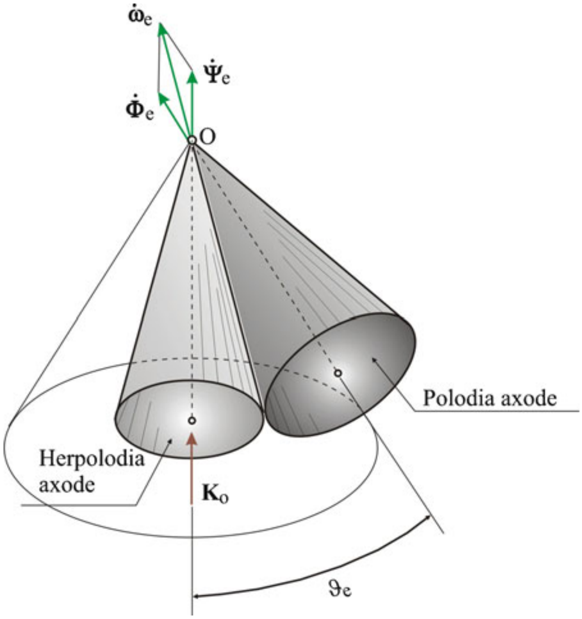

Fig. 2.16 Rolling of energy ellipsoid on invariant plane

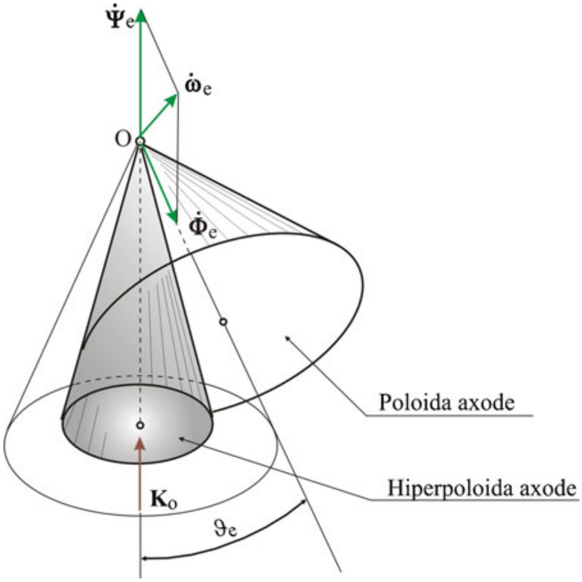

Polodias and herpolodias are directrices of two cones of a common vertex at point O. During the motion of the analyzed body the polodia cone becomes a movable axode, which rolls without sliding on a herpolodia cone, which is a fixed axode (Figs. 2.15 and 2.16).

Suppose that a rigid body with a fixed center of mass is axially symmetric $I_{X_2'''} = I_{X_3'''} = I_b$ (its central inertial ellipsoid is a rotational ellipsoid) and rotates about both a movable axis OX_1''' at angular velocity $\dot{\Phi}_e$ and a fixed axis OX_{3O} at angular velocity $\dot{\psi}_e$. Then, the ellipsoid rolls on the invariant plane $\boldsymbol{\pi}$ perpendicular to the constant angular momentum $\mathbf{K}_o$. In this case, all possible polodias are circles lying in planes perpendicular to the axis OX_1''', and herpolodias, which are also circles, are perpendicular to the axis OX_{3O}. Moreover, both movable and immovable axodes are cones simple circular with common vertex O (center of mass of the rigid body).

Figure 2.15 presents a case of motion of an oblate ellipsoid, i.e., when $I_{X_1'''} > I_b$. Then the movable axode moves outside on the surface of the immovable axode. In Fig. 2.16, the case of the lengthened ellipsoid is depicted ($I_{X_1'''} > I_b$), for which the fixed axode is located inside the movable axode rolling on the external surface.

As was already mentioned, Euler considered inertial motion of a body, i.e. the one, in which the sole force acting on the body is gravity at the fixed center of mass. In this case

$$M_{X_1'''} = M_{X_2'''} = M_{X_3'''} = 0. \tag{2.48}$$

Moreover, he assumed that a body was symmetric relative to the axis OX_3''', i.e., $I_{X_1'''} = I_{X_2'''}$. In this case we have

$$\tfrac{1}{2}\left[I_{X_1'''}\left(\omega^2_{X_1'''} + \omega^2_{X_2'''}\right) + I_{X_3'''}\omega^2_{X_3'''}\right] = T^o = \text{const}, \tag{2.49a}$$

$$I_{X_1'''}\left(\omega^2_{X_1'''} + \omega^2_{X_2'''}\right) + I_{X_3'''}\omega^2_{X_3'''} = K_o^2 = \text{const}, \tag{2.49b}$$

$$\omega_{X_3'''} = \omega^o_{X_3'''} = \text{const}. \tag{2.49c}$$

For this particular case the angular momentum $\mathbf{K}_o$ is constant, both the norm and the direction relative to the fixed coordinate system. In projections onto the fixed axes of the coordinate system vector $\mathbf{K}_o$ is as follows:

$$K_{X_1} = K_o \sin\vartheta_e \sin\Phi_e = I_{X_1'''}\omega_{X_1'''}, \tag{2.50a}$$

$$K_{X_2} = K_o \sin\vartheta_e \cos\Phi_e = I_{X_2'''}\omega_{X_2'''}, \tag{2.50b}$$

$$K_{X_3} = K_o \cos\vartheta_e = I_{X_3'''}\omega^o_{X_3'''}. \tag{2.50c}$$

By (2.50c) we have

$$\cos\vartheta_e = \frac{I_{X_3'''}\omega^o_{X_3'''}}{K_o} = \text{const}; \quad \vartheta_e = \vartheta_e^o = \text{const}; \quad \frac{\mathrm{d}\vartheta_e}{\mathrm{d}t} = 0. \tag{2.51}$$

Taking into account (2.51), formulas (2.49) and (2.50) can be expressed in the following form:

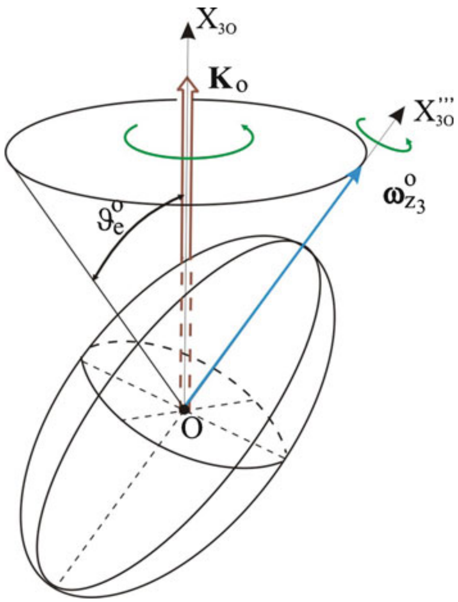

Fig. 2.17 Regular precession for the Euler case

$$\omega_{X_1'''} = \dot{\psi}_e \sin\vartheta_e \sin\Phi_e, \tag{2.52a}$$

$$\omega_{X_2'''} = \dot{\psi}_e \sin\vartheta_e \cos\Phi_e, \tag{2.52b}$$

$$\omega_{X_3'''} = \dot{\psi}_e \cos\vartheta_e + \dot{\Phi}_e, \tag{2.52c}$$

$$K_{X_1} = I_{X_1'''}\dot{\psi}_e \sin\vartheta_e^o \sin\Phi_e = K_o \sin\vartheta_e^o \sin\Phi_e; \quad I_{X_1'''}\dot{\psi}_e = K_o, \tag{2.53a}$$

$$K_{X_1} = I_{X_1'''}\dot{\psi}_e \sin\vartheta_e^o \cos\Phi_e = K_o \sin\vartheta_e^o \cos\Phi_e; \quad I_{X_1'''}\dot{\psi}_e = K_o. \tag{2.53b}$$

Equations (2.53a) and (2.53b) became identical, hence

$$\dot{\psi}_e = \frac{K_o}{I_{X_1'''}} = \text{const} = n_1; \quad \psi_e = n_1 t + \psi_e^o, \tag{2.54}$$

while from (2.52c) we have

$$\dot{\Phi}_e = \omega_{X_3'''}^o - n_1 \cos\vartheta_e^o = \text{const} = n_2; \quad \Phi_e = n_2 t + \Phi_e^o. \tag{2.55}$$

Thus, the Euler case presents the regular precession (Fig. 2.17).

Fig. 2.18 Lagrange case

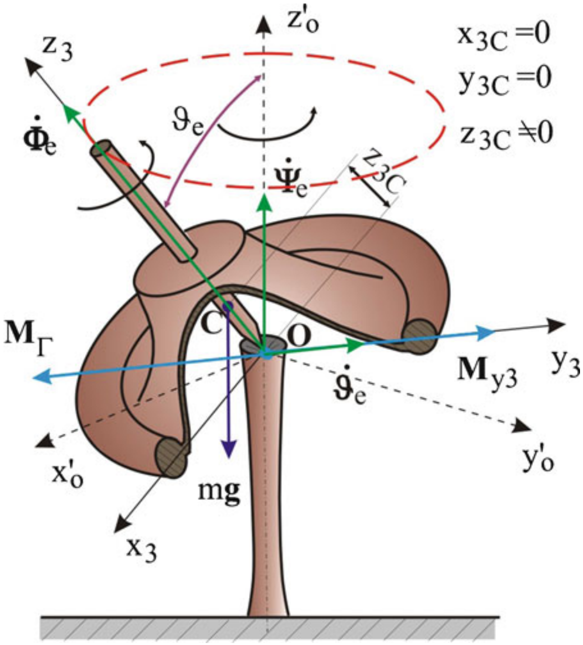

2.2.3 *Lagrange Case (Pseudoregular Precession)*

Consider the motion of a rigid body about a fixed pivot point for a case investigated by Lagrange. The case relies on the fact that the analyzed body is axially symmetric (the respective inertial ellipsoid is a prolate spheroid) $I_{X_1'''} = I_{X_2'''}$. The supporting point (rotation) O and center of mass C lie on the body's axis of symmetry, where $OC = X_{3C}'''$, and the body is under the influence only of gravitational forces. The body rotates at high angular velocity $\dot{\Phi}_e$ about the symmetry axis OX_3''' (Fig. 2.18). This kind of body is called a gyroscope, and in the given case we can call it the Lagrange gyroscope (a more detailed definition of a gyroscope will be given subsequently). Besides rotating about its own axis of symmetry, the body can rotate about the fixed axis OX_{3O} at angular velocity $\dot{\psi}_e$.

To analyze motion of the Lagrange gyroscope, we introduce two movable coordinate systems $OX_1''X_2''X_3''$ and $OX_1'''X_2'''X_3'''$, which slightly differ from the Euler case considered earlier. Similarly, we will select the axis OX_3'' as a symmetry axis of the body (Fig. 2.18). The axis OX_2'' lies on the line of nodes and the axis OX_1'' is selected in such a way that we obtain a rectangular coordinate system. The frame $OX_1'''X_2'''X_3'''$ is obtained by rotating the frame $OX_1''X_2''X_3''$ by an angle Φ_e about the axis OX_3''.

The matrices of transformation m_2^L and m_3^L from the fixed frame $OX_{1O}X_{2O}\ X_{3O}$ to movable ones $OX_1'''X_2'''X_3'''$ and $OX_1'''X_2'''X_3'''$ will take the forms

$$m_2^L = m^{\vartheta} m^{\psi} = \begin{bmatrix} \cos\vartheta_e \cos\psi_e & \cos\vartheta_e \sin\psi_e & -\sin\vartheta_e \\ -\sin\vartheta_e & \cos\psi_e & 0 \\ \sin\vartheta_e \cos\psi_e & \sin\vartheta_e \sin\psi_e & \cos\vartheta_e \end{bmatrix}, \tag{2.56a}$$

$$\begin{aligned} m_3^L &= m^{\Phi} m^{\vartheta} m^{\psi} \\ &= \begin{bmatrix} \begin{array}{c}\cos\vartheta_e \cos\psi_e \cos\Phi_e + \\ -\cos\vartheta_e \sin\psi_e \sin\Phi_e;\end{array} & \begin{array}{c}\cos\vartheta_e \cos\psi_e \sin\Phi_e + \\ +\cos\vartheta_e \sin\psi_e \cos\Phi_e;\end{array} & -\sin\vartheta_e \\ \begin{array}{c}-\sin\vartheta_e \cos\Phi_e + \\ -\cos\psi_e \sin\Phi_e;\end{array} & \begin{array}{c}-\sin\vartheta_e \sin\Phi_e + \\ +\cos\psi_e \cos\Phi_e;\end{array} & 0 \\ \begin{array}{c}\sin\vartheta_e \cos\psi_e \cos\Phi_e + \\ -\sin\vartheta_e \sin\psi_e \sin\Phi_e;\end{array} & \begin{array}{c}\sin\vartheta_e \cos\psi_e \sin\Phi_e + \\ +\sin\vartheta_e \sin\psi_e \cos\Phi_e;\end{array} & \cos\vartheta_e \end{bmatrix}. \end{aligned} \tag{2.56b}$$

We determine projections of the instantaneous angular velocity $\boldsymbol{\omega}_e$ as a result of composing three rotations about the particular axes of both assumed frames.

$$\boldsymbol{\omega}_e = \dot{\boldsymbol{\psi}}_e + \dot{\boldsymbol{\vartheta}}_e + \dot{\boldsymbol{\Phi}}_e. \tag{2.57}$$

Thus, projections onto the axes $OX_1'''X_2'''X_3'''$ of the components of the vector $\boldsymbol{\omega}_e$ are as follows:

$$\boldsymbol{\omega}_e^{OX_1'''X_2'''X_3'''} = m_3^L \begin{bmatrix} 0 \\ 0 \\ \dot{\psi}_e \end{bmatrix} + m_2^L \begin{bmatrix} 0 \\ \dot{\vartheta}_e \\ 0 \end{bmatrix} + \begin{bmatrix} 0 \\ 0 \\ \dot{\Phi}_e \end{bmatrix}, \tag{2.58}$$

$$\omega_{eX_1'''} = -\dot{\psi}_e \sin\vartheta_e, \tag{2.59a}$$

$$\omega_{eX_2'''} = \dot{\vartheta}_e, \tag{2.59b}$$

$$\omega_{eX_3'''} = \dot{\psi}_e \cos\vartheta_e + \dot{\Phi}_e. \tag{2.59c}$$

On the other hand, projections onto the axes $OX_1''X_2''X_3''$ yield

$$\boldsymbol{\omega}_e^{OX_1''X_2''X_3''} = m_2^L \begin{bmatrix} 0 \\ 0 \\ \dot{\psi}_e \end{bmatrix} + \begin{bmatrix} 0 \\ \dot{\vartheta}_e \\ 0 \end{bmatrix} + \begin{bmatrix} 0 \\ 0 \\ 0 \end{bmatrix},$$

$$\omega_{eX_1''} = -\dot{\psi}_e \sin\vartheta_e, \tag{2.60a}$$

$$\omega_{eX_2''} = \dot{\vartheta}_e, \tag{2.60b}$$

$$\omega_{eX_3'''} = \dot{\psi}_e \cos\vartheta_e. \tag{2.60c}$$

At an arbitrary position of the body, the axes $OX_1'''X_2'''X_3'''$ are the main axes of inertia, which is why the angular momentum $\mathbf{K}_o$ components of this body can be cast in the form

$$K_{X_1'''} = I_{X_1'''}\omega_{X_1'''}, \quad K_{X_2'''} = I_{X_2'''}\omega_{X_2'''}, \quad K_{X_3'''} = I_{X_3'''}\omega_{X_3'''}. \tag{2.61}$$

Making use of the theorem on angular momentum change, the equations of motion of Lagrange's gyroscope are written in the form

$$\frac{\mathrm{d}\mathbf{K}_o}{\mathrm{d}t} + \begin{vmatrix} \mathbf{E}_1''' & \mathbf{E}_2''' & \mathbf{E}_3''' \\ \omega_{X_1''} & \omega_{X_2''} & \omega_{X_3''} \\ I_{X_1'''}\omega_{X_1'''} & I_{X_2'''}\omega_{X_2'''} & I_{X_3'''}\omega_{X_3'''} \end{vmatrix} = \mathbf{M_o}.$$

Taking into account the fact that the components of the main moment $\mathbf{M_o}$ of external forces acting on a body have the form

$$\begin{bmatrix} M_{X_1'''} \\ M_{X_2'''} \\ M_{X_3'''} \end{bmatrix} = \begin{vmatrix} \mathbf{E}_1''' & \mathbf{E}_2''' & \mathbf{E}_3''' \\ 0 & 0 & x_{3C}''' \\ G\sin\vartheta_e & 0 & -G\cos\vartheta_e \end{vmatrix} = \begin{bmatrix} 0 \\ Gx_{3C}'''\sin\vartheta_e \\ 0 \end{bmatrix}, \tag{2.62}$$

and taking into account relations (2.49) and (2.50), the equations of motion of the Lagrange gyroscope (2.61),

$$\ddot{\psi}_e\sin\vartheta_e + 2\dot{\psi}_e\dot{\vartheta}_e\cos\vartheta_e - \frac{I_{X_3'''}}{I_{X_1'''}}\left(\dot{\psi}_e\cos\vartheta_e + \dot{\Phi}_e\right)\dot{\vartheta}_e = 0, \tag{2.63a}$$

$$\ddot{\vartheta}_e + \left[\frac{I_{X_3'''}}{I_{X_2'''}}\dot{\Phi}_e + \frac{I_{X_3'''} - I_{X_1'''}}{I_{X_2'''}}\dot{\psi}_e\cos\vartheta_e\right]\dot{\psi}_e\sin\vartheta_e = \frac{Gx_{3C}'''}{I_{X_2'''}}\sin\vartheta_e, \tag{2.63b}$$

$$\frac{\mathrm{d}}{\mathrm{d}t}\left(\dot{\psi}_e\cos\vartheta_e + \dot{\Phi}_e\right) = 0; \quad \dot{\psi}_e\cos\vartheta_e + \dot{\Phi}_e = \omega_o = \text{const.} \tag{2.63c}$$

Let us introduce designation $\dot{\psi} = \omega_1$ and transform (2.53a) into the form of a linear differential equation with respect to angular velocity ω_1:

$$\frac{\mathrm{d}\omega_1}{\mathrm{d}\vartheta_e} + 2\omega_1 ctan\vartheta_e = \frac{I_{X_3'''}\omega_o}{I_{X_1'''}\sin\vartheta_e}. \tag{2.64}$$

It is easy to determine by integration of (2.64)

$$\omega_1 = \frac{C - I_{X_3'''}\omega_o\cos\vartheta_e}{I_{X_1'''}\sin^2\vartheta_e}, \tag{2.65}$$

where C is an integration constant.

In order that a body in the Lagrange case could move in a regular precession (regular precession), the angular velocity ω_1 in this motion should be constant, –$\omega_1 = \text{const} = \dot{\psi}_e^o$. This implies, as shown clearly in (2.65), that angle ϑ_e will also be constant –$\vartheta_e = \text{const} = \vartheta_e^o$. Then, (2.53b) will be simplified to the following form:

$$\left[I_{X_3'''} - \left(I_{X_1'''} - I_{X_3'''} \right) \frac{\omega_1}{\omega_o} \cos\vartheta_e^o \right] \omega_1 \omega_o \sin\vartheta_e^o = G x_{3C}''' \sin\vartheta_e^o. \tag{2.66}$$

Taking into account that the angular velocity of eigenrotations ω_o takes large values, i.e., $\omega_1/\omega_o \ll 1$, (2.66) can be written in a simpler form:

$$G x_{3C}''' \sin\vartheta_e^o - I_{X_3'''} \omega_1 \omega_o \sin\vartheta_e^o = 0, \quad \mathbf{M}_g + I_{X_3'''} \boldsymbol{\omega}_o \times \boldsymbol{\omega}_1 = \mathbf{0},$$
$$\mathbf{M}_g + \mathbf{M}_\Gamma = \mathbf{0}. \tag{2.67}$$

We have obtained the equation of equilibrium of moments of external forces acting on the gyroscope $\mathbf{M}_g$ (in this case the moment of gravitation $M_g = G x_{3C}''' \sin\vartheta_e^o$) and moment of inertial forces $\mathbf{M}_\Gamma$ generated by rotational motion about the symmetry axis $O_{X_3'''}$. The aforementioned torque

$$\mathbf{M}_\Gamma = I_{X_3'''} \boldsymbol{\omega}_o \times \boldsymbol{\omega}_1 \tag{2.68}$$

is called a *gyroscopic moment*.

The formula on the gyroscopic moment can be obtained from (2.66) when the nutation angle equals $\vartheta_e = \pi/2$, i.e., when the angular velocity vector of eigenrotations of the gyroscope is perpendicular to the angular velocity vector of precession $\omega_1 = \dot{\psi}_e$. In this case, exact and approximated formulas are the same. From (2.67) we can determine the precession speed of the Lagrange gyroscope

$$\omega_1 = \dot{\psi}_e = \frac{M_g}{I_{X_3'''} \omega_o} = \frac{G x_{3C}'''}{I_{X_3'''} \dot{\Phi}_e}. \tag{2.69}$$

Let us rewrite (2.66), ignoring $\sin\vartheta_e$, in the following form:

$$\left[I_{X_3'''} \omega_o - \left(I_{X_1'''} - I_{X_3'''} \right) \dot{\psi}_e^o \cos\vartheta_e^o \right] \dot{\psi}_e^o = G x_{3C}'''. \tag{2.70}$$

Solving the preceding equation with respect to $\dot{\psi}_e^o$ we find

$$\dot{\psi}_{ei}^o = \frac{I_{X_3'''} \omega_o \mp \sqrt{I_{X_3'''}^2 \omega_o^2 - 4 \left(I_{X_1'''} - I_{X_3'''} \right) G x_{3C}''' \cos\vartheta_e^o}}{2 \left(I_{X_1'''} - I_{X_3'''} \right) \cos\vartheta_e^o}, \qquad i = 1, 2. \tag{2.71}$$

This implies that solutions exist when

$$I_{X_3'''}^2 \omega_o^2 - 4 \left(I_{X_1'''} - I_{X_3'''} \right) G x_{3C}''' \cos\vartheta_e^o > 0. \tag{2.72}$$

Inequality (2.72) will be preserved if the angular momentum of the Lagrange gyroscope $I_{X_3'''}^2\omega_o^2$ is sufficiently large. This is simultaneously a condition of realization of the regular precession of a gyroscope. Equation (2.71) shows that at a given numerical value of the angular velocity of eigenrotations ω_o, there are three possible types of precession of the examined body. To analyze the obtained result, let us substitute the square root in (2.71) with an approximated expression

$$\sqrt{I_{X_3'''}^2\omega_o^2 - 4\left(I_{X_1'''} - I_{X_3'''}\right)Gx_{3C}''' \cos\vartheta_e^o}$$
$$\cong I_{X_3'''}\omega_o - \frac{2\left(I_{X_1'''} - I_{X_3'''}\right)Gx_{3C}''' \cos\vartheta_e^o}{I_{X_3'''}\omega_o}. \tag{2.73}$$

Replacing the square root in (2.71) with its approximated value (2.73), we obtain the two following values of the angular velocity of precession:

$$\dot{\psi}_{e1}^o \cong \frac{Gx_{3C}'''}{I_{X_1'''}\omega_o}, \qquad \dot{\psi}_{e2}^o \cong \frac{I_{X_1'''}\omega_o}{\left(I_{X_1'''} - I_{X_3'''}\right)\cos\vartheta_e^o}. \tag{2.74}$$

The obtained expressions are two kinds of precession: precession of the first kind (*slow precession*) $\dot{\psi}_{e1}^o$ and precession of the second kind (*fast precession*) $\dot{\psi}_{e2}^o$.

The determined quantities $\dot{\psi}_e^o$, ω_o and ϑ_e^o can be considered initial conditions for equations of motion of the Lagrange gyroscope (2.63). Given these initial conditions and assuming that the motion of the body differs slightly from the regular precession $(\vartheta_e = \vartheta_e^o + \Delta\vartheta_e,$ where $\Delta\vartheta_e$ is sufficiently small), (2.63) govern the vibrations of a rigid body about the operation position (stationary), which is the regular precession described previously. The aforementioned vibrations have bounded amplitude and high frequency. The vibrations are called *nutation vibrations*. Thus, we have a superposition of fast vibrations (nutation) and slow vibrations (regular precession). This situation is depicted in Fig. 2.19.

In this figure, a path is drawn (on a sphere with its center at point O) by the intersection point of the axis OX_3''' of the eigenrotations and the sphere. The aforementioned track describes a spherical curve lying between two horizontal circles having the shape shown in Fig. 2.19. At large value of the gyroscope rotations, the nutation angle ϑ_e takes on small values, and consequently the gyroscope motion differs slightly from a regular precession. For this reason, the motion of the gyroscope for this case is called a *pseudoregular precession*.

2.2.4 The Kovalevskaya Case of Spherical Motion of a Rigid Body

Until the end of the nineteenth century, cases of spherical motions of a rigid body, investigated by Euler and Lagrange, had been the only ones, where (2.22) and (2.23) had been completely solved. The main problem remained finding the fourth first

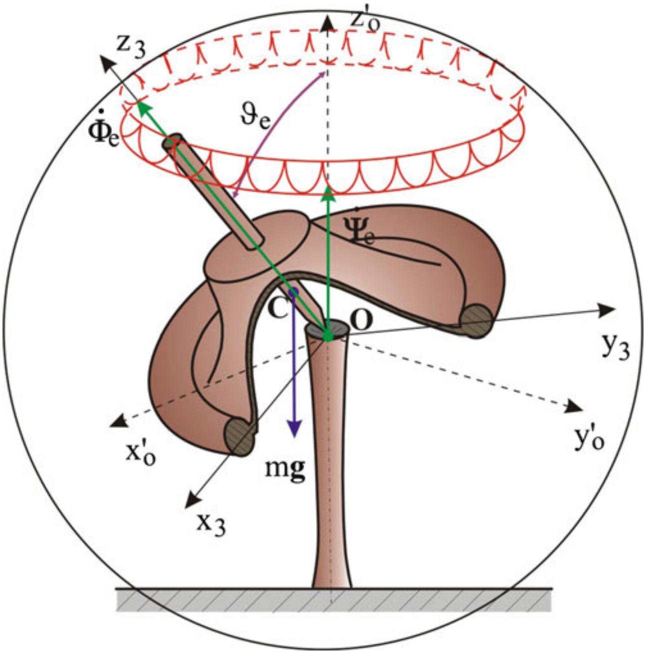

Fig. 2.19 Pseudoregular precession

integral of the Euler–Poisson equations. As was already mentioned, the three first integrals had been already determined: the trivial one $\gamma_1^2 + \gamma_2^2 + \gamma_3^2 = 1$, the energy integral $2T^2 =$ const, and the angular momentum integral $K_o^2 =$ const.

The Kovalevskaya[1] investigations showed that the fourth integral existed only for the Euler, Lagrange, and Kovalevskaya cases (i.e., for $I_{X_1'''} = I_{X_2'''} = 2I_{X_3'''}$, $x_{3C}''' = 0$) (Fig. 2.20).

Let us write the Euler–Poisson equations for the Kovalevskaya case, where the axes OX_1''' and OX_2''' are selected in a way that (we can always do this) the center of inertia lies on the axis OX_1''', hence $I_{X_1'''} = I_{X_2'''} = 2I_{X_3'''}$, $x_{2C}''' = x_{3C}''' = 0$, $x_{1C}''' = a$. Thus, we have the following system of equations:

$$2\frac{\mathrm{d}\omega_{eX_1'''}}{\mathrm{d}t} - \omega_{eX_2'''}\omega_{eX_3'''} = 0, \tag{2.75a}$$

$$2\frac{\mathrm{d}\omega_{eX_2'''}}{\mathrm{d}t} + \omega_{eX_3'''}\omega_{eX_1'''} = \overline{G}\gamma_3, \tag{2.75b}$$

---

[1] Sofia Kovalevskaya (1850–1891), Russian mathematician.

Fig. 2.20 Kovalevskaya case

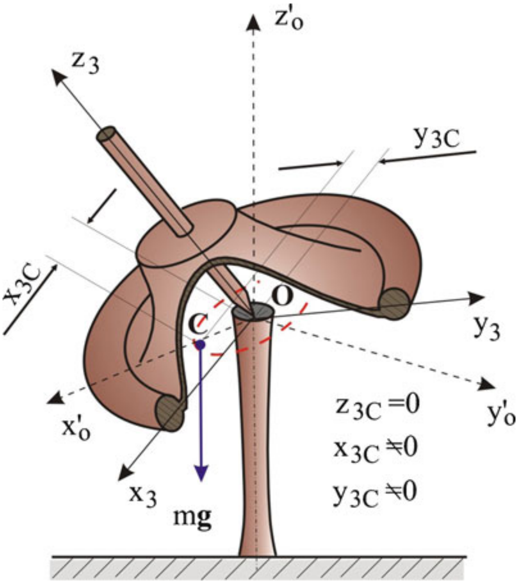

$$\frac{\mathrm{d}\omega_{eX_3'''}}{\mathrm{d}t} = -\overline{G}\gamma_2, \tag{2.75c}$$

$$\frac{\mathrm{d}\gamma_1}{\mathrm{d}t} = \omega_{eX_3'''}\gamma_2 - \omega_{eX_2'''}\gamma_3, \tag{2.76a}$$

$$\frac{\mathrm{d}\gamma_2}{\mathrm{d}t} = \omega_{eX_1'''}\gamma_3 - \omega_{eX_3'''}\gamma_1, \tag{2.76b}$$

$$\frac{\mathrm{d}\gamma_3}{\mathrm{d}t} = \omega_{eX_2'''}\gamma_1 - \omega_{eX_1'''}\gamma_2, \tag{2.76c}$$

where $\overline{G} = Ga/I_{X_3'''}$.

The preceding system of equations has three classic integrals, and we obtain them as in the Euler case. Besides the trivial integral $\gamma_1^2 + \gamma_2^2 + \gamma_3^2 = 1$, we have the energy integral

$$\frac{1}{2}\left(I_{X_1'''}\omega_{X_1'''}^2 + I_{X_2'''}\omega_{X_2'''}^2 + I_{X_3'''}\omega_{X_3'''}^2\right) + Ga\gamma_1 = \text{const} \tag{2.77}$$

and the angular momentum integral

$$I_{X_3'''}\left(\omega_{X_1'''}\gamma_1 + \omega_{X_2'''}\gamma_2 + \omega_{X_3'''}\gamma_3\right) = \text{const.} \tag{2.78}$$

We will determine the fourth integral in the following way. Let us introduce new variables

$$x_1^1 = \omega_{eX_1'''} + \mathrm{i}\omega_{eX_2'''}, \tag{2.79a}$$

$$x_1^2 = \gamma_1 + \mathrm{i}\gamma_2, \tag{2.79b}$$

where $\mathrm{i} = \sqrt{-1}$.

Let us multiply (2.75b) by i and sum up both sides with (2.75a). Then we obtain

$$2\dot{x}_1^1 + \mathrm{i}\omega_{eX_1'''}x_1^1 = \mathrm{i}\overline{G}\gamma_3. \tag{2.80}$$

Following similar manipulations in the first two equations of system (2.76), we find

$$\dot{x}_1^2 + \mathrm{i}\omega_{eX_1'''}x_1^2 = \mathrm{i}x_1^1\gamma_3. \tag{2.81}$$

Dividing both sides of (2.80) and (2.81) by each other, we obtain

$$2\dot{x}_1^1x_1^1 + \mathrm{i}\omega_{eX_1'''}(x_1^1)^2 - \overline{G}\dot{x}_1^2 - \mathrm{i}\overline{G}\omega_{eX_1'''}x_1^2 = 0. \tag{2.82}$$

Following simple manipulations we obtain

$$\frac{\mathrm{d}}{\mathrm{d}t}\left((x_1^1)^2 - \overline{G}x_1^2\right) + \mathrm{i}\omega_{eX_1'''}\left((x_1^1)^2 - \overline{G}x_1^2\right) = 0, \tag{2.83a}$$

$$\frac{\mathrm{d}}{\mathrm{d}t}\ln\left((x_1^1)^2 - \overline{G}x_1^2\right) = -\mathrm{i}\omega_{eX_1'''}. \tag{2.83b}$$

The equation conjugate to (2.83b) has the following form:

$$\frac{\mathrm{d}}{\mathrm{d}t}\ln\left(\left(\overline{x_1^1}\right)^2 - \overline{G}\,\overline{x_1^2}\right) = \mathrm{i}\omega_{eX_1'''}. \tag{2.84}$$

Adding both sides of (2.83a) and (2.83b), we have

$$\frac{\mathrm{d}}{\mathrm{d}t}\ln\left[\left((x_1^1)^2 - \overline{G}x_1^2\right)\left(\left(\overline{x}_1^1\right)^2 - \overline{G}\,\overline{x_1^2}\right)\right] = 0. \tag{2.85}$$

Equation (2.85) implies that

$$\left((x_1^1)^2 - \overline{G}x_1^2\right)\left(\left(\overline{x_1^1}\right)^2 - \overline{G}\,\overline{x_1^2}\right) = \text{const.} \tag{2.86}$$

Going back in (2.79) to the original variables, we obtain the desired fourth first integral:

$$\left(\omega_{eX_1'''}^2 - \omega_{eX_2'''}^2 - \overline{G}\gamma_1\right)^2 + \left(2\omega_{eX_1'''}\omega_{eX_2'''} - \overline{G}\gamma_2\right)^2 = \text{const.} \tag{2.87}$$

Thus, the Kovalevskaya problem reduces to quadratures of the hyperbolic type. The character of motion of a body in the Kovalevskaya case is much more complex than in the Euler and Lagrange cases. For this reason, in these two latter cases, the general properties of motion of a rigid body were thoroughly examined, contrary to the Kovalevskaya case.

It should be emphasized that Kovalevskaya's investigations caused in the fall of the nineteenth and in the first half of the twentieth century a kind of competition among renowned mathematicians to find new solutions to the Euler–Poisson equations. As an example one can give the results of investigations of Russian mathematicians Nekrasov and Appelrot from Moscow. They gave the relations between moments of inertia and coordinates of the center of inertia of a body, at which it is possible to integrate the system of equations (2.22) and (2.23). The relations are as follows:

$$x'''_{2C} = 0, \quad x'''_{1C}\sqrt{I_{X'''_1}\left(I_{X'''_2} - I_{X'''_3}\right)} + x'''_{3C}\sqrt{I_{X'''_3}\left(I_{X'''_2} - I_{X'''_3}\right)} = 0.$$

For several decades, many outstanding scientists struggled with finding the fourth integral for another more general cases since (as was already mentioned) this would allow for the integration of the basic system of (2.22) and (2.23) by means of quadratures.

However, presently, this problem can be considered as historic since modern computers allow one to easily solve a full system of equations of spherical motion of any rigid body, with arbitrarily acting external forces. For this reason, the problem of determining the fourth integral has been out of date for a long time, but it remains open.

2.2.5 Essence of Gyroscopic Effect

For many centuries the lack of constraints maintaining the pivot point of a humming top at a fixed position relative to the base has blocked the practical application of the humming top.

The humming top maintains the orientation of the main axis *AA* in space only on a base with no angular movements (Fig. 2.21). If the base is inclined at the angle χ (Fig. 2.22), the humming top goes down under the action of the gravitational force $mg \sin \chi$.

The Cardan suspension (Foucault – 1852) allowed for the transformation of a humming top into a compact, axially symmetric rotor spinning freely about the so-called main axis (also called an eigenaxis) *AA* (Fig. 2.23) in an internal frame (ring). The internal frame was mounted by means of two bearings located in the *BB* axis of the external frame [9, 10].

Such a suspension provided to the rotor, along with the internal frame, makes it possible to rotate about the *BB* axis. An external frame was also mounted by means

Fig. 2.21 Humming top on a horizontal base

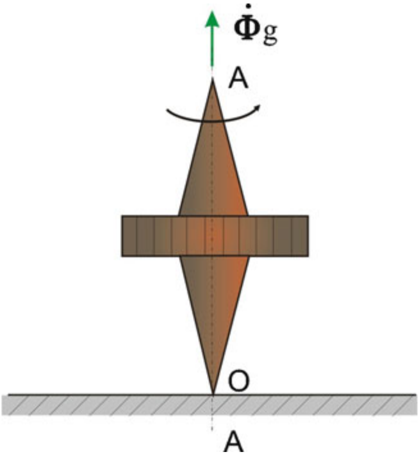

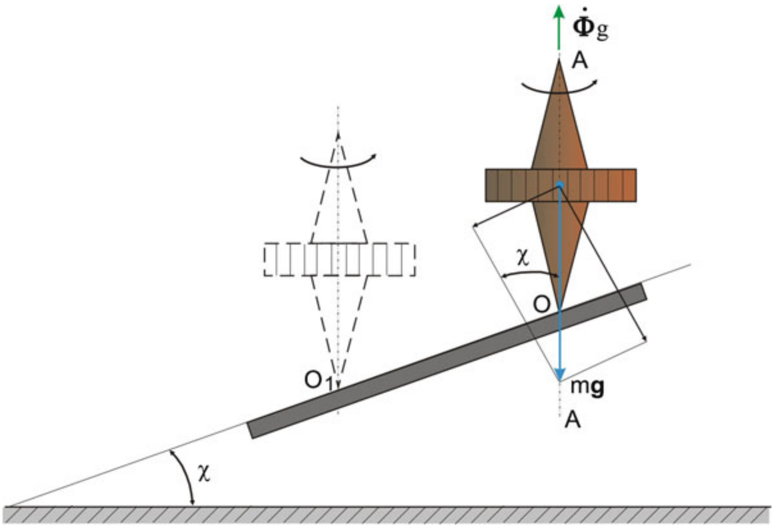

Fig. 2.22 Humming top on an inclined base

of two bearings, located on the *CC* axis, on the gyroscope base. In this way, the rotor, along with the internal and external frames, was given freedom of rotation about the external axis *CC* of suspension. Moreover, contrary to the case of the humming top, constraints imposed on support point *O* do not allow for displacement relative to the base.

Finally, a *gyroscope, in the technical sense, is a device in the form of a fast spinning rotor that rotates about an axis of symmetry and is suspended in a suspension (e.g., proposed by Foucault) and ensures free angular deviations relative to the base.*

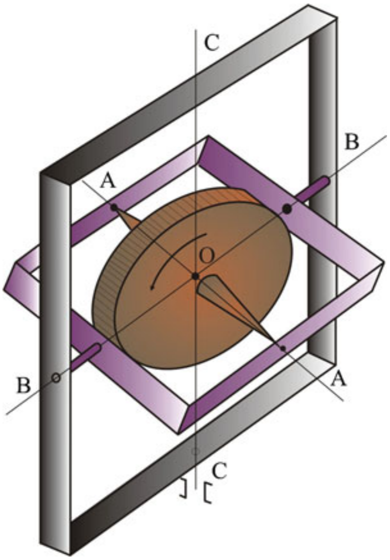

Fig. 2.23 Gyroscope in Cardan suspension

The gyroscopic effect of a fast spinning body relies on opposing any changes to its position in the space. For many centuries, the amazing phenomenon of the gyroscopic effect has seemed, to many observers, to contradict the fundamental laws of mechanics of the motion of bodies. We can observe these laws in the case of the effect of a force on the external frame of a gyroscope that attempts to turn the rotor about the *CC* axis and consequently move the main axis *AA* out of its initial position.

The external frame remains fixed, whereas the rotor with an internal frame starts to rotate about the *BB* axis. This anomaly in gyroscope motion can be explained by the fact that as the gyroscope axis changes its orientation, the Coriolis force occurs.

Let us consider, in more detail, the generation of the Coriolis force at the fast spinning gyroscope rotor about the axis OX_1''' at angular velocity $\boldsymbol{\omega}_o$ (Fig. 2.24) and simultaneously rotating about the axis OX_3''' at angular velocity $\boldsymbol{\omega}_1$. Thus in this case we are dealing with a compound motion of the rotor. Each point of the rotor participates in relative motion (rotational motion around the gyroscope axis) and in the drift motion (rotational motion about the axis OX_3'''). Then, the Coriolis acceleration will appear as a result of the drift velocity change in relative motion and the relative velocity change in drift motion.

Taking into account the fact that at an arbitrary instant of time, each material point n_i of the gyroscope rotor, distant from the axis OX_1''' at ρ_i, has a relative velocity $V_i = \omega_o \rho_i$ and angular velocity of drift ω_1 about the axis OX_3''', and its Coriolis acceleration reads

$$a_{ci} = 2\omega_o \rho_i \omega_1 \sin \Phi_i . \tag{2.88}$$

To make a material point of mass m_i accelerate with the above acceleration (2.89), one needs to apply an external force to it:

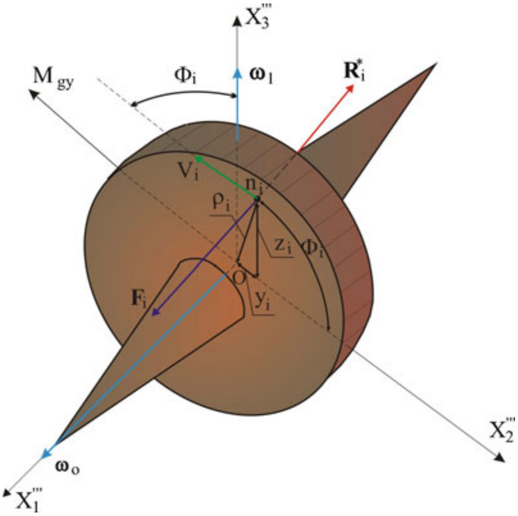

Fig. 2.24 Generation of gyroscopic moment

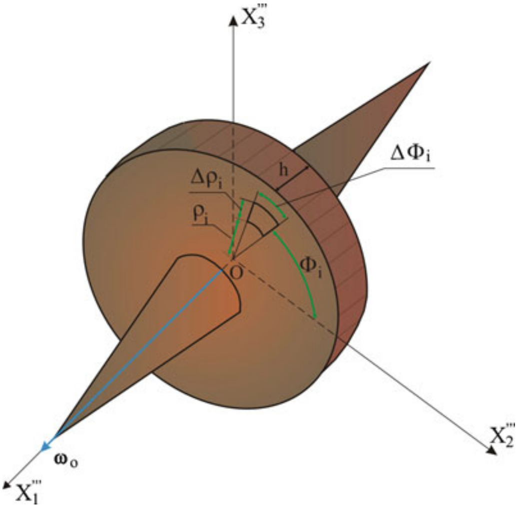

Fig. 2.25 Determining a gyroscope's mass

$$F_i = m_i a_{ci}\,. \tag{2.89}$$

Assuming, for the sake of simplicity, that the gyroscope rotor is disk-shaped and expressing the mass of the material point of the rotor as a product of volume and density d_r we obtain

$$m_i = d_r \Delta\rho_i \rho_i \Delta\Phi_i h, \tag{2.90}$$

where h denotes the width of the rotor disk. Substituting (2.88) and (2.90) into (2.89), we find the expression for an elemental Coriolis force (Figs. 2.24, 2.25):

$$F_i = 2 d_r \omega_0 \omega_1 h \rho_i^2 \Delta\rho_i \sin\Phi_i \Delta\Phi_i\,. \tag{2.91}$$

The inertial force $\boldsymbol{R}_i^*$ (Fig. 2.24), whose norm equals the norm of $\mathbf{F}_i$ and the opposite orientation, will oppose the Coriolis force (2.91). This force generates resistance torques relative to the two axes OX_2''' and OX_3''' of the form

$$M_{gx_2^i} = -R_i^* x_3^i = R_i^* \rho_i \sin \Phi_i , \tag{2.92}$$

$$M_{gx_3^i} = -R_i^* x_2^i = R_i^* \rho_i \cos \Phi_i . \tag{2.93}$$

Substituting $R_i^* = -F_i$ from (2.91), we obtain

$$M_{gx_2^i} = 2d_r \omega_0 \omega h \rho_i^3 \Delta\rho_i \sin^2 \Phi_i \, \Delta\Phi_i , \tag{2.94}$$

$$M_{gx_3^i} = 2d_r \omega_0 \omega h \rho_i^3 \Delta\rho_i \sin \Phi_i \cos \Phi_i \, \Delta\Phi_i . \tag{2.95}$$

The sum of the inertial moments values (2.94) and (2.95) for the whole rotor is as follows:

$$M_{gX_2} = 2d_r \omega_o \omega_1 h \int\limits_0^R \rho^3 \mathrm{d}\rho \int\limits_0^{2\pi} \sin^2 \Phi \mathrm{d}\Phi , \tag{2.96}$$

$$M_{gX_3} = 2d_r \omega_0 \omega_1 h \int\limits_0^R \rho^3 \mathrm{d}\rho \int\limits_0^{2\pi} \sin \Phi \cos \Phi \mathrm{d}\Phi , \tag{2.97}$$

where R is the radius of the gyroscope rotor.

Evaluating the integrals in (2.96) and (2.97) we obtain

$$M_{gX_2} = I_{go} \omega_o \omega_1 , \quad M_{gX_3} = 0 , \tag{2.98}$$

where $I_{go} = d_r \pi R^2 h \frac{R^2}{2} = m \frac{R^2}{2}$ is the moment of inertia of the rotor relative to the main axis OX_1'''.

It follows from the preceding considerations that if the external torque M_e about the axis OX_3''' is applied to a fast spinning rotor about the axis OX_1''', then the gyroscopic torque M_{gX_2} arises about the axis OX_2'''. In Fig. 2.24 one can observe that the gyroscopic moment attempts to rotate the rotor about the axis OX_2''' in such a way that the axis of its forced rotation OX_3''' will coincide with the main axis OX_1''' of the gyroscope in the shortest distance. The aforementioned operation of the gyroscopic moment will occur during the forced rotation of the rotor about an arbitrary axis that is not the main axis of the gyroscope.

Generally, one can apply the Zhukovski principle to determine the orientation of the gyroscopic moment $\mathbf{M}_\Gamma$, which is equal to

$$\mathbf{M}_\Gamma = I_{go} \boldsymbol{\omega}_o \times \boldsymbol{\omega}_1 , \tag{2.99}$$

where $\boldsymbol{\omega}_o$ is the angular velocity of eigenrotations of a gyroscope and $\boldsymbol{\omega}_1$ is the angular velocity of the forced rotation.

The principle states that making the rotor, which spins at the angular velocity $\boldsymbol{\omega}_o$ about the main axis *AA* (Fig. 2.23), rotate at the angular velocity $\boldsymbol{\omega}_1$ about any axis of those remaining (*BB* or *CC*) perpendicular to *AA*, a moment arises whose vector $\mathbf{M}_\Gamma$ is perpendicular to vectors $\boldsymbol{\omega}_o$ and $\boldsymbol{\omega}_1$ and indicates the direction in which the coincidence of vector $\boldsymbol{\omega}_o$ with $\boldsymbol{\omega}_1$ is performed on the shortest path counterclockwise.

Generally, one can state that the gyroscopic moment is a property of a gyroscope that is used to oppose the external torques attempting to change the position of its main axis in space. It is always generated in cases where a rotating body is attached to a movable base.

The law of precession, stated by *Foucault*, is as follows [5, 11, 12]:

As a result of the action of the external moment $\mathbf{M_o}$ exerted on a gyroscopic moment, the angular velocity vector of eigenrotations $\boldsymbol{\omega}_o$ and vector $\boldsymbol{\omega}_1$ obey the following formula

$$\omega_1 = \frac{M_o}{I_{go}\omega_o}. \tag{2.100}$$

It follows from (2.100) that the angular velocity ω_o of precession of a gyroscope is proportional to the value of the moment M_o of external forces. Thus, if there is no acting moment of external forces, then there is no precession motion of a gyroscope. The position of the gyroscope in such a case will remain unchanged (and thus stable) in space. Therefore, eliminating the influence of moments of external forces on a gyroscope, by putting it in Cardan rings (Fig. 2.23), the main axis will preserve its initial position independently of displacements, velocities, and accelerations of the base. The aforementioned property of the gyroscope has found application in various navigational instruments.

References

1. G.K. Suslov, *Theoretical Mechanics* (GOSTEKHIZDAT, Moscow/Leningrad, 1946), in Russian
2. J. Awrejcewicz, *Classical Mechanics: Kinematics and Statics* (Springer, Berlin, 2012)
3. J. Awrejcewicz, *Classical Mechanics: Dynamics* (Springer, Berlin, 2012)
4. L.G. Loytsyanskiy, A.I. Lurie, *Lectures on Theoretical Mecahanics. Part 2. Dynamics* (OGIZ, Leningrad, 1948), in Russian
5. V.A. Pavlov, *Aviational Giroscopic Devices* (GOSIZDAT of the Russian Defence Industry, Moscow, 1954), in Russian
6. V.N. Koshlyakov, *Problems of Solid Body Dynamics and Applied Theory of Gyroscopes* (Nauka, Moscow, 1985), in Russian
7. A.M. Lestev, *Nonlinear Gyroscopic Systems* (LGU, Leningrad, 1983), in Russian
8. V.Ph. Zhuravlev, D.M. Klimov, *Hemispherical Resonator Gyro* (Nauka, Moscow, 1985), in Russian.
9. J.B. Scarborough, *The Gyroscope: Theory and Application* (Interscience, New York, 1958)
10. A.Yu. Ishlinskii, *Mechanics of Gyroscopic Systems*. (English translation of Russian edition) (Oldbourne, London, 1965)
11. M.A. Pavlovskiy, T.B. Putiaga, *Theoretical Mechanics* (Vyshaya Shkola, Kiev, 1985), in Russian
12. M.A. Pavlovskiy, *Theory of the Gyroscope* (Vyshaya Shkola, Kiev, 1985), in Russian

Chapter 3
Theory of Gyroscopes

In this chapter, first a historical outline of the theory of gyroscopes is given. Elements of gyroscope classification are introduced, and then the evolution of the gyroscope concept is presented. In particular, the following gyroscope-type devices are considered: the directional gyroscope, the gyroscopic vertical, the stabilized gyroscopic platform, the laser gyroscope, the fiber-optic gyroscope, the piezoelectric gyroscope, the fork gyroscope, and the microgyroscope with a spinning disk and with a vibrating ring. Examples of devices for gyroscopic navigation and an observation device with a built-in gyroscope are provided. Finally, new challenges for gyroscopes are briefly summarized.

3.1 Elements of Gyroscope Classification

Presently, one can distinguish many types of gyroscope with regard to accepted criteria. Mostly, one classifies gyroscopes by the following criteria [1–3]:

1. Principle of operation:
   (a) Mechanical
   (b) Laser
   (c) Nuclear
2. Number of degrees of freedom of a gyroscope rotor:
   (a) One degree of freedom (one-step)
   (b) Two degrees of freedom (two-step)
   (c) Three degrees of freedom (three-step)
3. Type of suspension:
   (a) With Cardan suspension (external and internal)
   (b) Without Cardan suspension

J. Awrejcewicz and Z. Koruba, *Classical Mechanics*, Advances in Mechanics and Mathematics 30, DOI 10.1007/978-1-4614-3978-3_3,

4. Mutual position of intersection points of suspension axis (center of suspension) and center of rotor mass:
   (a) Astatic (center of suspension coincides with center of mass)
   (c) Non-static ("heavy")
5. Cardan-free (spherical mostly) gyroscopes with respect to suspension type:
   (a) Gasostatic
   (b) Gasodynamic
   (c) Floating
   (d) Electromagnetic
   (e) Electrodynamic
   (f) Cryogenic
6. Type of rotor:
   (a) With stiff rotor
   (b) With an elastic rotor
   (c) With liquid rotor
7. Constraints imposed on the rotor by the suspension:
   (a) Integrating
   (b) Differentiating
8. Dynamically tuned gyroscopes with respect to mutual ratio of centrifugal and elastic torques.

Generally, we can divide gyroscopes into three large classes (Fig. 3.1): (1) sensor, (2) navigation, (3) force.

Sensor gyroscopes are used as measuring devices and are located on a movable base. Navigation gyroscopes serve to determine a horizon plane and meridian. Force gyroscopes generate controlling torques in systems of angular stabilization and vibration damping (e.g., flatter types) and serve as stabilizing platforms in the targeting and tracking systems (e.g., cannons, missiles).

3.2 Evolution of Gyroscope Concept

In recent decades, the notion of the gyroscope has seen increasingly broader application. Presently, we call gyroscopes not only classical mechanical systems composed of a spinning rotor and elements of the rotor suspension, but also external devices that somewhat resemble the aforementioned mechanical system. In particular, in vibrating gyroscopes, the free motion of the rotor can take the form of translational or angular vibrations. A rotating or vibrating liquid can serve as a rotor in vibrating, hydrodynamical, or magnetohydrodynamical gyroscopes.

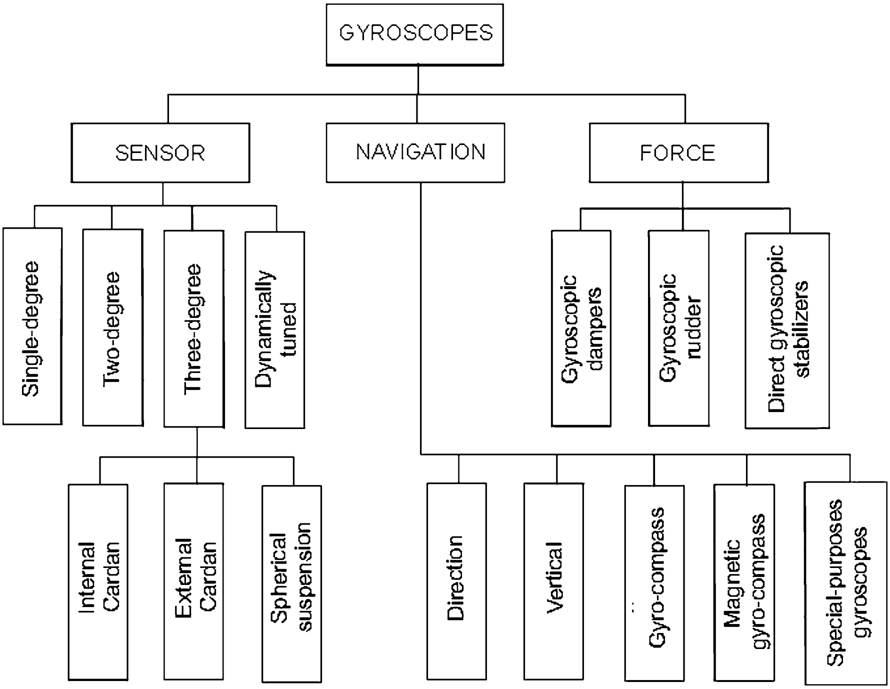

Fig. 3.1 Classification of gyroscopes

In molecular gyroscopes, carriers of angular momentum are particles—electrons, protons, neutrons, nuclei, or atoms. However, a general characteristic of gyroscopes, without regard to form, is that they contain angular momentum carriers.

The term “gyroscope” in recent decades has become increasingly broad. The word derives from the literal sense of an indicator of turns, rotation. Thus, by gyroscope we understand any device that allows one, e.g., without contact with the environment, to measure the rotation of a base relative to an inertial frame. Hence, we focus on gyroscopes such as optical, laser, and polarization gyroscopes and those based, e.g., on the interference of de Broglie waves of particles.

Initially, the concept of gyroscope was introduced by the French physicist Foucault as a name for a balanced, fast-spinning rotor in a uniaxial or biaxial Cardan suspension, incorporating the property of detection and measurement of rotations of a base. The name started to be applied as a general term for any device that had this property. In the literature, one can find nearly 100 physical phenomena that can be used to autonomously detect and measure turns, i.e., to build a gyroscope. In practical terms, just few of the physical phenomena are used. Until now, are applied the Foucault gyroscopes in a mechanical, stiff, fast-spinning rotor in a Cardan suspension. In order to unload bearings, one uses hydrostatic (floating) suspension.

Spherical gyroscopes with aerodynamic, electrostatic, and magnetic suspensions have gained widespread usage. The most modern solutions include gyroscopes with a cryogenic, magnetic suspension relying on superconductivity. A typical example of gyroscopes in the extended meaning of this notion, i.e., not having carriers of angular momentum, is a laser gyroscope. Nowadays, gyroscopic devices are used mainly on moveable objects such as airplanes, ships and submarines, rockets, and satellites. Their task is to navigate those objects and their orientation with respect to the assumed reference frame, stabilize the motion of an object relative to a given trajectory and automatically control this motion, and spatially stabilize devices located on-board a movable object.

3.3 Fundamental Stages of Gyroscope Development

The phenomenon of preserving the position in inertial space of a fast-spinning body around its symmetry axis was known in ancient times. For a long time, amazing feature (which seems at first glance to contradict the fundamental laws of nature) of a spinning body has not found its practical application. This feature was used only to build simple toys known as "humming tops." A humming top attracted the attention not only of children but of many outstanding scientists as well. It was Newton (1642–1727) who analyzed the behavior of a humming top for the first time. The theory of the gyroscope is based on a branch of mechanics dealing with the rotational motion of a rigid body around a fixed point. For this reason, the fundamentals of the theory of gyroscopes were studied along with the development of celestial mechanics. In the initial stages of the history of mechanics, was observed that spinning bodies were simply huge humming tops, having all the specific properties of spinning bodies. Research in the field of celestial mechanics was performed by L. Euler (1707–1783) (who created the theory of nutation of the Earth's axis and the theory of lunar libration), and his derivation of equations of the rotational motion of a rigid body around a fixed pivot point in the work *Theory of the Motion of Rigid Bodies*, published in 1765, became a fundamental contribution to the contemporary theory of gyroscopes. Further development of the theory of spinning bodies ensued in the works of Lagrange (1736–1813), Poinsot (1777–1859), and other brilliant scientists such as D'Alembert and Laplace, Kovalevskaya, Somov, Bobyliev, and Zhukovski [4–6].

The applied theory of gyroscopes, i.e., the theory of devices and gyroscopic systems, emerged mainly in the twentieth century; however, the first attempts at practical application of gyroscopes had been made much earlier.

In 1752 *Serson* suggested making use of a spinning body to obtain an "artificial horizon" on a ship [2]. Unfortunately, the attempt to apply this invention on the frigate *Victory* had a tragic end not only for the ship (which sank) but also the inventor himself. Thus, no attempt was made to apply a similar invention for the next hundred years, and the humming top remains merely a toy.

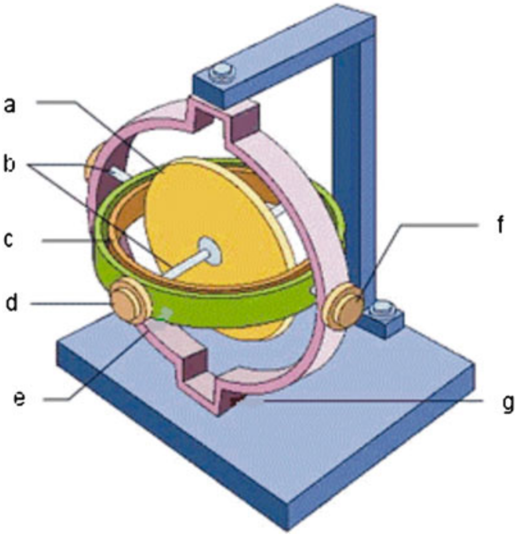

Fig. 3.2 Foucault gyroscope: (**a**) Rotor. (**b**) Spin axes. (**c**) Internal frame. (**d**) Internal joint. (**e**) External frame. (**f**) External joint. (**g**) Base

In the nineteenth century, *L. Foucault* decided to prove experimentally the existence of the Earth's rotation. To this end, he put a fast-spinning, axially symmetric body in a Cardan joint. He first presented the device (Fig. 3.2) at the meeting of the Paris Academy of Sciences in 1752 and called it a *gyroscope* (from the Greek *giros*, spinning, and *skopeo*, observe).

The French physicist investigated a gyroscope (gyro). However, not all the results were convincing due to technical difficulties, which were not overcome before the turn of the twentieth century. The main difficulties concerned the considerable friction in the bearings of the Cardan suspension rings and others related to the rotor drive's not allowing for a high and constant angular velocity to be maintained.

In those days an urgent need arose to build a device that could replace the magnetic compass because the operating conditions of the compass got worse on ships with steam engines and steal frames compared to the compass's operation on wooden sailboats. Foucault demonstrated the possibility of using a gyroscope to determine a meridional line at a given latitude [4]. Thus, the idea of a gyrocompass was presented for the first time. However, due to incorrect calculations on the value of period of free vibrations of the device and to technical difficulties, a gyrocompass that would be useful in practical applications could not be built sooner than in the early twentieth century. Since Foucault's experiments, the history of the development of gyroscopes has involved the continuous pursuit of lower disturbing torques that affect rotors and an increase in the angular velocity of gyroscopes.

In 1898, a lieutenant of the Austrian army, *Obri* [3], started using a gyroscope in practical applications. He built one with three degrees of freedom whose rotor was set in motion by means of the energy of compressed air. Slight friction in the Cardan suspension bearings was achieved with the application of ball bearings. Such a device was applied to stabilize a torpedo.

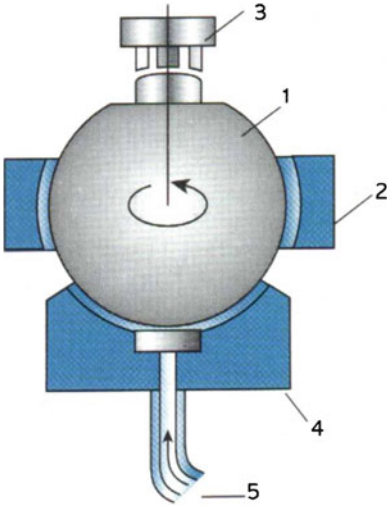

Fig. 3.3 Sperrs gyroscope: 1—steal rotor; 2—stator producing a rotational magnetic field; 3—sensor whose signals enable one to follow the ball axis on a swinging base (ship); 4—bronze bowl separated from rotor by layer of air of micrometer width; 5—inflow of compressed air suspending gyroscope

In 1905, the German engineer *Herman Anschütz Kaempfe* patented a gyrocompass, which was tested in practice. A few years later, in 1911, an American, *Elmer Sperry*, built another type of gyrocompass (Fig. 3.3). Thanks to continual improvements in these types of compass, they have been used on warships for many years [5, 6].

When *Zhukovski*'s works were published in 1912, new possibilities in the application of gyroscopic devices appeared [4, 6]. Zhukovski proposed mounting a gyroscope in an airplane in order to improve stability of flight. In that case, a gyroscope served as an actuator, by means of which controlling and damping torques were produced. In the 1920s, Soviet inventor *S.A. Nozdrovskiy* worked out a system for a gyroscopic stabilizer. Presently, gyroscopic actuators are widely applied in systems of angular stabilization of spaceships.

Gyroscopic tachometers were initially used in aeronautics as indicators of turn, and then in artillery of naval guns to determine the angle of shot lead. They found very wide applications in control systems of flying objects (automatic pilot), in gyroscopic stabilizers, and in systems of indirect stabilization. As aviation developed, vertical gyroscopes and course gyroscopes were commonly used as pilotage instruments, necessary for blind flights, i.e., flights without any visual external reference on the ground.

Integrating gyroscopes have been widely applied since no earlier than the second half of the twentieth century in the form of floating-integrating gyroscopes, which allowed one to obtain small drifts of the gyroscope axis.

In 1963, *E.W. Howe* worked out a gyroscope called a *dynamically tuned gyro*, or a gyroscope with an elastic suspension [7, 8].

The rotor of such a gyroscope is suspended on a Cardan joint (Fig. 3.4), where there is no bearing of the frame joint, which is made of elastic elements [9–11], e.g., torsion bars (Fig. 3.5).

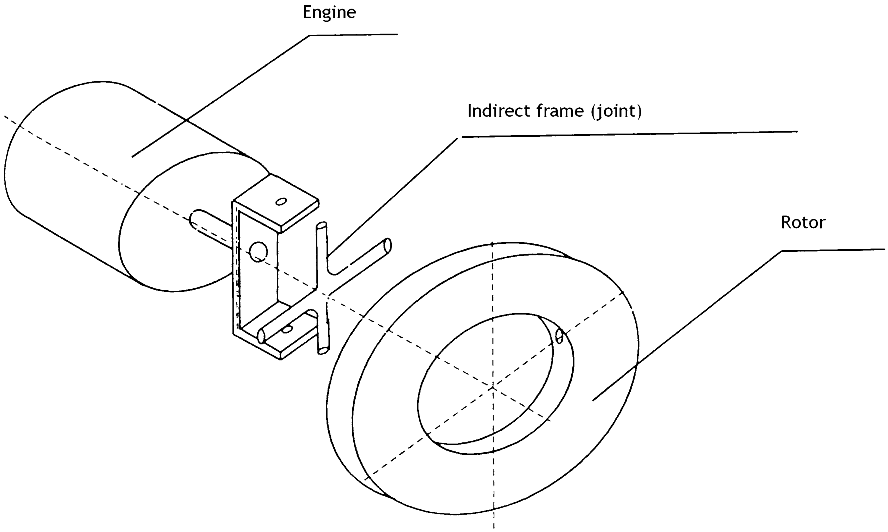

Fig. 3.4 Gyroscope with a rotor suspended on a Cardan (Hooke) joint

Fig. 3.5 Dynamically tuned gyroscope

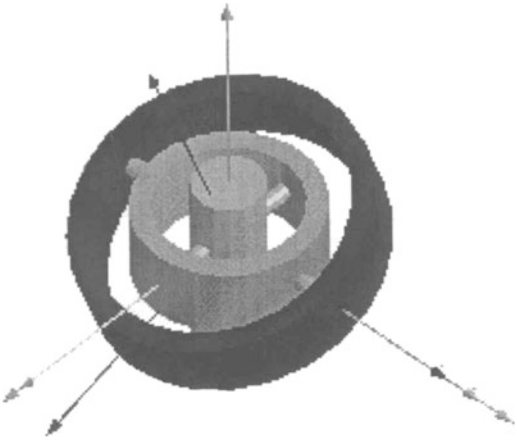

However, in his gyroscope, Zhukovski made use of the dynamical effects of inertia of a Cardan suspension frame to eliminate the elastic torques of torsion bars. It has become one of the most commonly produced velocity gyroscopes. It finds application mainly as a sensor in autonomous orientation referencing systems, inertial navigation, and stabilization of various objects such as aerial, marine, and land objects.

Presently, a free gyroscope enjoys the most common usage in navigation instruments.

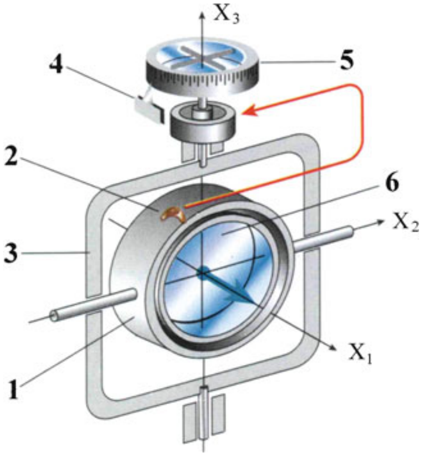

Fig. 3.6 Schematic diagram of a course gyroscope [8]:
1—internal frame;
2—gravitational sensor;
3—external frame;
4—pointer; 5—course disk;
6—gyroscope rotor

3.3.1 *Directional Gyroscope*

This is an on-board instrument used to determine the course of a flying object (FO). A fundamental element of the device is a gyroscope of three degrees of freedom with a main axis lying in the plane of horizon (Fig. 3.6). The axis of the external frame is perpendicular to the plane of the FO board. A directional gyro does not determine a constant direction (e.g., northern), but it can maintain an arbitrarily chosen direction, which can be regarded as a reference direction.

A correction system for the device is composed of a gravitational sensor and a corrective engine. Its objective is to maintain the rotor axis in the horizontal plane. As the course of the FO changes, the external frame moves relative to the gyroscope body. A disk with an angular scale on it allows one to read the change in the FO's course relative to the fixed stroke in the case window. In early solutions (despite the corrective systems), deviation of the gyroscope axis off the given position was even 15° per hour. Nowadays, this deviation can be only 0.5° per hour in improved systems.

3.3.2 *Gyroscopic Vertical*

This is an on-board device to measure the deviation of the FO off the horizontal and vertical planes. Its main element is a gyroscope of three degrees of freedom whose rotor axis is set vertically and suspension-frame axes are placed according to the tilt and inclination axes of the FO (Fig. 3.7).

Gravitational sensors, located on the gyroscope body (internal frame), measure the angular deviation of the angular momentum axis off the vertical and make the

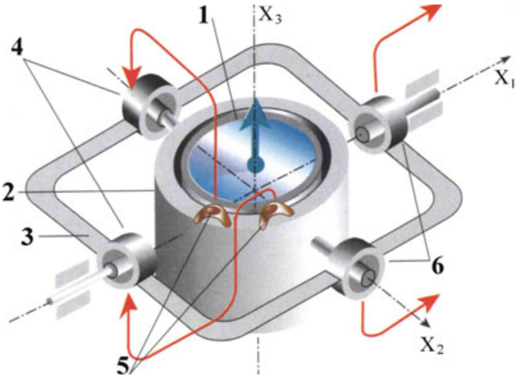

Fig. 3.7 Scheme of gyroscopic vertical [8]: 1—rotor; 2—internal frame; 3—external frame; 4—torque engines; 5—gravity sensors; 6—selsyns (angular position sensors)

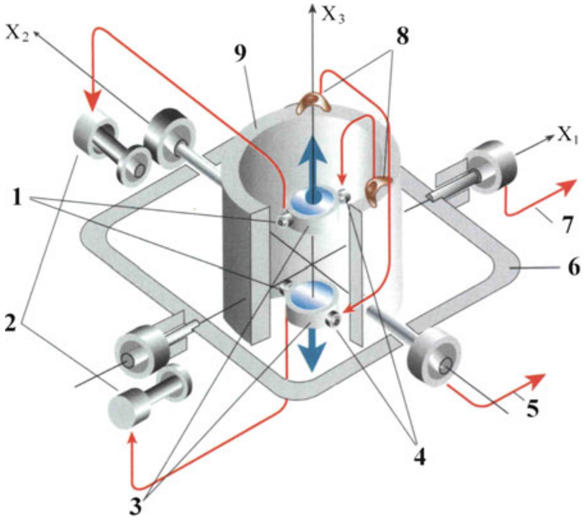

Fig. 3.8 Schematic diagram of a biaxial stabilized gyroscopic platform [8]: 1—angular position sensors; 2—correction engines; 3—internal frames; 4—torque engines; 5—inclination angle signal; 6—external frame; 7—tilt angle signal; 8—gravitational sensors; 9—stabilized element (platform)

correcting engines operate. The engines make the gyroscope move in precession, which eliminates deviations. Changes in the angular position of the FO are measured by selsyns or other sensors placed on the axes of both frames.

3.3.3 Stabilized Gyroscopic Platform

This is an on-deck device to precisely measure the vertical and course or simultaneously to measure the vertical and course of an Flying Object (FO). A biaxial stabilized, gyroscopic platform (Fig. 3.8) acts as a gyroscopic vertical. Two gyroscopes of two degrees of freedom are placed such that the axes of their suspension frames are mutually perpendicular and parallel to the axis of the platform and external frame of the platform suspension, respectively, while the axes of the

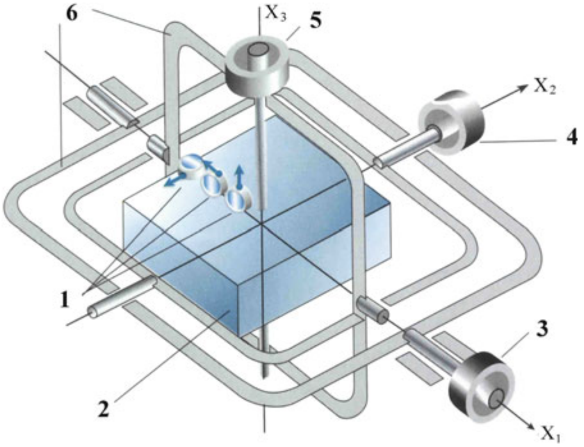

Fig. 3.9 Schematic diagram of four-axial stabilized gyroscopic platform [12] (www.docstoc.com/docs/19589480/Gyroscope.htm): 1—gyroscopes of two degrees of freedom; 2—stabilized elelement (platform); 3—tilt sensor; 4—inclination sensor; 5—course angle sensor; 6—suspension frames

gyroscope's rotors coincide with the vertical axis of the system. Maintaining the axes of rotors in the vertical position is ensured by a corrective device composed of a gravitational sensor and correcting engine. Precession of the gyroscopes generated by disturbing torques on the suspension axes is compensated by torques generated by sensors of inclination connected with corrective engines. Selsyns (or another sensor of angular position) placed on the axes of the platform and external frame produce output signals of tilt and inclination angles.

One can obtain complete information about the spatial position of the FO without angular limitations by means of a four-axial stabilized gyroscopic platform (Fig. 3.9).

The FO can rotate without disturbing the position of the stabilized element, in which there are three gyroscopes of two degrees of freedom such that their measuring axes are parallel to the axes X_1, X_2, X_3 of the system. Sensors of angular position on the axes X_1, X_2, X_3 generate tilt and inclination signals of the course, respectively.

3.3.4 Laser Gyroscope

The most modern solutions include an optical gyroscope, which makes use of the phenomenon of change in the propagating light wave. With regard to the lack of mechanical systems, optical gyroscopes are insensitive to rapid maneuvres and experience neither precession nor blocking. In early constructions of optical gyroscopes, there was a blurring of the fiber-optic block, which made the system life shorter, to about a year. Presently produced optical gyroscopes have a service life of about 60,000 h. They are able to measure angular velocities from 0.1°perhour to several hundreds of degrees per second.

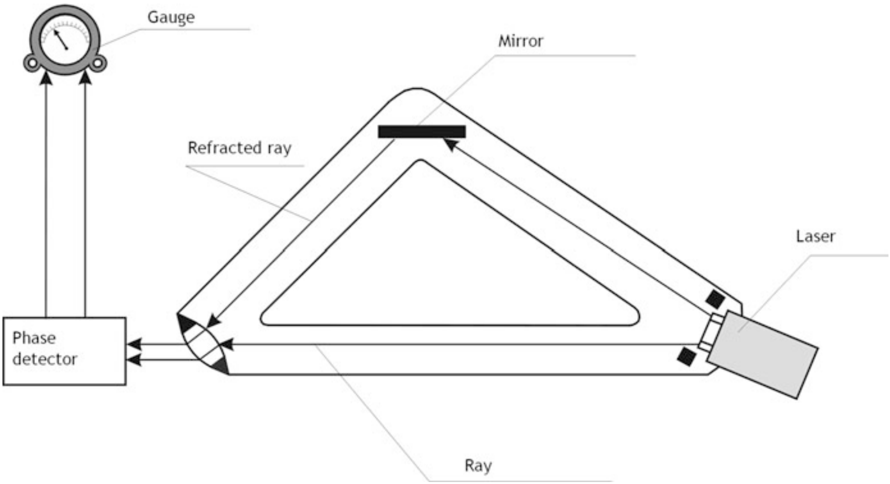

Fig. 3.10 Principle of operation of a laser gyroscope (www.meos.com/Laser_Metrology/laser_gyroscope.htm)

Optical gyroscopes can be classified as (1) laser and (2) fiber optic (www.alphapiezo.com/ring_laser_gyroscope.htm). The most typical example is the *laser gyroscope*, in which coherent light beams from a laser circulate a toroidal resonator in opposite directions. A rotation of the device in the resonator plane makes the frequency in both beams change in accordance with the Doppler effect. The frequency of the beam circulating the resonator in the direction coincident with the rotation decreases and increases in the opposite direction. The sensitivity difference is proportional to the angular velocity. In a photodetector, placed in the output of the system, one obtains a difference signal as a result of the coincidence of both bands. This signal can be used for navigation purposes.

In a laser gyroscope, one applies the method of comparing phases of laser rays running in a triangular fiber optic (Fig. 3.10). The phases of a linear and refracted ray are compared by a detector, transmitting a signal that is proportional to the difference of these phases. When the base of a gyro does not change its position, then the phases of both rays are identical and the pointer points to zero. At the moment of position change, rays of distinct phases reach the detector and the gauge shows the angular velocity of this change.

3.4 Fiber-Optic Gyroscope

Another example of an optical gyroscope is a fiber-optic one, which contains long optical fibers, wound in a coil, that make the instrument more sensitive [8] (www.alphapiezo.com/ring_laser_gyroscope.htm).

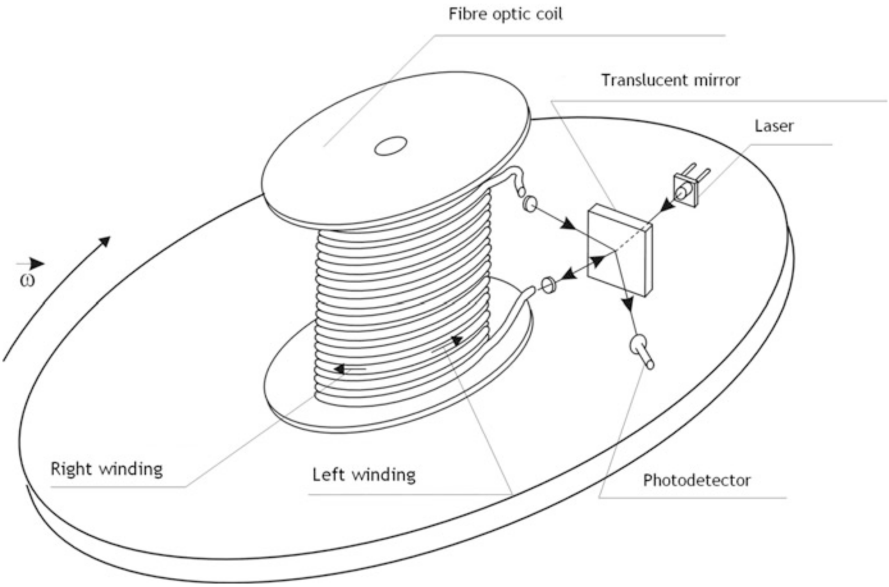

Fig. 3.11 Fiber-optic gyroscope scheme

In a fiber-optic gyroscope (Fig. 3.11), the sensitivity limit is lowered due to resonance phenomena. One measures the difference between the distances traveled by the ray in the left and right fiberglass. During coil rotation, a phase shift appears between the light rays, and when they are superposed on a half-transparent mirror, the resultant force of light follows changes in the angular velocity. The larger the coil area, the larger the phase shift, and sensitivity grows as the number of coils increases. This method is passive since an independent laser source is used. This device allows one to measure angular velocities up to $10^{-8}\mathrm{rad/s}$.

3.5 Piezoelectric Gyroscope

A modern vibrating piezoelectric gyroscope is designed and produced on a quartz crystal. The principle of operation is based on making use of vibrations, which increase the thickness of piezoelectric materials. Trihydrate lead acetate is a fundamental compound used to produce these gyroscopes. A thin layer of this compound is coated on the substrate Pt/Ti/SiO_2/Si.

The final steps in assembling a piezoelectric gyroscope are depicted in Fig. 3.12. A thin layer of Lead Zirconate Titanate (LZT) is coated on the substrate by means of a sol-gel method. PZT is coated layer by layer, by rotating at high velocity, on a titanium/platinum electrode at $3,500°\mathrm{C}$ for 20 s. Next, it is annealed at a temperature of $700°\mathrm{C}$ for 3 h to increase strength and crack toughness. After this process, on the

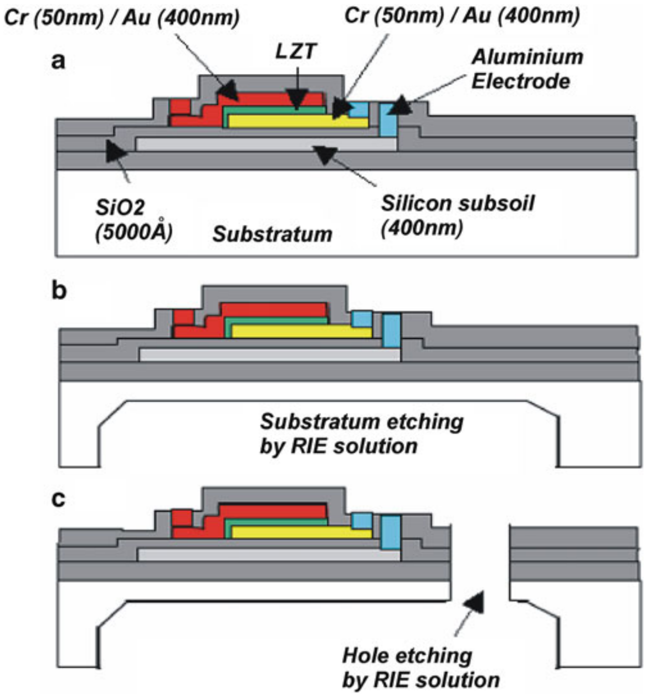

Fig. 3.12 Manufacturing a piezoelectric gyroscope (www.microstrain.com/3dm-gx1.aspx.)

layer LZT is sprayed layer of chromium/silver. It is the top electrode. The whole structure undergoes oxidization and pickling to obtain a suitable structure so that the gyroscope can operate.

The top view of four sensors of a piezogyroscope is shown in Fig. 3.13, where F_1 denotes the force caused by vibrations of the central mass and F_2 is the Coriolis force. Each sensor of dimension $388 \times 800\mu$m possesses a middle layer of a piezoelectric material, PZT, and top and bottom electrodes.

If we apply a signal of a particular frequency to the IN port, we obtain the piezoelectric effect. Sensors 1 and 3 start to vibrate at a frequency that is equal to the frequency of the input signal and make the central mass vibrate. The frequency of its vibrations is the same as that of elements 1 and 3.

A gyroscope is situated parallel to the X_1X_3 plane and set in rotational motion around the X_3 axis. Then, piezoelectric elements 2 and 4 experience cyclic changes in velocity in the X_2 direction. The Coriolis force, acting in the X_1 direction, is generated as a result of changes in the vibrations and angular velocity and has the form

$$\mathbf{F}_C = 2m\mathbf{V}_{X_1} \times \boldsymbol{\Omega}\,. \tag{3.1}$$

In (3.1) m is the mass of the central element. The Coriolis force can be regarded as a shear force in sensors plates 2 and 4, acting in the X_1X_3 plane and in the

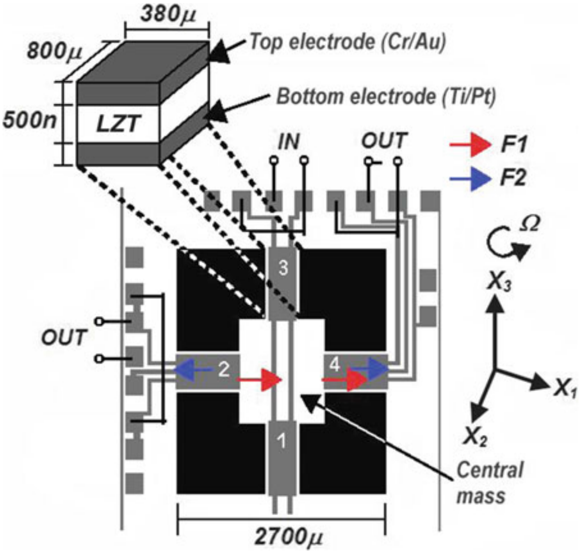

Fig. 3.13 Principle of operation of a piezoelectric gyroscope (www.microstrain.com/3dm-gx1.aspx.)

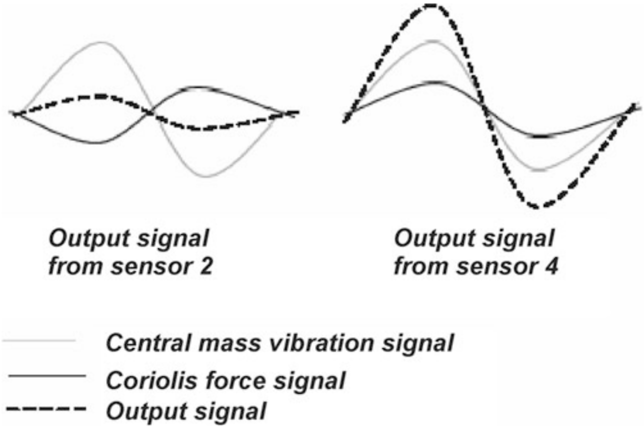

Fig. 3.14 Principle of operation of a piezoelectric gyroscope (www.microstrain.com/3dm-gx1.aspx.)

X_1 direction. It cause the emergence of an electric field that acts in the X_2 direction. Thus, a voltage appears on electrodes of elements 2 and 4. Since the output signal is a consequence of the Coriolis force, its frequency is exactly the same as the frequency of vibrations of a central mass, which is equal to the frequency of the output signal.

Two output sensors give two different signals, depending on the value of the angular velocity. The Coriolis force is generated in sensor 2 (Fig. 3.14) in the positive direction and in sensor 4 in the opposite direction. Two output signals, generated in sensors 2 and 4 are depicted in the Fig. 3.14.

The output signal, generated by vibrations of sensor 2, is in the same phase as the signal coming from the vibrating mass. While the amplitude of the output signal decreases as the angular velocity increases, the amplitude of the output signal in sensor 4 increases as the angular velocity grows.

3.6 Fork Gyroscope

These are electromechanic gyroscopes assembled on a silicon crystal with vibrating forks. They are driven by electrostatic force, while the Coriolis force is read as a change in the capacitance of the microcapacitors. Additionally, the module contains capacitors that measure feedback forces and for voltage application fix the resonance frequency of the forks.

Two separate masses A and B (Fig. 3.15), connected with the frame, will be excited by an electrostatic force after voltage is applied to electrode C, and they will in the X_1 direction. Their motion is guided by combs. The angular velocity in the X_2 direction will force the plate to vibrate, and the vibrations will be detected. The forks are affixed to supports D and E. The external electrodes F and G are used to control the amplitude and phase of mechanical vibrations. Three plates of the capacitor are located in the masses A and B to measure the Coriolis force (signal of the gyroscope effect) for the feedback force and for voltage application to fix the twisting resonance frequency.

A rotation relative to the axis perpendicular to the gyroscope generates the Coriolis force, which is perpendicular to the plane of the fork module. This force makes the masses move in the X_1 direction (Fig. 3.16). It causes changes in volume

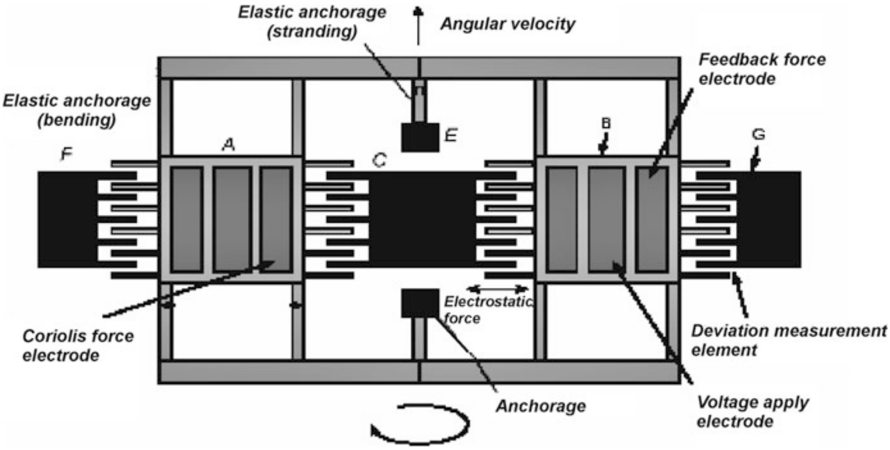

Fig. 3.15 Principle of operation of a fork gyroscope [8] (www.microstrain.com/3dm-gx1.aspx.)

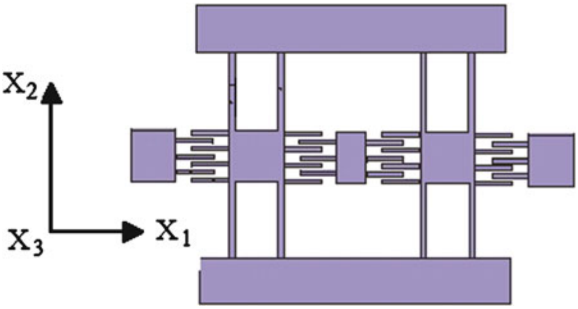

Fig. 3.16 Coriolis force in a fork gyroscope [8] (www.microstrain.com/3dm-gx1.aspx.)

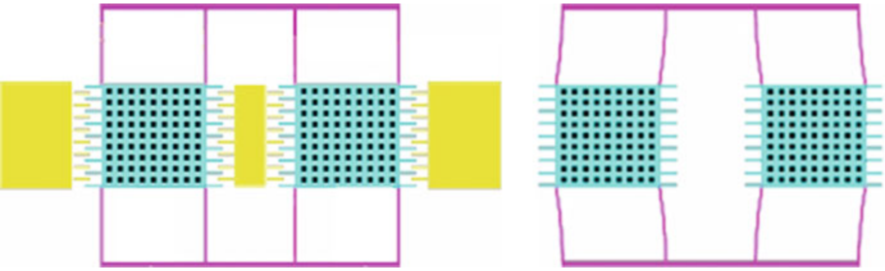

Fig. 3.17 Generation of the gyroscope effect [8] (www.microstrain.com/3dm-gx1.aspx.)

between the forks of mass and the frame. Thus, the amplitude of the vibrating-fork displacements is a basis for determining of the gyroscopic effect (Fig. 3.17).

3.7 Microgyroscope with a Spinning Disk

These gyroscopes possess a thin, magnetic levitating disk that spins at very high angular velocity. This high spinning velocity allows it to attain the gyroscope effect. When a sensor rotates at constant angular velocity with respect to an arbitrary axis, levitation forces make the disk move in precession, and it inclines at some angle. The inclination is proportional to the speed of rotation of the gyroscope (Fig. 3.18).

3.8 Microgyroscope with Vibrating Ring

A microgyroscope with a vibrating ring is composed of a ring, eight semicircular spring supports, and leading, detecting, and controlling electrodes (Figs. 3.19 and 3.20).

The symmetric structure of the gyroscope requires applying at least eight elastic supports to keep the ring in equilibrium. The ring is subject to the action of two elliptically shaped bending waves. The vibration ring is excited electrostatically.

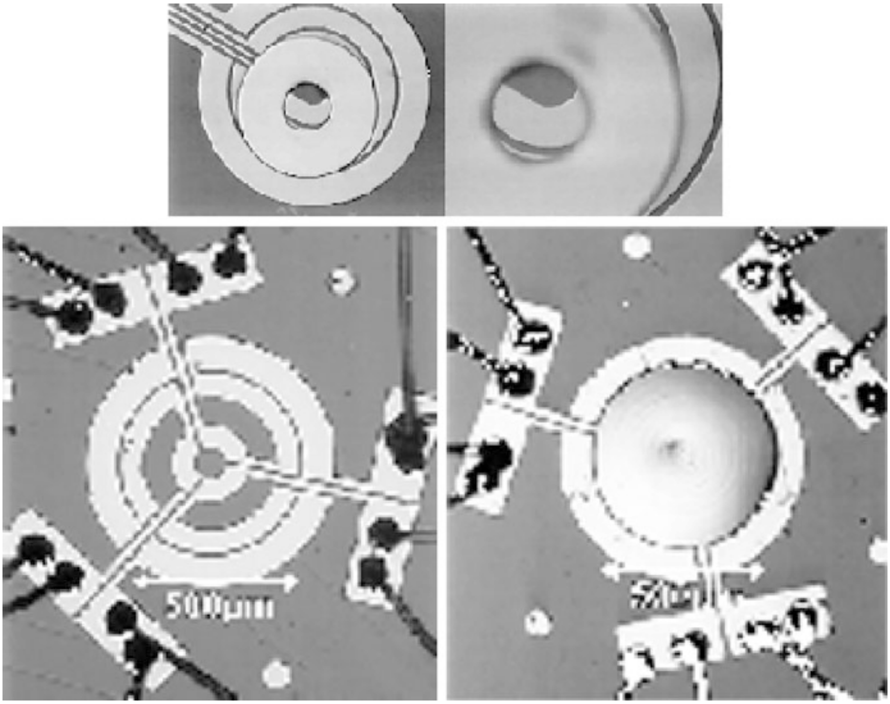

Fig. 3.18 Microgyroscope with spinning disk [8] (www.microstrain.com/3dm-gx1.aspx.)

Fig. 3.19 Microgyroscope with vibrating disk [8] (www.microstrain.com/3dm-gx1.aspx.)

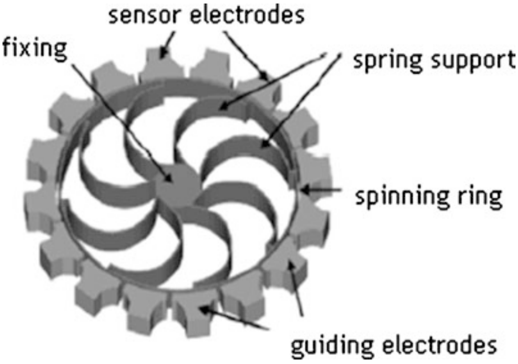

When the gyroscope is at rest (does not spin), the ring vibrates in the first mode of bending at a fixed amplitude. When the gyroscope is set in motion in the rotational motion about the normal axis, the Coriolis force makes a transition from the first bending mode to the other. Then the nodes and maxima are displaced at 45° (Fig. 3.21). The amplitude change is then detected by the electrodes as the capacitance changes. Finally, the signal is transmitted to the reading instruments.

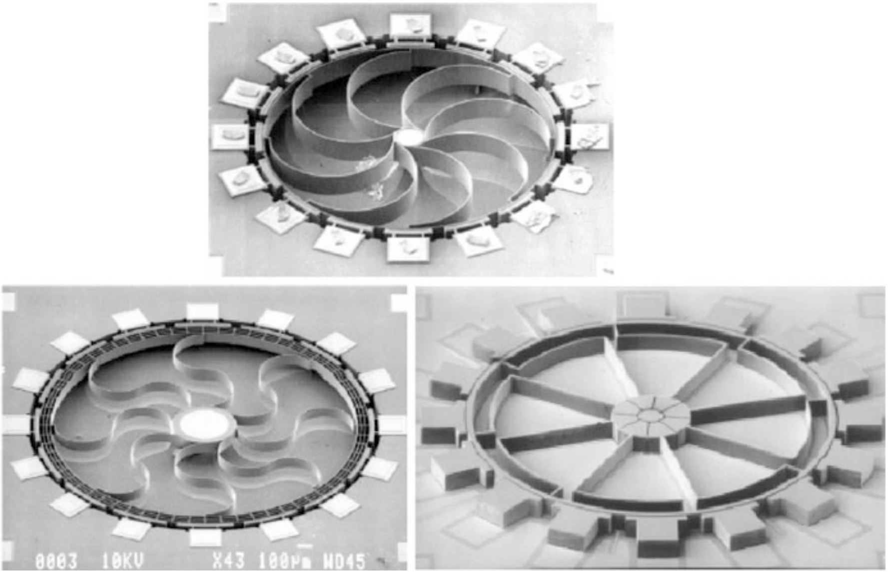

Fig. 3.20 Types of gyroscopes with a vibrating ring

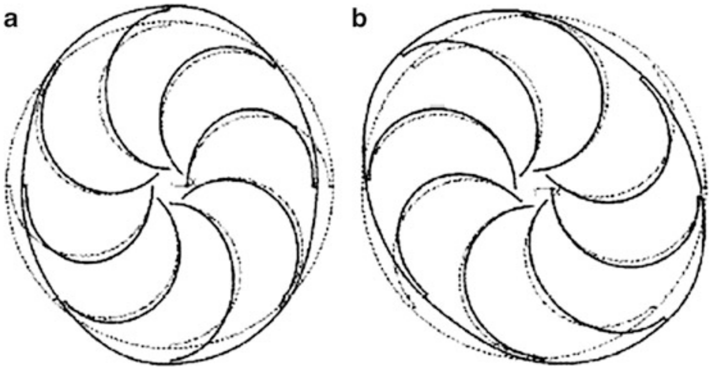

Fig. 3.21 Principle of operation of a gyroscope with a vibrating ring [8] (www.microstrain.com/3dm-gx1.aspx). (**a**) First bending wave. (**b**) Second bending wave shifted at 45° relative to first one

3.9 Examples of Gyroscopic Pilotage Devices

A *gyrocompass* is an on-board device pointing in the geographic northern direction (Fig. 3.22). It makes use of a basic feature of gyroscopes, namely, it maintains an unchanged position in the space of eigenrotations. A gyrocompass is independent of the magnetic field and declination of the object in which it is located.

Fig. 3.22 Gyrocompass (www.imar-navigation.de/englishside/dat_engl/ifog_e.htm)

A gyrocompass is the oldest aeronautic gyroscopic instrument. It was initially designed by Elmer Sperry for ships but as its size has been reduced, it is used in aviation. Its operation is based on that of a gyroscope, namely, when it spins, it maintains the position of its axis. A vertically placed gyroscopic disk is suspended on a Cardan joint, so that the orientation of the disk in space is unchanged. A rotation of an airplane about the gyroscope is transmitted on a 360-degree scale.

A Cardan system with a gyroscope can be placed inside or outside the device. In the latter case a gyrocompass is placed in a hermetic thermostat, and an indicator on the instrument panel (electromechanic or electronic) is electrically coupled with it.

In order to periodically update a gyrocompass one uses a compass. Such a system is called a gyromagnetic compass. The accurate so-called distant reading compass is located away from magnetic field sources (steal elements, electric energy receivers, cables), mostly placed in wing tips, and is electrically coupled with other systems.

A *turn indicator* allows for perfect turns without skidding or sideslipping (a so-called coordinated turn). The shape of the plane fixed to the gyroscope represents turn depth (angular velocity) (Fig. 3.23). A ball indicates the direction of the centrifugal force; it must stay in the marked area. A turn indicator can be made as a turn coordinator or a turn indicator with a vertical hand instead of an airplane shape.

An *artificial horizon* points indicates the position of an aircraft (horizontal flight, climb, descend, and tilt) relative to the real horizon plane (Fig. 3.24). The real horizon is called a plane that is perpendicular to the vertical at the observation point. The real horizon plane is parallel to the plane of visible horizon—it is specified by the rotor plane of a gyroscope. The real distance of the visible horizon depends on the curvature of the Earth's altitude and optical refraction (refraction of the track visible light rays in the atmosphere). As a result of refraction, an observer sees below something like a huge hollow; objects seem to be much farther away than they really are. Optical refraction depends on air temperature, humidity, pressure, pollination, and other factors.

Fig. 3.23 Turn indicator (www.imar-navigation.de/englishside/dat_engl/ifog_e.htm)

Fig. 3.24 Artificial horizon (www.imar-navigation.de/englishside/dat_engl/ifog_e.htm)

An artificial horizon is a base of flight without visibility. The artificial horizon indicates the real orientation of an airplane in space. The suspension of a gyroscope in an artificial horizon has three degrees of freedom. Therefore, the artificial horizon can rotate without limitations.

The first autopilot devices emerged from the gyrocompass and artificial horizon. Gyroscopic instruments controlled the actuators employed in airplane control systems by stabilizing the position in two planes. Previous autopilots were hydropneumatic devices without no electronics on-board.

Tachometer sights belong to a group of sight systems dealing with the problem of analytically determining the target hit by projectile.

The name refers to the fact that in sights of this kind, one measures the angular velocity of the vector radius determined between a target and a shooter. A typical solution of tachometer sights is coupling of the sight with a barrel of the canon.

Fig. 3.25 Tachometer sight (www.imar-navigation.de/englishside/dat_engl/ifog_e.htm)

The structure of a tachometer sight depends on the method of measuring the angular velocity, the method of determining the flight duration of a projectile, and the multiplying system. One uses gyroscopes or generators to determine the angular velocity.

When a gyroscope is used in a sight, it is mounted on the barrel lift unit in such a way that the main axis is parallel to the axis of a barrel under no external influence. An optical system is connected with the internal frame of a gyroscope. With an internal gyroscope frame is related to the optical system (sight) which optical axis is parallel to the axis of the gyroscope.

An example of a tachometer sight is the GP-02MR (Fig. 3.25), designed to manage gunfire and the naval cannon ZU-23-2M, which uses electromechanical equipment, the naval cannon ZU-23-2M. The sight is designed to shoot with antiaircraft short-range 9K32M missiles and ammo of various ballistics. During target tracking, it automatically determines the advanced and sight angles. The sight enables attacking targets on land or sea that are at rest or in motion.

3.10 Example of an Observation Instrument with a Built-in Gyroscope

Gyroscopic tracking systems represent a great improvement over binoculars in the observation of moving objects.

Modern binoculars, an example of which is the Stabiscope S1240 D/N (Fig. 3.26), are characterized by an internal built-in stabilizing system, so that the observed object remains motionless regardless of the vibrations of the holder's

Fig. 3.26 Binocular with a built-in gyroscopic stabilization system

hands or shaking generated by a car, helicopter, or ship. The stabilizing system consists of a fast-spinning gyroscope, coupled with a prism system suspended in a Cardan joint and placed in the optical axis between the lenses. When after a few seconds after it is turned on the rotating mass of the gyroscope is at full speed, and the suspension system is released—the binoculars are ready to work. The gyroscope ensures that the prism will maintain a fixed position independent of vibrations of the binoculars, so that an observer can see the object steadily.

3.11 New Challenges for a Gyroscope

An especially notable contribution to the development of gyroscopic devices came from the emergence and rapid growth of missile and spaceship technology. Gyroscopic devices were classified into two groups: seaborne and airborne. The former were characterized by relatively high accuracy, but they were large and massive. The latter, in contrast, had low accuracy but were of simple construction and small dimensions. The necessity of applying a gyroscope as a drive of an optoelectronic target coordinator in self-guided missiles forced the construction of gyroscopic devices of high accuracy and small overall dimensions, mass, and minimal energy consumption [8]. It should be emphasized that the high accuracy of a gyroscope needs to be maintained in hard, dynamic (overloads, vibrations), and climatic (large amplitudes of temperature and pressure) operating conditions. Thus the development of gyroscopic devices and their applications in missiles and spaceships has been revived. Scientists and engineers started new investigations into the causes of error generation and techniques of minimizing errors, construction improvements, inventing new materials of required properties providing high accuracy at small sizes and masses.

The development and improvement of precise and small gyroscopic instruments, working in complex conditions, has not ended and remains a scientific-engineering problem.

References

1. M. Davidson, *Gyroscope and Its Application* (Hutchinsons Scientific and Technical Publications, London, New York, 1946)
2. E.L. Nikolay, *Theory of the Gyroscopes* (OGIZ, Moscow, 1948), in Russian
3. R.F. Deimel, *Mechanics of the Gyroscope: The Dynamics of Rotation* (Dover, New York, 1950)
4. J.B. Scarborough, *The Gyroscope: Theory and Application* (Interscience Publishers, New York, 1958)
5. N.F. Babaeva, *Gyroscopes* (Mashinostroeniye, Leningrad, 1973), in Russian
6. V.A. Pavlov, *Aviational Giroscopic Devices* (GOSIZDAT of Defense Industry, Moscow, 1954), in Russian
7. L.Z. Novikov, M.Iu. Shatalov, *Mechanics of Dynamically Tunable Gyroscopes* (Nauka, Moscow, 1985), in Russian
8. Z. Koruba, *Elements of the Theory and Applications of Gyro-Controlled.* Monographs, Studies, Dissertation No. 25 (Kielce University of Technology, Kielce, 2008), in Polish
9. P.A. Abramov, *Errors of Dynamically Controlled Giroscopes* (Mashinostroeniye, Moscow, 1985), in Russian
10. M.A. Pavlovskiy, *Theory of the Gyroscopes* (Vyshaya Shkola, Kiev, 1986), in Russian
11. S. Popowski, *Methods to Improve the Metrological Characteristics of Dynamically Tuned Gyroscopes* (Military University of Technology, Warsaw, 1997), in Polish
12. A.A. Odintsov, *Theory and Computation of Gyroscopic Systems* (Vyshaya Shkola, Kiev, 1985), in Russian.

Chapter 4
Dynamics and Control of a Gyroscope

In this chapter theoretical investigations and the results of computer simulations are presented to show that the following factors affect the accuracy of realization of the required motion of a controlled gyroscope axis:

1. Compliance of initial conditions of the gyroscope motion with imposed initial conditions. In order to guide the gyroscope axis to the appropriate initial position one can apply additional time-independent control.
2. Values of the resistant-force coefficients in the bearings of gyroscope frames. Too small values of these coefficients, during external disturbance or kinematic excitation of the base, cause dynamical effects to arise and decrease the accuracy of realization of the preset motion. However, large values make the gyroscope axis drift off the preset position in space. Thus, one needs to minimalize the friction coefficients in the bearings of the gyroscope suspension and, additionally, to apply optimally selected dampers.
3. Influence of non-linearities in the model of gyroscope motion, which manifests especially at large angular deviations of the gyroscope axis.
4. Additional deviations of gyroscope—which, independently of the numerous technological tricks, always emerge during gyroscope operation—need to be reduced by means of the gyroscope's automatic control system. The proper position of the gyroscope axis is maintained by the automatic control system on the basis of the real position obtained from measurements and the required position of the gyroscope axis worked out by a digital machine.

4.1 Dynamics of a Gyroscope on a Movable Platform

Figure 4.1 shows a general view of a gyroscope and a movable base [board of flying object (FO)] along with acting forces and torques. We introduce the following frames [1–3]: $O_{g_1}X_1'X_2'X_3'$—movable frame fixed to an external frame

J. Awrejcewicz and Z. Koruba, *Classical Mechanics*, Advances in Mechanics and Mathematics 30, DOI 10.1007/978-1-4614-3978-3_4,

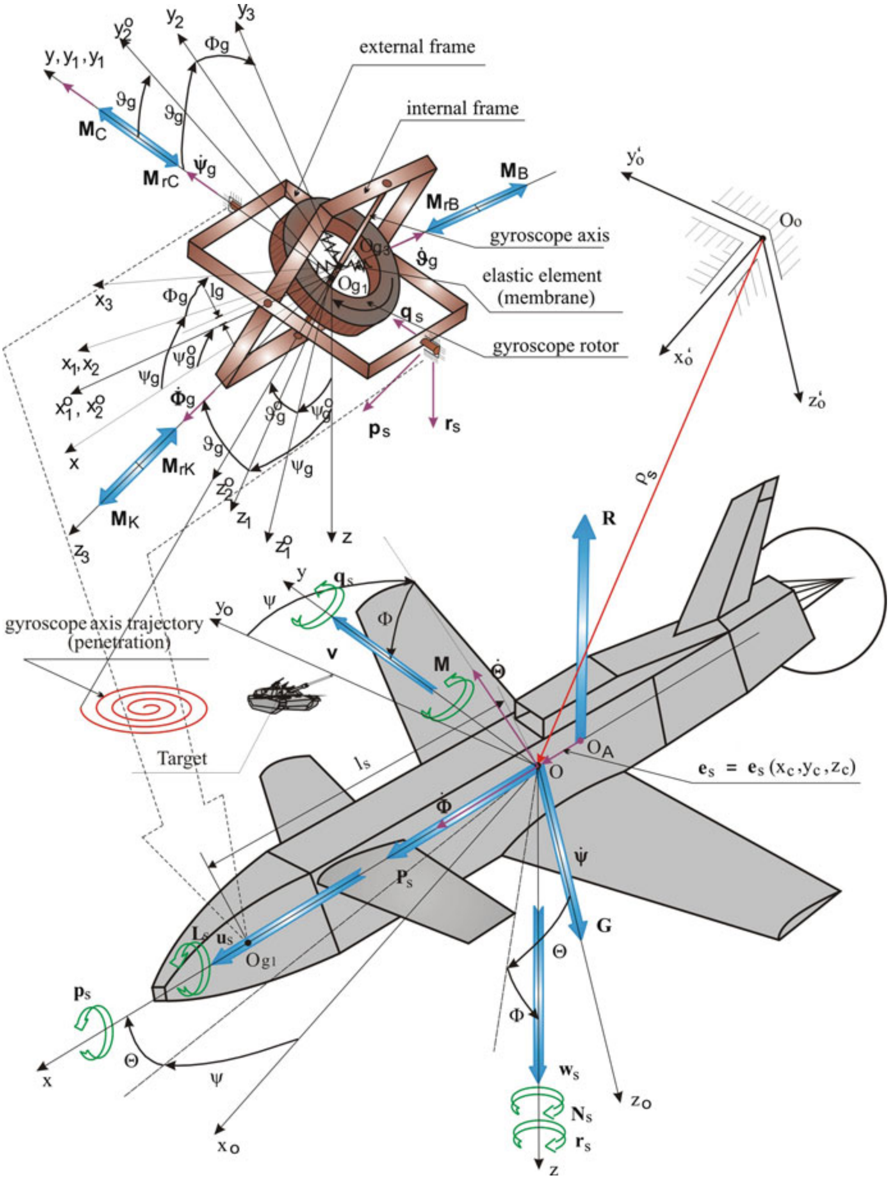

Fig. 4.1 General view of a gyroscope placed on a movable base (board of FO)

of the gyroscope; $O_{g_2}X_1''X_2''X_3''$—movable frame fixed to an internal frame of the gyroscope; $O_{g_3}X_1'''X_2'''X_3'''$—movable frame fixed to a rotor of the gyroscope; $O_{g_2}X_{10}''X_{20}''X_{30}''$—movable frame fixed to an axis of the gyroscope.

The mutual angular position of axes of the frames will be determined by means of a transformation matrix in the following way. The transformation matrix from the frame fixed to the platform to the frame fixed to the external frame governing the rotation of the frame $O_{g_1}X_1'X_2'X_3'$ relative to $OX_1X_2X_3$ about the axis $O_{g_1}X_2'$ at angle ψ_g has the following form:

$$M_{pz} = \begin{bmatrix} \cos\psi_g & 0 & -\sin\psi_g \\ 0 & 1 & 0 \\ \sin\psi_g & 0 & \cos\psi_g \end{bmatrix}. \tag{4.1}$$

The transformation matrix from the frame fixed to the external frame to that fixed to the internal frame (rotation of the frame $O_{g_2}X_1''X_2''X_3''$ relative to $O_{g_1}X_1'X_2'X_3'$ about the axis $O_{g_2}X_1''$ at angle ϑ_g) is as follows:

$$M_{zw} = \begin{bmatrix} 1 & 0 & 0 \\ 0 & \cos\vartheta_g & \sin\vartheta_g \\ 0 & -\sin\vartheta_g & \cos\vartheta_g \end{bmatrix}. \tag{4.2}$$

The transformation matrix from the frame fixed to the internal frame to that fixed to the rotor (rotation of the frame $O_{g_3}X_1'''X_2'''X_3'''$ relative to $O_{g_2}X_1''X_2''X_3''$ about the axis $O_{g_3}X_3'''$ at angle Φ_g) reads

$$M_{wr} = \begin{bmatrix} \cos\Phi_g & \sin\Phi_g & 0 \\ -\sin\Phi_g & \cos\Phi_g & 0 \\ 0 & 0 & 1 \end{bmatrix}. \tag{4.3}$$

The transformation matrix from the frame fixed to the platform to that fixed to the internal frame is obtained in the following way:

$$M_{pw} = M_{zw}\cdot M_{pz} = \begin{bmatrix} \cos\psi_g & 0 & -\sin\psi_g \\ \sin\vartheta_g\sin\psi_g & \cos\vartheta_g & \sin\vartheta_g\cos\psi_g \\ \cos\vartheta_g\sin\psi_g & -\sin\vartheta_g & \cos\vartheta_g\cos\psi_g \end{bmatrix}, \tag{4.4}$$

and the transformation matrix from the frame fixed to the platform to that fixed to the rotor is as follows:

$$M_{pr} = M_{wr}\cdot M_{pw} = \begin{bmatrix} \begin{matrix}\cos\psi_g\cos\Phi_g + \\ +\sin\vartheta_g\sin\psi_g\sin\Phi_g\end{matrix} & \cos\vartheta_g\sin\Phi_g & \begin{matrix}-\sin\psi_g\cos\Phi_g \\ +\sin\vartheta_g\cos\psi_g\sin\Phi_g\end{matrix} \\ \\ \begin{matrix}-\cos\psi_g\sin\Phi_g + \\ +\sin\vartheta_g\sin\psi_g\cos\Phi_g\end{matrix} & \cos\vartheta_g\cos\Phi_g & \begin{matrix}\sin\psi_g\cos\Phi_g + \\ +\sin\vartheta_g\cos\psi_g\sin\Phi_g\end{matrix} \\ \\ \cos\vartheta_g\sin\psi_g & -\sin\vartheta_g & \cos\vartheta_g\cos\psi_g \end{bmatrix}. \tag{4.5}$$

In the case where the gyroscope axis is connected with the rotor by means of an elastic element, the gyroscope gains an additional two degrees of freedom, and the corresponding matrices of transformation (analogically M_{pz}, M_{zw} and M_{pw}) take the form

$$M^0_{pz} = \begin{bmatrix} \cos\psi^0_g & 0 & -\sin\psi^0_g \\ 0 & 1 & 0 \\ \sin\psi^0_g & 0 & \cos\psi^0_g \end{bmatrix},$$

$$M^0_{zw} = \begin{bmatrix} 1 & 0 & 0 \\ 0 & \cos\vartheta^0_g & \sin\vartheta^0_g \\ 0 & -\sin\vartheta^0_g & \cos\vartheta^0_g \end{bmatrix},$$

$$M^0_{pw} = M^0_{pz} \cdot M^0_{zw} = \begin{bmatrix} \cos\psi^0_g & 0 & -\sin\psi^0_g \\ \sin\vartheta^0_g \sin\psi^0_g & \cos\vartheta^0_g & \sin\vartheta^0_g \cos\psi^0_g \\ \cos\vartheta^0_g \sin\psi^0_g & -\sin\vartheta^0_g & \cos\vartheta^0_g \cos\psi^0_g \end{bmatrix}. \tag{4.6}$$

The following assumptions are introduced:

1. The center of mass of the rotor coincides with the center of mass of the internal frame $O_{g_2} = O_{g_3}$, but it does not coincide with the center of motion O_{g_1}, i.e., with the point of intersection of the axes of rotor rotation and the frames. Hence, we consider a non-astatic gyroscope, also called a "heavy" gyroscope.
2. The axes $O_{g_1}X'_1$, $O_{g_1}X'_2$, $O_{g_1}X'_3$ are the main, central axes of inertia of the external frame; similarly, the axes $O_{g_2}X''_3$ and $O_{g_3}X'''_3$ are the main, central axes of inertia of the internal frame and the rotor, respectively. The remaining axes are the main ones of the corresponding systems.

The given quantities follow:

1. m_1, m_2, m_3—masses of external frame, internal (along with the axis) frame, and rotor of gyroscope, respectively.
2. l_s—distance between center of mass of base and center of gyroscope motion.
3. l_g—distance between center of mass of system: rotor—internal frame and center of motion.
4. $I_{X'_1}, I_{X'_2}, I_{X'_3}$—moments of inertia of external frame about axes $O_{g_1}X'_1$, $O_{g_1}X'_2$, $O_{g_1}X'_3$, respectively.
5. $I_{X''_1}, I_{X''_2}, I_{X''_3}$—moments of inertia of internal frame about axes $O_{g_2}X''_1$, $O_{g_2}X''_2$, $O_{g_2}X''_3$, respectively.
6. $I_{X'''_1}, I_{X'''_2}, I_{X'''_3}$—moments of inertia of rotor about axes $O_{g_3}X'''_1$, $O_{g_3}X'''_2$, $O_{g_3}X'''_3$, respectively.
7. $I^0_{X''_1}, I^0_{X''_2}$—moments of inertia of gyroscope axis about axes $O_{g_2}X''_{10}$, $O_{g_2}X''_{20}$, respectively.
8. $\boldsymbol{\omega}_g(p^*, q^*, r^*)$—components of angular velocity vector of base (kinematic interaction of the base).
9. $\mathbf{V}^*_g(V_{gX_1}, V_{gX_2}, V_{gX_3})$—components of linear velocity vector of base displacement—coordinates of point O_{g_1}.

10. $\mathbf{F}_g(F_{gX_1}, F_{gX_2}, F_{gX_3})$—components of force acting on center of mass of rotor in frame fixed to platform $O_{g_1}X_1X_2X_3$.
11. Moments of forces of interactions:
    (a) $\mathbf{M}_c(M_{cX_1}, M_{cX_2}, M_{cX_3})$—base on external frame;
    (b) $\mathbf{M}_b(M_{bX_1'}, M_{bX_2'}, M_{bX_3'})$—external frame on internal one;
    (c) $\mathbf{M}_k(M_{kX_1''}, M_{kX_2''}, M_{kX_3''})$—internal frame on rotor.
12. Moments of friction forces in bearings of internal and external frames:
    (a) Viscous

$$M_{rc} = M_{rc}^V = \eta_c \frac{\mathrm{d}\psi_g}{\mathrm{d}t}, \quad M_{rb} = M_{rb}^V = \eta_b \frac{\mathrm{d}\vartheta_g}{\mathrm{d}t};$$

    (b) Dry

$$M_{rc} = M_{rc}^{\mathrm{T}} = 0,5 \cdot T_{rc} \cdot d_c, \quad M_{rb} = M_{rb}^{\mathrm{T}} = 0,5 \cdot T_{rb} \cdot d_b;$$

where

$$T_{rc} = \mu_c N_c sign\left(\frac{\mathrm{d}\psi_g}{\mathrm{d}t}\right), \qquad T_{rb} = \mu_b N_b sign\left(\frac{\mathrm{d}\vartheta_g}{\mathrm{d}t}\right),$$

and $\eta_c, \eta_b, \mu_c, \mu_b$ are friction coefficients in the frame bearings; N_c, N_b are normal reactions in the bearings; d_c, d_b are diameters of the bearing pins.
13. M_{rk}—moment of friction forces in bearing of rotor in internal frame and aerodynamic resistance.
14. M_{zb}, M_{zc}—disturbing signals in form of torques acting directly on rotor.
15. κ—stiffness coefficient of elastic element connecting axis with rotor.

The desired quantities are as follows:

1. $\psi_g, \vartheta_g, \Phi_g$—angles by means of which one determines the position of the rotor relative to the frame $O_{g_1}X_1X_2X_3$;
2. ψ_g^0, ϑ_g^0—angles by means of which one determines the position of the gyroscope axis relative to the frame $O_{g_1}X_1X_2X_3$;
3. Angular velocities: $\dot{\psi}_g = \frac{\mathrm{d}\psi_g}{\mathrm{d}t}, \quad \dot{\vartheta}_g = \frac{\mathrm{d}\vartheta_g}{\mathrm{d}t}, \quad \dot{\Phi}_g = \frac{\mathrm{d}\Phi_g}{\mathrm{d}t};$
4. Angular velocities: $\dot{\psi}_g^0 = \frac{\mathrm{d}\psi_g^0}{\mathrm{d}t}, \quad \dot{\vartheta}_g^0 = \frac{\mathrm{d}\vartheta_g^0}{\mathrm{d}t}, \quad \dot{\Phi}_g^0 = \frac{\mathrm{d}\Phi_g^0}{\mathrm{d}t}.$

The vector of the angular velocity of the rotor reads

$$\boldsymbol{\omega}_g^* = \frac{d\boldsymbol{\psi}_g}{\mathrm{d}t} + \frac{d\boldsymbol{\vartheta}_g}{\mathrm{d}t} + \frac{d\boldsymbol{\Phi}_g}{\mathrm{d}t}, \tag{4.7}$$

whereas the angular velocity vector of the gyroscope has the following form:

$$\boldsymbol{\omega}_g^0 = \frac{d\boldsymbol{\psi}_g^0}{\mathrm{d}t} + \frac{d\boldsymbol{\vartheta}_g^0}{\mathrm{d}t}. \tag{4.8}$$

Projections of its components on particular axes of the coordinate system can be determined as follows:

$$\begin{bmatrix} \dot{\psi}_{gX_1'} \\ \dot{\psi}_{gX_2'} \\ \dot{\psi}_{gX_3'} \end{bmatrix} = \begin{bmatrix} 0 \\ \dot{\psi}_g \\ 0 \end{bmatrix}, \qquad \begin{bmatrix} \dot{\psi}_{gX_1''} \\ \dot{\psi}_{gX_2''} \\ \dot{\psi}_{gX_3''} \end{bmatrix} = \begin{bmatrix} 0 \\ \dot{\psi}_g \cos\vartheta_g \\ -\dot{\psi}_g \sin\vartheta_g \end{bmatrix},$$

$$\begin{bmatrix} \dot{\psi}_{gX_1'''} \\ \dot{\psi}_{gX_2'''} \\ \dot{\psi}_{gX_3'''} \end{bmatrix} = \begin{bmatrix} \dot{\psi}_g \cos\vartheta_g \sin\Phi_g \\ \dot{\psi}_g \cos\vartheta_g \cos\Phi_g \\ -\dot{\psi}_g \sin\vartheta_g \end{bmatrix}, \tag{4.9}$$

$$\begin{bmatrix} \dot{\vartheta}_{gX_1'} \\ \dot{\vartheta}_{gX_2'} \\ \dot{\vartheta}_{gX_3'} \end{bmatrix} = \begin{bmatrix} \dot{\vartheta}_g \cos\psi_g \\ 0 \\ -\dot{\vartheta}_g \sin\psi_g \end{bmatrix}, \qquad \begin{bmatrix} \dot{\vartheta}_{gX_1''} \\ \dot{\vartheta}_{gX_2''} \\ \dot{\vartheta}_{gX_3''} \end{bmatrix} = \begin{bmatrix} \dot{\vartheta}_g \\ 0 \\ 0 \end{bmatrix},$$

$$\begin{bmatrix} \dot{\vartheta}_{gX_1'''} \\ \dot{\vartheta}_{gX_2'''} \\ \dot{\vartheta}_{gX_3'''} \end{bmatrix} = \begin{bmatrix} \dot{\vartheta}_g \cos\Phi_g \sin \\ -\dot{\vartheta}_g \sin\Phi_g \\ 0 \end{bmatrix}, \qquad \begin{bmatrix} \dot{\Phi}_{gX_1'''} \\ \dot{\Phi}_{gX_2'''} \\ \dot{\Phi}_{gX_3'''} \end{bmatrix} = \begin{bmatrix} 0 \\ 0 \\ \dot{\Phi}_g \end{bmatrix}. \tag{4.10}$$

Analogously, projections of the components of the angular velocity vector of the gyroscope axis will take the following forms:

$$\begin{bmatrix} \dot{\psi}^0_{gX_1'} \\ \dot{\psi}^0_{gX_2'} \\ \dot{\psi}^0_{gX_3'} \end{bmatrix} = \begin{bmatrix} 0 \\ \dot{\psi}^0_g \\ 0 \end{bmatrix}, \qquad \begin{bmatrix} \dot{\psi}^0_{gX_1''} \\ \dot{\psi}^0_{gX_2''} \\ \dot{\psi}^0_{gX_3''} \end{bmatrix} = \begin{bmatrix} 0 \\ \dot{\psi}^0_g \cos\vartheta^0_g \\ -\dot{\psi}^0_g \sin\vartheta^0_g \end{bmatrix}, \tag{4.11}$$

$$\begin{bmatrix} \dot{\vartheta}^0_{gX_1'} \\ \dot{\vartheta}^0_{gX_2'} \\ \dot{\vartheta}^0_{gX_3'} \end{bmatrix} = \begin{bmatrix} \dot{\vartheta}^0_g \cos\psi^0_g \\ 0 \\ -\dot{\vartheta}^0_g \sin\psi^0_g \end{bmatrix}, \qquad \begin{bmatrix} \dot{\vartheta}^0_{gX_1''} \\ \dot{\vartheta}^0_{gX_2''} \\ \dot{\vartheta}^0_{gX_3''} \end{bmatrix} = \begin{bmatrix} \dot{\vartheta}^0_g \\ 0 \\ 0 \end{bmatrix}. \tag{4.12}$$

In what follows one may define the components of the angular velocity vector of the external frame in the coordinate system $O_{g_1}X_1'X_2'X_3'$:

$$\begin{bmatrix} \omega_{gX_1'} \\ \omega_{gX_2'} \\ \omega_{gX_3'} \end{bmatrix} = M_{pz} \begin{bmatrix} p^* \\ q^* \\ r^* \end{bmatrix} + \begin{bmatrix} \dot{\psi}_{gX_1'} \\ \dot{\psi}_{gX_2'} \\ \dot{\psi}_{gX_3'} \end{bmatrix} = \begin{bmatrix} p^* \cos\psi_g - r^* \sin\psi_g \\ \dot{\psi}_g + q^* \\ p^* \sin\psi_g + r^* \cos\psi_g \end{bmatrix}. \tag{4.13}$$

On the other hand, the components of the angular velocity vector of the internal frame in the coordinate system $O_{g_2}X_1''X_2''X_3''$ read

$$\begin{bmatrix} \omega_{gX_1''} \\ \omega_{gX_2''} \\ \omega_{gX_3''} \end{bmatrix} = M_{pw} \begin{bmatrix} p^* \\ q^* \\ r^* \end{bmatrix} + \begin{bmatrix} \dot{\vartheta}_{gX_1''} \\ \dot{\vartheta}_{gX_2''} \\ \dot{\vartheta}_{gX_3''} \end{bmatrix} + \begin{bmatrix} \dot{\psi}_{gX_1''} \\ \dot{\psi}_{gX_2''} \\ \dot{\psi}_{gX_3''} \end{bmatrix}$$

$$= \begin{bmatrix} p^* \cos\psi_g - r^* \sin\psi_g + \dot{\vartheta}_g \\ (p^* \sin\psi_g + r^* \cos\psi_g) \sin\vartheta_g + (q^* + \dot{\psi}_g) \cos\vartheta_g \\ (p^* \sin\psi_g + r^* \cos\psi_g) \cos\vartheta_g - (q^* + \dot{\psi}_g) \sin\vartheta_g \end{bmatrix}. \quad (4.14)$$

Components of the angular velocity vector in the coordinate system $O_{g_3}X_1'''X_2'''X_3'''$ have the form

$$\begin{bmatrix} \omega_{gX_1'''} \\ \omega_{gX_2'''} \\ \omega_{gX_3'''} \end{bmatrix} = M_{pr} \begin{bmatrix} p^* \\ q^* \\ r^* \end{bmatrix} + \begin{bmatrix} \dot{\vartheta}_{gX_1'''} \\ \dot{\vartheta}_{gX_2'''} \\ \dot{\vartheta}_{gX_3'''} \end{bmatrix} + \begin{bmatrix} \dot{\psi}_{gX_1'''} \\ \dot{\psi}_{gX_2'''} \\ \dot{\psi}_{gX_3'''} \end{bmatrix} + \begin{bmatrix} \dot{\Phi}_{gX_1'''} \\ \dot{\Phi}_{gX_2'''} \\ \dot{\Phi}_{gX_3'''} \end{bmatrix},$$

or, equivalently,

$$\begin{aligned} \omega_{gX_1'''} = {} & p^*(\cos\psi_g \cos\Phi_g + \sin\vartheta_g \sin\psi_g \sin\Phi_g) \\ & + (q^* + \dot{\psi}_g) \cos\vartheta_g \sin\Phi_g + \dot{\vartheta}_g \cos\Phi_g \\ & + r^*(\cos\psi_g \sin\vartheta_g \sin\Phi_g - \sin\psi_g \cos\Phi_g), \end{aligned} \quad (4.15)$$

$$\begin{aligned} \omega_{gX_2'''} = {} & -p^*(\cos\psi_g \sin\Phi_g - \sin\vartheta_g \sin\psi_g \cos\Phi_g) \\ & + (q^* + \dot{\psi}_g) \cos\vartheta_g \cos\Phi_g - \dot{\vartheta}_g \sin\Phi_g \\ & + r^*(\cos\psi_g \sin\vartheta_g \cos\Phi_g + \sin\psi_g \sin\Phi_g), \end{aligned} \quad (4.16)$$

$$\begin{aligned} \omega_{gX_3'''} = {} & p^* \sin\psi_g \cos\vartheta_g - (q^* + \dot{\psi}_g) \sin\vartheta_g \\ & + r^* \cos\psi_g \cos\vartheta_g + \dot{\Phi}_g. \end{aligned} \quad (4.17)$$

Components of the velocity vector of the gyroscope axis in the coordinate system $O_{g_1}X_1'X_2'X_3'$ read

$$\begin{bmatrix} \omega^0_{gX_1'} \\ \omega^0_{gX_2'} \\ \omega^0_{gX_3'} \end{bmatrix} = M^0_{pz} \begin{bmatrix} p^* \\ q^* \\ r^* \end{bmatrix} + \begin{bmatrix} \dot{\psi}^0_{gX_1'} \\ \dot{\psi}^0_{gX_2'} \\ \dot{\psi}^0_{gX_3'} \end{bmatrix} = \begin{bmatrix} p^* \cos\psi^0_g - r^* \sin\psi^0_g \\ \dot{\psi}^0_g + q^* \\ p^* \sin\psi^0_g + r^* \cos\psi^0_g \end{bmatrix}. \quad (4.18)$$

Finally, components of the velocity vector of the gyroscope axis in the coordinate system $O_{g_2}X''_{10}X''_{20}X''_{30}$ are as follows:

$$\begin{aligned}\begin{bmatrix}\omega^0_{gX''_1}\\ \omega^0_{gX''_2}\\ \omega^0_{gX''_3}\end{bmatrix} &= M_{pw}\begin{bmatrix}p^*\\ q^*\\ r^*\end{bmatrix} + \begin{bmatrix}\dot{\vartheta}^0_{gX''_1}\\ \dot{\vartheta}^0_{gX''_2}\\ \dot{\vartheta}^0_{gX''_3}\end{bmatrix} + \begin{bmatrix}\dot{\psi}^0_{gX''_1}\\ \dot{\psi}^0_{gX''_2}\\ \dot{\psi}^0_{gX''_3}\end{bmatrix}\\ &= \begin{bmatrix}p^*\cos\psi^0_g - r^*\sin\psi^0_g + \dot{\vartheta}^0_g\\ (p^*\sin\psi^0_g + r^*\cos\psi^0_g)\sin\vartheta^0_g + (q^* + \dot{\psi}^0_g)\cos\vartheta^0_g\\ (p^*\sin\psi^0_g + r^*\cos\psi^0_g)\cos\vartheta^0_g - (q^* + \dot{\psi}^0_g)\sin\vartheta^0_g\end{bmatrix}. \qquad (4.19)\end{aligned}$$

The linear velocity of the center of mass of the rotor is a sum of the drift velocity of point O_s (velocity of FO) and O_{g_1} (about point O_s) and the relative velocity relative to point O_{g_2} [2,4]:

$$\mathbf{V}_{g_2} = \mathbf{V}_s + \begin{vmatrix}\mathbf{E}_1 & \mathbf{E}_2 & \mathbf{E}_3\\ \mathbf{p}^* & \mathbf{q}^* & \mathbf{r}^*\\ l_s & 0 & 0\end{vmatrix} + \begin{vmatrix}\mathbf{E}'_1 & \mathbf{E}'_2 & \mathbf{E}'_3\\ \omega_{gX'_1} & \omega_{gX'_2} & \omega_{gX'_3}\\ 0 & 0 & l_g\end{vmatrix} + \begin{vmatrix}\mathbf{E}''_1 & \mathbf{E}''_2 & \mathbf{E}''_3\\ \omega_{gX''_1} & \omega_{gX''_2} & \omega_{gX''_3}\\ 0 & 0 & l_g\end{vmatrix},$$

or, equivalently,

$$V_{gX''_1} = u_s\cos\psi_g - (w_s - q^*l_s)\sin\psi_g + (\omega_{gX'_2} + \omega_{gX''_2})l_g, \qquad (4.20)$$

$$\begin{aligned}V_{gX''_2} &= (u_s\sin\psi_g + (w_s - q^*l_s)\cos\psi_g)\sin\vartheta_g\\ &\quad + (v_s + r^*l_s)\cos\vartheta_g - (\omega_{gX''_1} + \omega_{gX'_1}\cos\vartheta_g)l_g, \qquad (4.21)\end{aligned}$$

$$\begin{aligned}V_{gX''_3} &= (u_s\sin\psi_g + (w_s - q^*l_s)\cos\psi_g)\cos\vartheta_g\\ &\quad - (v_s + r^*l_s)\sin\vartheta_g + \omega_{gX'_1}l_g\sin\vartheta_g. \qquad (4.22)\end{aligned}$$

The linear velocity of the center of mass of the external frame reads

$$\mathbf{V}_{g_1} = \mathbf{V}_s + \begin{vmatrix}\mathbf{E}_1 & \mathbf{E}_2 & \mathbf{E}_3\\ \mathbf{p}^* & \mathbf{q}^* & \mathbf{r}^*\\ l_s & 0 & 0\end{vmatrix},$$

or, equivalently,

$$V_{gX'_1} = u_s\cos\psi_g - (w_s - q^*l_s)\sin\psi_g, \qquad (4.23)$$

$$V_{gX'_2} = v_s + r^*l_s, \qquad (4.24)$$

$$V_{gX'_3} = u_s\sin\psi_g + (w_s - q^*l_s)\cos\psi_g. \qquad (4.25)$$

Similarly, projections of the linear velocity of the center of mass of the external frame-axis system are

$$V^0_{gX''_1} = u_s \cos\psi^0_g - (w_s - q^* l_s)\sin\psi^0_g + (\omega^0_{gX'_2} + \omega^0_{gX''_2}) l_g, \tag{4.26}$$

$$\begin{aligned} V^0_{gX''_2} = &\ (u_s \sin\psi^0_g + (w_s - q^* l_s)\cos\psi^0_g)\sin\vartheta^0_g \\ &+ (v_s + r^* l_s)\cos\vartheta^0_g - (\omega^0_{gX''_1} + \omega^0_{gX'_1}\cos\vartheta^0_g) l_g, \end{aligned} \tag{4.27}$$

$$\begin{aligned} V^0_{gX''_3} = &\ (u_s \sin\psi^0_g + (w_s - q^* l_s)\cos\psi^0_g)\cos\vartheta^0_g \\ &- (v_s + r^* l_s)\sin\vartheta^0_g + \omega^0_{gX'_1} l_g \sin\vartheta^0_g. \end{aligned} \tag{4.28}$$

The axes $O_{g1}X'_1$, $O_{g1}X'_2$, $O_{g1}X'_3$, $O_{g2}X''_3$, and $O_{g3}X'''_3$ are the main central axes of inertia of the corresponding frames. The remaining axes are the main ones of the suitable systems. By $I^*_{X''_1}, I^*_{X''_2}, I^*_{X''_3}, I^*_{X'''_1}, I^*_{X'''_2}$, and $I^*_{X'''_3}$ we denote the moments of inertia of the corresponding frames about the axes parallel to the axes $O_{g2}X''_1$, $O_{g2}X''_2$, $O_{g2}X''_3$, $O_{g3}X'''_1$, $O_{g3}X'''_2$, and $O_{g3}X'''_3$ but passing through the center of mass.

We will derive equations of motion of the gyroscope by means of the Lagrange equations of the second kind. To that end, we will determine the kinetic E_k (equal to the sum of the kinetic energy of the external and internal frames, the rotor, and the axis) and the potential E_p energy of the system

$$\begin{aligned} E_k = &\ \frac{1}{2}\left[I_{X'_1}\omega^2_{gX'} + I_{X'_2}\omega^2_{gX'_2} + I_{X'_3}\omega^2_{gX'_3}\right] \\ &+ \frac{1}{2}\left[I^*_{X''_1}\omega^2_{gX''_1} + I^*_{X''_2}\omega^2_{gX''_2} + I^*_{X''_3}\omega^2_{gX''_3}\right] \\ &+ \frac{1}{2}\left[I^*_{X'''_1}\omega^2_{gX'''_1} + I^*_{X'''_2}\omega^2_{gX'''_2} + I^*_{X'''_3}\omega^2_{gX'''_3}\right] \\ &+ \frac{1}{2}\left[I^0_{X''_1}(\omega^0_{gX''_1})^2 + I^0_{X''_2}(\omega^0_{gX''_2})^2\right] \\ &+ \frac{1}{2}m_3 V_s^2 + \frac{1}{2}m_1\left(V^2_{gX'} + V^2_{gX'_2} + V^2_{gX'_3}\right) \\ &+ \frac{1}{2}m_3\left(V^2_{gX''_1} + V^2_{gX''_2} + V^2_{gX''_3}\right) \\ &+ \frac{1}{2}m_2\left[(V^0_{gX''_1})^2 + (V^0_{gX''_2})^2 + (V^0_{gX''_3})^2\right], \end{aligned} \tag{4.29a}$$

$$E_p = \frac{1}{2}\kappa(\psi_g - \psi^0_g)^2 + \frac{1}{2}\kappa(\vartheta_g - \vartheta^0_g)^2. \tag{4.29b}$$

The Lagrange function has the following form:

$$L = E_k - E_P. \tag{4.30}$$

Taking into account the fact that a generalized coordinate Φ_g is cyclic, we obtain equations of motion of the gyroscope in the following form:

1. Equations of motion of the gyroscope axis

$$\begin{aligned}
&I^0_{X_2''}\frac{\mathrm{d}}{\mathrm{d}t}(\omega^0_{gX_2'}\cos^2\vartheta^0_g) + m_2\cdot l_g^2(1+\cos\vartheta^0_g)^2\frac{\mathrm{d}\omega^0_{gX_2'}}{\mathrm{d}t} + I^0_{X_1''}\omega^0_{gX_1''}\omega^0_{gX_3'} \\
&\quad + \frac{1}{2}I^0_{X_2''}\omega^0_{gX_3'}\left[\sin 2\vartheta^0_g + (\omega^0_{gX_1''} - \omega^0_{gX_1'})\cos^2\vartheta^0_g\right] - \kappa(\psi_g - \psi^0_g) \\
&\quad + m_2 l_g\left\{(1+\cos\vartheta^0_g)\cdot(\dot{u}_s\cos\psi^0_g - (\dot{w}_s - \dot{q}^* l_s)\sin\psi^0_g)\right. \\
&\quad \left. - \dot{\psi}^0_g\left[u_s\sin\psi^0_g + (w_s - q^* l_s)\cos\psi^0_g\right] - V^0_{gX_1''}\dot{\vartheta}^0_g\sin\vartheta^0_g\right\} \\
&\quad + m_2 l_g^2\left[(\omega^0_{gX_2'} + \omega^0_{gX_2''})\omega^0_{gX_1'}\sin\vartheta^0_g - (1+\cos\vartheta^0_g)\omega^0_{gX_1''}\omega^0_{gX_3'}\right. \\
&\quad \left. + \dot{\vartheta}^0_g\omega^0_{gX_3''} + \dot{\omega}^0_{gX_3'}\sin\vartheta^0_g\right] + m_2 l_s l_g\left\{q_s\left[(\omega^0_{gX_1'} - \omega^0_{gX_1''})\sin\psi^0_g\sin\vartheta^0_g\right.\right. \\
&\quad \left. + (\omega^0_{gX_2'} + \omega^0_{gX_3''})\cos\psi^0_g - \omega^0_{gX_3'}\cos\Psi^0_g\sin\vartheta^0_g\cos\vartheta^0_g\right] \\
&\quad \left. + (1+\cos\vartheta^0_g)\cdot r^*\omega^0_{gX_3'}\right\} = M_c - M_{rc},
\end{aligned} \tag{4.31}$$

$$\begin{aligned}
&I^0_{X_1''}\frac{\mathrm{d}\omega^0_{gX_1''}}{\mathrm{d}t} + m_2 l_g^2\ddot{\vartheta}^0_g - I^0_{X_2''}\omega^0_{gX_2''}\omega^0_{gX_3''} - \kappa(\vartheta_g - \vartheta^0_g) \\
&- m_2 l_g\left\{\left[\dot{\psi}^0_g(u_s\cos\psi^0_g - (w_s - q^* l_s)\sin\psi^0_g) + \dot{u}_s\sin\psi^0_g\right.\right. \\
&\left. + (w_s - \dot{q}^* l_s)\cos\psi^0_g\right]\sin\vartheta^0_g + \dot{\vartheta}^0_g V^0_{gX_3''} + \dot{v}_s\cos\vartheta^0_g \\
&- \left[q^*(\omega^0_{gX_3''}\sin\psi^0_g + \omega^0_{gX_1''}\cos\psi^0_g\cos\vartheta^0_g) + r^*\omega^0_{gX_1''}\sin\vartheta^0_g - \dot{r}^*\cos\vartheta^0_g\right]\cdot l_s \\
&\left. - \left[(\omega^0_{gX_2'} + \omega^0_{gX_2''})\omega^0_{gX_3''} - \omega^0_{gX_1'}\omega^0_{gX_1''}\sin\vartheta^0_g + (1+\cos\vartheta^0_g)\dot{\omega}^0_{gX_1'}\right]\cdot l_g\right\} \\
&= M_b - M_{rb}.
\end{aligned} \tag{4.32}$$

2. Equations of motion of gyroscope rotor

$$
\begin{aligned}
&\Big[I_{X_2'} + I^*_{X_2''} + I^*_{X_2'''} + (I^*_{X_3''} - I^*_{X_2''} - I^*_{X_2'''})\sin^2\vartheta_g \\
&\quad + m_3 l_g^2(1+\cos\vartheta_g)^2\Big]\frac{\mathrm{d}\omega_{gX_2'}}{\mathrm{d}t} + \frac{I^*_{X_3''} - I^*_{X_2''} - I^*_{X_2'''}}{2}(\omega_{gX_2'}\dot{\vartheta}_g \\
&\quad - \dot{\omega}_{gX_3'})\sin 2\vartheta_g - (I_{X_3'} - I_{X_1'})\cdot\omega_{gX_1'}\omega_{gX_3'} \\
&\quad + I^*_{X_1'''}\omega_{gX_1''}\omega_{gX_3'} + \Big[I^*_{X_2''} + I^*_{X_2'''} + (I^*_{X_3''} - I^*_{X_2''} \\
&\quad - I^*_{X_2'''})\sin^2\vartheta_g\Big]\cdot\dot{\vartheta}_g\omega_{gX_3'} - \Big[(I^*_{X_2''} + I^*_{X_2'''})\cdot\omega_{gX_1''}\omega_{gX_2''} \\
&\quad + I^*_{X_3'''}\dot{\omega}_{gX_3'''}\Big]\sin\vartheta_g - \Big[I^*_{X_3''}\omega_{gX_3''} + I^*_{X_3'''}(\omega_{gX_3''} + \dot{\Phi}_g)\Big] \\
&\qquad \times\omega_{gX_1''}\cos\vartheta_g + m_3 l_g\Big\{(1+\cos\vartheta_g)\cdot\Big[\dot{u}_s\cos\psi_g \\
&\quad - (\dot{w}_s - \dot{q}^* l_s)\sin\psi_g\Big] - \dot{\psi}_g\Big[u_s\sin\psi_g + (w_s - q^* l_s)\cos\psi_g\Big] \\
&\quad - V_{gX_1''}\dot{\vartheta}_g\sin\vartheta_g\Big\} + m_3 l_g^2\Big[(\omega_{gX_2'} + \omega_{gX_2''})\omega_{gX_1'}\sin\vartheta_g \\
&\quad - (1+\cos\vartheta_g)\omega_{gX_1''}\omega_{gX_3'} + \dot{\vartheta}_g\omega_{gX_3''} + \dot{\omega}_{gX_3'}\sin\vartheta_g\Big] \\
&\quad + m_3 l_s l_g\Big\{q^*\Big[(\omega_{gX_1'} - \omega_{gX_1''})\sin\psi_g\sin\vartheta_g \\
&\quad + (\omega_{gX_2'} + \omega_{gX_3''})\cos\psi_g - \omega_{gX_3'}\cos\psi_g\sin\vartheta_g\cos\vartheta_g\Big] \\
&\quad + (1+\cos\vartheta_g)\cdot r^*\omega_{gX_3'}\Big\} + \kappa(\psi_g - \psi_g^0) = M_{zc},
\end{aligned}
\tag{4.33}
$$

$$
\begin{aligned}
&(I^*_{X_1''} + I^*_{X_1'''})\frac{\mathrm{d}\omega_{gX_1''}}{\mathrm{d}t} + m_3\cdot l_g^2\ddot{\vartheta}_g + (I^*_{X_3''} - I^*_{X_2''} - I^*_{X_2'''})\cdot\omega_{gX_2''}\omega_{gX_3''} \\
&\quad + I^*_{X_3'''}(\omega_{gX_3''} + \dot{\Phi}_g)\cdot\omega_{gX_2''} + \kappa(\vartheta_g - \vartheta_g^0) \\
&\quad - m_3 l_g\Big\{\Big[\dot{\psi}_g(u_s\cos\psi_g - (w_s - q^* l_s)\sin\psi_g) + \dot{u}_s\sin\psi_g \\
&\quad + (w_s - q^* l_s)\cos\psi_g\Big]\sin\vartheta_g + \dot{\vartheta}_g V_{gX_3''} + \dot{v}_s\cos\vartheta_g
\end{aligned}
$$

$$\begin{aligned}
&-\Big[q^*(\omega_{gX_3''}\sin\psi_g + \omega_{gX_1''}\cos\psi_g\cos\vartheta_g) + r^*\omega_{gX_1''}\sin\vartheta_g \\
&-\dot{r}^*\cos\vartheta_g\Big]\cdot l_s - \Big[(\omega_{gX_2'} + \omega_{gX_2''})\cdot\omega_{gX_3''} - \omega_{gX_1'}\omega_{gX_1''}\sin\vartheta_g \\
&+ (1+\cos\vartheta_g)\cdot\dot{\omega}_{gX_1'}\Big]\cdot l_g\Big\} = M_{zb},
\end{aligned} \tag{4.34}$$

$$I^*_{X_3'''}\frac{\mathrm{d}}{\mathrm{d}t}(\omega_{gX_3''} + \dot{\Phi}_g) = M_k - M_{rk}, \tag{4.35}$$

where

$$\dot{\omega}^0_{gX_1'} = \frac{\mathrm{d}\omega^0_{gX_1'}}{\mathrm{d}t} = \dot{p}^*\cos\psi^0_g - p^*\dot{\psi}^0_g\sin\psi^0_g - \dot{r}^*\sin\psi^0_g - r^*\cos\psi^0_g,$$

$$\dot{\omega}^0_{gX_3'} = \frac{\mathrm{d}\omega^0_{gX_3'}}{\mathrm{d}t} = \dot{p}^*\sin\psi^0_g + p^*\dot{\psi}^0_g\cos\psi^0_g + \dot{r}^*\cos\psi^0_g - r^*\sin\psi^0_g.$$

The preceding mathematical model of gyroscope motion, along with the equations of motion of the base (board of FO) on which the gyroscope is set, makes it possible to perform large-scale simulation investigations of gyroscope dynamics. Moreover, the presented form of equations has the most general and universal character. From these equations it is possible to derive all other equations describing the known types of gyroscopes. It should be emphasized that in the model governed by (4.31)–(4.35), deformability of the rotor is taken into account (elasticity coefficient κ) as is the position of the center of mass of the gyroscope at some distance l_s from the center of mass of the OL (which can matter in the case of a non-astatic gyroscope). Since no known analytical methods of solving the derived equations exist, investigation of the model will be performed by means of numerical methods. The universality of (4.31)–(4.35) relies on the fact that by ignoring specific terms of particular equations, it is possible to obtain the desired gyroscope models. In the next subsection, we will present an example of transformation of the aforementioned equations into forms describing a model of a classic, controlled gyroscope on a fixed base.

4.1.1 Astatic Gyroscope on a Fixed Platform with Axis Stiff-Connected to Rotor

Suppose that a gyroscope is located on a fixed base, which implies that $u_s = 0$, $v_s = 0$, $w_s = 0$, $p_s = 0$, $q_s = 0$, $r_s = 0$. We do not take into account the rotational motion of the Earth, and we assume that the gyroscope is astatic, i.e., the distance of the center of mass of the system rotor's internal frame $l_g = 0$. The equations of motion of the gyroscope take the form

$$I^0_{X_2''}\tfrac{\mathrm{d}^2\psi_g^0}{\mathrm{d}t^2}\cos^2\vartheta_g^0 - I^0_{X_2''}\dot{\psi}_g^0\dot{\vartheta}_g^0\sin 2\vartheta_g^0 - \kappa(\psi_g - \psi_g^0) = M_c - M_{rc}, \tag{4.36a}$$

$$I^0_{X_1''}\tfrac{\mathrm{d}^2\vartheta_g^0}{\mathrm{d}t^2} + \tfrac{1}{2}I^0_{X_2''}(\dot{\psi}_g^0)^2\sin 2\vartheta_g^0 - \kappa(\vartheta_g - \vartheta_g^0) = M_b - M_{rb}, \tag{4.36b}$$

$$\begin{aligned}
&\left[I_{X_2'} + I^*_{X_2''} + I^*_{X_2'''} + (I^*_{X_3''} - I^*_{X_2''} - I^*_{X_2'''})\sin^2\vartheta_g\right]\frac{\mathrm{d}^2\psi_g}{\mathrm{d}t^2}\\
&\quad + (I^*_{X_3''} - I^*_{X_2''} - I^*_{X_2'''})\cdot\dot{\psi}_g\dot{\vartheta}_g\sin 2\vartheta_g\\
&\quad - I^*_{X_3'''}\frac{\mathrm{d}}{\mathrm{d}t}(\dot{\Phi}_g - \dot{\psi}_g\sin\vartheta_g)\sin\vartheta_g\\
&\quad - I^*_{X_3'''}(\dot{\Phi}_g - \dot{\psi}_g\sin\vartheta_g)\dot{\vartheta}_g\cos\vartheta_g + \kappa(\psi_g - \psi_g^0) = M_{zc},
\end{aligned} \tag{4.37}$$

$$\begin{aligned}
&(I^*_{X_1''} + I^*_{X_1'''})\frac{\mathrm{d}^2\vartheta_g}{\mathrm{d}t^2} - \frac{1}{2}(I^*_{X_3''} - I^*_{X_2''} - I^*_{X_2'''})\dot{\psi}_g^2\sin 2\vartheta_g + \kappa(\vartheta_g - \vartheta_g^0)\\
&\quad + I^*_{X_3'''}(\dot{\Phi}_g - \dot{\psi}_g\sin\vartheta_g)\dot{\psi}_g\cos\vartheta_g = M_{zb},
\end{aligned} \tag{4.38}$$

$$I_{X_3'''}\frac{\mathrm{d}}{\mathrm{d}t}(\dot{\Phi}_g - \dot{\psi}_g\sin\vartheta_g) = M_k - M_{rk}. \tag{4.39}$$

Equations (4.36a) and (4.36b) yield

$$(\psi_g - \psi_g^0) = \frac{I^0_{X_2''}\frac{\mathrm{d}^2\psi_g^0}{\mathrm{d}t^2}\cos^2\vartheta_g - I^0_{X_2''}\dot{\psi}_g^0\dot{\vartheta}_g^0\sin 2\vartheta_g^0 - M_c + M_{rc}}{\kappa}, \tag{4.40a}$$

$$(\vartheta_g - \vartheta_g^0) = \frac{I^0_{X_1''}\frac{\mathrm{d}^2\vartheta_g^0}{\mathrm{d}t^2} + \frac{1}{2}I^0_{X_2''}(\dot{\psi}_g^0)^2\sin 2\vartheta_g^0 - M_b + M_{rb}}{\kappa}. \tag{4.40b}$$

Substituting (4.40a) into (4.37) and (4.40b) into (4.38), one obtains

$$\begin{aligned}
&\left[I_{X_2'} + I^*_{X_2''} + I^*_{X_2'''} + (I^*_{X_3''} - I^*_{X_2''} - I^*_{X_2'''})\sin^2\vartheta_g\right]\frac{\mathrm{d}^2\psi_g}{\mathrm{d}t^2}\\
&\quad + (I^*_{X_3''} - I^*_{X_2''} - I^*_{X_2'''})\dot{\psi}_g\dot{\vartheta}_g\sin 2\vartheta_g - I^*_{X_3'''}\frac{\mathrm{d}}{\mathrm{d}t}(\dot{\Phi}_g - \dot{\psi}_g\sin\vartheta_g)\sin\vartheta_g
\end{aligned}$$

$$\begin{aligned}
&- I^*_{X_3'''}(\dot{\Phi}_g - \dot{\psi}_g \sin\vartheta_g)\dot{\vartheta}_g \cos\vartheta_g + I^0_{X_2''}\frac{\mathrm{d}^2\psi_g^0}{\mathrm{d}t^2}\cos^2\vartheta_g \\
&- I^0_{X_2''}\dot{\psi}_g^0\dot{\vartheta}_g^0 \sin 2\vartheta_g^0 = M_{zc} + M_c - M_{rc},
\end{aligned} \tag{4.41}$$

$$\begin{aligned}
&(I^*_{X_1''} + I^*_{X_1'''})\frac{\mathrm{d}^2\vartheta_g}{\mathrm{d}t^2} - \frac{1}{2}(I^*_{X_3''} - I^*_{X_2''} - I^*_{X_2'''})\dot{\psi}_g^2 \sin 2\vartheta_g \\
&+ I^0_{X_1''}\frac{\mathrm{d}^2\vartheta_g^0}{\mathrm{d}t^2} + I^*_{X_3'''}(\dot{\Phi}_g - \dot{\psi}_g \sin\vartheta_g)\dot{\psi}_g \cos\vartheta_g \\
&+ \frac{1}{2}I^0_{X_2''}(\dot{\psi}_g^0)^2 \sin 2\vartheta_g^0 = M_{zb} + M_b - M_{rb}.
\end{aligned} \tag{4.42}$$

Consider the case where the stiffness coefficient $\kappa \to \infty$. It follows from (4.40a) and (4.40b) that

$$\psi_g^0 \approx \psi_g \quad \text{and} \quad \vartheta_g^0 \approx \vartheta_g. \tag{4.43}$$

Thus, we obtained constraint equations for (4.37) and (4.38). This means that the axis will be stiff-connected to the gyroscope rotor. Taking into account constraints (4.43), (4.41) and (4.42) take the form

$$\begin{aligned}
&\left[I_{X_2'} + I_{X_3''} + (I_{X_2''} + I^0_{X_2''} + I_{X_2'''} - I_{X_3''})\cos^2\vartheta_g\right]\frac{\mathrm{d}^2\psi_g}{\mathrm{d}t^2} \\
&\quad - (I_{X_2''} + I^0_{X_2''} + I_{X_2'''})\dot{\psi}_g\dot{\vartheta}_g \sin 2\vartheta_g \\
&\quad - I_{X_3'''}\frac{\mathrm{d}}{\mathrm{d}t}(\dot{\Phi}_g - \dot{\psi}_g \sin\vartheta_g)\sin\vartheta_g + I_{X_3'''}(\dot{\Phi}_g - \dot{\psi}_g \sin\vartheta_g)\dot{\vartheta}_g \cos\vartheta_g \\
&= M_{zc} + M_c - M_{rc},
\end{aligned} \tag{4.44}$$

$$\begin{aligned}
&(I_{X_1''} + I^0_{X_1''} + I_{X_1'''})\frac{\mathrm{d}^2\vartheta_g}{\mathrm{d}t^2} + \frac{1}{2}(I_{X_2''} + I^0_{X_2''} + I_{X_2'''} - I_{X_3''})\dot{\psi}_g^2 \sin 2\vartheta_g \\
&\quad + I_{X_3'''}(\dot{\Phi}_g - \dot{\psi}_g \sin\vartheta_g)\dot{\psi}_g \cos\vartheta_g = M_{zb} + M_b - M_{rb}.
\end{aligned} \tag{4.45}$$

If we ignore the inertia of the frames $I_{X_1''} = 0$, $I^0_{X_1''} = 0$, $I_{X_2''} = 0$, $I^0_{X_2''} = 0$, $I_{X_2'} = 0$, $I_{X_3''} = 0$ and the values of the disturbing torques $M_{zb} = 0$ and $M_{zc} = 0$, and if we introduce additional designations (bearing in mind that the rotor is axially symmetric), then $I_{X_1'''} = I_{X_2'''} = I_{gk}$, $I_{X_3'''} = I_{go}$, then formulas (4.41) and (4.42) are cast to the following form

$$\begin{aligned}
&I_{gk}\frac{\mathrm{d}^2\psi_g}{\mathrm{d}t^2}\cos^2\vartheta_g - I_{gk}\dot{\psi}_g\dot{\vartheta}_g \sin 2\vartheta_g - I_{go}(\dot{\Phi}_g - \dot{\psi}_g \sin\vartheta_g)\dot{\vartheta}_g \cos\vartheta_g \\
&\quad = M_c + M_k - M_{rc},
\end{aligned} \tag{4.46a}$$

$$I_{gk}\frac{\mathrm{d}^2\vartheta_g}{\mathrm{d}t^2}+\frac{1}{2}I_{gk}\dot{\psi}_g^2\sin 2\vartheta_g+I_{go}(\dot{\Phi}_g-\dot{\psi}_g\sin\vartheta_g)\dot{\psi}_g\cos\vartheta_g = M_b-M_{rb}. \quad (4.46b)$$

Suppose that the torque driving the rotor is equal to the moment of friction forces in the rotor bearings and aerodynamic resistance

$$M_k = M_{rk}, \quad (4.47a)$$

and hence

$$\frac{\mathrm{d}\Phi_g}{\mathrm{d}t}-\dot{\psi}_g\sin\vartheta_g = \mathrm{const} = n_g. \quad (4.47b)$$

Finally, taking into account (4.47a), (4.47b) will take the form

$$I_{gk}\frac{\mathrm{d}^2\psi_g}{\mathrm{d}t^2}\cos^2\vartheta_g-I_{gk}\dot{\psi}_g\dot{\vartheta}_g\sin 2\vartheta_g-I_{go}n_g\dot{\vartheta}_g\cos\vartheta_g = M_c-M_{rc}, \quad (4.48a)$$

$$I_{gk}\frac{\mathrm{d}^2\vartheta_g}{\mathrm{d}t^2}+\frac{1}{2}I_{gk}\dot{\psi}_g^2\sin 2\vartheta_g+I_{go}n_g\dot{\psi}_g\cos\vartheta_g = M_b-M_{rb}. \quad (4.48b)$$

We have obtained equations of motion of a classic gyroscope on a fixed base with the axis stiff-connected to the rotor.

Numerical investigations to be carried out later on in this work for systems describing gyroscope motion [such as (4.75a)], it is convenient to perform, not for a real time t, but for a “dimensionless” τ, which is determined as follows [5,6,8]:

$$\tau = \Omega\cdot t, \quad (4.49)$$

where

$$\Omega = \frac{I_{go}n_g}{I_{gk}}.$$

Rescaling time one obtains

$$\frac{\mathrm{d}}{\mathrm{d}t} = \frac{\mathrm{d}}{\mathrm{d}\tau}\frac{\mathrm{d}\tau}{\mathrm{d}t} = \Omega\frac{\mathrm{d}}{\mathrm{d}\tau} \quad (4.50)$$

and

$$\dot{\vartheta}_g = \Omega\frac{\mathrm{d}\vartheta_g}{\mathrm{d}\tau} = \Omega\vartheta_g', \qquad \ddot{\vartheta}_g = \Omega^2\frac{\mathrm{d}^2\vartheta_g}{\mathrm{d}\tau^2} = \Omega^2\vartheta_g'', \quad (4.51a)$$

and similarly

$$\dot{\psi}_g = \Omega\cdot\psi_g', \qquad \ddot{\psi}_g = \Omega^2\psi_g''. \quad (4.51b)$$

The change in time scale in the preceding examples makes the numerical analysis of the equation of motion easier because the change makes values of the equation elements equal and allows us to introduce a greater integration step. This makes numerical errors smaller.

Applying the dimensionless time τ in (4.48a)–(4.48b) and taking into account (4.50), (4.51a), and (4.51b) one finds

$$\frac{\mathrm{d}^2\psi_g}{\mathrm{d}\tau^2}\cos^2\vartheta_g - \psi_g'\vartheta_g'\sin 2\vartheta_g + b_b\psi_g' - \vartheta_g'\cos\vartheta_g = c_bM_c, \tag{4.52a}$$

$$\frac{\mathrm{d}^2\vartheta_g}{\mathrm{d}\tau^2} + \frac{1}{2}(\psi_g')^2\sin 2\vartheta_g + b_c\vartheta_g' + \psi_g'\cos\vartheta_g = c_cM_b, \tag{4.52b}$$

where

$$b_b = \frac{\eta_b}{I_{gk}\Omega}, \quad b_c = \frac{\eta_c}{I_{gk}\Omega}, \quad c_b = \frac{1}{I_{gk}\Omega^2}, \quad c_c = \frac{1}{I_{gk}\Omega^2}.$$

4.1.2 Simplified Equations (Technical) of Motion of a Gyroscope

Analysis of (4.48) and (4.52) is very troublesome because of the difficulties in obtaining analytical solutions. System (4.48) is strongly non-linear, which is why its solution can be obtained only by means of numerical methods. However, the system can be simplified considerably if we eliminate terms that have a slight effect on the motion character of the gyroscope.

Note that the value of the angular velocity of eigenrotations $\dot{\Phi}_g$ of the gyroscope is incomparably greater than the value of the velocities $\dot{\vartheta}_g$ and $\dot{\psi}_g$ of rotations of the internal and external frames. Hence, in (4.48) we can leave out those terms that include products $\dot{\vartheta}_g$ and $\dot{\psi}_g$ or their squares as higher-order quantities of smallness. Moreover, if we consider a fixed range of rotor operation corresponding to balancing the driving torque M_k with the resistance torques M_{rk}, i.e., an almost constant angular velocity of the eigenrotations of the gyroscope, $\dot{\Phi}_g \cong \text{const} = n_g$, then (4.48) will take the following forms:

$$I_{gk}\frac{\mathrm{d}^2\vartheta_g}{\mathrm{d}t^2} + I_{go}n_g\dot{\psi}_g\cos\vartheta_g = M_b - M_{rb}, \tag{4.53a}$$

$$I_{gk}\frac{\mathrm{d}^2\psi_g}{\mathrm{d}t^2} - I_{go}n_g\dot{\vartheta}_g\cos\vartheta_g = M_c - M_{rc}. \tag{4.53b}$$

The preceding forms of equations, governing the motion of a gyroscope about a fixed point of its suspension, are called *technical equations* or the *technical theory* of the *gyroscope* [7, 9, 10].

Taking into account the fact that (as was earlier assumed) angular velocities $\dot{\vartheta}_g$ and $\dot{\psi}_g$ have small values and assuming that the initial conditions equal zero, one can assume, with sufficient accuracy from a practical viewpoint, that $\cos\vartheta_g \cong 1$. If we assume that the moments of friction forces in the frame bearings are small, i.e., $M_{rb} = 0$, $M_{rc} = 0$, then (4.53) will take simpler, final forms:

$$I_{gk}\frac{\mathrm{d}^2\vartheta_g}{\mathrm{d}t^2} + I_{go}n_g\dot{\psi}_g = M_b, \tag{4.54a}$$

$$I_{gk}\frac{\mathrm{d}^2\psi_g}{\mathrm{d}t^2} - I_{go}n_g\dot{\vartheta}_g = M_c. \tag{4.54b}$$

4.1.3 Remarks on the Model of Gyroscopic Motion

The most general mathematical model of a controlled gyroscope has been derived. It follows from the literature overview that the complete numerical investigations of the dynamics of the controlled gyroscope have not been performed satisfactorily, especially when the full equations describing the motion of a gyroscope base (e.g., board of a FO) are taken into account. This option is ensured by the model given in this chapter and governed by (4.31)–(4.35). In particular, it makes it possible to examine the influence of the following factors on the accuracy of maintaining the preset motion (position) in space by the gyroscope axis:

1. Inertia of suspension frames.
2. Distance l_g between the center of mass of the gyroscope and the center of its rotation (unbalanced gyroscope).
3. Distances l_s between the center of mass of the gyroscope and the center of mass of the FO.
4. Stiffness κ of the element connecting the rotor to the gyroscope axis.
5. Kinematic excitations in the form of linear u_s, v_s, w_s and angular p_s, q_s, r_s velocities (and their first derivatives with respect to time) affecting the gyroscope suspension.
6. Rotational motion of the Earth.

The generality of the model enables us to analyze various types of gyroscopes by means of elimination of appropriate terms in (4.31)–(4.35). Thus, one could pass from the description of a non-astatic gyroscope on an elastic suspension to a classic description of an astatic gyroscope.

The computing power of today's computers allows one, in a relatively simple way, to verify the results obtained thus far of the theoretical investigations of gyroscopes—reduced to simplified models in most cases—with the results obtained from numerical simulations of a completely non-linear model.

4.2 Gyroscope Control

The motion of a gyroscope axis can be realized under the influence of the controlling torques M_b and M_c and angular motion of its base, determined by angular velocities $p^*(t)$, $q^*(t)$, and $r^*(t)$, or the linear movements of its base (in the case of a non-astatic gyroscope), determined by linear velocities $u_s(t)$, $v_s(t)$, and $w_s(t)$. While the torques cause the excitation of motion of a gyroscope axis by external forces, the angular and linear velocities of the base reflect the parametrical excitation of the motion.

In this subsection, we will consider programmable control of motion of a gyroscope axis in an open system and corrective and stabiling control of motion of a gyroscope axis in a closed system. We will examine the effect of gyroscope errors on the realization of preset motion. Moreover, we will give optimal control algorithms of position of a gyroscope axis relative to a preset trajectory.

4.2.1 Motion Control of Gyroscope Axis in an Open System: The Inverse Problem in Gyroscope Dynamics

The inverse problem of a gyroscope relies on determining the torques $M_b(t)$ and $M_c(t)$ that, acting on the gyroscope frames, will set the gyroscope axis in motion, specified by the angles $\vartheta_{gz}(t)$ and $\psi_{gz}(t)$. Thus, the problem is reduced to determining programs according to which the torques $M_b(t)$ and $M_c(t)$ are to change in time, i.e., the programmable control of the gyroscope axis motion in an open system [11–13].

In order to determine the torques $M_b(t)$ and $M_c(t)$ we make use of the general definition, which says that inverse problems of dynamics are called problems that rely on *determining the external forces, the parameters of this system, and the constraints imposed on the system at which motion with preset properties is the only motion among all possible motions*. In practice, these problems refer to the particular cases relying on formulating the algorithms that determine the controlling forces and realize the desired motion of a dynamical system—regardless of the problem conditions—though they are not always achieved.

Thus, the inverse problem relies on task of runs as functions of time $\vartheta_g = \vartheta_g(t)$ and $\psi_g = \psi_g(t)$, substituting them into the left-hand sides of the equations of motion of a gyroscope axis and evaluating $M_b(t)$ and $M_c(t)$ (i.e., the right-hand sides of these equations). The determined torques M_b and M_c, plugged into the right-hand sides of the equations of motion, give a unique (appropriate) result only for the angular velocities $\dot{\vartheta}_g(t)$ and $\dot{\psi}_g(t)$, while only for the angles will the result not be unique in general since it depends on integration constants of the angles' derivatives. This can be compensated by appropriate selection of the integration constants in the solution to the equations.

This implies that the determined $M_b(t)$ and $M_c(t)$, on the basis of the inverse problem solution, can be used to programmatically control only of the derivatives angles and not the angles of the gyroscope position. A scheme for an algorithm to control a gyroscope in an open system is depicted in Fig. 4.2.

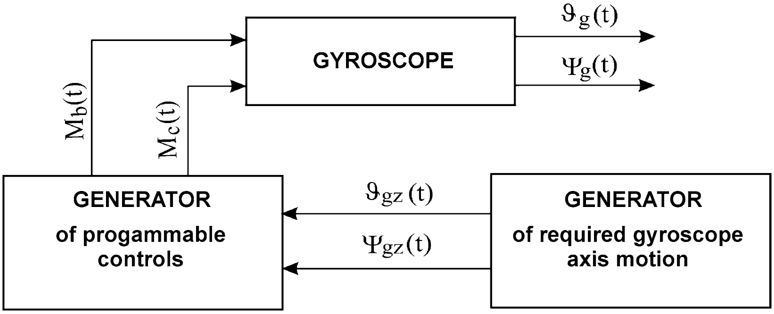

Fig. 4.2 Scheme of algorithm for controlling a gyroscope in an open system

Consider the following problem: let a gyroscope axis describe the a surface of a cone (Fig. 4.3a). Then the following equations must be satisfied:

$$\begin{aligned} \vartheta_{gz}(t) &= \Theta_k \sin \nu_k t, & \psi_{gz}(t) &= \Theta_k \cos \nu_k t, \\ \frac{\vartheta_{gz}}{\mathrm{d}t} &= \Theta_k \nu_k \cos \nu_k t, & \frac{\psi_{gz}}{\mathrm{d}t} &= -\Theta_k \nu_k \sin \nu_k t, \\ \frac{\mathrm{d}^2\vartheta_{gz}}{\mathrm{d}t^2} &= -\Theta_k \nu_k^2 \sin \nu_k t, & \frac{\mathrm{d}^2\psi_{gz}}{\mathrm{d}t^2} &= -\Theta_k \nu_k^2 \cos \nu_k t. \end{aligned} \tag{4.55}$$

Let us make use of the linearized equations of a gyroscope (4.53b)–(4.53b) in which we suppose that $\Theta_g \ll 1$ and the friction in the suspension bearings is of a viscous type. Then they will have the following form [14–16]:

$$\begin{aligned} \frac{\mathrm{d}^2\vartheta_g}{\mathrm{d}t^2} + \eta_b \Omega \frac{\mathrm{d}\vartheta_g}{\mathrm{d}t} - \Omega \frac{\mathrm{d}\psi_g}{\mathrm{d}t} &= \frac{M_b}{I_{gk}}, \\ \frac{\mathrm{d}^2\psi_g}{\mathrm{d}t^2} + \eta_c \Omega \frac{\mathrm{d}\psi_g}{\mathrm{d}t} + \Omega \frac{\mathrm{d}\vartheta_g}{\mathrm{d}t} &= \frac{M_c}{I_{gk}}. \end{aligned} \tag{4.56}$$

Substituting (4.55) into the left-hand side of (4.56) we obtain

$$\begin{aligned} \frac{\mathrm{d}^2\vartheta_{gz}}{\mathrm{d}t^2} + \eta_b \Omega \frac{\mathrm{d}\vartheta_{gz}}{\mathrm{d}t} - \Omega \frac{\mathrm{d}\psi_{gz}}{\mathrm{d}t} &= \Theta_k \nu_k (\Omega - \nu_k) \sin \nu_k t + \eta_b \Theta_k \nu_k \Omega \cos \nu_k t, \\ \frac{\mathrm{d}^2\psi_{gz}}{\mathrm{d}t^2} + \eta_c \Omega \frac{\mathrm{d}\psi_{gz}}{\mathrm{d}t} + \Omega \frac{\mathrm{d}\vartheta_{gz}}{\mathrm{d}t} &= \Theta_k \nu_k (\Omega - \nu_k) \cos \nu_k t - \eta_c \Theta_k \nu_k \Omega \sin \nu_k t, \end{aligned} \tag{4.57}$$

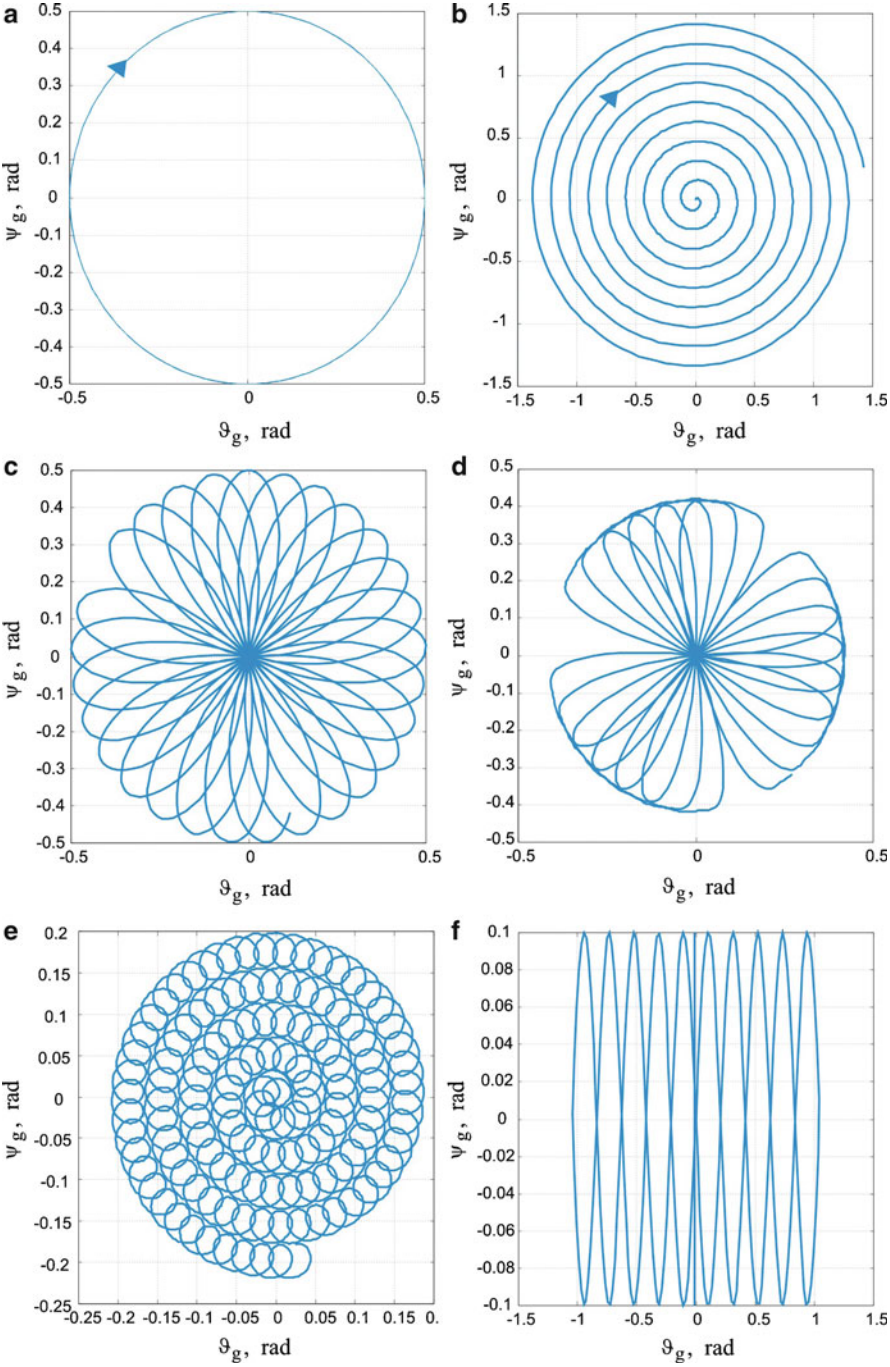

Fig. 4.3 Examples of curves drawn by the gyroscope axis: (**a**) on a cone surface, (**b**) along Archimedes spiral, (**c**) n-flute rosette, (**d**) modified n-flute rosette, (**e**) described by (4.67), (**f**) described by (4.68)

and hence

$$\begin{aligned} M_b &= I_{gk}[\Theta_k \nu_k (\Omega - \nu_k) \sin \nu_k t + \eta_b \Theta_k \nu_k \Omega \cos \nu_k t], \\ M_c &= I_{gk}[\Theta_k \nu_k (\Omega - \nu_k) \cos \nu_k t - \eta_b \Theta_k \nu_k \Omega \sin \nu_k t]. \end{aligned} \tag{4.58}$$

Thus, we have the torques $M_b(t)$ and $M_c(t)$ determined as functions of time. Now let us check what trajectory will be generated by these torques. Let us substitute them into the right-hand sides of (4.56):

$$\begin{aligned} \frac{\mathrm{d}^2\vartheta_g}{\mathrm{d}t^2} + \eta_b \Omega \frac{\mathrm{d}\vartheta_g}{\mathrm{d}t} - \Omega \frac{\mathrm{d}\psi_g}{\mathrm{d}t} &= \Theta_k \nu_k (\Omega - \nu_k) \sin \nu_k t + \eta_b \Theta_k \nu_k \Omega \cos \nu_k t, \\ \frac{\mathrm{d}^2\psi_g}{\mathrm{d}t^2} + \eta_c \Omega \frac{\mathrm{d}\psi_g}{\mathrm{d}t} + \Omega \frac{\mathrm{d}\vartheta_g}{\mathrm{d}t} &= \Theta_k \nu_k (\Omega - \nu_k) \cos \nu_k t - \eta_c \Theta_k \nu_k \Omega \sin \nu_k t. \end{aligned} \tag{4.59}$$

The inverse problem is unique for the derivatives of angles ϑ_g and ψ_g with respect to time, but for stationary motion [17, 18], i.e., as $t \to \infty$ (a transient process is depicted in Figs. 4.6b and 4.7b). However, that question arises as to whether the solutions to the preceding equations will also describe the preset motion of the gyroscope axis. If we impose the initial angular position of the axis as required, $\vartheta_{gz}(0) = 0$ and $\psi_{gz}(0) = \Theta_k$, then we will obtain the required angular displacements of the gyroscope axis. If, however, the initial position of the axis is not the one we need, e.g., $\vartheta_{gz}(0) = 0.1$ rad and $\psi_{gz}(0) = 0.1$ rad, then despite the fact that the angular velocities are the ones we need, the gyroscope axis does not describe the required surface (Figs. 4.5 and 4.7).

In the case of angular deviations taking large values of the gyroscope axis, the control moments $M_b(\tau)$ and $M_c(\tau)$, as functions of non-dimensional time τ, are determined from the non-linear (4.52a)–(4.52b):

$$M_b(\tau) = \frac{\mathrm{d}^2\vartheta_{gz}}{\mathrm{d}\tau^2} + b_b \frac{\mathrm{d}\vartheta_{gz}}{\mathrm{d}\tau} + \frac{1}{2}\left(\frac{\mathrm{d}\psi_{gz}}{\mathrm{d}\tau}\right)^2 \sin 2\vartheta_{gz} + \frac{\mathrm{d}\psi_{gz}}{\mathrm{d}\tau} \cos \vartheta_{gz}, \tag{4.60}$$

$$M_c(\tau) = \frac{\mathrm{d}^2\psi_{gz}}{\mathrm{d}\tau^2} \cos^2 \vartheta_{gz} + b_c \frac{\mathrm{d}\psi_{gz}}{\mathrm{d}\tau} - \frac{\mathrm{d}\psi_{gz}}{\mathrm{d}\tau} \frac{\mathrm{d}\vartheta_{gz}}{\mathrm{d}\tau} \sin 2\vartheta_{gz} + \frac{\mathrm{d}\vartheta_{gz}}{\mathrm{d}\tau} \cos \vartheta_{gz}, \tag{4.61}$$

where

$$b_b = \frac{\eta_b}{I_{gk}\Omega}, \quad b_c = \frac{\eta_c}{I_{gk}\Omega}.$$

If, also in this case, we require that the gyroscope axis must move on the surface of a cone, then programmable controls (4.60) and (4.61) take the following form:

$$\begin{aligned} M_b(\tau) = \frac{1}{c_b}\Bigg[&- \Theta_k \left(\frac{\nu_k}{\Omega}\right)^2 \sin \frac{\nu_k}{\Omega}\tau + b_b \Theta_k \frac{\nu_k}{\Omega} \cos \frac{\nu_k}{\Omega}\tau \\ &+ \frac{1}{2}\Theta_k^2 \sin^2 \frac{\nu_k}{\Omega}\tau \sin 2\left(\Theta_k \sin \frac{\nu_k}{\Omega}\tau\right) \\ &- \Theta_k \frac{\nu_k}{\Omega} \sin \frac{\nu_k}{\Omega}\tau \cos\left(\Theta_k \sin \frac{\nu_k}{\Omega}\tau\right)\Bigg], \end{aligned} \tag{4.62}$$

$$\begin{aligned} M_c(\tau) = \frac{1}{c_c}\Bigg[&- \Theta_k^2 \left(\frac{\nu_k}{\Omega}\right)^2 \cos \frac{\nu_k}{\Omega}\tau \cos^2\left(\Theta_k \sin \frac{\nu_k}{\Omega}\right) \\ &- b_c \Theta_k \frac{\nu_k}{\Omega} \sin \frac{\nu_k}{\Omega}\tau + \frac{1}{2}\Theta_k^2 \left(\frac{\nu_k}{\Omega}\right)^2 \sin 2\frac{\nu_k}{\Omega}\tau \sin 2(\Theta_k \sin p\tau) \\ &+ \Theta_k \frac{\nu_k}{\Omega} \cos \frac{\nu_k}{\Omega}\tau \cos\left(\Theta_k \sin \frac{\nu_k}{\Omega}\right)\Bigg]. \end{aligned} \tag{4.63}$$

The preceding problem of gyroscope axis control on a cone's surface is one of the possible problems. We can substitute other functional relations for the angles $\vartheta_{gz}(\tau)$ and $\psi_{gz}(\tau)$ and their first and second derivatives into the programmable controls governed by (4.60) and (4.61). Some of the most characteristic examples of the required motion of a gyroscope axis that can be applied in detection or tracking systems are depicted below [19, 20]:

1. Motion of gyroscope axis along Archimedes spiral (Fig. 4.3b):

$$\begin{aligned} \vartheta_{gz}(\tau) &= a_g \frac{\nu_s}{\Omega}\tau \sin\left(\frac{\nu_s}{\Omega}\right), \\ \psi_{gz}(\tau) &= b_g \nu_s \tau \cos\left(\frac{\nu_s}{\Omega}\right). \end{aligned} \tag{4.64}$$

2. Motion of gyroscope axis along n-flute rosette (Fig. 4.3c)

$$\begin{aligned} \vartheta_{gz}(\tau) &= \Theta_r \sin\left(\frac{\nu_2}{\Omega}\tau\right) \cos\left(\frac{\nu_1}{\Omega}\tau\right), \\ \psi_{gz}(\tau) &= \Theta_r \sin\left(\frac{\nu_2}{\Omega}\tau\right) \sin\left(\frac{\nu_1}{\Omega}\tau\right). \end{aligned} \tag{4.65}$$

3. Motion of a gyroscope axis along a modified *n*-flute rosette:

$$\begin{aligned}\vartheta_{gz}(\tau) &= \varTheta_r\left[\sin\left(\frac{\nu_2}{\varOmega}\tau\right) + 0,2\sin\left(3\frac{\nu_2}{\varOmega}\tau\right) + 0.04\sin\left(5\frac{\nu_2}{\varOmega}\tau\right)\right]\cos\left(\frac{\nu_1}{\varOmega}\tau\right),\\ \psi_{gz}(\tau) &= \varTheta_r\left[\sin\left(\frac{\nu_2}{\varOmega}\tau\right) + 0,2\sin\left(3\frac{\nu_2}{\varOmega}\tau\right) + 0.04\sin\left(5\frac{\nu_2}{\varOmega}\tau\right)\right]\sin\left(\frac{\nu_1}{\varOmega}\tau\right).\end{aligned} \tag{4.66}$$

4. Motion of gyroscope axis along curve depicted in Fig. 4.3e and described by the following relationships:

$$\begin{aligned}\vartheta_{gz} &= \frac{a_b}{\varOmega}\tau\cos\left(\frac{\nu_b}{\varOmega}\tau\right) + 0,2a_b\cos\left[2,5\frac{\nu_b}{\varOmega}\left(1+\frac{5}{\varOmega}\tau\right)\tau\right],\\ \psi_{gz} &= \frac{a_b}{\varOmega}\tau\sin\left(\frac{\nu_b}{\varOmega}\tau\right) + 0,2a_b\sin\left[2,5\frac{\nu_b}{\varOmega}\left(1+\frac{5}{\varOmega}\tau\right)\tau\right].\end{aligned} \tag{4.67}$$

5. Motion of gyroscope axis along curve depicted in Fig. 4.3f and described by the following relationships:

$$\begin{aligned}\vartheta_{gz} &= \begin{cases} 2\pi/(3\varOmega)\tau & \text{dla} \quad 0 \le \tau < 0,25\tau_c,\\ -2\pi/(3\varOmega)(\tau - 0,5\tau_c) & \text{dla} \quad 0,25\tau_c \le \tau < 0,75\tau_c,\\ 2\pi/(3\varOmega)(\tau - \tau_c) & \text{dla} \quad 0,75\tau_c \le \tau < \tau_c,\end{cases}\\ \psi_{gz} &= a_h\sin\left(\frac{\nu_h}{\varOmega}\right);\end{aligned} \tag{4.68a}$$

$$\begin{aligned}\frac{\vartheta_{gz}}{\mathrm{d}\tau} &= \begin{cases} 2\pi/(3\varOmega) & \text{dla} \quad 0 \le \tau < 0,25\tau_c,\\ -2\pi/(3\varOmega) & \text{dla} \quad 0,25\tau_c \le \tau < 0,75\tau_c,\\ 2\pi/(3\varOmega) & \text{dla} \quad 0,75\tau_c \le \tau < \tau_c,\end{cases}\\ \frac{\psi_{gz}}{\mathrm{d}\tau} &= a_h\frac{\nu_h}{\varOmega}\cos\left(\frac{\nu_h}{\varOmega}\tau\right);\end{aligned} \tag{4.68b}$$

$$\frac{\mathrm{d}^2\vartheta_{gz}}{\mathrm{d}\tau^2} = 0, \qquad \frac{\mathrm{d}^2\psi_{gz}}{\mathrm{d}\tau^2} = -a_h\left(\frac{\nu_h}{\varOmega}\right)^2\sin\left(\frac{\nu_h}{\varOmega}\right). \tag{4.68c}$$

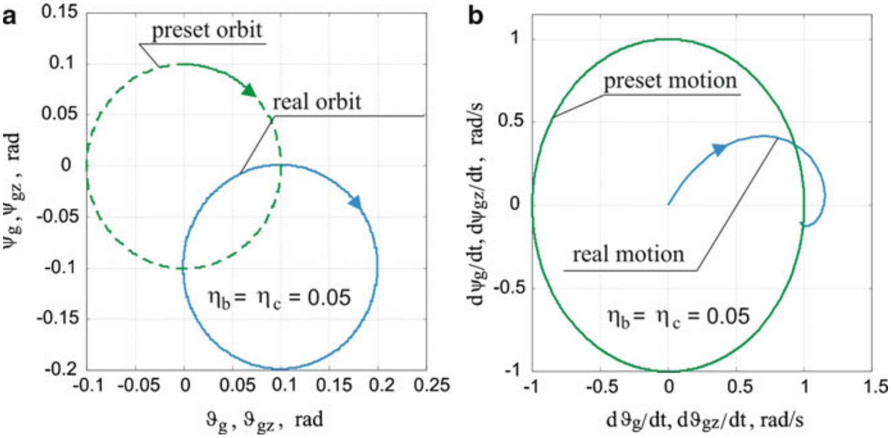

Fig. 4.4 Influence of the initial conditions on realization of motion on the cone surface by the gyroscope axis: (**a**) for angular displacements, (**b**) for angular velocities

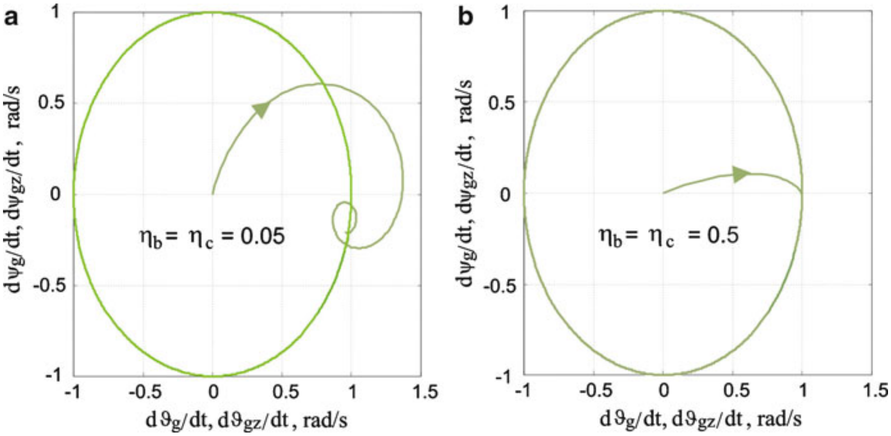

Fig. 4.5 Effect of friction in frame bearings on realization of motion on cone surface by gyroscope axis: (**a**) for small values, (**b**) for large values of viscous damping coefficients

4.2.2 Numerical Example

In Figs. 4.4–4.7, are shown (presented) selected results of computer simulations for two basic motions of a gyroscope axis: (a) describing a cone surface; (b) unfolding the surface after the Archimedes spiral.

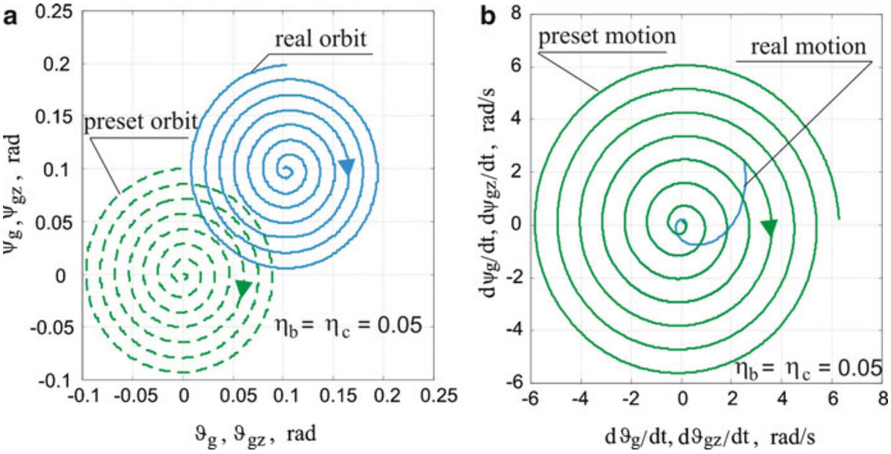

Fig. 4.6 Influence of the initial conditions on realization of the preset motion on the surface described after the Archimede spiral: (**a**) for angular displacements, (**b**) for angular velocities

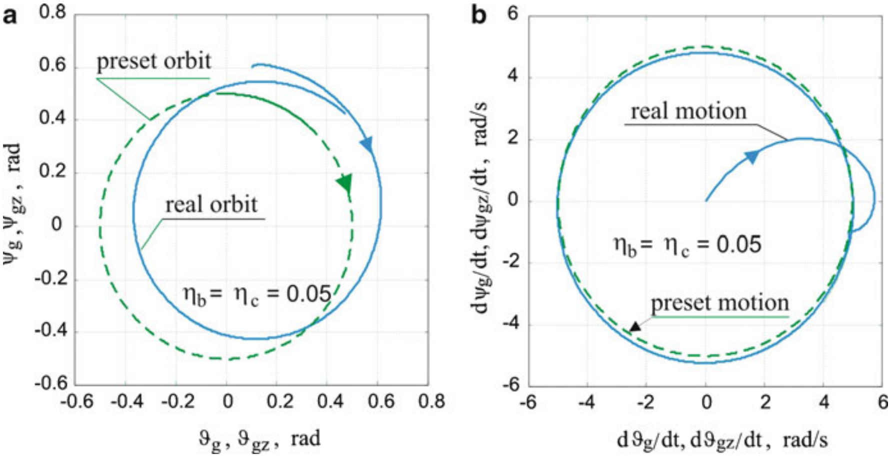

Fig. 4.7 Effect of non-linearities on realization of motion on cone surface by gyroscope axis: (**a**) for angular displacements, (**b**) for angular velocities

Calculations were performed for the following values:

$$I_{go} = 5 \cdot 10^{-4}\text{kgm}^2, \quad I_{gk} = 2.5 \cdot 10^{-4}\text{kgm}^2, \quad \eta_b = \eta_c = 0.1\text{Nms},$$
$$n_g = 600\,\text{rad/s}, \quad \nu_k = 8\,\text{rad/s}, \quad \Omega = 1{,}200\,\text{rad/s}.$$

Figures 4.4 and 4.5 present the negative influence of the initial conditions and coefficients of the friction force η_b, η_c in the frame bearings on the realization of the desired motion. In the initial conditions, unlike in the required ones, $\vartheta_g(0) = -0.1$,

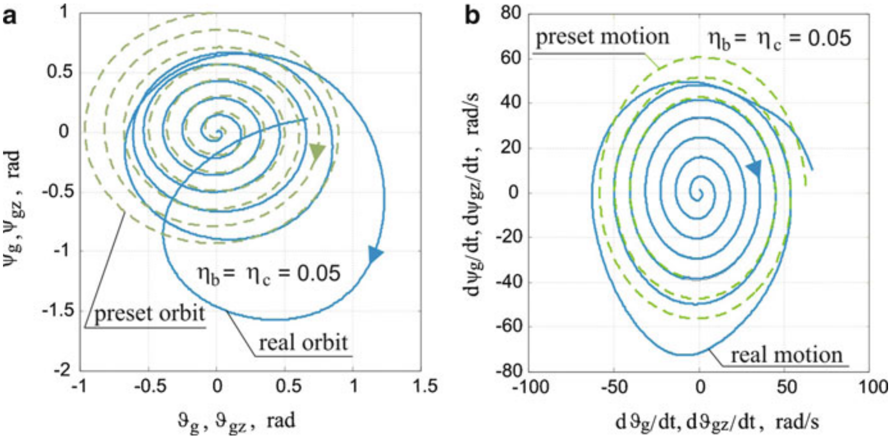

Fig. 4.8 Effect of non-linearities on realization of preset motion on surface described after the Archimedes spiral: (**a**) for angular displacements, (**b**) for angular velocities

$\vartheta_{gz}(0) = 0$, $\psi_g(0) = 0$, $\psi_{gz}(0) = -0.1$, the gyroscope axis does not delineate the required path (Figs. 4.4a and 4.6a), while the angular velocities of the axes are the one we need. However, one can see a transient process (Figs. 4.4b and 4.6b), which is certainly longer at smaller values η_b, η_c and shorter at larger ones (Fig. 4.5a, b).

Figures 4.7 and 4.8 illustrate the effect of large angular displacements on the accuracy of the required motion on the cone surface and along the Archimedes spiral.

4.2.3 Control with Constant Programmable Moments

In order to put a gyroscope axis into a preset path, one needs to change the torques controlling the gyroscope [5, 21]. It is convenient to require to guide, from given initial positions $\vartheta_g(t_0) = \vartheta_{go}$ and $\psi_g(t_0) = \psi_{go}$, the gyroscope axis to the position $\vartheta_{go}(t_0) = \vartheta_{gk}$ and $\psi_{go}(t_0) = \psi_{gk}$ by means of $M_{b_1} = \text{const}$ and $M_{c_1} = \text{const}$. The earlier determined torques M_b and M_c, which we will denote by M_{b_2} and M_{c_2}, will take the gyroscope axis from this position on the preset surface (cone, unfolded along a spiral, rosette, etc.). Thus, we control the gyroscope axis in two stages: in the first stage, the constant moments are applied, and after we reach $\vartheta_g = \vartheta_{go} = \vartheta_{gk}$ and $\psi_g = \psi_{go} = \psi_{gk}$, we go to the second stage, where the moments described by (4.60) and (4.61) are applied.

In the first stage, at the initial conditions $\ddot{\vartheta}_{go} = 0$, $\dot{\vartheta}_{go} = 0$, $\ddot{\psi}_{go} = 0$, $\dot{\psi}_{go} = 0$, we obtain the following solution to (4.56):

$$\vartheta_g(t) = \vartheta_{go} + \frac{\mathit{\Omega}(\eta_c M_{b_1} + M_{c_1})}{I_{gk}\omega_{go}^2}\left[t - \frac{2h_g^*}{\omega_{go}^2}\left(1 - \mathrm{e}^{-h_g^* t}\cos\omega_g^* t\right) - \frac{(\omega_g^*)^2 - (h_g^*)^2}{\omega_{go}^2\omega_g^*}\mathrm{e}^{-h_g^* t}\sin\omega_g^* t\right], \quad (4.69a)$$

$$\psi_g(t) = \vartheta_{go} + \frac{\mathit{\Omega}(\eta_b M_{c_1} - M_{b_1})}{I_{gk}\omega_{go}^2}\left[t - \frac{2h_g^*}{\omega_{go}^2}\left(1 - \mathrm{e}^{-h_g^* t}\cos\omega_g^* t\right) - \frac{(\omega_g^*)^2 - (h_g^*)^2}{\omega_{go}^2\omega_g^*}\mathrm{e}^{-h_g^* t}\sin\omega_g^* t\right], \quad (4.69b)$$

where

$$\omega_g^0 = \sqrt{\omega_{go}^2 - (h_g^*)^2}, \quad \omega_{go}^2 = (1 + \eta_b\eta_c)\mathit{\Omega}^2, \quad h_g^* = \frac{\mathit{\Omega}}{2}(\eta_b + \eta_c).$$

At large values of h_g^* and short time of motion in the first stage, we can make the following approximation:

$$\vartheta_g(t) \approx \vartheta_{go} + \frac{\mathit{\Omega}(\eta_c M_{b_1} + M_{c_1})}{I_{gk}\omega_{go}^2}t, \quad (4.70a)$$

$$\psi_g(t) \approx \psi_{go} + \frac{\mathit{\Omega}(\eta_b M_{c_1} - M_{b_1})}{I_{gk}\omega_{go}^2}t. \quad (4.70b)$$

Now we impose the time during which the axis of the gyroscope travels from the position ϑ_{go}, ψ_{go} to $\vartheta_g = \vartheta_{gk}$, $\psi_g = \psi_{gk}$. Let us denote this time by t_u. Then from the preceding equalities (in truth, they are approximated) we obtain

$$\vartheta_{go} + \frac{\mathit{\Omega}(\eta_c M_{b_1} + M_{c_1})}{I_{gk}\omega_{go}^2}t_u = \vartheta_{gk}, \quad (4.71a)$$

$$\psi_{go} + \frac{\mathit{\Omega}(\eta_b M_{c_1} - M_{b_1})}{I_{gk}\omega_{go}^2}t_u = \psi_{gk}. \quad (4.71b)$$

This is a system of two equations with two unknown quantities M_{b_1} and M_{c_1}, and it yields

$$M_{b_1} = -\frac{(\psi_{gk} - \psi_{go} - \eta_b(\vartheta_{gk} - \vartheta_{go}))\cdot I_{go}n_g}{t_u}, \quad (4.72)$$

$$M_{c_1} = \frac{(\vartheta_{gk} - \vartheta_{go} + \eta_c(\psi_{gk} - \psi_{go})) \cdot I_{go} n_g}{t_u}. \tag{4.73}$$

If we want to displace the axis of the gyroscope from the known initial position $\vartheta_{go}, \psi_{go}$ to the given position on the surface of the cone $\vartheta_g = \vartheta_{gk}, \psi_g = \psi_{gk}$, then the controls have the form

$$M_{b_1} = -\frac{(\psi_{gk} - \psi_{go} + \eta_b \vartheta_{go}) \cdot I_{go} n_g}{t_u}, \tag{4.74a}$$

$$M_{c_1} = \frac{[(\psi_{gk} - \psi_{go})\eta_c - \vartheta_{go}] \cdot I_{go} n_g}{t_u}. \tag{4.74b}$$

When we want to do the same for the preset motion of the axis along the Archimedes spiral, then

$$M_{b_1} = -\frac{(\eta_b \vartheta_{go} - \psi_{go}) \cdot I_{go} n_g}{t_u}, \tag{4.75a}$$

$$M_{c_1} = -\frac{(\eta_c \psi_{go} + \vartheta_{go}) \cdot I_{go} n_g}{t_u}. \tag{4.75b}$$

Summing up, we can say that for the realization of the desired motion, we apply the following algorithm: (1) for $t < t_u$ we control the torques $M_b = M_{b_1}$ and $M_c = M_{c_1}$; (2) for $t \geq t_u$ we control the torques $M_b = M_{b_2}$ and $M_c = M_{c_2}$.

4.2.4 Numerical Example

Figures 4.9 and 4.10 present a process of motion, inconsistent with the preset one, of the gyroscope axis from the initial position to the required one by means of controls M_{b_1}, M_{c_1} described by expressions (4.73). These figures show that a precise realization of the motion of the gyroscope axis is possible along the Archimedes spiral after the gyroscope axis is moved to the required initial position.

4.3 Motion Control of Gyroscope Axis in a Closed System

The results of the preceding section show that programmable control of a gyroscope axis in an open system cannot provide satisfactory accuracy of realization of the preset motion of the axis. The cause are many disturbances, which acts on the gyroscope base.

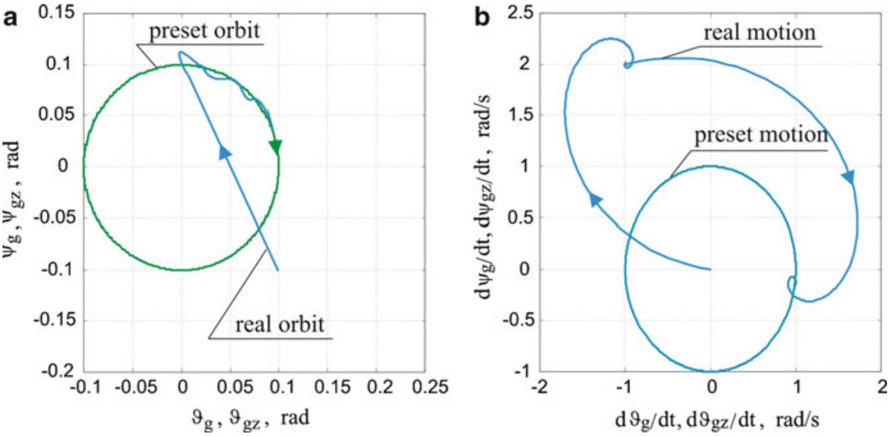

Fig. 4.9 Taking the gyroscope axis to the preset initial position at its motion on the cone surface: (**a**) for angular displacements, (**b**) for angular velocities

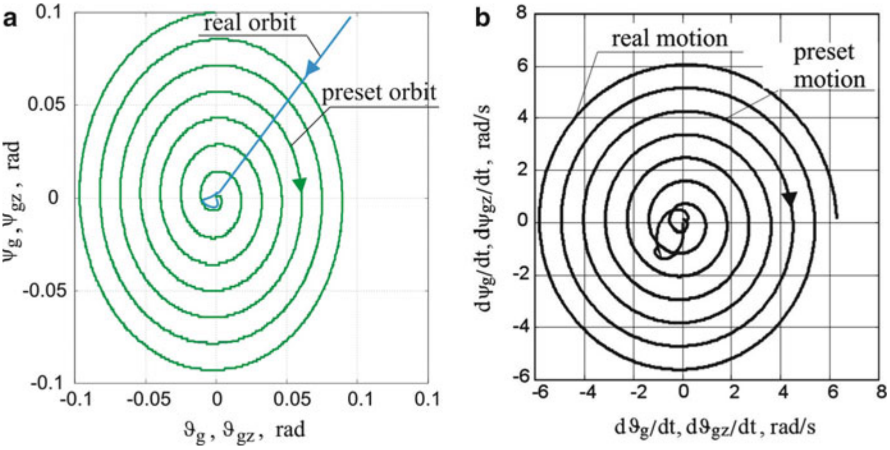

Fig. 4.10 Taking the gyroscope axis to the preset initial position at its motion on the surface, unfolded after the Archimedes spiral: (**a**) for angular displacements, (**b**) for angular velocities

The fundamental elements affecting the errors of not only navigation but also controlled gyroscopes are as follows [22, 23]:

(a) Dry and viscous friction in frame bearings.
(b) Inertia of frames.
(c) Unbalance (static and dynamic) of rotor relative to intersection of frame axes—center of rotation.
(d) Linear and angular accelerations of base.
(e) Elasticity of elements of construction.

(f) Errors of Cardan suspension.
(g) Instability of rotor drive.
(h) Intersection of frames at incorrect angles.
(i) Large angles and angular velocities of deviation of main axis from preset direction.
(j) Rotational motion of Earth.

In order to eliminate the detrimental interaction of the preceding elements one needs to apply systems of automatic correction of the motion of the gyroscope axis.

4.3.1 Gyroscopic System with PID Regulator

Here we will consider control of the gyroscope axis, which relies on tracking, by this axis, a preset direction, which is either time dependent or time independent. The application of such control takes place in various observation instruments, in automatic detection and angular tracking systems, in optical target coordinators of self-guided missiles, etc. [21, 24]. The tracking requires the measurement of the results of control; thus it belongs to the group of *closed control systems* (with feedback) [22]. We will distinguish a *desired* motion (signal) $\vartheta_{gz}(t)$ and $\psi_{gz}(t)$, i.e., the motion of a gyroscope that we would like to realize, and the motion (signal) *realized* $\vartheta_g(t)$ and $\psi_g(t)$ by the gyroscope axis. We will call the deviation of the realized motion from the desired one

$$\Delta_g = \sqrt{(\vartheta_g - \vartheta_{gz})^2 + (\psi_g - \psi_{gz})^2} \tag{4.76}$$

a *real deviation* of the control. Moreover, we will use the notion of *partial deviations*:

$$e_b = \vartheta_g - \vartheta_{gz}, \tag{4.77}$$

$$e_c = \psi_g - \psi_{gz}, \tag{4.78}$$

The basic block diagram of control in a closed system is depicted in Fig. 4.11. Such a scheme of deviation control, in which a *proportional-integral-derivative* (PID) regulator is applied, can serve to control the motion of the gyroscope. Values of the torques M_b and M_c are assumed to be as follows:

$$\begin{aligned}\frac{M_b}{I_{bk}\Omega^2} &= k_b e_b + h_b \frac{\mathrm{d}e_b}{\mathrm{d}t} + h_{b_1}\int_0^t e_b(\tau)\mathrm{d}\tau,\\ \frac{M_c}{I_{bk}\Omega^2} &= k_c e_c + h_c \frac{\mathrm{d}e_c}{\mathrm{d}t} + h_{c_1}\int_0^t e_c(\tau)\mathrm{d}\tau.\end{aligned} \tag{4.79}$$

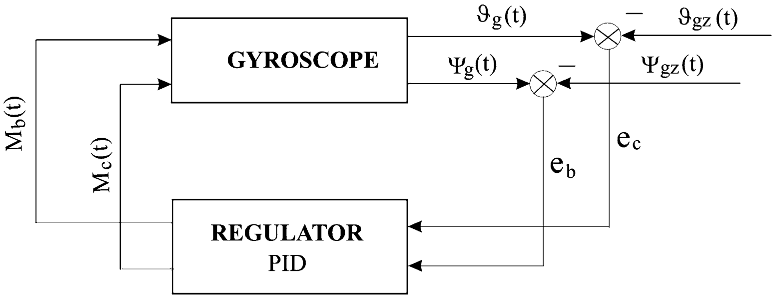

Fig. 4.11 Control scheme in a closed system

One mostly assumes $k_b = k_c, h_b = h_c, h_{b_1} = h_{c_1}$ [22]. However, this is not the most effective control method, which will be shown later in this chapter. The control system should be examined with regard to stability (closed system).

The result of control system operation can be verified by means of a numerical method (computer simulation). For this purpose, we write the linearized equations of motion of gyroscope (4.53), provided that $\vartheta_g << 1$, in the following form:

$$\begin{aligned} I_{gk}\Omega^2\vartheta_g'' + \eta_b\Omega\vartheta_g' - I_{go}n_g\Omega\psi_g' &= M_b, \\ I_{gk}\Omega^2\psi_g'' + \eta_c\Omega\psi_g' + I_{go}n_g\Omega\vartheta_g' &= M_c, \end{aligned} \tag{4.80}$$

or

$$\begin{aligned} \psi_g'' + b_c\psi_g' + \vartheta_g' &= c_cM_c, \\ \vartheta_g'' + b_b\vartheta_g' - \psi_g' &= c_bM_b, \end{aligned} \tag{4.81}$$

where

$$b_b = \frac{\eta_b}{I_{gk}\Omega}, \quad b_c = \frac{\eta_c}{I_{gk}\Omega}, \quad c_b = \frac{1}{I_{gk}\Omega^2}, \quad c_c = \frac{1}{I_{gk}\Omega^2}.$$

Equations of motion of a gyroscope axis in tracking mode are as follows:

$$\vartheta_g'' + b_b\vartheta_g' - \psi_g' = \bar{k}_b(\vartheta_{gz} - \vartheta_g) + \bar{h}_b(\vartheta_{gz}' - \vartheta_g') + \bar{h}_{b_1}\int_0^\tau [\vartheta_{gz}(\tau_1) - \vartheta_g(\tau_1)]\mathrm{d}\tau_1, \tag{4.82a}$$

$$\psi_g'' + b_c\psi_g' + \vartheta_g' = \bar{k}_c(\psi_{gz} - \psi_g) + \bar{h}_c(\psi_{gz}' - \psi_g') + \bar{h}_{c_1}\int_0^\tau [\psi_{gz}(\tau_1) - \psi_g(\tau_1)]\mathrm{d}\tau_1, \tag{4.82b}$$

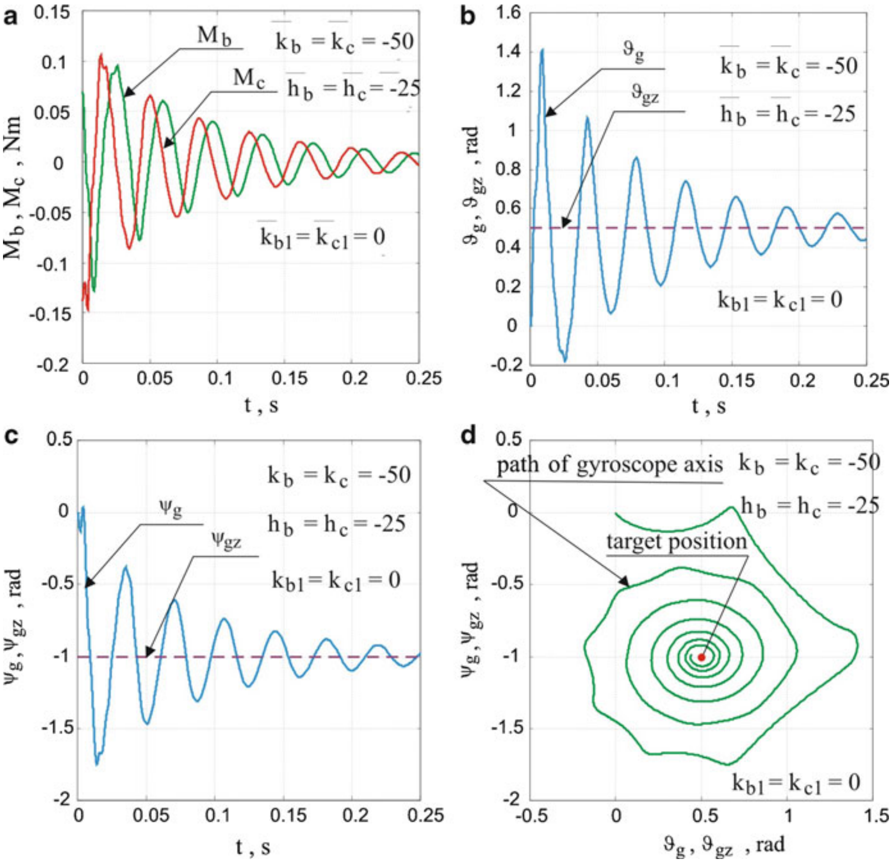

Fig. 4.12 Results of control of gyroscope axis with using PID regulator with small values of damping coefficients at tracking of the fixed point: (**a**) change in control torques as a function of time; (**b, c**) change in angular deviations as a function of time; (**d**) path of gyroscope axis

where

$$\bar{k}_b = \frac{k_b}{I_{gk}\Omega^2}, \quad \bar{k}_c = \frac{k_c}{I_{gk}\Omega^2}, \quad \bar{h}_b = \frac{h_b}{I_{gk}\Omega^2}, \quad \bar{h}_c = \frac{h_c}{I_{gk}\Omega^2}.$$

As a first example, let us examine a procedure for taking a gyroscope axis from the zero position, i.e., $\vartheta_g(0) = 0$, $\dot{\vartheta}_g(0) = 0$, $\psi_g(0) = 0$, and $\dot{\psi}_g(0) = 0$, to the position specified by the angles $\vartheta_g = \vartheta_{c0}$ and $\psi_g = \psi_{c0}$.

Figure 4.12 presents the result of controlling with the use of only a PD-type regulator (without the integrating element $h_{b_1} = h_{c_1} = 0$, $k_b = k_c = -50$, $h_b = h_c = -25$).

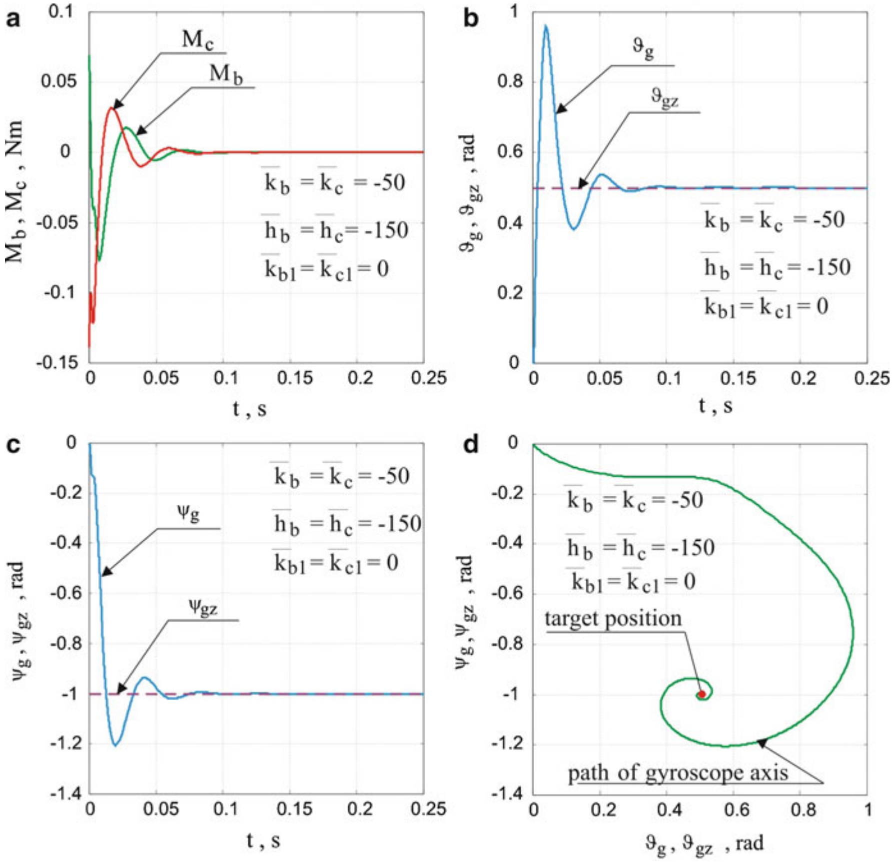

Fig. 4.13 Results of control of gyroscope axis using PID regulator with large values of damping coefficients at tracking of fixed point: (**a**) change of the control torques as a function of time; (**b, c**) change of angular deviations as a function of time; (**d**) path of gyroscope axis

The gyroscope axis makes large displacements, reaching the desired angles over a relatively long time. Increasing values of the damping coefficients $h_b = h_c = -150$ improve this result considerably (Fig. 4.13).

When one selects the regulator parameters $(k_b, k_c, h_b, h_c, h_{b_1}, h_{c_1})$, one needs to check what values the control moments M_b and M_c should be given. In other words, we need to check if these values are not too large to damage the gyroscope. These moments (Fig. 4.12) take on values much larger than those in Fig. 4.13.

The results presented in Figs. 4.12 and 4.13 confirm that a differentiating term, besides a proportional term, plays an important role in the control of a gyroscope axis. The former decides whether regulation is to be realized, whereas the latter increases the damping of system that have a great importance in control of gyroscope. In what follows we will discuss this problem thoroughly. The second

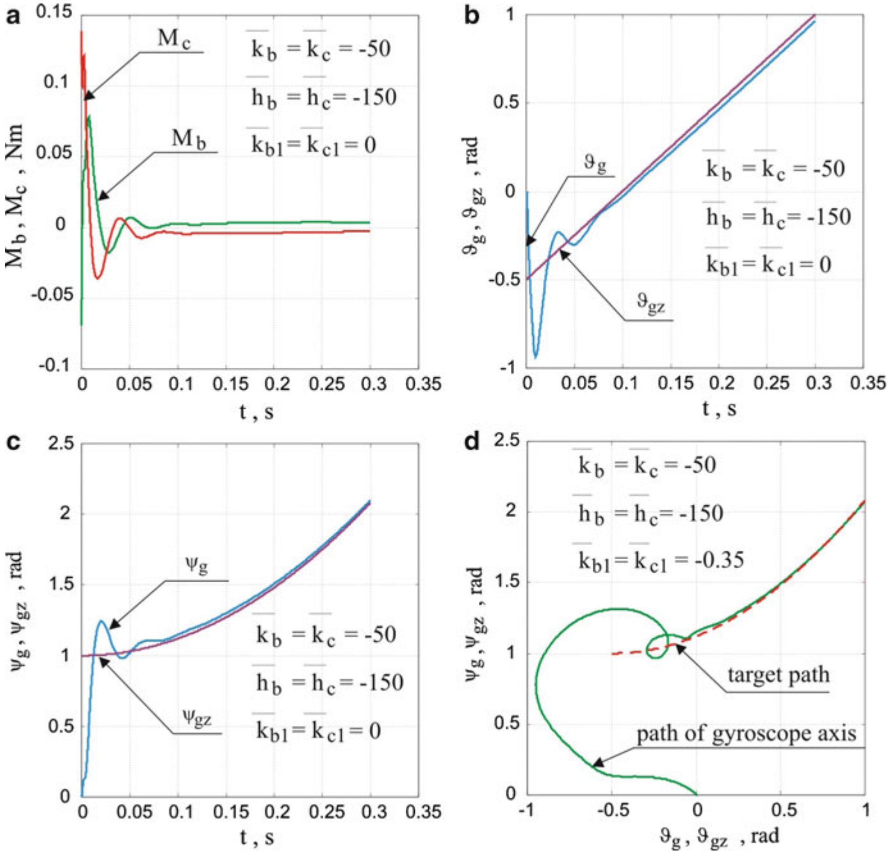

Fig. 4.14 Results of control of gyroscope axis with use of PID regulator with large values of damping coefficients at tracking of movable point: (**a**) change of the control torques as a function of time; (**b, c**) change of angular deviations as a function of time; (**d**) path of gyroscope axis

example covers the tracking of a movable point. The moving point in space is observed from Earth by means of a telescope. The optical axis of the telescope is not coincident with the line connecting this point with the telescope (i.e., the so-called observation line of the target). The telescope objective is located in the gyroscope axis. The problem of control relies on making the axis of the gyroscope coincide with the observation line of the target. Consequently, tracking of the target is performed. In the example, whose results are presented in Figs. 4.14–4.16, a moving point (target) specifies the angles that are required signals according to the following formulas:

$$\vartheta_{gz}(\tau) = \vartheta_{c0} + 0.2 \cdot \omega_c \cdot \tau^2,$$

$$\psi_{gz}(\tau) = \psi_{c0} + \omega_c \cdot \tau.$$

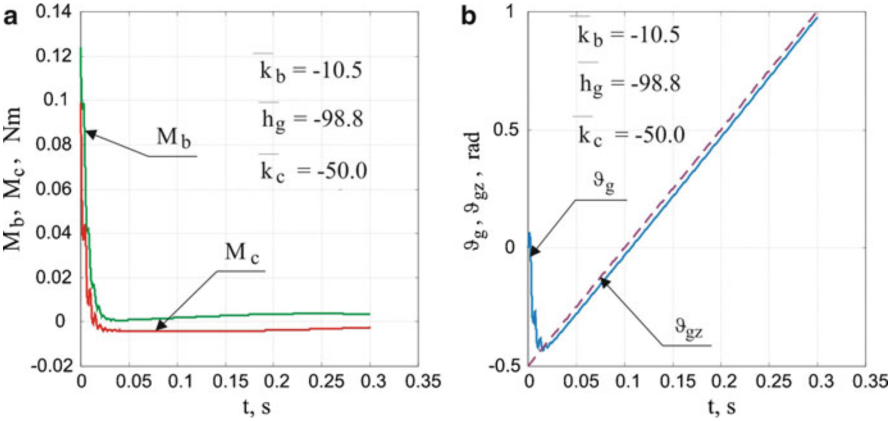

Fig. 4.15 Results of control of gyroscope axis using PID regulator to track fixed point: (**a**) change in control torques as a function of time, (**b**) change in angular deviations as a function of time

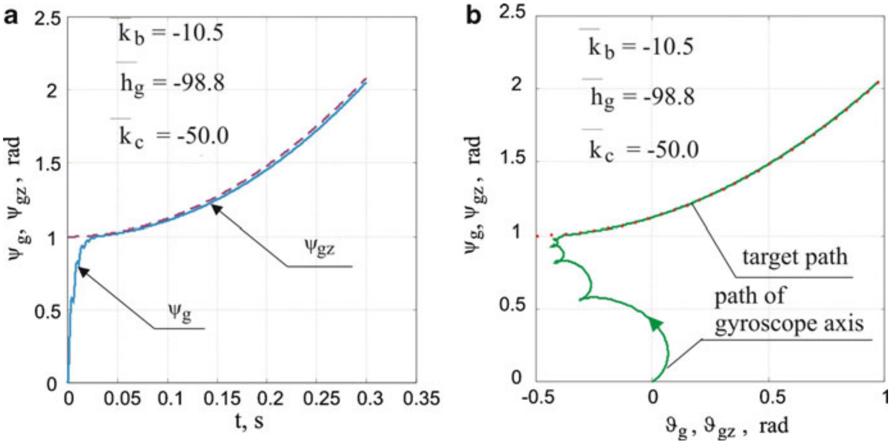

Fig. 4.16 Results of control of gyroscope axis using PID regulator to track movable point: (**a**) change in angular deviations as a function of time, (**b**) path of gyroscope axis

In Fig. 4.14, a regulator without integrating elements leads to the relatively large error Δ_g of the target tracking. Applying a PID-type regulator with specific values of the coefficients improves the tracking (Fig. 4.15).

A more advanced example of gyroscope usage would be a combined method of control of the gyroscope motion. A fixed or movable point in space is to be automatically detected and tracked by an optical system placed in the gyroscope axis, as in the previous examples. The *visual field of the objective* (angle of view) is defined. We have here two states of control of the gyroscope axis. In the first state (seeking the target), the axis "draws" lines in space (e.g., spiral). When the axis approaches the target, so that it is in the vicinity of the objective, a transition to the second control state occurs. This is a state of target tracking. The axis of the gyroscope approaches the observation line of the target.

4.3.2 Program Control with Feedback

The investigation results mentioned in Sect. 4.1 show that controlling a gyroscope in an open system is saddled with errors caused by the influence of non-linearities. Despite the fact that friction forces in the frame bearings shorten the duration of the transient process, a gyroscope must have those friction forces minimalized. This is implied by the essential task of a gyroscope. Therefore, it is necessary to incorporate a regulator into a gyroscope control system whose role is to minimize errors between the preset and real motions.

In order to determine a program control algorithm with feedback, let us assume that deviations

$$e_b = \vartheta_{gz} - \vartheta_g, \qquad e_c = \psi_{gz} - \psi_g \tag{4.83}$$

change according to the following rules [18]:

$$e_b = C_{b_1} e^{-\lambda_{b_1} t} + C_{b_2} e^{-\lambda_{b_2} t}, \tag{4.84a}$$

$$e_c = C_{c_1} e^{-\lambda_{c_1} t} + C_{c_2} e^{-\lambda_{c_2} t}, \tag{4.84b}$$

which are equivalent to the differential equations

$$\frac{\mathrm{d}^2 e_b}{\mathrm{d}t^2} + (\lambda_{b_1} + \lambda_{b_2}) \frac{\mathrm{d}e_b}{\mathrm{d}t} + \lambda_{b_1}\lambda_{b_2} e_b = 0, \tag{4.85a}$$

$$\frac{\mathrm{d}^2 e_c}{\mathrm{d}t^2} + (\lambda_{c_1} + \lambda_{c_2}) \frac{\mathrm{d}e_c}{\mathrm{d}t} + \lambda_{c_1}\lambda_{c_2} e_c = 0. \tag{4.85b}$$

From (4.85) and (4.84) we have

$$\frac{\mathrm{d}^2 \vartheta_g}{\mathrm{d}t^2} = \frac{\mathrm{d}^2 \vartheta_{gz}}{\mathrm{d}t^2} - (\lambda_{b_1} + \lambda_{b_2}) \frac{\mathrm{d}e_b}{\mathrm{d}t} - \lambda_{b_1}\lambda_{b_2} e_b, \tag{4.86a}$$

$$\frac{\mathrm{d}^2 \psi_g}{\mathrm{d}t^2} \cos^2 \vartheta_g = \left[\frac{\mathrm{d}^2 \psi_{gz}}{\mathrm{d}t^2} - (\lambda_{c_1} + \lambda_{c_2}) \frac{\mathrm{d}e_c}{\mathrm{d}t} - \lambda_{c_1}\lambda_{c_2} e_c \right] \cos^2 \vartheta_g. \tag{4.86b}$$

Substituting the preceding expressions into (4.48) and leaving terms up to the first order of smallness with respect to the deviations e_b and e_c, one obtains the desired control algorithm in a closed system:

$$M_b(t) = M_b^p(t) + u_b(t), \tag{4.87a}$$

$$M_c(t) = M_c^p(t) + u_c(t). \tag{4.87b}$$

The quantities $M_b(t)$ and $M_c(t)$ occurring in (4.87) are program controls of the form

$$M_b^p(t) = I_{gk}\frac{\mathrm{d}^2\vartheta_{gz}}{\mathrm{d}t^2} + \frac{1}{2}I_{gk}\left(\frac{\mathrm{d}\psi_{gz}}{\mathrm{d}t}\right)^2 \sin 2\vartheta_{gz} - I_{go}n_g\frac{\mathrm{d}\psi_{gz}}{\mathrm{d}t}\cos\vartheta_{gz} + \eta_b\frac{\mathrm{d}\vartheta_{gz}}{\mathrm{d}t}, \tag{4.88a}$$

$$M_c^p(t) = I_{gk}\frac{\mathrm{d}^2\psi_{gz}}{\mathrm{d}t^2} - I_{gk}\frac{\mathrm{d}\psi_{gz}}{\mathrm{d}t}\frac{\mathrm{d}\vartheta_{gz}}{\mathrm{d}t}\sin 2\vartheta_{gz} + I_{go}n_g\frac{\mathrm{d}\vartheta_{gz}}{\mathrm{d}t}\cos\vartheta_{gz} + \eta_c\frac{\mathrm{d}\psi_{gz}}{\mathrm{d}t}. \tag{4.88b}$$

The quantities $u_b(t)$ and $u_c(t)$ are correcting controls of the following form:

$$u_b(t) = k_{b_1}(t)\cdot e_b + k_{c_1}(t)\cdot e_c + h_{b_1}(t)\cdot\frac{\mathrm{d}e_b}{\mathrm{d}t} + h_{c_1}(t)\cdot\frac{\mathrm{d}e_c}{\mathrm{d}t}, \tag{4.89a}$$

$$u_c(t) = k_{b_2}(t)\cdot e_b + k_{c_2}(t)\cdot e_b + h_{b_2}(t)\cdot\frac{\mathrm{d}e_b}{\mathrm{d}t} + h_{c_2}(t)\cdot\frac{\mathrm{d}e_c}{\mathrm{d}t}, \tag{4.89b}$$

where

$$\begin{aligned}
k_{b_1}(t) &= \frac{1}{2}\left(\frac{\mathrm{d}\psi_{gz}}{\mathrm{d}t}\right)^2\cos 2\vartheta_{gz} + \frac{\psi_{gz}}{\mathrm{d}t}\sin\vartheta_{gz} - \lambda_{b_1}\lambda_{b_2},\\
k_{b_2}(t) &= \frac{\mathrm{d}\psi_{gz}}{\mathrm{d}t}\frac{\mathrm{d}\vartheta_{gz}}{\mathrm{d}t}\cos 2\vartheta_{gz} + \frac{\vartheta_{gz}}{\mathrm{d}t}\sin\vartheta_{gz},\\
k_{c_1}(t) &= 0, \qquad k_{c_2}(t) = -\lambda_{c_1}\lambda_{c_2}\cos^2\vartheta_{gz},\\
h_{b_1}(t) &= -(\eta_b + \lambda_{b_1} + \lambda_{b_2}),\\
h_{b_2}(t) &= -\left(\frac{\mathrm{d}\psi_{gz}}{\mathrm{d}t}\sin 2\vartheta_{gz} - \cos\vartheta_{gz}\right),\\
h_{c_1}(t) &= \left(\frac{\mathrm{d}\psi_{gz}}{\mathrm{d}t}\sin 2\vartheta_{gz} - \cos\vartheta_{gz}\right),\\
h_{c_2}(t) &= -\left[\eta_c + (\lambda_{c_1} + \lambda_{c_2})\cos^2\vartheta_{gz} - \frac{\mathrm{d}\psi_{gz}}{\mathrm{d}t}\sin 2\vartheta_{gz}\right].
\end{aligned}$$

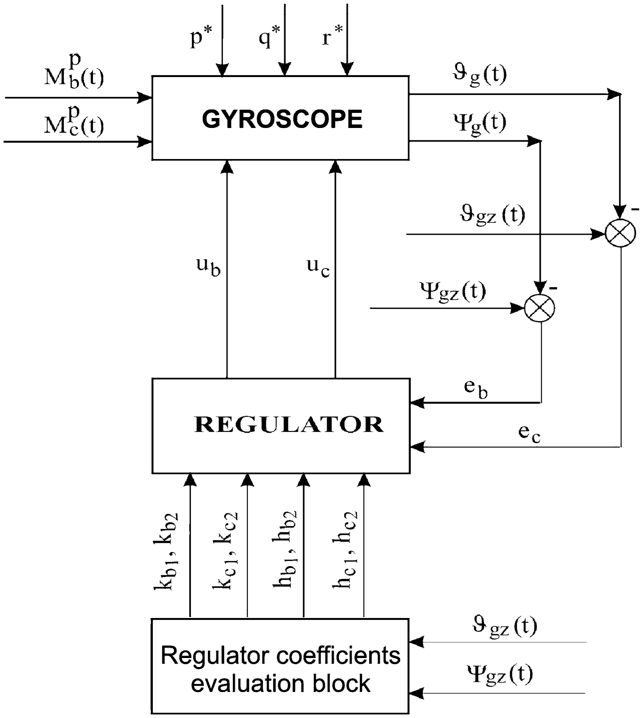

Fig. 4.17 Control scheme of a gyroscope in a closed system

In Fig. 4.17 one can see a functional scheme of the position control of the gyroscope axis in a closed system.

The control algorithm depicted in Fig. 4.17 needs a pre-set change in time of the coefficients of the regulator $k_{b_1}, k_{b_2}, k_{c_2}, h_{b_1}, h_{b_2}, h_{c_1}, h_{c_2}$, which depend on the required values of angular deviations of the gyroscope axis ϑ_{gz}, ψ_{gz} and their first and second derivatives with respect to time. However, one should note that for the quantities ϑ_{gz}, ψ_{gz}, $\frac{\mathrm{d}\vartheta_{gz}}{\mathrm{d}t}$, $\frac{\mathrm{d}\psi_{gz}}{\mathrm{d}t}$, $\frac{\mathrm{d}^2\vartheta_{gz}}{\mathrm{d}t^2}$, $\frac{\mathrm{d}^2\psi_{gz}}{\mathrm{d}t^2}$ attaining small values we can assume, with a sufficient accuracy from practical viewpoint, constant values of the regulator coefficients, namely,

$$\begin{aligned}
&k_{b_1} = -\lambda_{b_1}\lambda_{b_2}, \quad k_{b_2} = 0, \quad k_{c_1} = 0, \quad k_{c_2} = -\lambda_{b_1}\lambda_{b_2}, \\
&h_{b_1} = -\left(\eta_b + \lambda_{b_1} + \lambda_{b_2}\right), \quad h_{c_1} = -I_{go}n_g, \\
&h_{b_2} = I_{go}n_g, \quad h_{c_2} = -\left(\eta_c + \lambda_{c_1} + \lambda_{c_2}\right).
\end{aligned} \tag{4.90}$$

The quantities λ_{b_1}, λ_{b_2}, λ_{c_1}, λ_{c_2} in (4.90) are constants optimally selected with respect to the minimum of the mean square error and stability of a gyroscope system, which is discussed in the following sections.

4.4 Selection of Optimal Parameters of a Gyroscopic System in Elastic Suspension

In this section, we consider how to select the optimal parameters of a gyroscope whose axis is connected with the rotor by means of an elastic element [16, 18]; this can also be regarded as taking into account the deformability of the rotor construction. It concerns a situation in which the selection of parameters at which the dynamical effects emerging in the transient process will vanish in the shortest time. However, during control of the gyroscope, a sufficient accuracy of the preset position of the gyroscope axis in space can be ensured not just by the gyroscope's construction parameters due to various disturbances. That is why in order to ensure the assumed accuracy of the gyroscope motion, one also needs to select the optimal parameters of the automatic control system of the gyroscope motion. The optimization of the whole gyroscopic system can minimize the dynamical effects. The optimization of parameters is particularly important in the case of scanning of the target coordinator of a self-guided missile or a system for detecting and tracking a target in an unmanned FO (a more detailed discussion is carried out in Chap. 5). In both cases, accuracy is required in the realization of the preset motion and maintenance of the required direction by the gyroscope axis and the fastest damping of transient processes generated from changes in the gyroscope axis motion.

We will consider separately a problem related to the selection of optimal gyroscope parameters and of its automatic control parameters.

4.4.1 *Selection of Optimal Parameters of a Gyroscope in Elastic Suspension*

The linearized equations of motion (*technical theory*) of a gyroscope in an elastic suspension [derived from (4.31)–(4.35)] are presented in the following form:

$$I_{gk}^{0}\frac{\mathrm{d}}{\mathrm{d}t}\left(\dot{\vartheta}_{g}^{0}+\mathbf{q}^{*}\right)+\eta_{b}\dot{\vartheta}_{g}^{0}-\kappa\left(\vartheta_{g}-\vartheta_{g}^{0}\right)=M_{b}, \tag{4.91a}$$

$$I_{gk}^{0}\frac{\mathrm{d}}{\mathrm{d}t}\left(\dot{\psi}_{g}^{0}+\mathbf{r}^{*}\right)+\eta_{c}\dot{\psi}_{g}^{0}-\kappa\left(\psi_{g}-\psi_{g}^{0}\right)=M_{c}, \tag{4.91b}$$

$$I_{gk}\frac{\mathrm{d}}{\mathrm{d}t}\left(\dot{\vartheta}_{g}+\mathbf{q}^{*}\right)+I_{go}n\left(\dot{\psi}_{g}+\mathbf{r}^{*}\right)+\kappa\left(\vartheta_{g}-\vartheta_{g}^{0}\right)=M_{zb}, \tag{4.91c}$$

$$I_{gk}\frac{\mathrm{d}}{\mathrm{d}t}\left(\dot{\psi}_{g}+\mathbf{r}^{*}\right)-I_{go}n\left(\dot{\vartheta}_{g}+\mathbf{q}^{*}\right)+\kappa\left(\psi_{g}-\psi_{g}^{0}\right)=M_{zc}. \tag{4.91d}$$

Let us apply to the preceding system a dimensionless time

$$\tau = \Omega \cdot t, \tag{4.92a}$$

where

$$\Omega = \frac{I_{go} \cdot n_g}{I_{gk} + I_{gk}^0}. \tag{4.92b}$$

Introducing the independent variable τ (4.92a) and making appropriate transformations, the linearized (4.91) take the following form [15]:

$$\frac{\mathrm{d}^2 \nu_g}{\mathrm{d}\tau^2} = \upsilon_g \frac{\mathrm{d}\sigma_g}{\mathrm{d}\tau} + \upsilon_g \frac{\mathrm{d}\psi_g^0}{\mathrm{d}\tau} + b_b \frac{\mathrm{d}\vartheta_g^0}{\mathrm{d}\tau} - -(\kappa_p + \kappa_0)\nu_g + \bar{M}_{zb} - \bar{M}_b - \mathbf{r}^*, \tag{4.93a}$$

$$\frac{\mathrm{d}^2 \sigma_g}{\mathrm{d}\tau^2} = \upsilon_g \frac{\mathrm{d}\nu_g}{\mathrm{d}\tau} + \upsilon_g \frac{\mathrm{d}\vartheta_g^0}{\mathrm{d}\tau} + b_c \frac{\mathrm{d}\psi_g^0}{\mathrm{d}\tau} - -(\kappa_p + \kappa_0)\sigma_g + \bar{M}_{zc} - \bar{M}_c + \mathbf{q}^*, \tag{4.93b}$$

$$\frac{\mathrm{d}^2 \vartheta_g^0}{\mathrm{d}\tau^2} = -b_b \frac{\mathrm{d}\vartheta_g^0}{\mathrm{d}\tau} + \kappa_0 \nu_g + \bar{M}_b - \frac{\mathrm{d}\mathbf{q}^*}{\mathrm{d}\tau}, \tag{4.93c}$$

$$\frac{\mathrm{d}^2 \psi_g^0}{\mathrm{d}\tau^2} = -b_c \frac{\mathrm{d}\psi_g^0}{\mathrm{d}\tau} + \kappa_0 \sigma_g + \bar{M}_c - \frac{\mathrm{d}\mathbf{r}^*}{\mathrm{d}\tau}, \tag{4.93d}$$

where

$$\nu_g = \vartheta_g - \vartheta_g^0, \quad \sigma_g = \psi_g - \psi_g^0, \quad \upsilon_g = \frac{I_{gk}^0 + I_{gk}}{I_{gk}}, \tag{4.94a}$$

$$b_b = \frac{\eta_b}{I_{gk}^0 \Omega}, \quad b_c = \frac{\eta_c}{I_{gk}^0 \Omega}, \quad \kappa_0 = \frac{\kappa}{I_{gk}^0 \Omega^2}, \quad \kappa_p = \frac{\kappa}{I_{gk}^0 \Omega^2}, \tag{4.94b}$$

$$\bar{M}_b = \frac{M_b}{I_{gk}^0 \Omega^2}, \quad \bar{M}_c = \frac{M_c}{I_{gk}^0 \Omega^2}, \quad \bar{M}_{zb} = \frac{M_{zb}}{I_{gk} \Omega^2}, \quad \bar{M}_{zc} = \frac{M_{zc}}{I_{gk} \Omega^2}.$$

In order to determine stable and optimal parameters we introduce the following designations:

$$x_1 = \nu_g, \qquad x_2 = \frac{\mathrm{d}\nu_g}{\mathrm{d}\tau}, \quad x_3 = \sigma_g,$$

$$x_4 = \frac{\mathrm{d}\sigma_g}{\mathrm{d}\tau}, \quad x_5 = \frac{\mathrm{d}\vartheta_g^0}{\mathrm{d}\tau}, \quad x_6 = \frac{\mathrm{d}\psi_g^0}{\mathrm{d}\tau}. \tag{4.95a}$$

Additionally, let us introduce the following quantities:

$$\bar{b}_b = h_b + b_b, \quad \bar{b}_c = h_c + b_c, \tag{4.95b}$$

where h_b and h_c denote the desired damping needed in the gyroscopic system.

System (4.93), taking into account (4.95), is as follows:

$$\frac{\mathrm{d}\mathbf{x}_g}{\mathrm{d}\tau} = \mathbf{A}_g\mathbf{x}_g, \tag{4.96}$$

where

$$\mathbf{x}_g = [x_1 \quad x_2 \quad x_3 \quad x_4 \quad x_5 \quad x_6]^{\mathrm{T}},$$

$$\mathbf{A}_g = \begin{bmatrix} 0 & 1 & 0 & 0 & 0 & 0 \\ -(\kappa_p + \kappa_0) & 0 & 0 & \upsilon_g & \bar{b}_b & \upsilon_g \\ 0 & 0 & 0 & 1 & 0 & 0 \\ 0 & -\upsilon_g & -(\kappa_p + \kappa_0) & 0 & -\upsilon_g & \bar{b}_c \\ \kappa_0 & 0 & 0 & 0 & -\bar{b}_b & 0 \\ 0 & 0 & \kappa_0 & 0 & 0 & -\bar{b}_c \end{bmatrix}. \tag{4.97}$$

According to the modified Golubientsev method [22, 25], let us introduce a new variable defined as follows:

$$\mathbf{x}_g(\tau) = \mathbf{y}_g(\tau) \cdot e^{\delta_g^*(\tau)}, \tag{4.98}$$

where

$$\delta_g^* = \frac{1}{6}\mathrm{Tr}\mathbf{A}_g = -\frac{1}{6}(\bar{b}_b + \bar{b}_c). \tag{4.99}$$

After some transformations we have

$$\frac{\mathrm{d}\mathbf{y}_g}{\mathrm{d}\tau} = \mathbf{B}_g^*\mathbf{y}_g, \tag{4.100}$$

where

$$\mathbf{B}_g^* = \begin{bmatrix} -\delta_g^* & 1 & 0 & 0 & 0 & 0 \\ -(\kappa_p + \kappa_0) & -\delta_g^* & 0 & \upsilon_g & \bar{b}_b & \upsilon_g \\ 0 & 0 & -\delta_g^* & 1 & 0 & 0 \\ 0 & -\upsilon_g & -(\kappa_p + \kappa_0) & -\delta_g^* & -\upsilon_g & \bar{b}_c \\ \kappa_0 & 0 & 0 & 0 & -\bar{b}_b - \delta_g^* & 0 \\ 0 & 0 & \kappa_0 & 0 & 0 & -\bar{b}_c - \delta_g^* \end{bmatrix}. \tag{4.101}$$

A characteristic equation of matrix $\mathbf{B}_g^*$, whose $\mathrm{Tr}\mathbf{B}_g^* = 0$, is transformed into a characteristic polynomial of the form

$$\lambda_g^6 + b_2\lambda_g^4 - b_3\lambda_g^3 + b_4\lambda_g^2 - b_5\lambda_g + b_6 = 0. \tag{4.102}$$

For matrix $\mathbf{B}_g^*$ we seek values κ_0, κ_p, $\bar{b}_b$, $\bar{b}_c$ such that the characteristic (4.102) could possess only imaginary or zero roots [25]. To this end, the coefficients of the characteristic (4.102) b_2, b_3, b_4, b_5, b_6 (coefficient $b_1 = \mathrm{Tr}\mathbf{B}_g^* = 0$) must be determined as sums over all possible combinations of leading-diagonal determinants of degrees 2, 3, 4, 5, and 6 of matrix $\mathbf{B}_g^*$ [(4.101)]. Introducing an additional designation $\bar{\kappa} = (\kappa_0 + \kappa_p)$, we obtain

$$b_2 = -15(\delta_g^*)^2 + 2(\kappa_0 + \kappa_p) + \upsilon_g^2 + \bar{b}_b\bar{b}_c > 0, \tag{4.103}$$

$$b_3 = 40(\delta_g^*)^2 + (2\kappa_p - \kappa_0 + \upsilon_g^2 - 2\bar{b}_b\bar{b}_c)\delta_g^* = 0, \tag{4.104}$$

$$\begin{aligned} b_4 = &-45(\delta_g^*)^2 + 6(\delta_g^*)^2(\bar{b}_b\bar{b}_c - \kappa_0 - 4\kappa_p - 2\upsilon_g^2) \\ &+ 2\kappa_p\bar{b}_b\bar{b}_c + (\bar{b}_b\bar{b}_c + 2\kappa_0)\upsilon_g^2 + (\kappa_0 + \kappa_p)^2 > 0, \end{aligned} \tag{4.105}$$

$$\begin{aligned} b_5 = {}&24(\delta_g^*)^5 - 2(\delta_g^*)^3(2\bar{b}_b\bar{b}_c - 5\kappa_0 - 14\kappa_p - 7\upsilon_g^2) \\ &- 2\delta_g^*\Big[\bar{b}_b\bar{b}_c(2\kappa_p + \upsilon_g^2)\Big] + (\kappa_0 + \kappa_p)\cdot(\kappa_0 - 2\kappa_p) - \kappa_0\upsilon_g^2 = 0, \end{aligned} \tag{4.106}$$

$$b_6 = \begin{vmatrix} -\delta_g^* & 1 & 0 & 0 & 0 & 0 \\ -\bar{\kappa} & -\delta_g^* & 0 & \upsilon_g & \bar{b}_b & \upsilon_g \\ 0 & 0 & -\delta_g^* & 1 & 0 & 0 \\ 0 & -\upsilon_g & -\bar{\kappa} & -\delta_g^* & -\upsilon_g & b_c \\ \kappa_0 & 0 & 0 & 0 & -\bar{b}_b - \delta_g^* & 0 \\ 0 & 0 & \kappa_0 & 0 & 0 & -\bar{b}_c - \delta_g^* \end{vmatrix} > 0,$$

$$\begin{aligned} b_6 = &-5(\delta_g^*)^6 + (\delta_g^*)^4(\bar{b}_b\bar{b}_c - 4\kappa_0 - 10\kappa_p - 5\upsilon_g^2) \\ &+ (\delta_g^*)^2\Big[\bar{b}_b\bar{b}_c(2\kappa_p + \upsilon_g^2) - 4\kappa_0\upsilon^2 + (\kappa_0 + \kappa_p)(\kappa_0 - 5\kappa_p)\Big] \\ &+ \bar{b}_b\bar{b}_c\kappa_p + \kappa_0^2\upsilon_g^2 > 0. \end{aligned} \tag{4.107}$$

Moreover, one needs to take into account a very important condition of absolute maximization of the trace of matrix $\mathbf{A}_g$ defined by (4.97):

$$|\mathrm{Tr}\mathbf{A}_g| = |-(\bar{b}_b + \bar{b}_c)| = \max. \tag{4.108}$$

From the preceding relationships (4.104) and (4.106) for $b_3 = 0$ and $b_5 = 0$ we can determine

$$\kappa_p = \frac{\left[288(\delta_g^*)^2 - 68\bar{b}_b\bar{b}_c + 8\upsilon_g^2(\delta_g^*)^2\right](\delta_g^*)^2 - \bar{b}_b\bar{b}_c\upsilon_g^2 + 4\bar{b}_b^2\bar{b}_c^2}{-36(\delta_g^*)^2 + 4\bar{b}_b\bar{b}_c - \upsilon_g^2}, \tag{4.109a}$$

$$\kappa_0 = 20(\delta_g^*)^2 + \upsilon_g^2 - 2\bar{b}_b\bar{b}_c + 2\kappa_p. \tag{4.109b}$$

From (4.94a) and (4.94b) we have

$$\frac{I_{gk}^0}{I_{gk}} = \frac{\kappa_p}{\kappa_0}, \tag{4.110a}$$

$$\upsilon_g = \frac{\kappa_p}{\kappa_0} + 1, \tag{4.110b}$$

$$\kappa = \frac{\kappa_p}{I_{gk}}\left(\frac{n_g}{\upsilon_g}\right)^2. \tag{4.110c}$$

It follows from (4.110a) that a ratio of transversal moments of inertia of the axis and rotor should equal the ratio of optimal parameters κ_p and κ_0 given in (4.109a) and (4.109b). Formula (4.110c) shows that the coefficient of membrane stiffness κ is directly proportional to the square of the angular velocities of eigenrotations n_g of the gyroscope and inversely proportional to the moment of inertia of the rotor I_{gk}.

Figure 4.18 depicts a scheme of an optimization procedure of linear system parameters of arbitrary dimension. On the basis of the aforementioned scheme, a Matlab Simulink program was created that determines the numerically optimal parameters of the considered dynamical systems.

Figures 4.19 and 4.20 show the dynamical effects of a gyroscope on an elastic suspension excited by the initial conditions. At these optimal parameters (Fig. 4.19) vanishing of the transient process is considerably faster than at parameters that are not optimally selected (Fig. 4.20).

4.4.2 Optimal Control of a Gyroscope in an Elastic Suspension

We will define the law of control of a gyroscope in an elastic suspension by means of the method of linear-square optimization [24, 25] using a functional of the form

$$I = \int_0^\infty \left(\mathbf{x}_g^{\mathrm{T}}\mathbf{Q}_g\mathbf{x}_g + \mathbf{u}_g^{\mathrm{T}}\mathbf{R}_g\mathbf{u}_g\right)\mathrm{d}t. \tag{4.111}$$

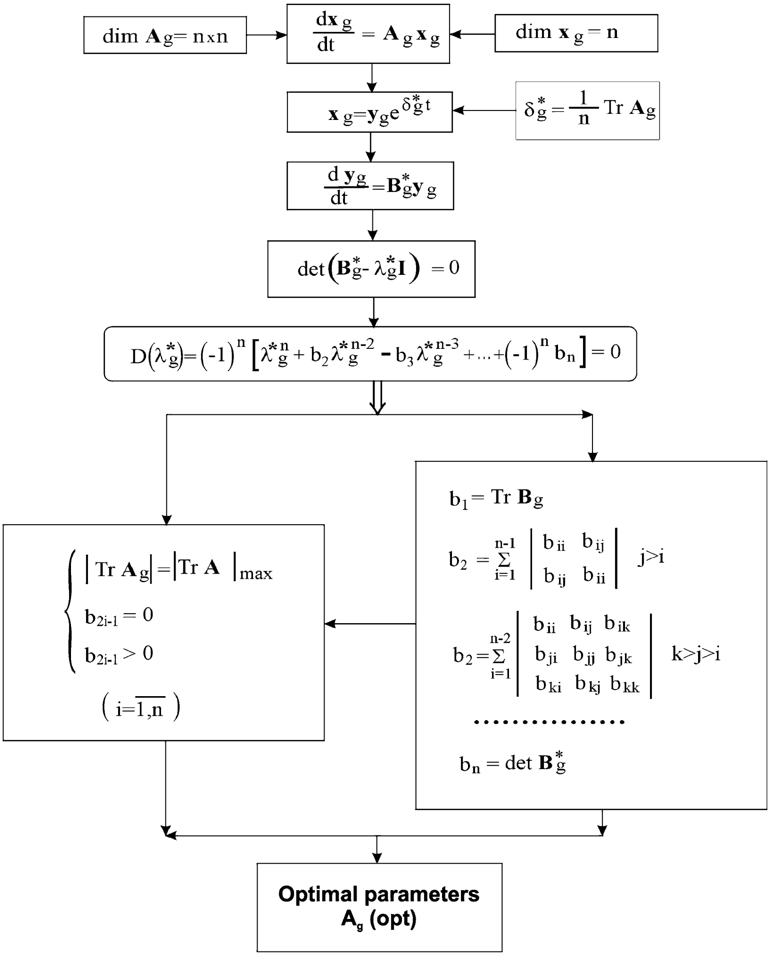

Fig. 4.18 Scheme of optimization of linear system parameters

We will present this law in the following form [23, 24]:

$$\mathbf{u}_g = -\mathbf{K}_g \mathbf{x}_g, \tag{4.112}$$

where

$$\mathbf{u}_g = [U_{zb} \quad U_{zc} \quad U_b \quad U_c]^{\mathrm{T}},$$

$$\mathbf{x}_g = \left[\vartheta_g \quad \frac{\mathrm{d}\vartheta_g}{\mathrm{d}t} \quad \psi_g \quad \frac{\mathrm{d}\psi_g}{\mathrm{d}t} \quad \vartheta_g^0 \quad \frac{\mathrm{d}\vartheta_g^0}{\mathrm{d}t} \quad \psi_g^0 \quad \frac{\mathrm{d}\psi_g^0}{\mathrm{d}t}\right]^{\mathrm{T}}.$$

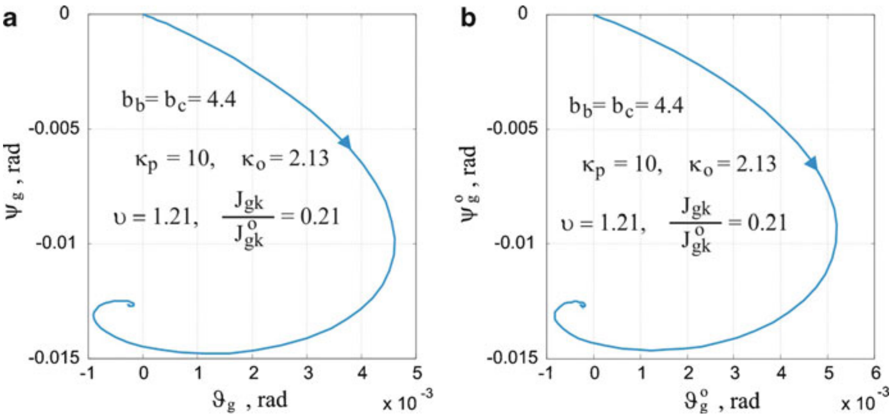

Fig. 4.19 Damping of transient process of optimal gyroscopic system: (**a**) path of gyroscope axis motion, (**b**) motion path of gyroscope axis

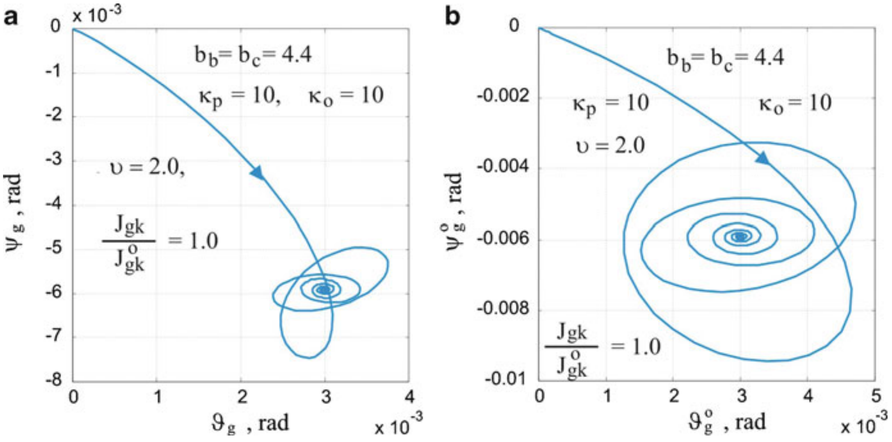

Fig. 4.20 Damping of transient process of non-optimal gyroscopic system: (**a**) motion path of gyroscope rotor axis, (**b**) motion path of gyroscope axis

The coupling matrix $\mathbf{K}_g$ in (4.112) is determined from the following relationship:

$$\mathbf{K}_g = \mathbf{R}_g^{-1}\mathbf{B}_g^{\mathrm{T}}\mathbf{P}_g, \tag{4.113}$$

where

$$\mathbf{B}_g^{\mathrm{T}} = \begin{bmatrix} 0 & c_g & 0 & 0 & 0 & 0 & 0 & 0 \\ 0 & 0 & 0 & c_g & 0 & 0 & 0 & 0 \\ 0 & 0 & 0 & 0 & 0 & c_{go} & 0 & 0 \\ 0 & 0 & 0 & 0 & 0 & 0 & 0 & c_{go} \end{bmatrix}^{\mathrm{T}},$$

$$c_g = \frac{1}{I_{gk}\Omega^2}, \qquad c_{go} = \frac{1}{I_{gk}^0\Omega^2}.$$

Matrix $\mathbf{P}_g$ is a solution of the algebraic Riccati equation

$$\mathbf{A}_g^{\mathrm{T}}\mathbf{P}_g + \mathbf{P}_g\mathbf{A}_g - 2\mathbf{P}_g\mathbf{B}_g\mathbf{R}_g^{-1}\mathbf{B}_g^{\mathrm{T}}\mathbf{P}_g + \mathbf{Q}_g = \mathbf{0}, \tag{4.114a}$$

where $\mathbf{A}_g$ is a state matrix of the form

$$\mathbf{A}_g = \begin{bmatrix} 0 & 1 & 0 & 0 & 0 & 0 & 0 & 0 \\ -\kappa_p & 0 & 0 & -1 & \kappa_p & 0 & 0 & 0 \\ 0 & 0 & 0 & 1 & 0 & 0 & 0 & 0 \\ 0 & 1 & -\kappa_p & 0 & 0 & 0 & \kappa_p & 0 \\ 0 & 0 & 0 & 0 & 0 & 1 & 0 & 0 \\ \kappa_0 & 0 & 0 & 0 & -\kappa_0 & -b_b & 0 & 0 \\ 0 & 0 & 0 & 0 & 0 & 0 & 0 & 1 \\ 0 & 0 & \kappa_0 & 0 & 0 & 0 & -\kappa_0 & -b_c \end{bmatrix}. \tag{4.114b}$$

The weight matrices $\mathbf{R}_g$ and $\mathbf{Q}_g$ in (4.113) and (4.114a), transformed into diagonal forms, are selected experimentally, where the search is initiated from the following values [22]:

$$q_{ii} = \frac{1}{2x_{i_{\max}}}, \qquad r_{ii} = \frac{1}{2u_{i_{\max}}}, \qquad (i = 1, 2, \ldots, 8), \tag{4.115}$$

where $x_{i_{\max}}$ is the maximal range of change of the ith value of the state variable, $u_{i_{\max}}$ is the maximal range of change of the ith value of the control variable.

Solving numerically the matrix Ricatti (4.114a) and determining the gain matrix $\mathbf{K}_g$, one can observe that for the analyzed case, particular elements of the matrix satisfy the following relationships:

$$k_{11} = k_{23} = k_{z\vartheta}, \qquad k_{12} = k_{24} = h_{z\vartheta}, \qquad k_{13} = -k_{21} = k_{z\psi},$$

$$k_{14} = k_{22} = h_{z\psi} = 0, \quad k_{15} = k_{27} = k_{z\vartheta_0}, \quad k_{16} = -k_{28} = h_{z\vartheta_0},$$

$$k_{17} = k_{25} = k_{z\psi_0}, \qquad k_{18} = -k_{26} = h_{z\psi_0}, \quad k_{31} = k_{43} = k_{\vartheta},$$

$$k_{32} = k_{44} = h_{\vartheta}, \qquad k_{33} = -k_{41} = k_{\psi}, \qquad k_{34} = -k_{42} = h_{\psi},$$

$$k_{35} = k_{47} = k_{\vartheta_0}, \qquad k_{36} = k_{48} = h_{\vartheta_0}, \qquad k_{37} = -k_{45} = k_{\psi_0},$$

$$k_{38} = k_{46} = h_{\psi_0} = 0.$$

It follows from the preceding relationships and (4.112) that the control torques influencing the gyroscope will have the form

$$U_{zb} = -k_{z\vartheta}\vartheta_g - h_{z\vartheta}\frac{\mathrm{d}\vartheta_g}{\mathrm{d}\tau} + k_{z\psi}\psi_g - k_{z\vartheta_0}\vartheta_g^0 + h_{z\vartheta_0}\frac{\mathrm{d}\vartheta_g^0}{\mathrm{d}\tau} - k_{z\psi_0}\psi_g^0 + h_{z\psi_0}\frac{\mathrm{d}\psi_g^0}{\mathrm{d}\tau}, \tag{4.116}$$

$$U_{zc} = -k_{z\psi}\vartheta_g - h_{z\vartheta}\frac{\mathrm{d}\psi_g}{\mathrm{d}\tau} - k_{z\vartheta}\psi_g - k_{z\psi_0}\vartheta_g^0 - h_{z\psi_0}\frac{\mathrm{d}\vartheta_g^0}{\mathrm{d}\tau} - k_{z\vartheta_0}\psi_g^0 - h_{z\vartheta_0}\frac{\mathrm{d}\psi_g^0}{\mathrm{d}\tau}, \tag{4.117}$$

$$U_b = -k_{\vartheta}\vartheta_g - h_{\vartheta}\frac{\mathrm{d}\vartheta_g}{\mathrm{d}\tau} - k_{\psi}\psi_g + h_{\psi}\frac{\mathrm{d}\psi_g}{\mathrm{d}\tau} - k_{\vartheta_0}\vartheta_g^0 - h_{\vartheta_0}\frac{\mathrm{d}\vartheta_g^0}{\mathrm{d}\tau} + k_{\psi_0}\psi_g^0, \tag{4.118}$$

$$U_c = -k_{\psi}\vartheta_g - h_{\psi}\frac{\mathrm{d}\vartheta_g}{\mathrm{d}\tau} - k_{\vartheta}\psi_g - h_{\vartheta}\frac{\mathrm{d}\psi_g}{\mathrm{d}\tau} - k_{\psi_0}\vartheta_g^0 - h_{\vartheta_0}\frac{\mathrm{d}\psi_g^0}{\mathrm{d}\tau} - k_{\vartheta_0}\psi_g^0. \tag{4.119}$$

Applying the preceding controls to the gyroscope described by (4.96), we obtain a new gyroscopic system of the form

$$\frac{\mathrm{d}\mathbf{x}_g}{\mathrm{d}\tau} = \mathbf{A}_g^*\mathbf{x}_g, \tag{4.120}$$

where

$$\mathbf{A}_g^* = \mathbf{A}_g - \mathbf{B}_g\mathbf{R}_g^{-1}\mathbf{B}_g^{\mathrm{T}}\mathbf{P}_g.$$

System (4.120) can be optimized according to the algorithm depicted in Fig. 4.18. The additional optimization by means of the modified Golubientsev method can be carried out if the gyroscopic system (4.120) is to be applied in devices of target detection and tracking systems [21]. This concerns the minimization of the transient process duration at the moment of target detection, which holds great significance for the maintenance of this target near the tracking system [22, 25].

A block diagram of the algorithm of a linear-square optimization, along with the modified Golubientsev method of any control system, is presented in Fig. 4.21.

4.4.3 Results of Digital Investigations

The results of controlling a gyroscope suspended in an elastic suspension are depicted in Figs. 4.22–4.26. A control problem depends on putting the gyroscope axis in the pre-set motion, in which the gyroscope axis moves on a cone surface

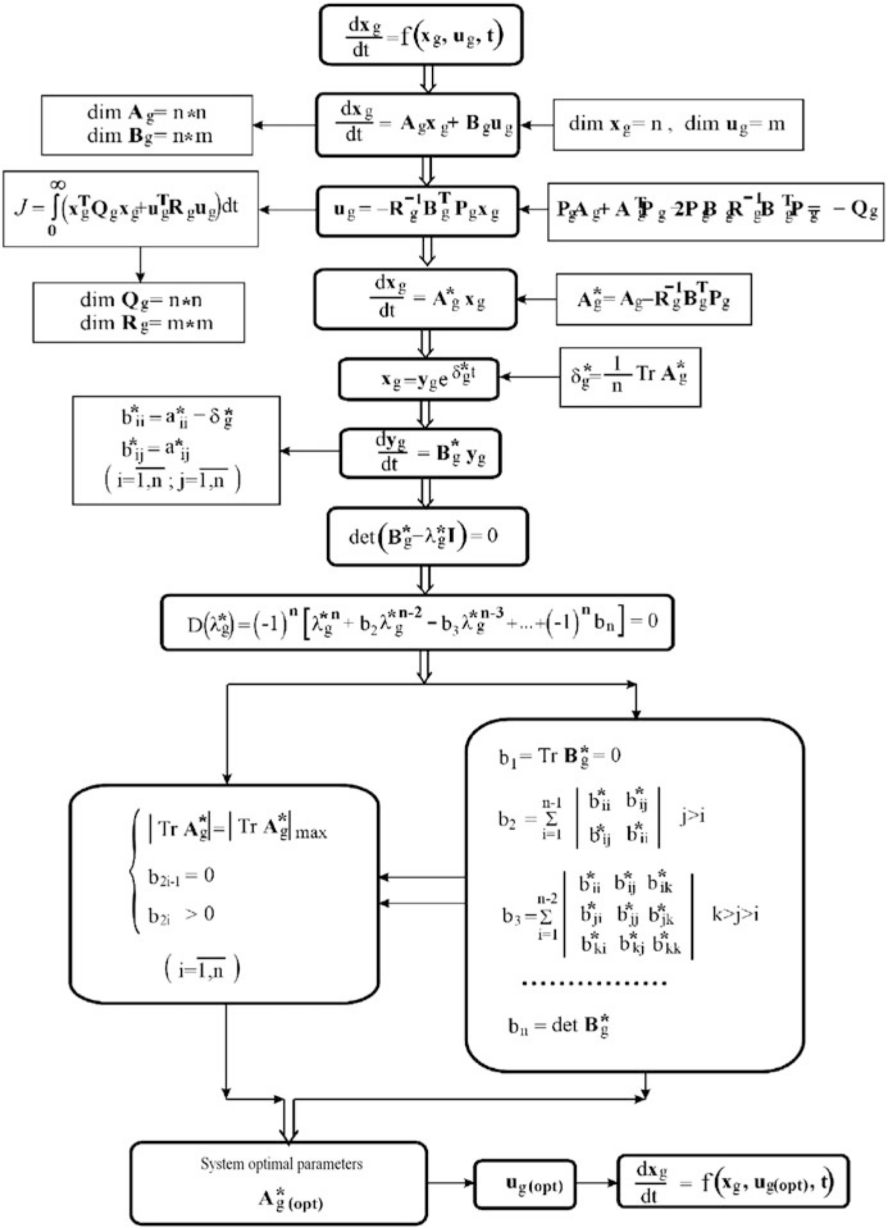

Fig. 4.21 Block diagram of complete system optimization

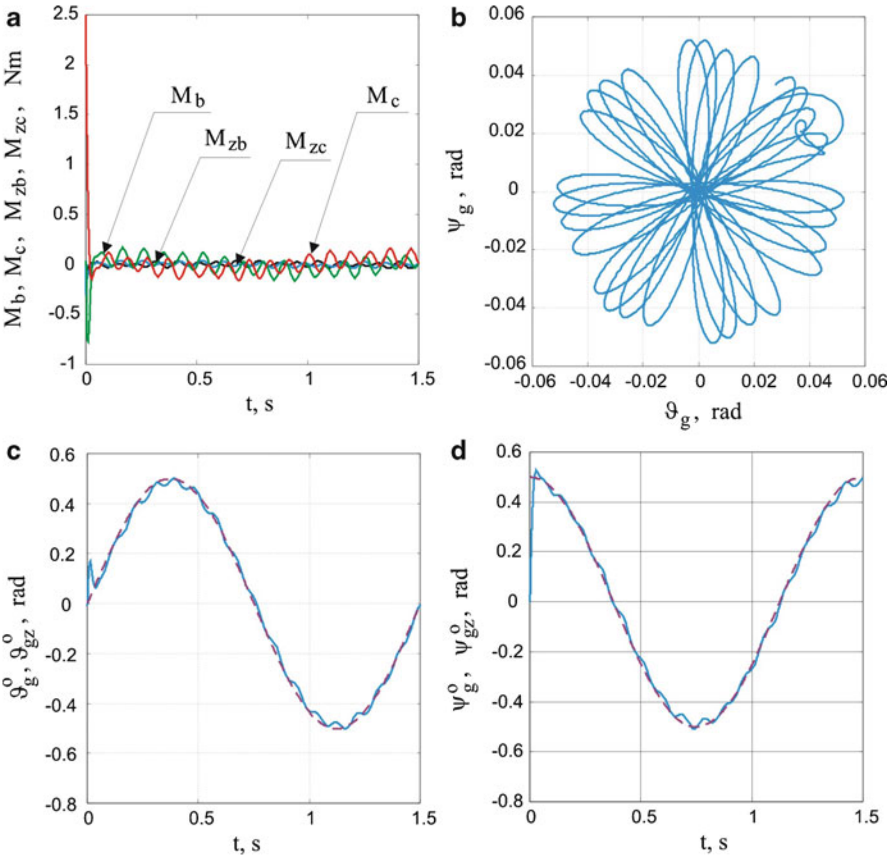

Fig. 4.22 Gyroscope control in elastic suspension using PID regulator: (**a**) change in control torques as a function of time, (**b**) path of gyroscope axis, (**c**), (**d**) change in preset and realized angular deviations of gyroscope axis as a function of time

(Figs. 4.22–4.24) or on an Archimedes spiral (Figs. 4.25 and 4.26), and the rotor axis plots n-flute rosette. For all of the cases the gyroscope parameters are the same as in Sect. 4.2. Figures 4.22 and 4.23 present the behavior of a gyroscope with the PID regulator applied, with non-optimal coefficients.

In Fig. 4.24 one can observe an essential improvement in realization of motion, preset by the gyroscope after introduction of controls, selected on the basis of the algorithm illustrated in Fig. 4.21. The efficiency of the optimal control is depicted in Fig. 4.25, where, despite the action of the impulse of torque, the preset motion is instantiated. We have a similar situation in the case of the effect of kinematic excitations on gyroscope suspension in the form of harmonic vibrations.

We applied optimal gain coefficients of the control torques described by relationships (4.117)–(4.120) with the following values:

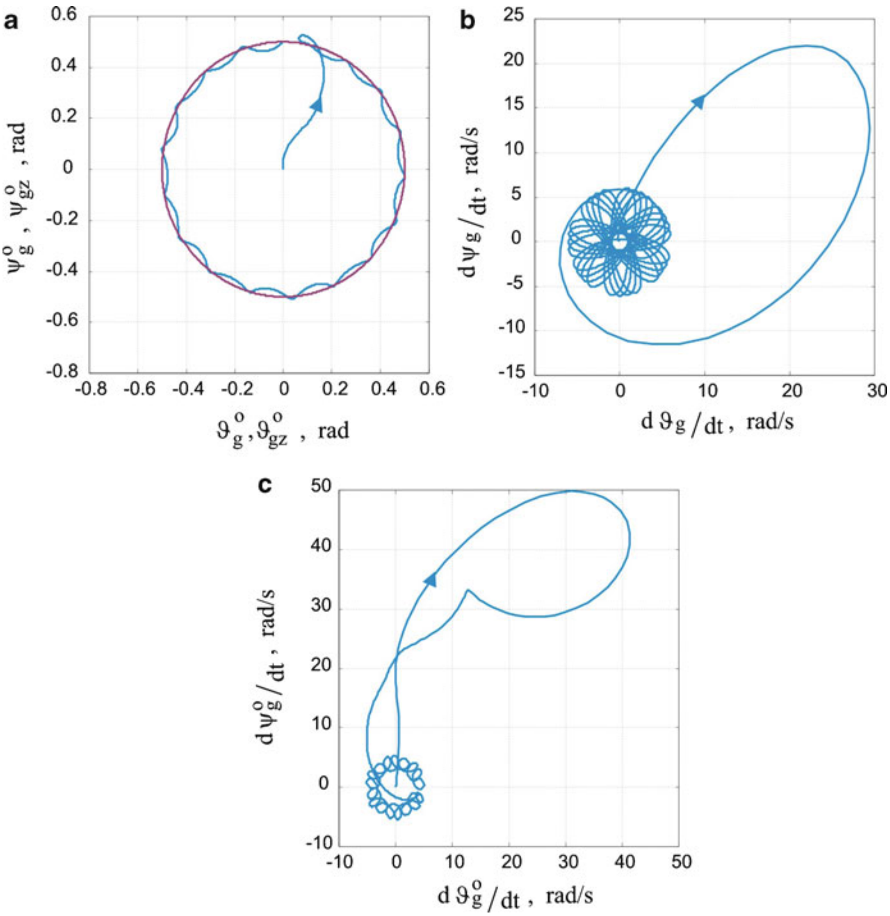

Fig. 4.23 Gyroscope control in elastic suspension using PID regulator: (**a**) preset and realized path of gyroscope axis, (**b**) angular velocities of rotor axis of gyroscope in phase plane, (**c**) angular velocities of gyroscope axis in phase plane

$$k_{z\vartheta} = -0.0155, \quad h_{z\vartheta} = 73.67, \quad k_{z\psi} = -0.355, \quad h_{z\psi} = 0.00,$$

$$k_{z\vartheta_0} = 0.477, \quad h_{z\vartheta_0} = 0.756, \quad k_{z\psi_0} = -0.471, \quad h_{z\psi} = -0.0146,$$

$$k_{\vartheta} = -0.128, \quad h_{\vartheta} = 3.549, \quad k_{\psi} = -2.125, \quad h_{\psi} = 0.0686,$$

$$k_{\vartheta_0} = 12.574, \quad h_{\vartheta_0} = 20.898, \quad k_{\psi_0} = -2.633, \quad h_{\psi_0} = 0.00.$$

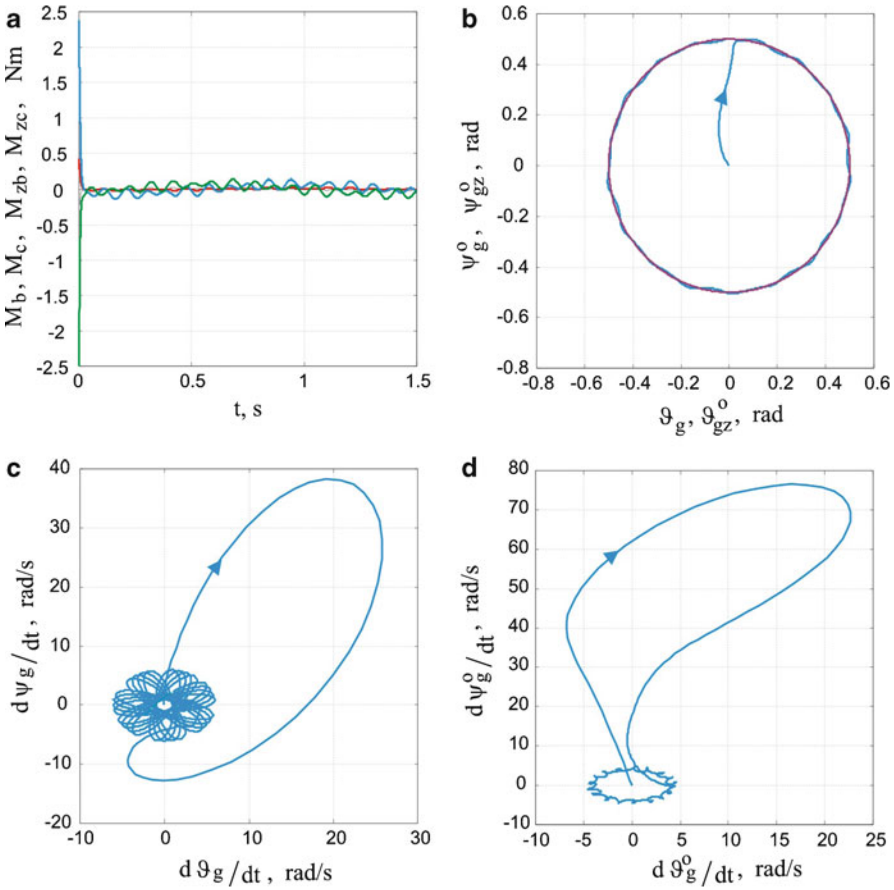

Fig. 4.24 Gyroscope control in elastic suspension using optimal control torques: (**a**) change in control torques as a function of time, (**b**) preset and realized path of gyroscope axis, (**c**) angular velocities of rotor axis of gyroscope in phase plane, (**d**) angular velocities of gyroscope axis in phase plane

4.5 Selection of Optimal Parameters of a Gyroscopic System with an Axis Fixed to Rotor

4.5.1 Optimization of a Classic Controlled Gyroscope

The linearized model of a controlled gyroscopic system with an axis permanently connected to a rotor is presented as follows

$$\frac{\mathrm{d}\mathbf{x}_g}{\mathrm{d}\tau} = \mathbf{A}_g\mathbf{x}_g + \mathbf{B}_g\mathbf{u}_g, \tag{4.121}$$

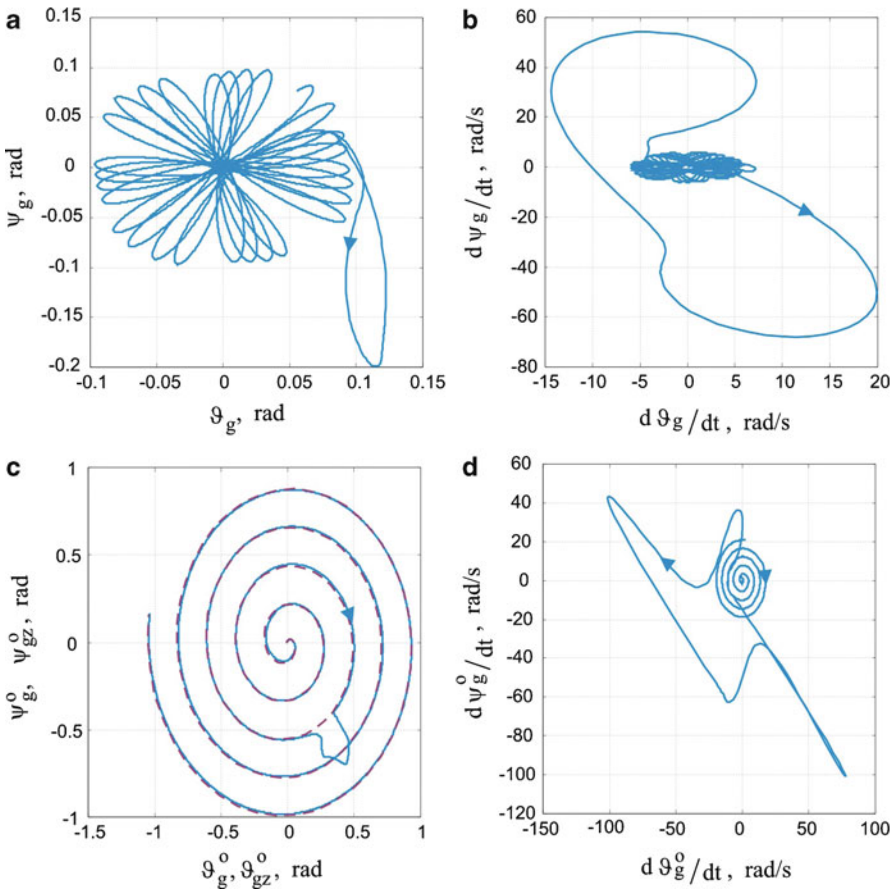

Fig. 4.25 Gyroscope control in elastic suspension using optimal control torques under action of impulse of pair of forces: (**a**) path of rotor axis of gyroscope, (**b**) angular velocities of rotor axis of gyroscope in phase plane, (**c**) preset and realized path of gyroscope axis, (**d**) angular velocities of gyroscope axis in phase plane

where

$$\mathbf{x}_g = \begin{bmatrix} \vartheta_g & \dfrac{\mathrm{d}\vartheta_g}{\mathrm{d}\tau} & \psi_g & \dfrac{\mathrm{d}\psi_g}{\mathrm{d}\tau} \end{bmatrix}^{\mathrm{T}}, \qquad \mathbf{u}_g = [u_b \quad u_c]^{\mathrm{T}},$$

$$\mathbf{A}_g = \begin{bmatrix} 0 & 1 & 0 & 0 \\ 0 & -b_b & 0 & -1 \\ 0 & 0 & 0 & 1 \\ 0 & 1 & 0 & -b_c \end{bmatrix}, \qquad \mathbf{B}_g = \begin{bmatrix} 0 & 0 \\ c_b & 0 \\ 0 & 0 \\ 0 & c_c \end{bmatrix}.$$

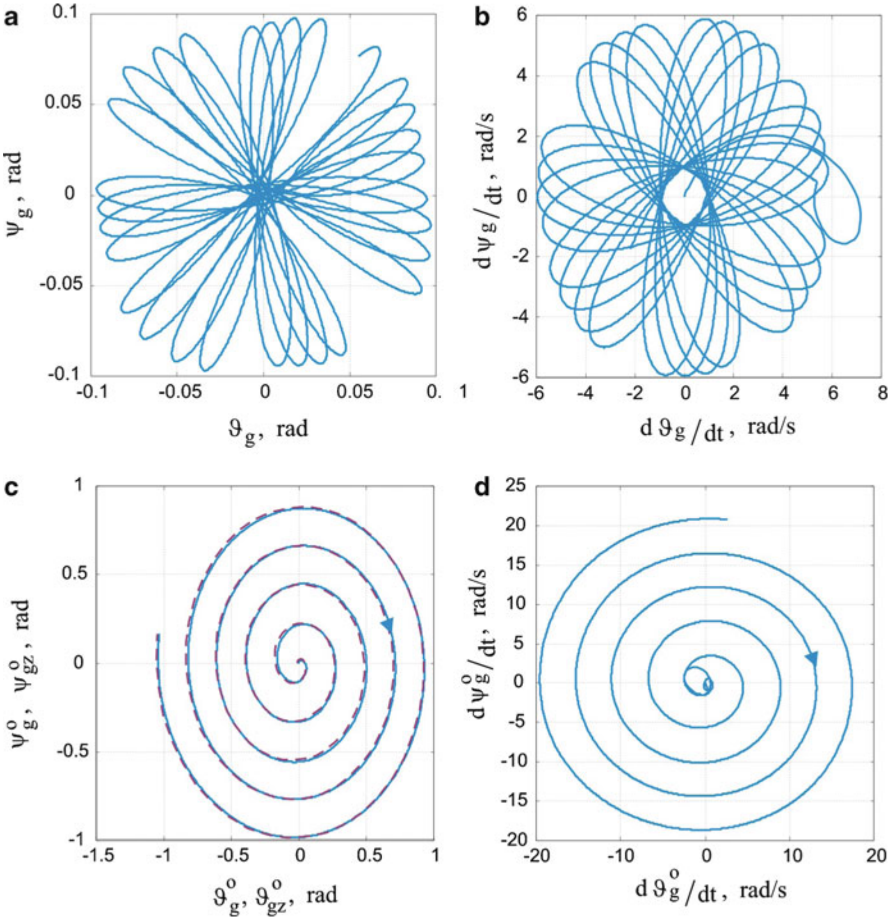

Fig. 4.26 Controlling a gyroscope suspended in an elastic suspension using optimal control torques under action of kinematic excitements of base: (**a**) path of rotor axis, (**b**) angular velocities of rotor axis in phase plane, (**c**) preset and realized path of gyroscope axis, (**d**) angular velocities of gyroscope axes in phase plane

In order to ensure that the controlled gyroscope governed by (4.121) has stability and a shortest transient process, as in the preceding section, we will introduce an optimal control of the form

$$\mathbf{u}_g = -\mathbf{K}_g \mathbf{x}_g, \tag{4.122}$$

where

$$\mathbf{K}_g = \begin{bmatrix} k_{11} & k_{12} & k_{13} & k_{14} \\ k_{21} & k_{22} & k_{23} & k_{24} \end{bmatrix}.$$

Similarly to the case of the gyroscopic system in an elastic suspension described by state matrix (4.114a), the particular elements of gain matrix $\mathbf{K}_g$ satisfy the following relationships for the analyzed case:

$$\begin{aligned} k_{11} &= k_{23} = \bar{k}_b, \\ k_{12} &= k_{14} = k_{22} = k_{24} = \bar{h}_g, \\ k_{21} &= -k_{13} = \bar{k}_c. \end{aligned} \tag{4.123}$$

Substituting the gain coefficients (4.123) into (4.122), the correcting controls take the form

$$u_b = -\bar{k}_b \vartheta_g + \bar{k}_c \psi_g - \bar{h}_g \frac{\mathrm{d}\vartheta_g}{\mathrm{d}\tau}, \tag{4.124a}$$

$$u_c = -\bar{k}_c \vartheta_g - \bar{k}_b \psi_g - \bar{h}_g \frac{\mathrm{d}\psi_g}{\mathrm{d}\tau}, \tag{4.124b}$$

where

$$\bar{k}_b = \frac{k_b}{I_{gk}\Omega^2}, \quad \bar{k}_c = \frac{k_c}{I_{gk}\Omega^2}, \quad \bar{h}_g = \frac{h_g}{I_{gk}\Omega}. \tag{4.125}$$

Thus, the gyroscopic system in the closed system (4.121), including (4.124), is reduced to a new form:

$$\frac{\mathrm{d}\mathbf{x}_g}{\mathrm{d}\tau} = \mathbf{A}_g^* \mathbf{x}_g, \tag{4.126}$$

where

$$\mathbf{A}_g^* = \begin{bmatrix} 0 & 1 & 0 & 0 \\ -\bar{k}_b & -\bar{h}_g - b_b & \bar{k}_c & 1 \\ 0 & 0 & 0 & 1 \\ -\bar{k}_c & -1 & -\bar{k}_b & -\bar{h}_g - b_c \end{bmatrix}. \tag{4.127}$$

Henceforth, we will assume that friction in the suspension bearings is negligible, i.e., $b_b = b_c = 0$. For a gyroscopic system like this, we will seek two more parameters and relations between them for which the duration of the transient process damping is the shortest. In this case, we will also apply the modified optimization method of Golubientsev, whose algorithm is presented in Fig. 4.18.

We obtain the following system of equations and inequalities from the stability conditions of Hurwitz and modified Golubientsev optimization method [25]:

$$\bar{k}_b > 0, \quad \bar{k}_c > 0, \quad \bar{h}_g > 0, \tag{4.128}$$

$$2\bar{k}_b - \frac{1}{2}\bar{h}_g^2 + 1 > 0, \tag{4.129}$$

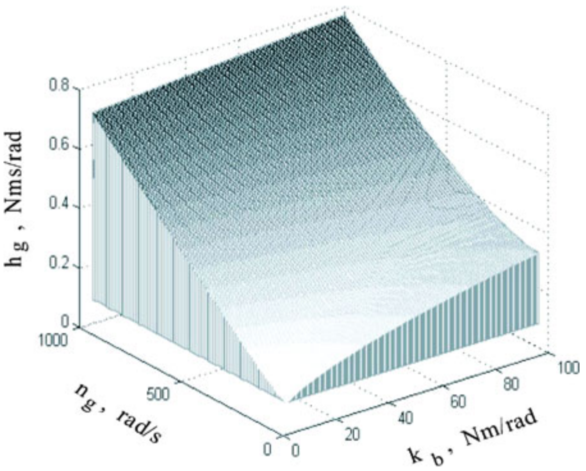

Fig. 4.27 Graph of mutually optimal relations of damping coefficient of regulator h_g, angular velocity n_g, and gain factor k_b

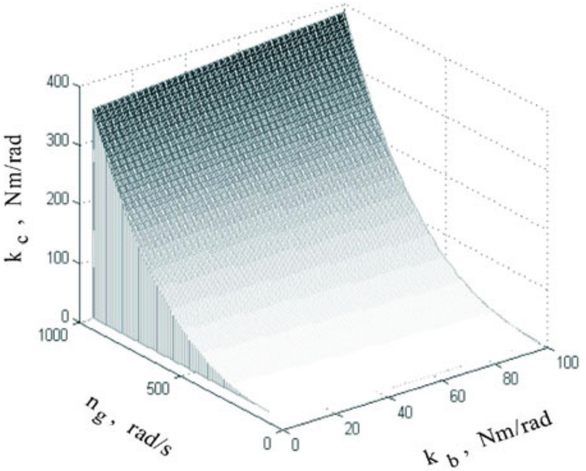

Fig. 4.28 Graph of mutual optimal relationships of gain coefficient of regulator k_c, angular velocity n_g, and gain coefficient k_b

$$\bar{k}_c = \frac{1}{2}\bar{h}_g, \tag{4.130}$$

$$\frac{1}{16}\bar{h}_g^4 + \frac{1}{4}\bar{h}_g^2 - \frac{1}{2}\bar{h}_g^2\bar{k}_b - \bar{h}_g\bar{k}_c + \bar{k}_b^2 + \bar{k}_c^2 > 0. \tag{4.131}$$

Taking into account the condition of maximization of absolute value of a trace of matrix $\mathbf{A}_g^*$ yields

$$|\mathrm{Tr}\mathbf{A}_g^*| \to \max. \tag{4.132}$$

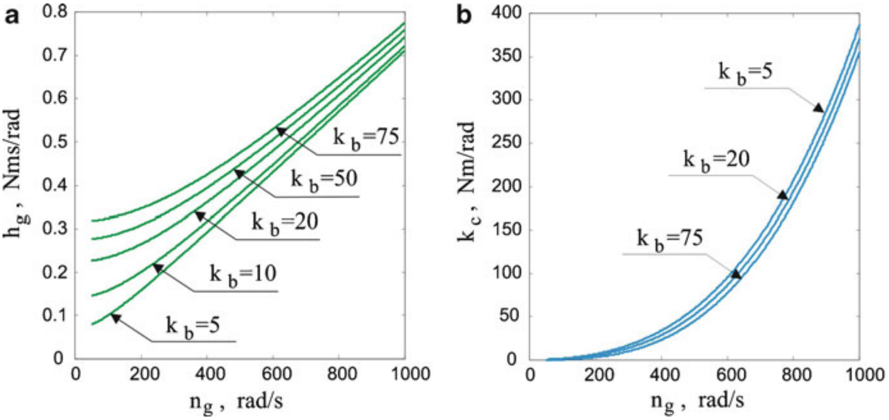

Fig. 4.29 Graph of optimal relationships of regulator coefficients (**a**) h_g, (**b**) k_c vs. angular velocity n_g at different gain coefficient k_b

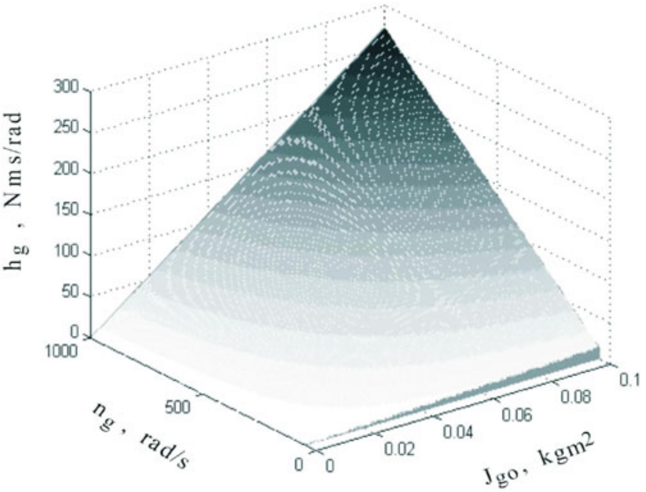

Fig. 4.30 Graph of mutual optimal relationships of damping coefficient of regulator h_g, angular velocity n_g, and moment of inertia I_{go}

From (4.129) we obtain the following value of the damping coefficient:

$$\bar{h}_g = \sqrt{2 + 4\bar{k}_b}. \tag{4.133}$$

Substituting (4.133) into (4.130) we obtain

$$\bar{k}_c = \frac{1}{2}\sqrt{2 + 4\bar{k}_b}. \tag{4.134}$$

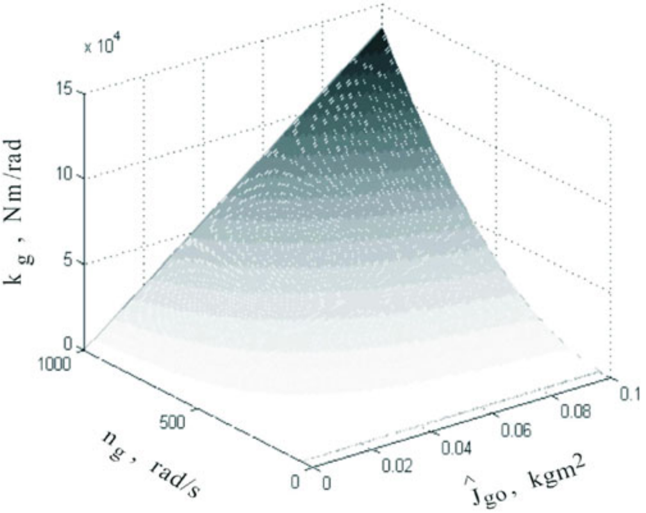

Fig. 4.31 Graph of mutual optimal relationships of gain coefficient of regulator k_g, angular velocity n_g, and moment of inertia I_{go}

Taking into account (4.125) we have

$$h_g = \sqrt{2I_{go}^2 n_g^2 + 4I_{gk}k_b}, \tag{4.135}$$

$$k_c = \frac{1}{2}\sqrt{2I_{go}^2 n_g^2 + 4I_{gk}k_b} \cdot \frac{I_{go}^2 n_g^2}{I_{gk}}. \tag{4.136}$$

Thus, the coefficients $\bar{h}_g$ and $\bar{k}_c$ are uniquely determined as functions of the gyroscope parameters I_{go}, I_{gk}, n_g and the coefficient $\bar{k}_b$, which should satisfy the stability conditions, and technical constraints resulting from the strength of the gyroscope.

The obtained relationships can be used to gyroscope control under conditions of alternating angular velocity of eigenrotations (e.g., in some self-guided missiles or target-seeking systems with a wide range of angular deviations of the gyroscope axis). Then one needs to measure simultaneously $n_g(t)$ and update the values of the regulator coefficients h_g and k_c according to the relationships (4.135) and (4.136). The coefficient k_b is given in a programmable way and it allows for adaptive control of the gyroscope.

Figures 4.27–4.31 graphically present the character of the relationships between particular gyroscope parameters. In order to obtain these relationships, one assumed that

$$I_{gk} = I_{go}/2.$$

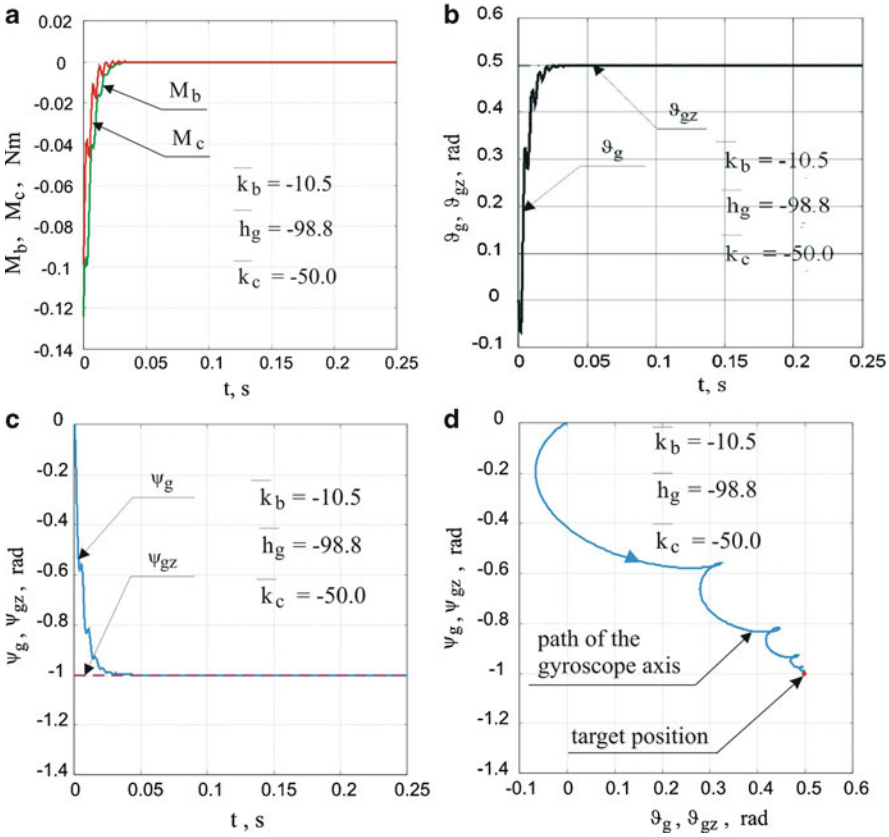

Fig. 4.32 Results of gyroscope axis control using optimal regulator during tracking of fixed point: (**a**) change of control torques as a function of time, (**b, c**) change in angular deviations as a function of time, (**d**) path of gyroscope axis

Thus, if the system of conditions (4.128)–(4.133) is satisfied, then the transient process of the gyroscopic system (4.121) will be damped during the shortest time [22]. Figures 4.32 and 4.33 present the results of gyroscope axis control upon tracking of a movable and fixed target using an optimal regulator of the coefficients determined from relationships (4.135) and (4.136).

In comparison with the results presented in Figs. 4.12–4.16 we can observe a significant improvement in the control quality of the gyroscope axis, i.e., considerable reduction of the duration of the transient process.

A gyroscope is a strongly non-linear system, which implies that errors of the preset and performed motion are generated at large values of angular velocities and deviations of the gyroscope axis. Therefore, when we apply program control within the non-linear range and under the influence of disturbance of gyroscope operation, it should also apply additional optimal control in a closed system.

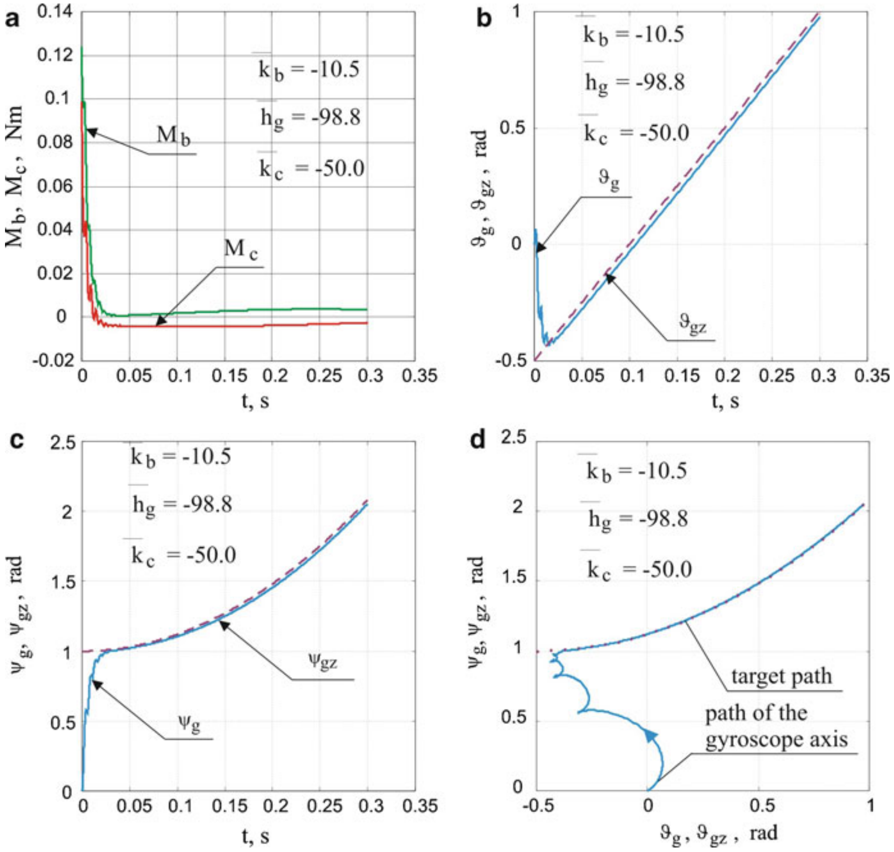

Fig. 4.33 Results of gyroscope axis control using optimal regulator during tracking of moving point: (**a**) change in control torques as a function of time, (**b, c**) change in angular deviations as a function of time, (**d**) path of gyroscope axis

References

1. Z. Koruba, in *Dynamics and control model of gyroscope located on deck of unmanned aerial vehicle.* North Atlantic Treaty Organization Unmanned Vehicles for Aerial, Ground and Naval Military Operations: A Symposium organized by the Applied Vehicle Technology Panel, Ankara, Turkey, 9–13 October 2000
2. J. Nizio, Dynamics of gyroscopes with a special emphasis on integrating gyroscopes in deterministic and probabilistic nonlinear formulations. *Mechanics* (Cracow University of Technology Press, Cracow, 1975), in Polish
3. V.A. Pavlov, *Aviational Gyroscopic Devices* (GOSIZDAT of Defense Industry, Moscow, 1954), in Russian
4. R. Grammel, *The Gyroscope: Its Theory and Applications* (Springer, Berlin, 1950), in German
5. M.A. Pavlovskiy, *Theory of the Gyroscopes* (Vyshaya Shkola, Kiev, 1986), in Russian
6. R.N. Arnold, L. Maunder, *Gyrodynamics and Its Engineering Applications* (Academic, New York, 1961)

7. K. Magnus, *Gyroscopes, Theory and Applications* (Springer, Berlin, 1971), in German
8. N.F. Babaeva, *Gyroscopes* (Mashinostroenie, Leningrad, 1973), in Russian
9. M. Davidson, *The Gyroscope and Its Application* (Hutchinson's Scientific and Technical Publications, London, New York, 1946)
10. R.F. Deimel, *Mechanics of the Gyroscope: The Dynamics of Rotation* (Dover, New York, 1950)
11. L.I. Kargu, *Measurement Devices of Flying Objects* (Mashinostroenie, Moscow, 1988), in Russian
12. J.W. Osiecki, A. Zgoa, in *Gyroscope axis movement control in nonlinear aspect.* Proceedings of the 1st National Conference on Avionics BIESZCZADY'95. Rzeszow-Jawor, vol. 1, no. (45) (Rzeszow University of Technology Scientific Papers Press, Avionics, Rzeszow, 1995), pp. 299–307, in Polish
13. Z. Koruba, Algorithm of direct gyroscope stabilizer control and correction. Int. J. Eng. Modell. **17**(1–2), 21–32 (2004)
14. L.I. Kargu, *Gyroscopic Devices and Systems* (Sudostroyeniye, Leningrad, 1988), in Russian
15. A.A. Odintsov, *Theory and Computation of Gyroscopic Systems* (Vyshaya Shkola, Kiev, 1985), in Russian
16. Z. Koruba, in *Dynamics of a gyroscope under control and its axis stabilization.* Proceedings of the 2nd School on "Methods for Active Vibration and Noise Reduction." Cracow–Zakopane, 26–28 April 1995, pp. 1955–1960
17. C.W. de Silva, *Mechatronics: A Foundation Course* (University of British Columbia, Vancouver, 2010)
18. Z. Koruba, A process of gyroscope motion control in an autonomous system, target detection and tracking. J. Theor. Appl. Mech. **37**(4), 908–927 (1999)
19. V.N. Koshlyakov, *Problems of Solid Body Dynamics and Applied Theory of Gyroscopes* (Nauka, Moscow, 1985), in Russian
20. M. Fusik, Z. Koruba, in *Model of a scanning device in a unmanned flying object.* Proceedings of the 7th Polish Conference on Automation and Exploitation of Control Systems, Gdynia, 13–15 October 1999, pp. 165–170, in Polish
21. Z. Koruba, J. Osiecki, *Construction, Dynamics and Navigation of Close-Range Missiles, Part 1.* University Course Book No. 348 (Kielce University of Technology Publishing House, Kielce, 1999), in Polish
22. Z. Koruba, Selection of the optimum parameters of the gyroscope system on elastic suspension in the homing missile system. J. Tech. Phys. **40**(3), 341–354 (1999), Warsaw, in Polish
23. R.B. Guenther, *An Introduction to Numerical Methods: A MATLAB Approach* (Oregon State University, Corvallis, 2005)
24. W.Bober, *Numerical and Analytical Methods with MATLAB* (Florida Atlantic University, Boca Raton, 2009)
25. S. Dubiel, Linear mechanical systems with the fastest damping. Theor. Appl. Mech. **3**(24), 15–28, (1986), Warsaw, in Polish

Chapter 5
Gyroscopic Control in Self-Guidance Systems of Flying Objects

In this chapter a gyroscopic control in self-guidance systems of flying objects (FOs) is presented, and a gyroscopic control in an unmanned aerial vehicle is studied. First, the navigational kinematics of an unmanned aerial vehicle (UAV) is analyzed, and then the control of a gyroscope fixed on its board as well as its full control are discussed. Furthermore, a gyroscope in a guided aerial bomb is studied. It includes analysis of kinematics of a bomb self-guided motion to a ground target, equations of motion of a guided bomb, and a description of a gyroscopic system designed for bomb control including automatic pilot control.

5.1 Gyroscope in an Unmanned Aerial Vehicle

The functioning of a UAV at every stage of its operation is a complicated process that requires a complex of technical tasks. The basis of this is the UAV control system. In the course of a mission, there occurs, firstly, the measurement, evaluation, and checking of flight parameters and technical systems, and, secondly, the appropriate control of the flight, system observation, and laser illumination conducted according to the results of identification and checking of the aforementioned parameters. Both the identification and checking, as well as the control, are realized either directly by the operator or automatically.

A fundamental drawback of UAV functioning is the need to maintain two-way communications (often continuously) with a ground control post, which may disclose the post's location, although a variety of means is used to hide the communications. That is why in modern UAV systems autonomy during the realisation of the task of seeking and tracking a ground target is of the utmost importance. It is required that during a programmed flight of a UAV, there must be a way to adjust or even completely change the flight path, depending on the situation, for instance, after target detection.

Modern so-called precision weapons, such as missiles, rockets, and bombs (MRBs), controlled by semiactive self-guidance to a target, find a wide range of

J. Awrejcewicz and Z. Koruba, *Classical Mechanics*, Advances in Mechanics and Mathematics 30, DOI 10.1007/978-1-4614-3978-3_5,

applications. Semiactive methods of MRB path control require so-called target illumination, which is realized by means of a radar beam or rays in the infrared band. The latter are exploited ever more often because of their well-known advantages.

Target illumination is usually conducted from ground stations or from the air, from airplanes and helicopters. This kind of target illumination has many disadvantages. Illumination requires exposing a target. In the case of illumination from ground stations, the target can be covered by natural obstacles. Moreover, the station can be easily detected and destroyed by the enemy. With illumination from the air, manned airplanes or helicopters are used. The need for illumination for a limited amount of time exposes the aerial vehicles to possible danger. Those drawbacks are largely mitigated if a small UAV is used for illumination. If produced using "stealth" technology, given its small dimensions, it is less likely to be detected and shot down. The control problem then becomes illuminating targets with sufficient accuracy.

On the modern battlefield, light, small UAVs produced using stealth technology, which makes them difficult to detect and shoot down, are used for the detection, tracking, and laser illumination of ground targets. A further development of these vehicles is the combat UAV, whose task is the autonomous detection and destruction of targets. An example of this is the use of onboard homing missiles with infrared sensors (trials have been made with a combat version of the Israeli Pioneer [1, 2]. Another example is a UAV equipped with a warhead that can automatically direct itself toward a target according to a defined guidance algorithm (e.g., the American Lark [3]). In this research, a control algorithm for this kind of combat UAV independently attacking detected targets (e.g., radar stations, combat vehicles, tanks) or conducting illumination using a laser has been proposed (Fig. 5.1).

5.1.1 Navigation Kinematics of a UAV

Figure 5.2 schematically depicts the geometric relationships of the kinematics of relative motion of particles S and C (mass centers of UAV and target) and G (point of intersection of a target seeking and observation line—the TSOL—with Earth's surface).

Based on this and the following figures (Figs. 5.3 and 5.4), the equations of the kinematics of motion of a UAV, TSOL, point G, and a target are derived.

5.1.1.1 Kinematic Equations of UAV Motion

The relative position of axes of the Earth-fixed coordinate system $O_o x'_o y'_o z'_o$ and the system associated with position vector $\mathbf{R}_{es}$ (joining points O_o and S) $O_o x_{es} y_{es} z_{es}$ is defined by two angles φ_χ^s and φ_γ^s.

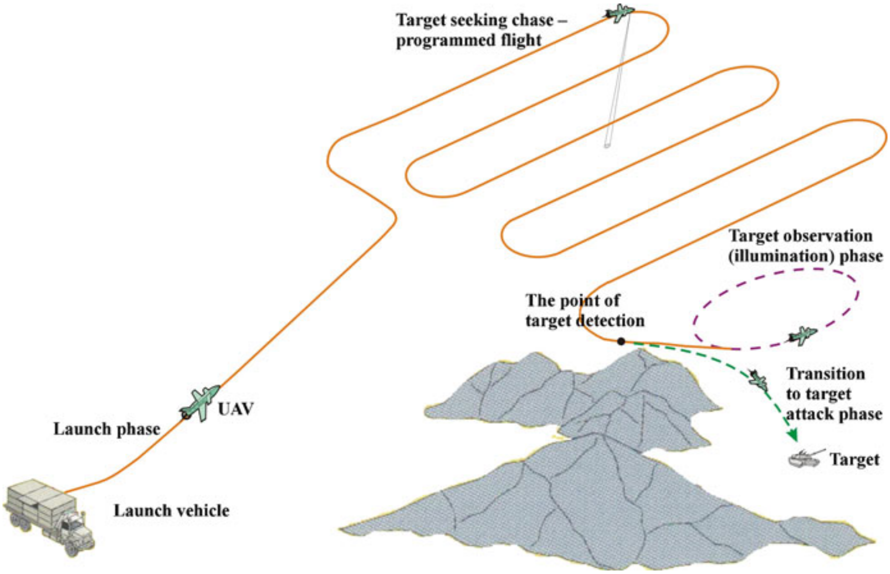

Fig. 5.1 Overall view of process of mission realization by a combat UAV

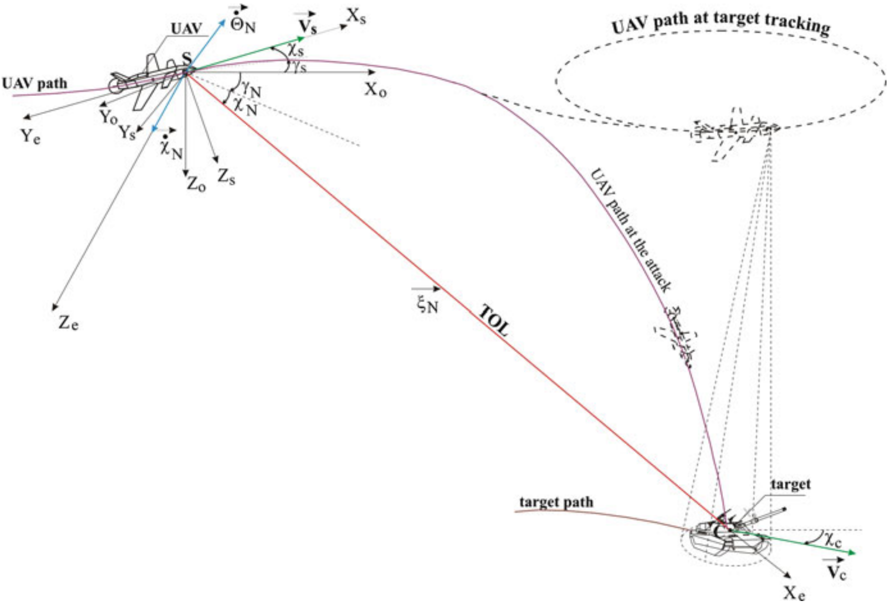

Fig. 5.2 Kinematics of a combat UAV guidance to a moving target

The relative angular positions of the axes of the coordinate systems are defined by direction cosines given in the form of tables or matrices. We obtain the following tables of direction cosines (transformation matrices).

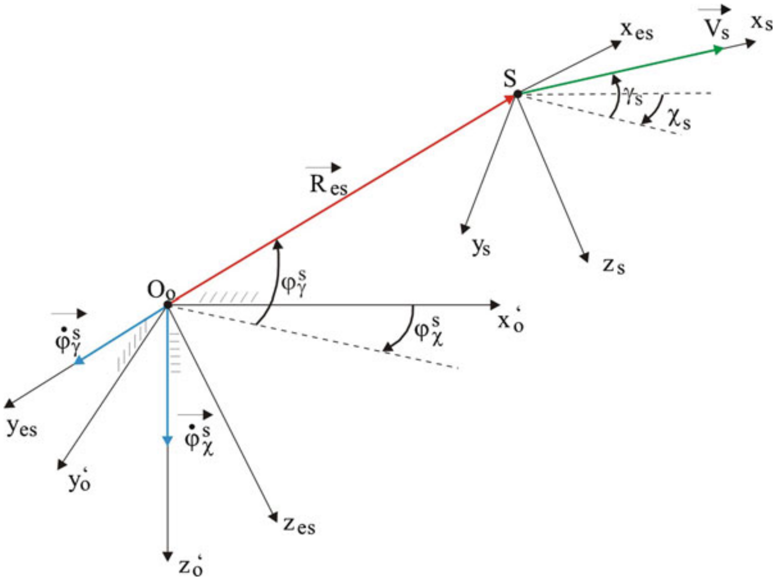

Fig. 5.3 Kinematics of UAV motion

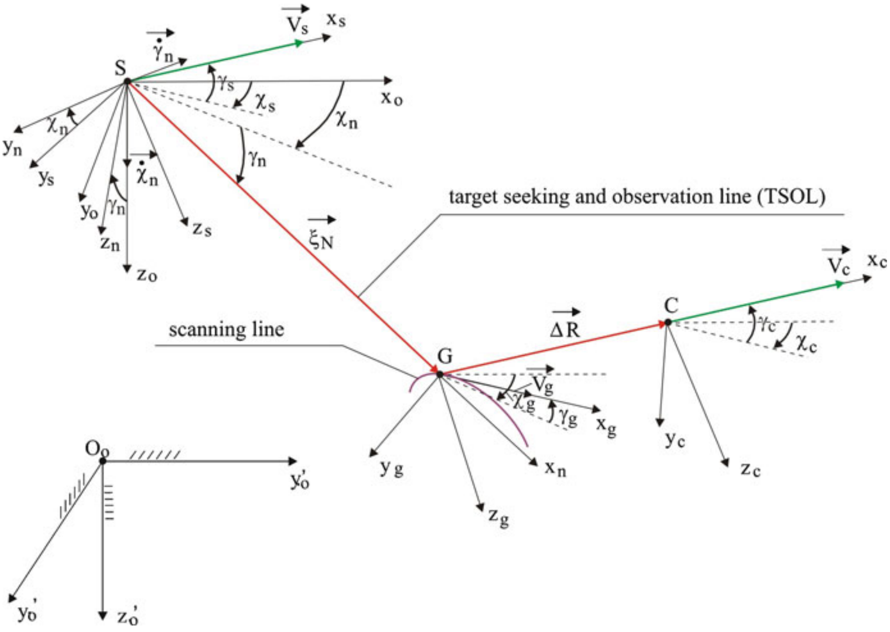

Fig. 5.4 Kinematics of TSOL line motion

The matrix of transformation from the stationary Earth-fixed coordinate system $O_o x'_o y'_o z'_o$ to the instantaneous coordinate system $O_o x_\chi y_\chi z_\chi$ (after the first rotation about the axis $O_o z_o$) is as follows:

$$M_\chi = \begin{array}{c|c|c|c} & x_o & y_o & z_o \\ \hline x_\chi & \cos\varphi_\chi^s & \sin\varphi_\chi^s & 0 \\ \hline y_\chi & -\sin\varphi_\chi^s & \cos\varphi_\chi^s & 0 \\ \hline z_\chi & 0 & 0 & 1 \end{array}$$

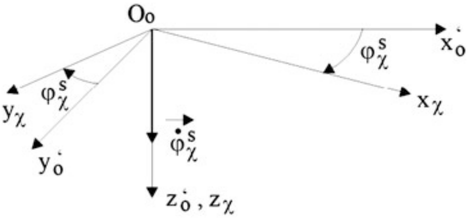

The matrix of transformation from the system $O_o x_\chi y_\chi z_\chi$ to the system $O_o x_{es} y_{es} z_{es}$ (after the second rotation about the instantaneous axis of rotation $O_o y_\chi$) is

$$M_\gamma = \begin{array}{c|c|c|c} & x_\chi & y_\chi & z_\chi \\ \hline x_{es} & \cos\varphi_\gamma^s & 0 & -\sin\varphi_\gamma^s \\ \hline y_{es} & 0 & 1 & 0 \\ \hline z_{es} & \sin\varphi_\gamma^s & 0 & \cos\varphi_\gamma^s \end{array}$$

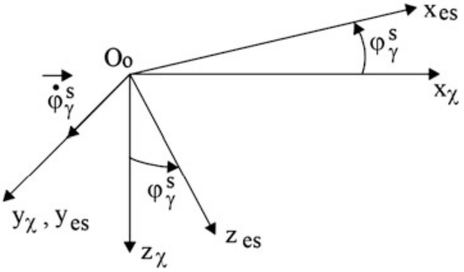

The matrix of transformation from the Earth-fixed coordinate system $O_o x_o y_o z_o$ to the system $O_o x_{es} y_{es} z_{es}$ is as follows:

$$M_{\chi\gamma} = M_\chi \cdot M_\gamma = \begin{bmatrix} \cos\varphi_\gamma^s \cos\varphi_\chi^s & \cos\varphi_\gamma^s \sin\varphi_\chi^s & -\sin\varphi_\gamma^s \\ -\sin\varphi_\chi^s & \cos\varphi_\chi^s & 0 \\ \sin\varphi_\gamma^s \cos\varphi_\chi^s & \sin\varphi_\gamma^s \sin\varphi_\chi^s & \cos\varphi_\gamma^s \end{bmatrix}. \tag{5.1}$$

Proceeding in an analogous way we obtain the matrix of transformation from the Earth-fixed coordinate system $O_o x_o y_o z_o$ to the system associated with the velocity vector of the UAV $S x_s y_s z_s$, i.e.,

$$M_{\chi\gamma}^s = \begin{bmatrix} \cos\gamma_s \cos\chi_s & \cos\gamma_s \sin\chi_\chi & -\sin\gamma_s \\ -\sin\chi_s & \cos\chi_s & 0 \\ \sin\gamma_s \cos\chi_s & \sin\gamma_s \sin\chi_s & \cos\gamma_s \end{bmatrix}. \tag{5.2}$$

The time derivative of vector $\mathbf{R}_{es}$ is equal to the vector of flight velocity $\mathbf{V}_s$ of the UAV, namely,

$$\frac{\mathrm{d}\mathbf{R}_{es}}{\mathrm{d}t} = \mathbf{V}_s. \tag{5.3}$$

Let us project the preceding vector equation onto the axes of the coordinate system $O_o x_{es} y_{es} z_{es}$:

$$\frac{\mathrm{d}\mathbf{R}_{es}}{\mathrm{d}t} = \mathbf{i}_{es}\frac{\mathrm{d}R_{es}}{\mathrm{d}t} + \boldsymbol{\omega}_{es} \times \mathbf{R}_{es} = \mathbf{i}_{es}\frac{\mathrm{d}R_{es}}{\mathrm{d}t} + \begin{vmatrix} \mathbf{i}_{es} & \mathbf{j}_{es} & \mathbf{k}_{es} \\ \omega_{xes} & \omega_{yes} & \omega_{zes} \\ R_{es} & 0 & 0 \end{vmatrix}$$

$$= \mathbf{i}_{es}\frac{\mathrm{d}R_{es}}{\mathrm{d}t} + \mathbf{j}_{es} R_{es}\omega_{zes} - \mathbf{k}_{es} R_{es}\omega_{yes}. \tag{5.4}$$

Vector $\boldsymbol{\omega}_{es}$ in (5.4) is the vector of angular velocity of vector $\mathbf{R}_{es}$, and it can be represented in the form of the following sum of vectors:

$$\boldsymbol{\omega}_{es} = \dot{\boldsymbol{\varphi}}_{\chi}^{s} + \dot{\boldsymbol{\varphi}}_{\gamma}^{s}. \tag{5.5}$$

The projections are determined by means of matrix (5.1), and we obtain

$$\begin{bmatrix} \omega_{xes} \\ \omega_{xes} \\ \omega_{xes} \end{bmatrix} = M_{\chi\gamma} \begin{bmatrix} 0 \\ 0 \\ \dot{\varphi}_{\chi}^{s} \end{bmatrix} + \begin{bmatrix} 0 \\ \dot{\varphi}_{\gamma}^{s} \\ 0 \end{bmatrix}. \tag{5.6}$$

Hence

$$\begin{aligned} \omega_{xes} &= -\dot{\varphi}_{\chi}^{s} \sin \varphi_{\gamma}^{s}, \\ \omega_{yes} &= -\dot{\varphi}_{\gamma}^{s}, \\ \omega_{zes} &= -\dot{\varphi}_{\chi}^{s} \cos \varphi_{\gamma}^{s}, \end{aligned} \tag{5.7}$$

and by virtue of (5.4) we obtain

$$\left(\frac{\mathrm{d}\mathbf{R}_{es}}{\mathrm{d}t}\right)_{xes} = \frac{\mathrm{d}R_{es}}{\mathrm{d}t}, \quad \left(\frac{\mathrm{d}\mathbf{R}_{es}}{\mathrm{d}t}\right)_{yes} = R_{es}\dot{\varphi}_{\chi}^{s} \cos \varphi_{\gamma}^{s}, \quad \left(\frac{\mathrm{d}\mathbf{R}_{es}}{\mathrm{d}t}\right)_{zes} = -R_{es}\dot{\varphi}_{\gamma}^{s}. \tag{5.8}$$

Similarly, projecting velocity vector $\mathbf{V}_s$ onto the axes $O_o x_{es} y_{es} z_{es}$ we obtain

$$\begin{bmatrix} V_{sxes} \\ V_{syes} \\ V_{szes} \end{bmatrix} = M_{\chi\gamma} \cdot M_{\chi\gamma}^{\mathrm{T}} \begin{bmatrix} V_s \\ 0 \\ 0 \end{bmatrix},$$

or equivalently

$$\begin{aligned} V_{sxes} &= V_s\left[\cos\left(\varphi_{\chi}^{s} - \chi_s\right) \cos \varphi_{\gamma}^{s} \cos \gamma_s + \sin \varphi_{\gamma}^{s} \sin \gamma_s\right], \\ V_{syes} &= -V_s \sin\left(\varphi_{\chi}^{s} - \chi_s\right) \cos \gamma_s, \\ V_{szes} &= V_s\left[\cos\left(\varphi_{\chi}^{s} - \chi_s\right) \sin \varphi_{\gamma}^{s} \cos \gamma_s - \cos \varphi_{\gamma}^{s} \sin \gamma_s\right]. \end{aligned} \tag{5.9}$$

Projections of the left- and right-hand sides of (5.3) onto axes of the system $O_o x_{es} y_{es} z_{es}$ give the following system of equations:

$$\frac{\mathrm{d}R_{es}}{\mathrm{d}t} = V_s \left[\cos\left(\varphi_\chi^s - \chi_s\right) \cos\varphi_\gamma^s \cos\gamma_s + \sin\varphi_\gamma^s \sin\gamma_s \right], \tag{5.10a}$$

$$\frac{\mathrm{d}\varphi_\chi^s}{\mathrm{d}t} R_{es} \cos\varphi_\gamma^s = -V_s \sin\left(\varphi_\chi^s - \chi_s\right) \cos\gamma_s, \tag{5.10b}$$

$$\frac{\mathrm{d}\varphi_\gamma^s}{\mathrm{d}t} R_{es} = V_s \left[\cos\left(\varphi_\chi^s - \chi_s\right) \sin\varphi_\gamma^s \cos\gamma_s - \cos\varphi_\gamma^s \sin\gamma_s \right]. \tag{5.10c}$$

The preceding equations represent the motion of point S (mass center of a UAV) with respect to the stationary point O_o (the origin of the Earth-fixed coordinate system). The path of motion of the UAV in the Earth-fixed coordinate system is described by the following equations:

$$\begin{aligned} x_{sx_0} &= R_{es} \cos\varphi_\gamma^s \cos\varphi_\chi^s, \\ y_{sx_0} &= R_{es} \cos\varphi_\gamma^s \sin\varphi_\chi^s, \\ z_{sz_0} &= -R_{es} \sin\varphi_\gamma^s. \end{aligned} \tag{5.11}$$

5.1.1.2 Equations of Motion of the Target Seeking and Observation Line (TSOL)

Proceeding in an analogous way to the case of the kinematic equations of motion of a UAV we obtain the following equations: of motion of the TSOL:

$$\begin{aligned} \frac{\mathrm{d}\xi_N}{\mathrm{d}t} &= \Pi(t_0, t_w) \cdot (V_{sxn} - V_{gxn}) + [\Pi(t_w, t_s) \\ &\quad + \Pi(t_s, t_k)] \cdot (V_{sxn} - V_{cxn}), \end{aligned} \tag{5.12}$$

$$\begin{aligned} -\frac{\mathrm{d}\chi_n}{\mathrm{d}t} \xi_N \cos\gamma_n &= \Pi(t_0, t_w) \cdot (V_{syn} - V_{gyn}) \\ &\quad + [\Pi(t_w, t_s) + \Pi(t_s, t_k)] \cdot (V_{syn} - V_{cyn}), \end{aligned} \tag{5.13}$$

$$\begin{aligned} \frac{\mathrm{d}\gamma_n}{\mathrm{d}t} \xi_N &= \Pi(t_0, t_w) \cdot (V_{szn} - V_{gzn}) \\ &\quad + [\Pi(t_w, t_s) + \Pi(t_s, t_k)] \cdot (V_{szn} - V_{czn}). \end{aligned} \tag{5.14}$$

Equations (5.12)–(5.14) are distributive equations with respect to the functions of a square impulse $\Pi(\cdot)$. Thus, they offer way to describe the changes in motion of the TSOL in its various phases.

The components of velocity vectors $\mathbf{V}_S$, $\mathbf{V}_G$, and $\mathbf{V}_C$ in the relative coordinate system $Sx_ny_nz_n$ are as follows:

$$V_{sxn} = V_s\left[\cos(\chi_n - \chi_s)\cos\gamma_n\cos\gamma_s - \sin\gamma_n\sin\gamma_s\right], \tag{5.15a}$$

$$V_{syn} = -V_s\sin(\chi_n - \chi_s)\cos\gamma_s, \tag{5.15b}$$

$$V_{szn} = V_s\left[\cos(\chi_n - \chi_s)\sin\gamma_n\cos\gamma_s - \cos\gamma_n\sin\gamma_s\right], \tag{5.15c}$$

$$V_{gxn} = V_g\left(\cos(\chi_n - \chi_g)\cos\gamma_n\cos\gamma_g - \sin\gamma_n\sin\gamma_g\right), \tag{5.16a}$$

$$V_{gyn} = -V_g\sin(\chi_n - \chi_g)\cos\gamma_g, \tag{5.16b}$$

$$V_{gzn} = V_g\left(\cos(\chi_n - \chi_g)\sin\gamma_n\cos\gamma_g - \cos\gamma_n\sin\gamma_g\right), \tag{5.16c}$$

$$V_{cxn} = V_c\left[\cos(\chi_n - \chi_c)\cos\gamma_n\cos\gamma_c - \sin\gamma_n\sin\gamma_c\right], \tag{5.17a}$$

$$V_{cyn} = -V_c\sin(\chi_n - \chi_c)\cos\gamma_c, \tag{5.17b}$$

$$V_{czn} = V_c\left[\cos(\chi_n - \chi_c)\sin\gamma_n\cos\gamma_c - \cos\gamma_n\sin\gamma_c\right]. \tag{5.17c}$$

5.1.1.3 Path of Motion of Point *G*

This motion is governed by the following equations (Fig. 5.5):

$$\begin{aligned}\frac{\mathrm{d}R_{eg}}{\mathrm{d}t} &= \Pi(t_0, t_w)V_g\cos\left(\varphi_g - \chi_g\right),\\ \frac{\mathrm{d}\varphi_g}{\mathrm{d}t} &= \Pi(t_0, t_w)V_g\sin\left(\varphi_g - \chi_g\right),\end{aligned} \tag{5.18a}$$

$$\begin{aligned}x_{gx_0} &= R_{eg}\cos\varphi_g,\\ y_{gy_0} &= R_{eg}\sin\varphi_g.\end{aligned} \tag{5.18b}$$

5.1.1.4 Kinematics of Motion of a Target

Proceeding in an analogous way to the case of the derivation of kinematic equations of motion of a UAV and using Fig. 5.4, we obtain the following equations of motion of a target (Fig. 5.6):

$$\frac{\mathrm{d}R_{ec}}{\mathrm{d}t} = V_c\left[\cos\left(\varphi_\chi^c - \chi_c\right)\cos\varphi_\gamma^c\cos\gamma_c + \sin\varphi_\gamma^c\sin\gamma_c\right], \tag{5.19a}$$

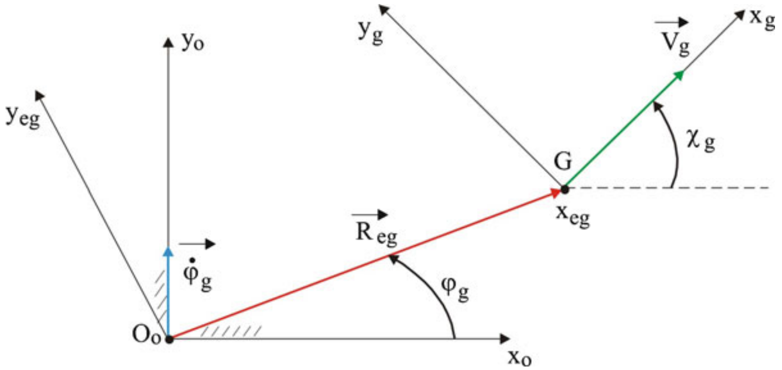

Fig. 5.5 Kinematics of motion of the point *G*

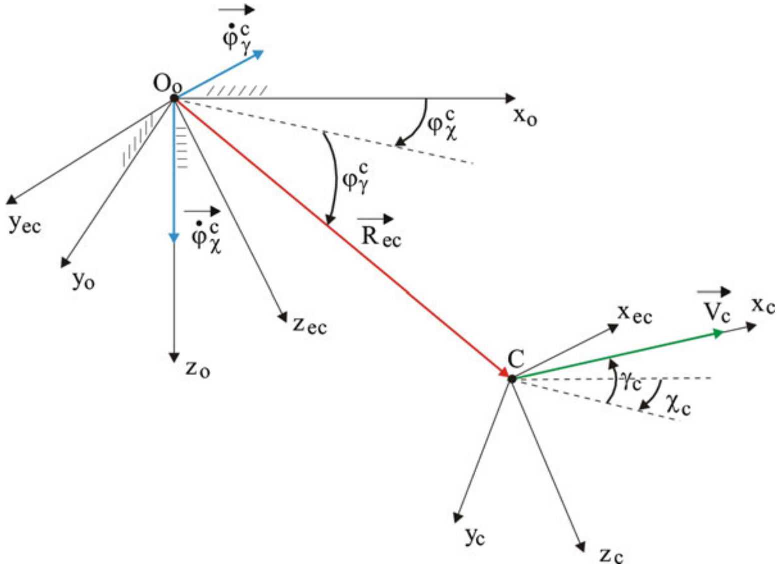

Fig. 5.6 Kinematics of target motion

$$\frac{d\varphi_\chi^c}{dt} R_{ec} \cos\varphi_\gamma^c = -V_c \sin\left(\varphi_\chi^c - \chi_s\right) \cos\gamma_c, \tag{5.19b}$$

$$\frac{d\varphi_\gamma^c}{dt} R_{ec} = V_c \left[\cos\left(\varphi_\chi^c - \chi_c\right) \sin\varphi_\gamma^c \cos\gamma_c - \cos\varphi_\gamma^c \sin\gamma_c\right]. \tag{5.19c}$$

A path of target motion in an Earth-fixed coordinate system is described by the equations

$$x_{cx_0} = R_{ec} \cos\varphi_\gamma^c \cos\varphi_\chi^c,$$

$$\begin{aligned} y_{sx_0} &= R_{ec} \cos\varphi_\gamma^c \sin\varphi_\chi^c, \\ z_{sz_0} &= -R_{ec} \sin\varphi_\gamma^c. \end{aligned} \tag{5.20}$$

Determining desired angles of flight of a UAV

The angles of flight χ_s and γ_s of a UAV seeking and attacking a detected target are determined from the following relationships:

$$\chi_s^* = \Pi\,(t_o, t_w) \cdot \chi_s^p + \Pi\,(t_w, t_k) \cdot \chi_s^n, \tag{5.21}$$

$$\gamma_s^* = \Pi\,(t_o, t_w) \cdot \gamma_s^p + \Pi\,(t_w, t_k) \cdot \gamma_s^n. \tag{5.22}$$

The functions of square impulse $\Pi(\cdot)$ offer a method for describing the changes in angles of UAV flight in various phases.

In turn, the angles of flight of the UAV χ_s and γ_s during seeking, the transition to a tracking phase, and laser illumination of a detected target are as follows:

$$\chi_s^* = \Pi\,(t_o, t_w) \cdot \chi_s^p + \Pi\,(t_w, t_s) \cdot \chi_s^t + \Pi\,(t_s, t_k) \cdot \chi_s^o, \tag{5.23}$$

$$\gamma_s^* = \Pi\,(t_o, t_w) \cdot \gamma_s^p + \Pi\,(t_w, t_s) \cdot \gamma_s^t + \Pi\,(t_s, t_k) \cdot \gamma_s^o. \tag{5.24}$$

The quantities χ_s^p and γ_s^p denote the programmed angles of flight of a UAV while patrolling the Earth's surface (target seeking), and they are the prescribed time functions

$$\chi_s^p = \chi_s^p\,(t)\,, \qquad \gamma_s^p = \gamma_s^p\,(t)\,. \tag{5.25}$$

Before determining a UAV's flight angles χ_s^o and γ_s^o for the case of tracking and simultaneous laser illumination of a detected target, let us introduce the following assumptions [4–6].

For the sake of simplification of calculation, let us assume that UAV motion, both during penetration and tracking, takes place in a horizontal plane at a given altitude H_S, whereas the target and point G move in the Earth's plane. Then we can assume that

$$\gamma_s^o = 0, \qquad \gamma_c = 0, \qquad \gamma_g = 0. \tag{5.26}$$

Let us additionally introduce, for the convenience of notation, the following symbol:

$$r_N = \xi_N \cos\gamma_n \tag{5.27}$$

and calculate the time derivative of this expression:

$$\frac{\mathrm{d}r_N}{\mathrm{d}t} = \frac{\mathrm{d}\xi_N}{\mathrm{d}t} \cos\gamma_n - \xi_N \frac{\mathrm{d}\gamma_n}{\mathrm{d}t} \sin\gamma_n. \tag{5.28}$$

Taking into account (5.26)–(5.28), we can limit our further calculations to plane motion in the horizontal plane and represent (5.12)–(5.14), after the substitution of (5.26)–(5.28), in the following form:

$$\begin{aligned}\frac{\mathrm{d}r_N}{\mathrm{d}t} &= \Pi(t_0,t_w)\left[V_s\cos\left(\chi_n-\chi_s^p\right)-V_g\cos\left(\chi_n-\chi_g\right)\right]\\&\quad+\Pi(t_w,t_s)\left[V_s\cos\left(\chi_n-\chi_s^t\right)-V_c\cos\left(\chi_n-\chi_c\right)\right]\\&\quad+\Pi(t_s,t_k)\left[V_s\cos\left(\chi_n-\chi_s^s\right)-V_c\cos\left(\chi_n-\chi_c\right)\right],\end{aligned} \tag{5.29}$$

$$\begin{aligned}\frac{\mathrm{d}\chi_n}{\mathrm{d}t} &= \Pi(t_0,t_w)\frac{V_s\sin\left(\chi_n-\chi_g\right)-V_g\sin\left(\chi_n-\chi_s^p\right)}{r_N}\\&\quad+\Pi(t_w,t_s)\cdot\frac{V_s\sin\left(\chi_n-\chi_c\right)-V_c\sin\left(\chi_n-\chi_s^t\right)}{r_N}\\&\quad+\Pi(t_s,t_k)\frac{V_s\sin\left(\chi_n-\chi_c\right)-V_c\sin\left(\chi_n-\chi_s^s\right)}{r_N}.\end{aligned} \tag{5.30}$$

Let us require that at the instant of target detection the UAV must automatically commence transition to a target tracking flight, which relies on the movement of an aerial vehicle at the constant prescribed distance from the target $r_{N0} = \xi_{N0}\cos\gamma_n =$ const (in the horizontal plane at the constant altitude H_s).

Until the relative distance r_N of points S and C is equal to r_{N0}, the program of change of yaw angle $\chi_s = \chi_s^t$ and $\gamma_s = \gamma_s^t$ are determined from the relationship [7]

$$\frac{\mathrm{d}\chi_s^t}{\mathrm{d}t} = a_\chi\cdot\operatorname{sign}\left(r_{N0}-r_N\right)\frac{\mathrm{d}\chi_n}{\mathrm{d}t},\quad \gamma_s^t = 0, \tag{5.31}$$

which results in steering of the UAV so as to approach or depart from the target (depending on the sign of the function sign$(r_{N0} - r_N)$), according to the so-called proportional navigation method [8–10]. Upon satisfaction of the condition $r_{N0} = r_N$, the program of change of the angle χ_s^o is determined from (5.30), which is transformed into

$$V_s\cos\left(\chi_n-\chi_s^o\right) = V_c\cos\left(\chi_n-\chi_c\right). \tag{5.32}$$

Hence, the flight angles of the UAV during laser illumination of the detected target χ_s^o and γ_s^o, on the assumption that the UAV moves in the horizontal plane at a constant altitude H_s, will be determined from the relationships

$$\chi_s^o = \chi_n - \arccos\left[\frac{V_c}{V_s}\cos(\chi_n-\chi_c)\right],\quad \gamma_s^o = 0. \tag{5.33}$$

The flight angles of the UAV while attacking a detected target χ_s^n and γ_s^n will be determined from the relationships describing the proportional navigation method [7, 11]:

$$\frac{\mathrm{d}\chi_s^n}{\mathrm{d}t} = a_\chi\frac{\mathrm{d}\chi_n}{\mathrm{d}t}, \tag{5.34}$$

$$\frac{\mathrm{d}\gamma_s^n}{\mathrm{d}t} = a_\gamma \frac{\mathrm{d}\gamma_n}{\mathrm{d}t}. \tag{5.35}$$

The angles χ_s^* and γ_s^* define the prescribed position of the velocity vector of a missile in space. The difference between the prescribed and actual angular positions of the velocity vector of a UAV is an error, also known as a discrepancy parameter, for a system of automatic control in autopilot. Based on the value and direction of the error, a control signal is elaborated, and after the appropriate transformation, it is transferred to an actuator for displacing control surfaces in a transverse channel and a longitudinal channel by the determined values of the angles.

5.1.2 Control of an Axis of a Gyroscope on Board a Combat UAV

It follows from the previous sections that during seeking of a ground target from on-board a UAV, a gyroscope axis should perform required movements, and consequently, because it is being directed downward, it should draw strictly defined lines on the Earth's surface. In this way, the optical system installed in the gyroscope axis, with its angle of view, may encounter a visible light or infrared radiation emitted by a moving apparatus. Thus, the kinematic parameters of relative motion of the gyroscope axis and the UAV board should be selected so that the target can be detected with the highest possible probability. After location of the target (upon reception of the signal by an infrared detector) the gyroscope transitions to a tracking state, that is, from that moment on its axis assumes the specific position in space so as to be directed toward its target.

Control moments M_b, M_c acting on the gyroscope located on board the UAV, will be represented in the following way:

$$M_b = \Pi(t_o, t_w) \cdot M_b^p(t) + \Pi(t_s, t_k) \cdot M_b^s, \tag{5.36}$$

$$M_c = \Pi(t_o, t_w) \cdot M_c^p(t) + \Pi(t_s, t_k) \cdot M_c^s. \tag{5.37}$$

The programmed control moments $M_b^p(t)$ and $M_c^p(t)$ set the gyroscope axis into the required motion and are determined by means of a method for solving the inverse dynamics problem [12, 13]:

$$M_b^p(\tau) = \Pi\left(\tau_0, \tau_w\right) \cdot \left[\frac{\mathrm{d}^2\vartheta_{gz}}{\mathrm{d}\tau^2} + b_b \frac{\mathrm{d}\vartheta_{gz}}{\mathrm{d}\tau} - \frac{1}{2}\left(\frac{\mathrm{d}\psi_{gz}}{\mathrm{d}\tau}\right)^2 \sin 2\vartheta_{gz} + \right.$$
$$\left. - \frac{\mathrm{d}\psi_{gz}}{\mathrm{d}\tau} \cos\vartheta_{gz}\right] \cdot \frac{1}{c_b}, \tag{5.38}$$

$$M_c^p(\tau) = \Pi\,(\tau_0, \tau_w) \cdot \left[\frac{\mathrm{d}^2\psi_{gz}}{\mathrm{d}\tau^2} \cos^2\vartheta_{gz}^p + b_c \frac{\mathrm{d}\psi_{gz}}{\mathrm{d}\tau} + \frac{\mathrm{d}\psi_{gz}}{\mathrm{d}\tau}\frac{\mathrm{d}\vartheta_{gz}}{\mathrm{d}\tau} \sin 2\vartheta_{gz} + \frac{\mathrm{d}\vartheta_{gz}}{\mathrm{d}\tau} \cos\vartheta_{gz} \right] \cdot \frac{1}{c_c}, \tag{5.39}$$

where $\tau = t \cdot \Omega$, $\Omega = \frac{J_{go} n_g}{J_{gk}}$, $c_b = c_c = \frac{1}{J_{gk}\Omega^2}$.

The time instant when the target enters a field of view of objective TSOL is equivalent to the following relationship:

$$|\Delta \mathbf{r}| = \left|\mathbf{r}_c - \mathbf{r}_g\right| \le \Delta r_{zad}, \tag{5.40}$$

where Δr_{zad} is the prescribed radius of a circle of view of objective TSOL, the control of a gyroscope passes to a tracking state.

If we denote the angular error between the actual angles ϑ_g and ψ_g and the required angles ϑ_{gz} and ψ_{gz} by

$$e_\vartheta = \vartheta_g - \vartheta_{gz}, \tag{5.41a}$$

$$e_\psi = \psi_g - \psi_{gz}, \tag{5.41b}$$

then the control moments of a gyroscope at tracking have the following form:

$$M_b^s(\tau) = \Pi\,(\tau_s, \tau_k) \cdot \left(\bar{k}_b \cdot e_\vartheta - \bar{k}_c \cdot e_\psi + \bar{h}_g \frac{\mathrm{d}e_\vartheta}{\mathrm{d}\tau} \right), \tag{5.42}$$

$$M_c^s(\tau) = \Pi\,(\tau_s, \tau_k) \cdot \left(\bar{k}_b \cdot e_\psi + \bar{k}_c \cdot e_\vartheta + \bar{h}_g \frac{\mathrm{d}e_\psi}{\mathrm{d}\tau} \right), \tag{5.43}$$

where $\bar{k}_b = \frac{k_b}{J_{gk}\Omega^2}$, $\bar{k}_c = \frac{k_c}{J_{gk}\Omega^2}$, $\bar{h}_g = \frac{h_g}{J_{gk}\Omega}$. The coefficients k_b, k_c, and h_g are selected in an optimal way using the algorithm presented in [5].

The prescribed angles ϑ_{gz} and ψ_{gz} and their first and second time derivatives occurring in the control laws (5.38), (5.39), (5.42), and (5.43) are determined as presented in [5,9]. If a prismatic scanning device is applied in UWSLOC, the control moments M_b, M_c acting on a gyroscope are as follows:

$$M_b = \Pi(t_o, t_w) \cdot M_b^p(t) + \Pi(t_w, t_z) \cdot M_b^t(t) + \Pi(t_s, t_k) \cdot M_b^s, \tag{5.44a}$$

$$M_c = \Pi(t_o, t_w) \cdot M_c^p(t) + \Pi(t_w, t_z) \cdot M_c^t(t) + \Pi(t_s, t_k) \cdot M_c^s. \tag{5.44b}$$

The additional (as compared to (5.36) and (5.37)) quantities M_b^t and M_c^t that occur in the preceding equations denote the programmed control moments whose task is to move the axis along the shortest path onto the target observation line—the TOL (the line joining points S and C—Fig. 5.4).

Since the moment when the target enters the field of view of a scanning device—the controls of the gyroscope transits to a state where it moves the axis onto the TOL

$$|\Delta\boldsymbol{\rho}^*| = \left|\boldsymbol{\rho}_z^* - \boldsymbol{\rho}_w^*\right| \leq \Delta\rho_{zad}, \tag{5.45}$$

where $\Delta\rho_{zad}$ is the prescribed width of a ring of view of a scanning device.

In order to the determine of the control moments M_b^t and M_c^t that move the gyroscope axis onto the TOL, one should apply the control algorithm described in [10]. Thus, it is necessary to change the moments of forces controlling a gyroscope. It is most convenient at first to require that from the given initial position following detection of the target ϑ_{gz}^w and ψ_{gz}^w the gyroscope axis should be led to the position ϑ_{gz}^* and ψ_{gz}^* by means of $M_b^t = \text{const}$ and $M_c^t = \text{const}$. Thus, we control gyroscope axes in two stages:

1. We act with constant moments $M_b^t = \text{const}$ and $M_c^t = \text{const}$ and after reaching $\vartheta_g = \vartheta_{gz}^*$ and $\psi_g = \psi_{gz}^*$ we proceed to the second stage.
2. We act with moments M_b^s, M_c^s.

Assuming that the target moves at a relatively low speed, that is, $\ddot{\vartheta}_{zo}^w \approx 0$, $\dot{\vartheta}_{gz}^w \approx 0$, $\ddot{\psi}_{gz}^w \approx 0$, $\dot{\psi}_{gz}^w \approx 0$, we obtain the following relationships:

$$\vartheta_g(t) \approx \vartheta_{gz}^w + \frac{\Omega\left(\eta_c M_b^t + M_c^t\right)}{J_{gk}\omega_{go}^2} t, \tag{5.46a}$$

$$\psi_g(\mathrm{t}) \approx \psi_{gz}^w + \frac{\Omega\left(\eta_b M_c^t - M_b^t\right)}{J_{gk}\omega_{go}^2} t, \tag{5.46b}$$

where $\omega_{go}^2 = (1 + \eta_b\eta_c) \cdot \Omega^2$.

The time during which the gyroscope axis is transits from the position ϑ_{gz}^w, ψ_{gz}^w to the position ϑ_{gz}^*, ψ_{gz}^* is equal to the time of maximum prism intensitivity T_w^*. Then, from the preceding equations we obtain

$$\vartheta_{gz}^w + \frac{\Omega\left(\eta_c M_b^t + M_c^t\right)}{J_{gk}\omega_{go}^2} T_w^* = \vartheta_{gz}^*, \tag{5.47a}$$

$$\psi_{gz}^w + \frac{\Omega\left(\eta_b M_c^t - M_b^t\right)}{J_{gk}\omega_{go}^2} T_w^* = \psi_{gz}^*. \tag{5.47b}$$

This is a system of two equations with two unknowns M_b^t and M_c^t. Hence we obtain

$$M_b^t = -\frac{\left(\left(\psi_{gz}^* - \psi_{gz}^w\right) - \left(\vartheta_{gz}^* - \vartheta_{gz}^w\right)\eta_b\right) J_{go} n_g}{T_w^*}, \tag{5.48a}$$

$$M_c^t = \frac{\left(\left(\psi_{gz}^* - \psi_{gz}^w\right) \eta_c + \left(\vartheta_{gz}^* - \vartheta_{gz}^w\right)\right) J_{go} n_g}{T_w^*}. \tag{5.48b}$$

Eventually, for the realization of the gyroscope axis motion intended to obtain alignment with the TOL we apply the following algorithm:

1. For $t_w \leq t < T_w^*$ we control with the moments $M_b = M_b^t$ and $M_c = M_c^t$.
2. For $T_w^* \geq t \geq t_k$ we control with the moments $M_b = M_b^s$ and $M_c = M_c^s$.

If in this case we denote the angular errors between the actual angles ϑ_g and ψ_g and the required angles ϑ_{gz}^* and ψ_{gz}^* by

$$e_\vartheta = \vartheta_g - \vartheta_{gz}^*, \qquad e_\psi = \psi_g - \psi_{gz}^*, \tag{5.49}$$

then we write the control moments of the gyroscope at tracking in the form of a law described by (5.42) and (5.43).

The presented mathematical model of the operation of a scanning device installed on board a UAV allows us to conduct numerical investigations of seeking, locating, and tracking of a mobile target (a ground or water one) emitting the infrared radiation.

5.1.3 Control of UAV Motion

The control of UAV motion takes place by means of displacement of control surfaces of ailerons, a rudder, and an elevator respectively by angles δ_l, δ_m, and δ_n.

The realization of a required flight path of the UAV is effected by an automatic pilot (AP), which elaborates control signals for the actuating system of the control based on the derived relationships (5.21)–(5.24).

The control law for the autopilot, including the dynamics of displacement of the rudder and elevator, is described in the following way:

$$\frac{\mathrm{d}^2\delta_m}{\mathrm{d}t^2} + h_{ms}\frac{\mathrm{d}\delta_m}{\mathrm{d}t} + k_{ms}\delta_m = k_m\left(\gamma_s - \gamma_s^*\right) + h_m\left(\frac{\mathrm{d}\gamma_s}{\mathrm{d}t} - \frac{\mathrm{d}\gamma_s^*}{\mathrm{d}t}\right) + b_m \cdot u_m, \tag{5.50}$$

$$\frac{\mathrm{d}^2\delta_n}{\mathrm{d}t^2} + h_{ns}\frac{\mathrm{d}\delta_n}{\mathrm{d}t} + k_{ns}\delta_n = k_n\left(\chi_s - \chi_s^*\right) + h_m\left(\frac{\mathrm{d}\chi_s}{\mathrm{d}t} - \frac{\mathrm{d}\chi_s^*}{\mathrm{d}t}\right) + b_n \cdot u_n. \tag{5.51}$$

Quantities u_m and u_n occurring in the preceding equations denote stabilizing controls elaborated by the automatic control system AP. The rule for the elaboration of the stabilizing controls is presented in [14].

In the course of a mission, a light UAV can be affected by various kinds of disturbances such as wind blasts, vertical ascending and descending motions of air masses, or shockwaves from missiles exploding in the vicinity. At the instant when the target is detected, the UAV automatically transits from its flight along the programmed trajectory to a flight tracking the target according to the assumed algorithm, in the considered case, maintaining a constant distance from the target. In this way the best conditions are ensured for maintaining the target in the field of view of the objective of a tracking system. A rapid switching of the control system (from one flight stage to the other) can be the cause of disturbance effects of UAV motion dynamics. In turn, the dynamic effects that are the result of the aforementioned disturbances and control switching produce changes in the flight state and the aerodynamic characteristics of the airplane. The time history of maneuvers necessary for the realization of the posed task indicates the existence of distinctly non-linear characteristics of the controlled apparatus [5, 6, 14]. Therefore, for a UAV one should apply the autopilot such that it would be able to provide the assumed accuracy of realization of the programmed and tracking flight while simultaneously ensuring its stability.

5.1.4 Final Remarks

The presented model of navigation and control of a UAV describes the fully autonomous motion of a combat apparatus whose task is not only the detection and identification of a ground target but also its laser illumination or direct attack. The intervention of an operator in the UAV steering can be reduced only to cases where the apparatus is completely diverted off the prescribed course or the target is lost from the field of view of the tracking system's objective (due to wind, missiles, etc.). Thus, there should be a way to automatically send information about such events, and the operator should have the option of taking over the UAV flight control. In further research, both theoretically computational and simulative-experimental, it would be recommended to

(a) Determine the optimal program of a UAV flight.
(b) Elaborate an algorithm for scanning the Earth's surface to provide the quickest detection of targets.
(c) Elaborate a program of time-minimum transition of a UAV from programmed flight to target tracking flight or to self-guidance to a detected target according to the prescribed algorithm.

5.2 Gyroscope in a Guided Aerial Bomb

One characteristic of a bomb attack is that the target is most often known in the form of an image. Even if it emits electromagnetic waves or infrared radiation, the waves or radiation would possess such a small intensity as to be virtually useless. Thus, the target of a bomb attack should be satisfactorily illuminated. Current solutions of guided bombs can be divided into three main groups: bombs requiring marking of the target by illumination using a laser beam emitted from a separate device, bombs having their own target illumination system, and bombs guided to targets with the aid of a navigation satellite system like a GPS. Within all those groups a fundamental problem is the reliable and accurate guidance of the bomb to the target along an optimal trajectory with respect to time and curvature and at the appropriate angle. A device that is capable of satisfying these requirements would likely be a controlled gyroscope whose axis was a target observation line for a bomb's self-guidance system. It should be emphasized that a gyroscope is not vulnerable to disturbances, and in emergency situations it can replace a GPS system.

Just before a bomb drops from a carrier, the axis of a controlled gyroscope is being directed to the target. From that moment on it represents a target observation line (TOL) that for the bomb's autopilot is the reference for realization of the assumed guidance algorithm (Fig. 5.1). The controlled gyroscope can also be applied in a bomb's television-based guidance system to a ground target. An image of the target's surroundings is transmitted telemetrically or by means of a cable with a bundle of optical fibers to a display being viewed by the operator. With the aid of the display the operator indicates the attack target, that is, he or she appropriately directs the gyroscope axis. From that point the bomb can be steered automatically according to a preset guidance algorithm.

An example of a classic gyroscope suspended on a Cardan joint is the operational unit of a TOL's position control in a target coordinator of a self-guided aerial bomb. Along the gyroscope axis there is installed an optical system of a target-seeking and tracking head. Thus, the accuracy of guidance depends largely on the gyroscope correction system whose task is the minimization of the error between the prescribed motion determined on the fly by the image analysis system and the actual motion. Gyroscope errors are caused mainly by the existence of friction in suspension bearings and non-coincidence of the mass center of the gyroscope's rotor with the point of intersection of suspension frames. For this reason the gyroscope reacts to the kinematic excitation of the base on which it is mounted, that is, to angular motions and changes in the linear velocity of an aerial bomb.

Particularly large changes in the flight parameters of a bomb take place in the initial stage of the guidance process, that is, after the bomb is detached from the carrier and the bomb's native control system is activated. The TOL according to which the bomb guides itself to the target is then determined improperly. With the appearance of excessive deviations of the gyroscope axis from the prescribed orientation, the target's image may be lost from the field of view.

Therefore, a correction system and the parameters of the gyroscope itself should be selected in an optimal way so as to minimize the influence of vibrations of the base (the board of an aerial bomb) on the accuracy of orientation of the gyroscope axis. In this study it was achieved using linear-quadratic regulation (optimization) LQR [15–17].

It is assumed that FO moves ideally along a computed path determined on the basis of the motion of the gyroscope axis. The gyroscope axis, in turn, is controlled in such a way as to obtain its coincidence with the TOL during the self-guidance process.

5.2.1 *Kinematics of a Bomb's Self-Guided Motion to a Ground Target*

Let us write the equations of motion of a TOL as follows:

$$\begin{aligned}\frac{\mathrm{d}r_b}{\mathrm{d}t} &= V_c\left[\cos\left(\varepsilon-\gamma_c\right)\cos\sigma\cos\chi_c+\sin\sigma\sin\chi_c\right]\\ &\quad -V_b\left[\cos\left(\varepsilon-\gamma_b\right)\cos\sigma\cos\chi_b+\sin\sigma\sin\chi_b\right],\end{aligned} \tag{5.52a}$$

$$\begin{aligned}\frac{\mathrm{d}\sigma}{\mathrm{d}t} &= \frac{V_b\left[\cos\left(\varepsilon-\gamma_b\right)\sin\sigma\cos\chi_b-\cos\sigma\sin\chi_b\right]}{r_b}\\ &\quad +\frac{-V_c\left[\cos\left(\varepsilon-\gamma_c\right)\sin\sigma\cos\chi_c-\cos\sigma\sin\chi_c\right]}{r_b},\end{aligned} \tag{5.52b}$$

$$\frac{\mathrm{d}\varepsilon}{\mathrm{d}t} = \frac{V_b\sin\left(\varepsilon-\gamma_b\right)\cos\chi_b-V_c\sin\left(\varepsilon-\gamma_c\right)\cos\chi_c}{r_b\cos\sigma}, \tag{5.52c}$$

where r_b is the relative distance of the bomb from the target; σ and ϵ are the yaw angle and pitch angle of the TOL, respectively; V_b and V_c are the velocities of motion of the bomb and the target, respectively; χ_b and γ_b are the bomb's angles of flight; and χ_c and γ_c are the angles of flight of the target.

Let us apply a proportional navigation method [6,7] to the guidance of the bomb to the target:

$$\frac{\mathrm{d}\chi_b}{\mathrm{d}t} = a_\sigma\frac{\mathrm{d}\sigma}{\mathrm{d}t}, \tag{5.53}$$

where a_σ, a_ϵ are the constant coefficients of the proportional navigation.

The initial conditions of a bomb's self-guidance are as follows (Fig. 5.7):

$$r_o = \sqrt{\left(x_{bo}-x_{co}\right)^2+\left(y_{bo}-y_{co}\right)^2+\left(z_{bo}-z_{co}\right)^2}, \tag{5.54a}$$

$$\sigma_o = \arcsin\frac{y_{co}-y_{bo}}{r_o}, \tag{5.54b}$$

$$\varepsilon_o = \arctan\frac{z_{bo}-z_{co}}{x_c-x_b}. \tag{5.54c}$$

Let us consider the possibilities for the self-guidance of a bomb such that the attack on the target at the final stage occurs at prescribed angles to the level. Let us additionally assume that the guidance process takes place in the vertical plane. Equations (5.52a) and (5.53) simplify, then, to the form

$$\frac{\mathrm{d}r}{\mathrm{d}t} = V_c\cos\left(\varepsilon-\gamma_c\right)-V_s\cos\left(\varepsilon-\gamma_b\right), \tag{5.55a}$$

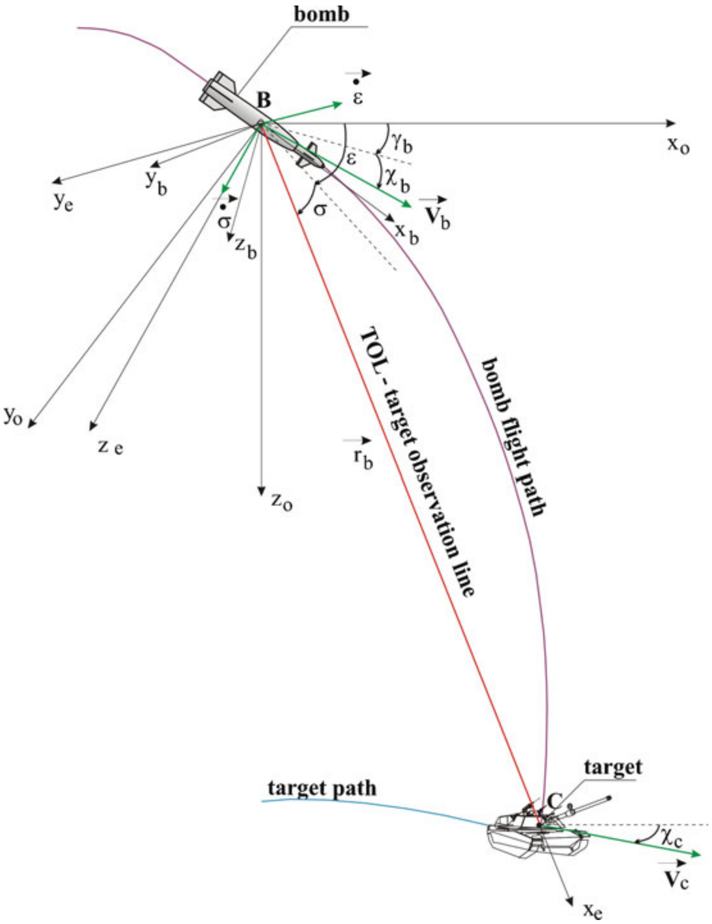

Fig. 5.7 Kinematics of self-guidance of a bomb aimed at a ground target

$$\frac{\mathrm{d}\varepsilon}{\mathrm{d}t} = \frac{V_b \sin(\varepsilon - \gamma_b) - V_c \sin(\varepsilon - \gamma_c)}{r}, \tag{5.55b}$$

$$\frac{\mathrm{d}\gamma_b}{\mathrm{d}t} = a_\varepsilon \frac{\mathrm{d}\varepsilon}{\mathrm{d}t}. \tag{5.55c}$$

Let us move on to the analysis of the kinematics of the self-guidance of a bomb for three special cases of target attack: (1) at an angle of 0° (Fig. 5.8), (2) at an angle of 90° (Fig. 5.9), (3) at an angle of 180° (Fig. 5.10).

Case 1. The attack on a stationary target from a forward hemisphere at an angle of 0°.

Figure 5.8 depicts a possible way to attack a target in the considered case. For this and the two remaining cases, equations of kinematics of motion of a self-guided

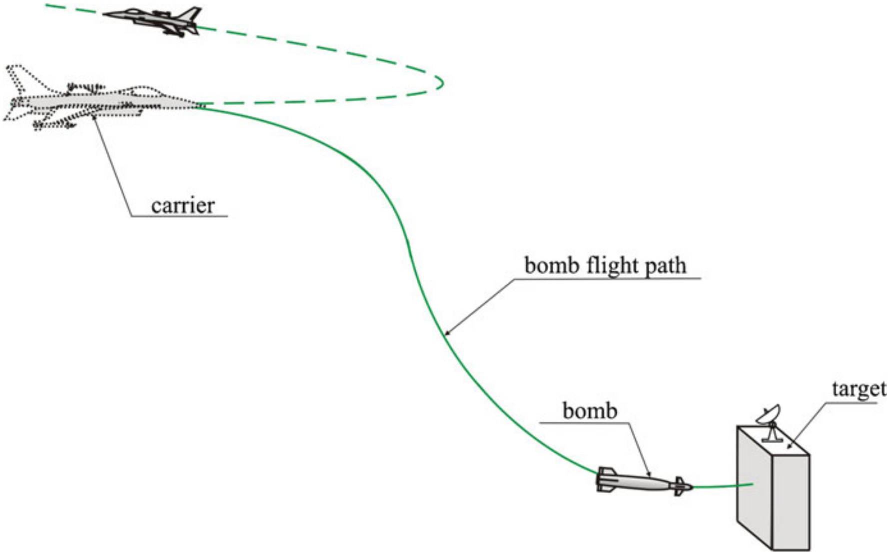

Fig. 5.8 Overall view of self-guidance of a bomb attacking a target at an angle of 0°

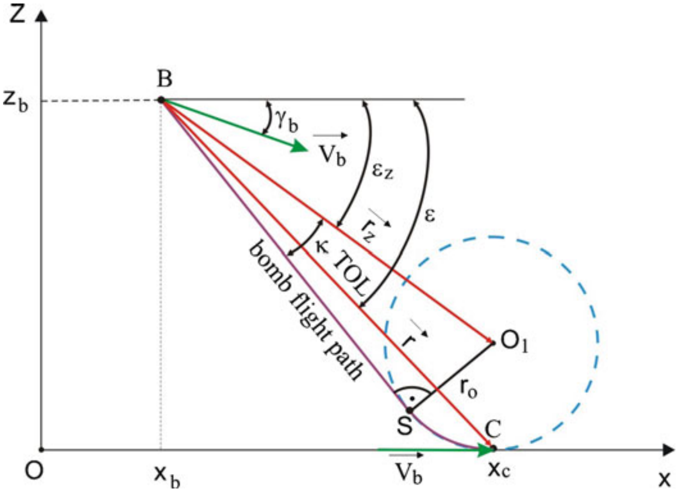

Fig. 5.9 Overall view of self-guidance of a bomb attacking a target at an angle of 90°

bomb will be represented in the following way:

$$\frac{\mathrm{d}r_z}{\mathrm{d}t} = V_c \cos\left(\varepsilon_z - \gamma_c\right) - V_b \cos\left(\varepsilon_z - \gamma_b\right), \tag{5.56a}$$

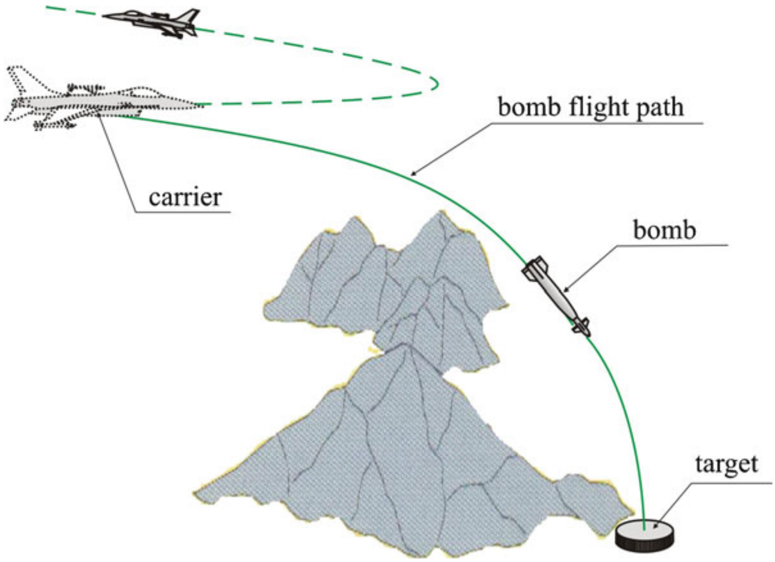

Fig. 5.10 Overall view of self-guidance of a bomb attacking a target at an angle of 180°

$$\frac{\mathrm{d}\varepsilon_z}{\mathrm{d}t} = \frac{V_b \sin(\varepsilon_z - \gamma_b) - V_b \sin(\varepsilon_b - \gamma_c)}{r_z}, \tag{5.56b}$$

$$\frac{\mathrm{d}\gamma_b}{\mathrm{d}t} = a_\gamma \frac{\mathrm{d}\varepsilon^*}{\mathrm{d}t}. \tag{5.56c}$$

According to Fig. 5.11, in which the trigonometric relationships of a bomb's motion are shown, we have

$$\varepsilon^* = \varepsilon_z + \kappa, \qquad \kappa = \arcsin\frac{r_o}{r_z},$$

$$\varepsilon_z = \arctan\frac{z_c - z_b + r_o}{x_c - x_b}, \quad r_z = \sqrt{(z_b - z_c - r_o)^2 + (x_c - x_b)^2},$$

hence

$$\frac{\mathrm{d}\varepsilon^*}{\mathrm{d}t} = \frac{\mathrm{d}\varepsilon_z}{\mathrm{d}t} - \frac{r_o}{\sqrt{r_z^2 - r_o^2}r_z}\frac{\mathrm{d}r_z}{\mathrm{d}t}, \tag{5.57}$$

where r_o is the prescribed radius of the circle on whose arc (SC) the bomb moves at the final stage of the flight; r_Z is the distance from point B (mass center of bomb) to the center of the circle that passes through point C (a selected point on the target); κ is the angle between segments BO_1 and BS; and ϵ_z is the "angle of observation" of point O_1.

Case 2. Attacking a stationary target from a forward hemisphere at an angle of 90°.

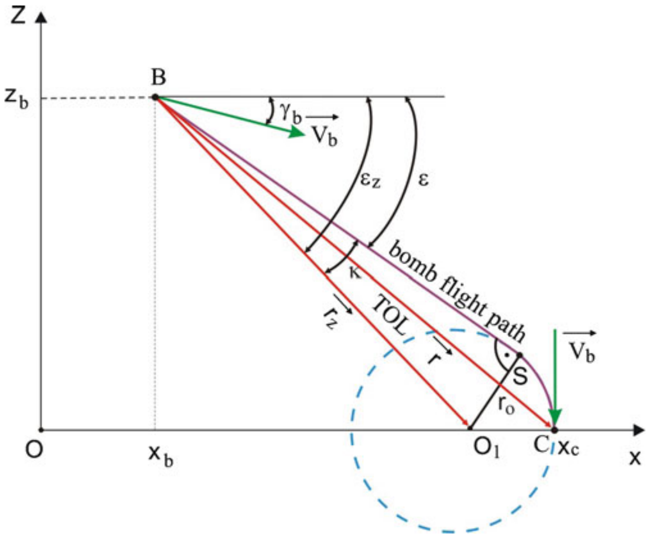

Fig. 5.11 Kinematic schematic of self-guidance of a bomb attacking a target at an angle of 0°

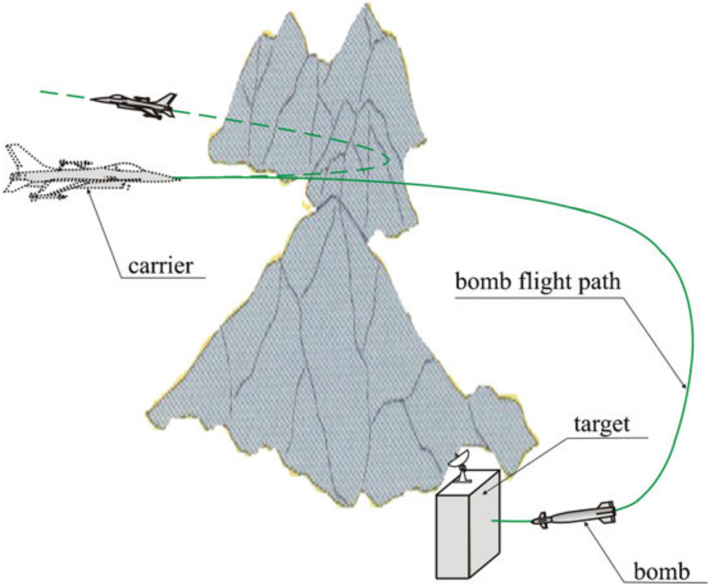

Fig. 5.12 Kinematic schematic of self-guidance of a bomb attacking a target at an angle of 90°

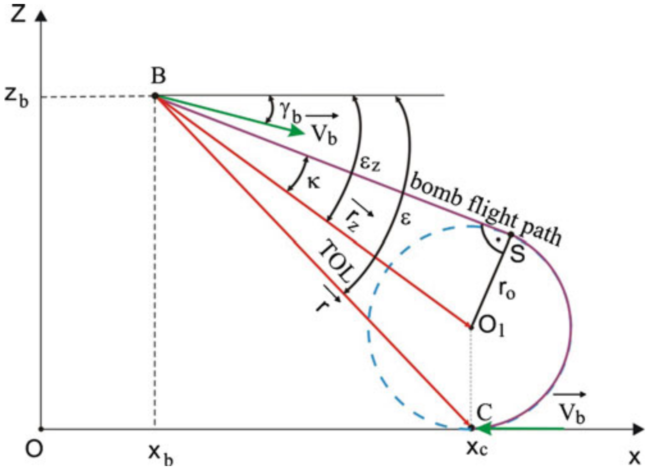

Fig. 5.13 Kinematic schematic of self-guidance of a bomb attacking a target at an angle of 180°

According to Fig. 5.12 we have

$$\varepsilon^* = \varepsilon_z - \kappa, \qquad \kappa = \arcsin\frac{r_o}{r_z},$$

$$\varepsilon_z = \arctan\frac{z_c - z_b}{x_c - x_b - r_o}, \quad r_z = \sqrt{(z_b - z_c)^2 + (x_c - x_b - r_o)^2},$$

hence

$$\frac{\mathrm{d}\varepsilon^*}{\mathrm{d}t} = \frac{\mathrm{d}\varepsilon_z}{\mathrm{d}t} + \frac{r_o}{\sqrt{r_z^2 - r_o^2}\,r_z}\frac{\mathrm{d}r_z}{\mathrm{d}t}. \tag{5.58}$$

Case 3. Attack on a stationary target from a backward hemisphere at an angle of 180°.

According to Fig. 5.13, we have

$$\varepsilon^* = \varepsilon_z - \kappa, \qquad \kappa = \arcsin\frac{r_o}{r_z},$$

$$\varepsilon_z = \arctan\frac{z_c - z_b + r_o}{x_c - x_b}, \quad r_z = \sqrt{(z_b - z_c - r_o)^2 + (x_c - x_b)^2},$$

hence

$$\frac{\mathrm{d}\varepsilon^*}{\mathrm{d}t} = \frac{\mathrm{d}\varepsilon_z}{\mathrm{d}t} + \frac{r_o}{\sqrt{r_z^2 - r_o^2}\,r_z}\frac{\mathrm{d}r_z}{\mathrm{d}t}. \tag{5.59}$$

In all the cases considered previously, at the instant when the bomb reaches point S, that is, at a distance from the target of $r_z = r_o$, it starts moving on a circle of radius $r_o = \text{const}$, and (5.55a) takes the form

$$V_c \cos(\varepsilon_z - \gamma_c) - V_b \cos(\varepsilon_z - \gamma_b) = 0. \tag{5.60}$$

Hence

$$\gamma_b = \varepsilon_z - \arccos\left[\frac{V_c}{V_b}\cos(\varepsilon_z - \gamma_c)\right]. \tag{5.61}$$

In turn, (5.56b) and (5.56c) have the following form:

$$\frac{\mathrm{d}\varepsilon_z}{\mathrm{d}t} = \frac{V_b \sin\left\{\arccos\left[\frac{V_c}{V_b}\cos(\varepsilon_z - \gamma_c)\right]\right\} - V_c \sin(\varepsilon_z - \gamma_c)}{r_o}, \tag{5.62a}$$

$$\frac{\mathrm{d}\gamma_b}{\mathrm{d}t} = \frac{\mathrm{d}\varepsilon_z}{\mathrm{d}t} + \frac{\frac{V_c}{V_b}\left[(\dot{\gamma}_c - \dot{\varepsilon}_z)\sin(\varepsilon_z - \gamma_c) + \left(\frac{\dot{V}_c}{V_c} - \frac{\dot{V}_b}{V_b^2}\right)\cos(\varepsilon_z - \gamma_c)\right]}{\sqrt{1 - \left[\frac{V_c}{V_b}\cos(\varepsilon_z - \gamma_c)\right]^2}}. \tag{5.62b}$$

If the target is stationary ($V_c = 0$), then

$$\gamma_b = \varepsilon_z - \frac{\pi}{2}. \tag{5.63}$$

5.2.2 Equations of Motion of a Guided Bomb

We assume that a bomb is a non-deformable (rigid) body of a constant mass. That is why, using Fig. 5.14, the motion of an apparatus can be represented by two systems of equations describing the motion of the mass center of the apparatus and the motion about the mass center [18, 19].

Equations of translational motion

The equations of translational motion of a bomb in its associated coordinate system $O_b xyz$ are as follows:

$$m_b\left(\frac{\mathrm{d}\boldsymbol{u}_b}{\mathrm{d}t} + \boldsymbol{w}_b\boldsymbol{q}_b - \boldsymbol{v}_b\boldsymbol{r}_b\right) - S_x\left(\boldsymbol{q}_b^2 + \boldsymbol{r}_b^2\right) + S_z\left(\frac{\mathrm{d}\boldsymbol{q}_b}{\mathrm{d}t} + \boldsymbol{p}_b\boldsymbol{r}_b\right) = F_x, \tag{5.64a}$$

$$m_b\left(\frac{\mathrm{d}\boldsymbol{v}_b}{\mathrm{d}t} + \boldsymbol{u}_b\boldsymbol{r}_b - \boldsymbol{w}_b\boldsymbol{p}_b\right) + S_x\left(\frac{\mathrm{d}\boldsymbol{r}_b}{\mathrm{d}t} + \boldsymbol{q}_b\boldsymbol{p}_b\right) - S_z\left(\frac{\mathrm{d}\boldsymbol{p}_b}{\mathrm{d}t} - \boldsymbol{q}_b\boldsymbol{r}_b\right) = F_y, \tag{5.64b}$$

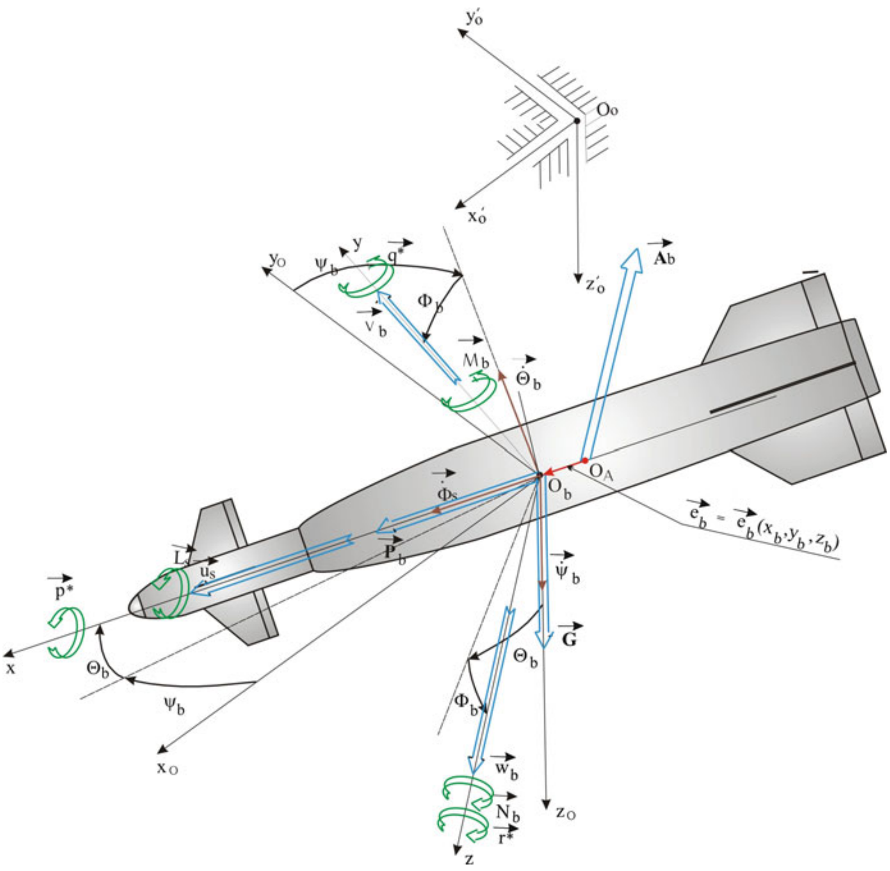

Fig. 5.14 System of forces and moments acting on an FO during flight

$$m_b\left(\frac{\mathrm{d}\boldsymbol{w}_b}{\mathrm{d}t}+\boldsymbol{p}_b\boldsymbol{v}_b-\boldsymbol{q}_b\boldsymbol{u}_b\right)-S_x\left(\frac{\mathrm{d}\boldsymbol{q}_b}{\mathrm{d}t}-\boldsymbol{p}_b\boldsymbol{r}_b\right)-S_z\left(\boldsymbol{q}_b^2+\boldsymbol{p}_b^2\right)=F_z, \quad (5.64\text{c})$$

where

$$\begin{bmatrix}\boldsymbol{F}_x\\ \boldsymbol{F}_y\\ \boldsymbol{F}_z\end{bmatrix}=\begin{bmatrix}\boldsymbol{X}_b+\boldsymbol{G}_x\\ \boldsymbol{Y}_b+\boldsymbol{G}_y\\ \boldsymbol{Z}_b+\boldsymbol{G}_z\end{bmatrix}, \qquad \begin{bmatrix}\boldsymbol{X}_b\\ \boldsymbol{Y}_b\\ \boldsymbol{Z}_b\end{bmatrix}=\frac{d\,(H_b)\,V_b^2}{2}S_b\cdot M_{oz}\cdot\begin{bmatrix}C_x\\ C_y\\ C_z\end{bmatrix}+\begin{bmatrix}\boldsymbol{P}_b\\ 0\\ 0\end{bmatrix},$$

$$V_b=\sqrt{\boldsymbol{u}_b^2+\boldsymbol{v}_b^2+\boldsymbol{w}_b^2},$$

$$M_{oz}=\begin{bmatrix}\cos\Psi_b\cos\Theta_b & \sin\Psi_b\cos\Theta_b & -\sin\Theta_b\\ \sin\varphi_b\cos\Psi_b\sin\Theta_b-\cos\varphi_b\sin\Psi_b & \sin\varphi_b\sin\Psi_b\sin\Theta_b+\cos\varphi_b\cos\Psi_b & \sin\varphi_b\cos\Theta_b\\ \cos\varphi_b\cos\Psi_b\sin\Theta_b+\sin\varphi_b\sin\Psi_b & \cos\varphi_b\sin\Psi_b\sin\Theta_b-\sin\varphi_b\cos\Psi_b & \cos\varphi_b\cos\Theta_b\end{bmatrix},$$

$$\begin{bmatrix}C_x\\ C_y\\ C_z\end{bmatrix}=\begin{bmatrix}C_{xo}\\ C_{yo}\\ C_{zo}\end{bmatrix}+\begin{bmatrix}\frac{\partial C_x}{\partial\alpha} & \frac{\partial C_x}{\partial\beta} & \frac{\partial C_x}{\partial p_s} & \frac{\partial C_x}{\partial q_s} & \frac{\partial C_x}{\partial r_s} & \frac{\partial C_x}{\partial\delta_l} & \frac{\partial C_x}{\partial\delta_m} & \frac{\partial C_x}{\partial\delta_n} & \frac{\partial C_x}{\partial\delta_t}\\ \frac{\partial C_y}{\partial\alpha} & \frac{\partial C_y}{\partial\beta} & \frac{\partial C_y}{\partial p_s} & \frac{\partial C_y}{\partial q_s} & \frac{\partial C_y}{\partial r_s} & \frac{\partial C_y}{\partial\delta_l} & \frac{\partial C_y}{\partial\delta_m} & \frac{\partial C_y}{\partial\delta_n} & \frac{\partial C_y}{\partial\delta_t}\\ \frac{\partial C_z}{\partial\alpha} & \frac{\partial C_z}{\partial\beta} & \frac{\partial C_z}{\partial p_s} & \frac{\partial C_z}{\partial q_s} & \frac{\partial C_z}{\partial r_s} & \frac{\partial C_z}{\partial\delta_l} & \frac{\partial C_z}{\partial\delta_m} & \frac{\partial C_z}{\partial\delta_n} & \frac{\partial C_z}{\partial\delta_t}\end{bmatrix}\cdot\begin{bmatrix}\alpha_b\\ \beta_b\\ \hat{p}_b\\ \hat{q}_b\\ \hat{r}_b\\ \delta_l\\ \delta_m\\ \delta_n\\ \delta_t\end{bmatrix},$$

$$\hat{p}_b=\frac{\boldsymbol{p}_b\cdot b_b}{V_b},\qquad \hat{q}_b=\frac{\boldsymbol{q}_b\cdot\bar{c}_b}{V_b},\qquad \hat{r}_b=\frac{\boldsymbol{r}_b\cdot b_b}{V_b},\qquad \begin{bmatrix}\boldsymbol{G}_x\\ \boldsymbol{G}_y\\ \boldsymbol{G}_z\end{bmatrix}=M_{oz}\cdot\begin{bmatrix}0\\ 0\\ m_b g\end{bmatrix},$$

where m_b is the bomb's mass; $L_b,\ M_b,\ N_b$ are the components of the vector of moment of force acting on the bomb; $u_b,\ v_b,\ w_b$ are the components of the vector of linear velocity of the bomb flight; $p_b,\ q_b,\ r_b$ are the components of the vector of angular velocity of the bomb flight; $F_x,\ F_y,\ F_z$ are the components of the net vector of external forces acting on the bomb; $S_x,\ S_y,\ S_z$ are the static moments with respect to particular axes; $C_x,\ C_y,\ C_z$ are the coefficients of the components of the net aerodynamic force; $d(H_b)$ is the density of the air at a given altitude of bomb flight H_b.

Equations of motion about a point of the FO

Equations of motion about a point of the FO in its associated coordinate system O_Sxyz are described by the following system:

$$J_x\frac{\mathrm{d}\boldsymbol{p}_b}{\mathrm{d}t}-(J_y-J_z)\boldsymbol{q}_b\boldsymbol{r}_b-J_{xz}\left(\frac{\mathrm{d}\boldsymbol{r}_b}{\mathrm{d}t}+\boldsymbol{q}_b\boldsymbol{p}_b\right)$$
$$-S_z\left(\frac{\mathrm{d}\boldsymbol{v}_b}{\mathrm{d}t}-\boldsymbol{w}_b\boldsymbol{p}_b+\boldsymbol{u}_b\boldsymbol{r}_b\right)=\boldsymbol{L}_b, \qquad (5.65a)$$

$$\begin{aligned} J_y \frac{\mathrm{d}\boldsymbol{q}_b}{\mathrm{d}t} &- (J_z - J_x)\boldsymbol{r}_b \boldsymbol{p}_b - J_{xz}(\boldsymbol{r}_b^2 - \boldsymbol{p}_b^2) \\ &+ S_x \left(\frac{\mathrm{d}\boldsymbol{w}_b}{\mathrm{d}t} \boldsymbol{v}_b \boldsymbol{p}_b - \boldsymbol{u}_b \boldsymbol{q}_b \right) + S_z \left(\frac{\mathrm{d}\boldsymbol{u}_b}{\mathrm{d}t} - \boldsymbol{v}_b \boldsymbol{r}_b + \boldsymbol{w}_b \boldsymbol{q}_b \right) = \boldsymbol{M}_b, \end{aligned} \tag{5.65b}$$

$$\begin{aligned} J_z \frac{\mathrm{d}\boldsymbol{r}_b}{\mathrm{d}t} &- \left(J_x - J_y\right) \boldsymbol{p}_b \boldsymbol{q}_b - J_{zx} \left(\frac{\mathrm{d}\boldsymbol{p}_b}{\mathrm{d}t} - \boldsymbol{r}_b \boldsymbol{q}_b \right) \\ &+ S_x \left(\frac{\mathrm{d}\boldsymbol{v}_b}{\mathrm{d}t} - \boldsymbol{w}_b \boldsymbol{p}_b + \boldsymbol{u}_b \boldsymbol{r}_b \right) = \boldsymbol{N}_b, \end{aligned} \tag{5.65c}$$

where $J_x,\ J_y,\ J_z$ are the moments of inertia of the bomb with respect to particular axes; $J_{xy},\ J_{yz},\ J_{zx}$ are products of inertia of the bomb.

Furthermore, we have

$$\begin{bmatrix} \boldsymbol{L}_b \\ \boldsymbol{M}_b \\ \boldsymbol{N}_b \end{bmatrix} = \begin{bmatrix} \boldsymbol{L}^A + \boldsymbol{L}_G \\ \boldsymbol{M}^A + \boldsymbol{M}_G \\ \boldsymbol{N}^A + \boldsymbol{N}_G \end{bmatrix}, \qquad \begin{bmatrix} \boldsymbol{L}^A \\ \boldsymbol{M}^A \\ \boldsymbol{N}^A \end{bmatrix} = \frac{d\,(H_b)\,V_b^2}{2} S \cdot M_{oz} \cdot \begin{bmatrix} b_b C_l \\ \bar{c}_b C_m \\ b_b C_n \end{bmatrix},$$

$$\begin{bmatrix} \boldsymbol{L}_G \\ \boldsymbol{M}_G \\ \boldsymbol{N}_G \end{bmatrix} = \begin{bmatrix} m_b g\,(z_b \sin\varphi_b \cos\Theta_b - y_b \cos\varphi_b \cos\Theta_b) \\ m_b g\,(x_b \cos\varphi_b \cos\Theta_b + z_b \sin\Theta_b) \\ -m_b g\,(y_b \sin\Theta_b + x_b \sin\varphi_b \cos\Theta_b) \end{bmatrix},$$

$$\begin{bmatrix} C_l \\ C_m \\ C_n \end{bmatrix} = \begin{bmatrix} C_{lo} \\ C_{mo} \\ C_{no} \end{bmatrix} + \begin{bmatrix} \frac{\partial C_l}{\partial \alpha} & \frac{\partial C_l}{\partial \beta} & \frac{\partial C_l}{\partial p_s} & \frac{\partial C_l}{\partial q_s} & \frac{\partial C_l}{\partial r_s} & \frac{\partial C_l}{\partial \delta_l} & \frac{\partial C_l}{\partial \delta_m} & \frac{\partial C_l}{\partial \delta_n} & \frac{\partial C_l}{\partial \delta_t} \\ \frac{\partial C_m}{\partial \alpha} & \frac{\partial C_m}{\partial \beta} & \frac{\partial C_m}{\partial p_s} & \frac{\partial C_m}{\partial q_s} & \frac{\partial C_m}{\partial r_s} & \frac{\partial C_m}{\partial \delta_l} & \frac{\partial C_m}{\partial \delta_m} & \frac{\partial C_m}{\partial \delta_n} & \frac{\partial C_m}{\partial \delta_t} \\ \frac{\partial C_n}{\partial \alpha} & \frac{\partial C_n}{\partial \beta} & \frac{\partial C_z}{\partial p_s} & \frac{\partial C_n}{\partial q_s} & \frac{\partial C_n}{\partial r_s} & \frac{\partial C_n}{\partial \delta_l} & \frac{\partial C_n}{\partial \delta_m} & \frac{\partial C_n}{\partial \delta_n} & \frac{\partial C_n}{\partial \delta_t} \end{bmatrix}$$

$$\cdot \begin{bmatrix} \alpha_b \\ \beta_b \\ \hat{p}_b \\ \hat{q}_b \\ \hat{r}_b \\ \delta_l \\ \delta_m \\ \delta_n \\ \delta_t \end{bmatrix},$$

where $C_l,\ C_m,\ C_n$ are the aerodynamic coefficients of a rolling moment L_b, a pitching moment M_b, and a yawing moment N_b, respectively; and g is the acceleration of gravity.

The Kinematic relationships between angular velocities follow

$$\frac{\mathrm{d}\Psi_b}{\mathrm{d}t} = (\boldsymbol{q}_b \sin\varphi_b + \boldsymbol{r}_b \cos\varphi_b) \sec\Theta_b, \tag{5.66a}$$

$$\frac{\mathrm{d}\Theta_b}{\mathrm{d}t} = \boldsymbol{q}_b \cos\varphi_b - \boldsymbol{r}_b \sin\varphi_b, \tag{5.66b}$$

$$\frac{\mathrm{d}\varphi_b}{\mathrm{d}t} = \boldsymbol{p}_b + (\boldsymbol{q}_b \sin\varphi_b + \boldsymbol{r}_b \cos\varphi_b) \tan\Theta_b, \tag{5.66c}$$

where Θ_b, Ψ_b, φ_b are the angles of pitch, yaw, and roll of the longitudinal axis of the bomb, respectively.

The kinematic relationships between linear velocities (a trajectory of a bomb flight) are as follows

$$\begin{aligned}\frac{\mathrm{d}x_o}{\mathrm{d}t} &= \boldsymbol{u}_b \cos\Theta_b \cos\Psi_b + \boldsymbol{v}_b(\sin\varphi_b \sin\Theta_b \cos\Psi_b \\ &\quad - \cos\varphi_b \sin\Psi_b) + \boldsymbol{w}_b \left(\cos\varphi_b \sin\Theta_b \cos\Psi_b + \sin\varphi_b \sin\Psi_b\right),\end{aligned} \tag{5.67a}$$

$$\begin{aligned}\frac{\mathrm{d}y_o}{\mathrm{d}t} &= \boldsymbol{u}_b \cos\Theta_b \sin\Psi_b + \boldsymbol{v}_b(\sin\varphi_b \sin\Theta_b \sin\Psi_b \\ &\quad + \cos\varphi_b \cos\Psi_b) + \boldsymbol{w}_b \left(\cos\varphi_b \sin\Theta_b \cos\Psi_b + \sin\varphi_b \sin\Psi_b\right),\end{aligned} \tag{5.67b}$$

$$\frac{\mathrm{d}z_o}{\mathrm{d}t} = -\boldsymbol{u}_b \sin\Theta_b + \boldsymbol{v}_b \sin\varphi_b \cos\Theta_b + \boldsymbol{w}_b \cos\varphi_b \cos\Theta_b, \tag{5.67c}$$

where $x_o,\ y_o,\ z_o$ are the coordinates of the center of mass of the bomb in an Earth-fixed coordinate system.

Supplementary relationships are

$$\alpha_b = \arctan\frac{\boldsymbol{w}_b}{\boldsymbol{u}_b}, \tag{5.68a}$$

$$\beta_b = \arcsin\frac{\boldsymbol{v}_b}{\sqrt{\boldsymbol{u}_b^2 + \boldsymbol{v}_b^2 + \boldsymbol{w}_b^2}}, \tag{5.68b}$$

where $\alpha_b,\ \beta_b$ are the angles of attack and slip.

5.2.3 A Gyroscopic System of Bomb Control

The task of a gyroscope in a self-guidance system of a bomb can be the determination of a TOL at every time instant. The TOL can be determined in two different

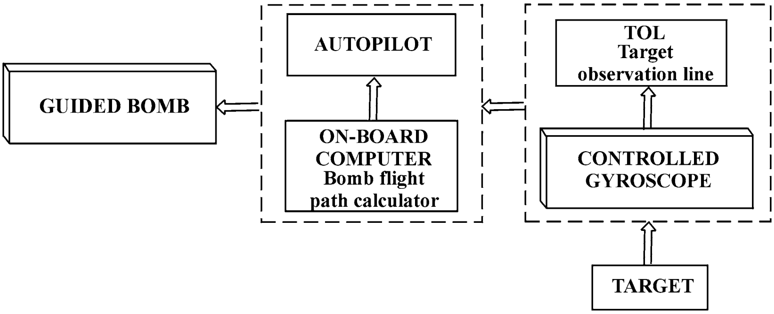

Fig. 5.15 Simplified schematic of bomb self-guidance to a ground target

ways: (1) for targets that are mobile and emit a heat wave (e.g., tanks, armored fight vehicles)—a follow-up control of the orientation of the gyroscope axis based on signals from the head equipped with an infrared detector or (2) for stationary targets (e.g., underground bunkers, bridges)—a program control of the orientation of a gyroscope axis based on exact data about the target's positions. The determination of the TOL corresponds to the solution of the system of differential equations (5.52) and (5.53). Next, an on-board computer calculates the kinematic path of a bomb flight for one of the previously considered cases (target attack at an angle of 0°, 90°, and 180°). The obtained data are transmitted to the bomb's automatic pilot, where control signals are elaborated for actuators of a rudder and an elevator.

In general, the schematic of gyroscopic control of a bomb control automatically moving toward a ground target is presented in Fig. 5.15.

Programmed control moments for the case of tracking of a stationary target (very often a hidden, underground one) are as follows:

$$\begin{aligned} M_b = M_b^n = J_{gk}\frac{\mathrm{d}^2\vartheta_{gz}}{\mathrm{d}t^2} + \frac{1}{2}J_{gk}\dot{\psi}_{gz}^2 \sin 2\vartheta_{gz} \\ + J_{go}n_g\dot{\psi}_{gz}\cos\vartheta_{gz} + \eta_b\dot{\vartheta}_{gz}, \end{aligned} \tag{5.69a}$$

$$\begin{aligned} M_c = M_c^n = J_{gk}\frac{\mathrm{d}^2\psi_{gz}}{\mathrm{d}t^2}\cos^2\vartheta_{gz} - J_{gk}\dot{\psi}_{gz}\dot{\vartheta}_{gz}\sin 2\vartheta_{gz} \\ - J_{go}n_g\dot{\vartheta}_{gz}\cos\vartheta_{gz} + \eta_c\dot{\psi}_{gz}, \end{aligned} \tag{5.69b}$$

where $\vartheta_{gz} = \epsilon$, $\psi_{gz} = \sigma$ are the angles defining the required orientation of the gyroscope axis in space.

Quantities ϵ and σ and their first and second time derivatives are determined from relationship (5.52a) and then substituted into (5.69a)

$$
\begin{aligned}
\frac{\mathrm{d}^2\varepsilon}{\mathrm{d}t^2} &= \frac{r_b\dot{\varepsilon}\dot{\sigma}\sin\sigma - \dot{r}_b\dot{\varepsilon}\cos\sigma}{r_b\cos\sigma} \\
&+ \frac{V_c\dot{\chi}_c\sin\chi_c\sin(\varepsilon-\gamma_c) - \dot{V}_c\cos\chi_c\sin(\varepsilon-\gamma_c) - V_c(\dot{\varepsilon}-\dot{\gamma}_c)\cos\chi_c\cos(\varepsilon-\gamma_c)}{r_b\cos\sigma} \\
&+ \frac{V_b\dot{\chi}_b\sin\chi_b\sin(\varepsilon-\gamma_b) - \dot{V}_b\cos\chi_b\sin(\varepsilon-\gamma_b) + V_b(\dot{\varepsilon}-\dot{\gamma}_b)\cos\chi_b\cos(\varepsilon-\gamma_b)}{r_b\cos\sigma},
\end{aligned}
$$

$$
\begin{aligned}
\frac{\mathrm{d}^2\sigma}{\mathrm{d}t^2} &= -\frac{\dot{r}_b}{r_b}\dot{\sigma} - \frac{\dot{V}_c}{r_b}\left[\cos(\varepsilon-\gamma_c)\sin\sigma\cos\chi_c - \cos\sigma\sin\chi_c\right] \\
&- \frac{V_c}{r_b}\left[\dot{\chi}_c\sin\chi_c\sin\sigma\cos(\varepsilon-\gamma_c) - \dot{\sigma}\cos\chi_c\cos\sigma\cos(\varepsilon-\gamma_c)\right. \\
&\left.+ (\dot{\varepsilon}-\dot{\gamma}_c)\cos\chi_c\sin\sigma\sin(\varepsilon-\gamma_c) + \dot{\chi}_c\cos\chi_c\cos\sigma - \dot{\sigma}\sin\chi_c\sin\sigma\right] \\
&+ \frac{\dot{V}_b}{r_b}\left[\cos(\varepsilon-\gamma_b)\sin\sigma\cos\chi_b - \cos\sigma\sin\chi_b\right] \\
&- \frac{V_b}{r_b}\left[\dot{\chi}_b\sin\chi_b\sin\sigma\cos(\varepsilon-\gamma_b) + \dot{\sigma}\cos\chi_b\cos\sigma\cos(\varepsilon-\gamma_b)\right. \\
&\left.+ (\dot{\varepsilon}-\dot{\gamma}_b)\cos\chi_b\sin\sigma\sin(\varepsilon-\gamma_b) + \dot{\chi}_b\cos\chi_b\cos\sigma - \dot{\sigma}\sin\chi_b\sin\sigma\right],
\end{aligned}
$$

where

$$
\begin{aligned}
\frac{\mathrm{d}^2 r_b}{\mathrm{d}t^2} &= \dot{V}_c\left[\cos(\varepsilon-\gamma_c)\cos\sigma\cos\chi_c + \sin\sigma\sin\chi_c\right] \\
&- V_c\left[\dot{\chi}_c\sin\chi_c\cos\sigma\cos(\varepsilon-\gamma_c) + \dot{\sigma}\cos\chi_c\sin\sigma\cos(\varepsilon-\gamma_c)\right. \\
&\left.+ (\dot{\varepsilon}-\dot{\gamma}_c)\cos\chi_c\cos\sigma\sin(\varepsilon-\gamma_c) - \dot{\chi}_c\cos\chi_c\sin\sigma - \dot{\sigma}\sin\chi_c\cos\sigma\right] \\
&- V_b\left[\cos(\varepsilon-\gamma_b)\cos\sigma\cos\chi_b + \sin\sigma\sin\chi_b\right] \\
&- \dot{V}_b\left[\cos(\varepsilon-\gamma_b)\cos\sigma\cos\chi_b + \sin\sigma\sin\chi_b\right] \\
&- V_b\left[\dot{\chi}_b\sin\chi_b\cos\sigma\cos(\varepsilon-\gamma_b) + \dot{\sigma}\cos\chi_b\sin\sigma\cos(\varepsilon-\gamma_b)\right. \\
&\left.+ (\dot{\varepsilon}-\dot{\gamma}_b)\cos\chi_b\cos\sigma\sin(\varepsilon-\gamma_b) - \dot{\chi}_b\cos\chi_b\sin\sigma - \dot{\sigma}\sin\chi_b\cos\sigma\right].
\end{aligned}
$$

In the case where $V_c = 0$ (a stationary target), we have

$$\vartheta_{gz} = \varepsilon, \qquad \psi_{gz} = \sigma, \tag{5.70}$$

$$\frac{\mathrm{d}\vartheta_{gz}}{\mathrm{d}t} = \frac{\mathrm{d}\varepsilon}{\mathrm{d}t} = \frac{V_b\sin(\varepsilon-\gamma_b)\cos\chi_b}{r\cos\sigma}, \tag{5.71}$$

$$\frac{\mathrm{d}\psi_{gz}}{\mathrm{d}t} = \frac{\mathrm{d}\sigma}{\mathrm{d}t} = V_b \frac{\cos(\varepsilon - \gamma_b)\sin\sigma\cos\chi_b - \cos\sigma\sin\chi_b}{r}, \tag{5.72}$$

$$\frac{\mathrm{d}^2\vartheta_{gz}}{\mathrm{d}t^2} = \frac{\mathrm{d}^2\varepsilon}{\mathrm{d}t^2} = \frac{\sin(\varepsilon - \gamma_b)\cos\chi_b}{r\cos\sigma}\left(\frac{\mathrm{d}V_b}{\mathrm{d}t} - V_b\frac{\frac{\mathrm{d}r}{\mathrm{d}t}\cos\sigma - r\frac{\mathrm{d}\sigma}{\mathrm{d}t}\sin\sigma}{r\cos\sigma}\right)$$
$$+V_b\frac{\left(\frac{\mathrm{d}\varepsilon}{\mathrm{d}t} - \frac{\mathrm{d}\gamma_b}{\mathrm{d}t}\right)\cos(\varepsilon - \gamma_b) - \frac{\mathrm{d}\chi_b}{\mathrm{d}t}\sin(\varepsilon - \gamma_b)\sin\chi_b}{r\cos\sigma}, \tag{5.73}$$

$$\frac{\mathrm{d}^2\psi_{gz}}{\mathrm{d}t^2} = \frac{\mathrm{d}^2\sigma}{\mathrm{d}t^2} = \frac{\cos(\varepsilon - \gamma_b)\sin\sigma\cos\chi_b - \cos\sigma\sin\chi_b}{r}\left(\frac{\mathrm{d}V_b}{\mathrm{d}t} - \frac{V_b}{r}\frac{\mathrm{d}r}{\mathrm{d}t}\right)$$
$$+\frac{V_b}{r}\left[\left(\frac{\mathrm{d}\gamma_b}{\mathrm{d}t} - \frac{\mathrm{d}\varepsilon}{\mathrm{d}t}\right)\sin(\varepsilon - \gamma_b)\sin\sigma\cos\chi_b + \frac{\mathrm{d}\sigma}{\mathrm{d}t}\sin\sigma\sin\chi_b - \frac{\mathrm{d}\chi_b}{\mathrm{d}t}\cos\sigma\cos\chi_b\right]$$
$$+\cos(\varepsilon - \gamma_b)\left(\frac{\mathrm{d}\sigma}{\mathrm{d}t}\cos\sigma\cos\chi_b - \frac{\mathrm{d}\chi_b}{\mathrm{d}t}\sin\sigma\sin\chi_b\right). \tag{5.74}$$

As a result of the influence of all kinds of external disturbances on a gyroscope, the gyroscope axis can perform a prescribed motion with certain unacceptable errors. In this case one should additionally apply correcting control moments M_b^k and M_c^k, which can be represented in the following way:

$$M_b^k = k_b\left(\vartheta_g - \varepsilon\right) - k_c\left(\psi_g - \sigma\right) + h_g\left(\frac{\mathrm{d}\vartheta_g}{\mathrm{d}t} - \frac{\mathrm{d}\varepsilon}{\mathrm{d}t}\right), \tag{5.75a}$$

$$M_c^k = k_b\left(\psi_g - \sigma\right) - k_c\left(\vartheta_g - \varepsilon\right) + h_g\left(\frac{\mathrm{d}\psi_g}{\mathrm{d}t} - \frac{\mathrm{d}\sigma}{\mathrm{d}t}\right), \tag{5.75b}$$

where k_b, k_c, h_g are the gain coefficients of the system of automatic control of a gyroscope.

5.2.4 Control Law for Automatic Pilot of a Guided Bomb

The steering of the flight of a guided bomb is accomplished by means of displacement of control surfaces of ailerons, a rudder, and an elevator respectively by the angles δ_l, δ_m, and δ_n. However, the change in the bomb's flight path is influenced only by the rudder and elevator, which means that we should limit ourselves to determining a control rule for the change in displacement of angles δ_m and δ_n.

The realization of the desired flight path of the guided bomb is carried out by the automatic pilot (AP), which elaborates control signals for the actuator system of the control.

Let us write the control rule for the AP, with the dynamics of displacement of control surfaces taken into account, using the following relationships:

$$\begin{aligned}\frac{\mathrm{d}^2\delta_m}{\mathrm{d}t^2} + h_{mb}\frac{\mathrm{d}\delta_m}{\mathrm{d}t} + k_{mb}\delta_m &= k_{m1}\left(\gamma_{br} - \gamma_b\right)\\ &\quad + k_{m2}\left(\frac{\mathrm{d}\gamma_{br}}{\mathrm{d}t} - \frac{\mathrm{d}\gamma_b}{\mathrm{d}t}\right) + h_m\left(\frac{\mathrm{d}^2\gamma_{br}}{\mathrm{d}t^2} - \frac{\mathrm{d}^2\gamma_b}{\mathrm{d}t^2}\right),\end{aligned} \tag{5.76a}$$

$$\begin{aligned}\frac{\mathrm{d}^2\delta_n}{\mathrm{d}t^2} + h_{nb}\frac{\mathrm{d}\delta_n}{\mathrm{d}t} + k_{nb}\delta_n &= k_{n1}\left(\chi_{br} - \chi_b\right)\\ &\quad + k_{n2}\left(\frac{\mathrm{d}\chi_{br}}{\mathrm{d}t} - \frac{\mathrm{d}\chi_b}{\mathrm{d}t}\right) + h_n\left(\frac{\mathrm{d}^2\chi_{br}}{\mathrm{d}t^2} - \frac{\mathrm{d}^2\chi_b}{\mathrm{d}t^2}\right),\end{aligned} \tag{5.76b}$$

where $\gamma_{br},\ \chi_{br}$ are the actual angles of the bomb's flight; $h_{mb},\ k_{mb},\ h_{nb},\ k_{nb}$ are coefficients of appropriately selected constants of control surface drives; and $h_m,\ k_{mb},\ h_n,\ k_n$ are coefficients of appropriately selected constants of a PD-type controller in the autopilot of the bomb.

5.2.5 Results and Final Conclusions

In order to validate the system operation, a numerical simulation for a "hypothetical" bomb equipped with a self-guidance system was conducted, where the drive was a controlled gyroscope with the following parameters:

$$J_{gk} = 2.5\cdot 10^{-4}\,\mathrm{kg}\cdot\mathrm{m}^2, \qquad n_g = 600\,\frac{\mathrm{rad}}{\mathrm{s}}, \qquad \eta_b = \eta_c = 0.01\,\frac{\mathrm{N}\cdot\mathrm{m}\cdot\mathrm{s}}{\mathrm{rad}}.$$

Parameters of the gyroscope controller were selected in an optimal way with respect to minimal error between the prescribed and actual motions. The value of the coefficient was taken as

$$k_b = 10\,\frac{\mathrm{N}\cdot\mathrm{m}}{\mathrm{rad}},$$

whereas the remaining ones are determined in the following way [19]:

$$k_c = \frac{1}{2}\frac{J_{go}^2 n_g^2}{J_{gk}}\sqrt{2J_{go}^2 n_g^2 + 4J_{gk}k_b}, \qquad h_g = \sqrt{2J_{go}^2 n_g^2 + 4J_{gk}k_b}.$$

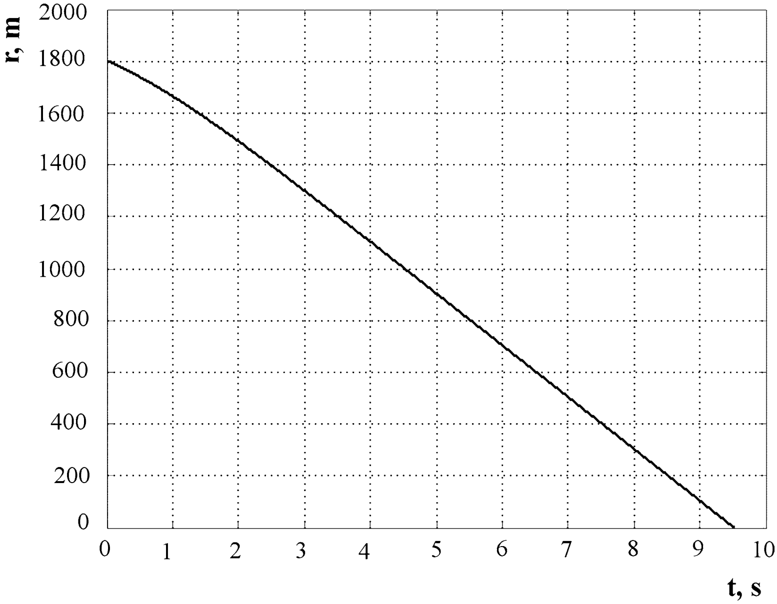

Fig. 5.16 Change in time of relative distance r between bomb and target

The coefficients of gain and damping of the autopilot of the guided bomb are obtained in a similar way:

$$k_{m1} = k_{n1} = 2.703, \qquad k_{m2} = k_{n2} = 11.439, \qquad h_m = h_n = 9.887.$$

Some results of investigations are presented in Figs. 5.16–5.31, where Figs. 5.16–5.19 show the flight trajectories of a bomb guiding itself to a stationary ground target. For comparison we refer to the trajectories for guidance with proportional navigation method (dashed lines) and trajectories for attacks on the aforementioned ground targets at different angles: 90°, 0°, 180° (dashed lines).

It should be emphasized that the TOL in the considered self-guidance system of a bomb is identified with the axis of the controlled gyroscope. An open-loop control system of a gyroscope axis does not function properly (it indicates the target inaccurately), even when there are no external disturbances (Figs. 5.20–5.23). The cause of errors is the friction in the bearings of the gyroscope's suspension. If additionally there appears a disturbance (acting in the time interval $3.0\,\mathrm{s} \leq t \leq 4.5\,\mathrm{s}$), then a large discrepancy occurs between the prescribed and actual (realized) motions of both the axis of the gyroscope (Figs. 5.24 and 5.25) and the flight path of the bomb itself (Figs. 5.26 and 5.27).

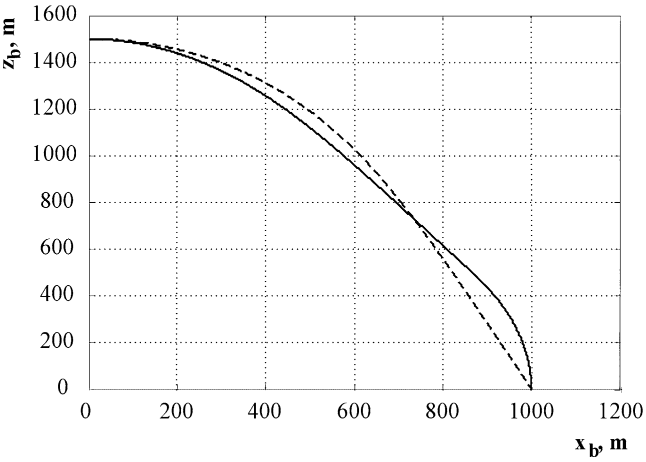

Fig. 5.17 Bomb flight trajectory in accordance with proportional navigation (dashed line) and during attack at an angle of 90° (continuous line)

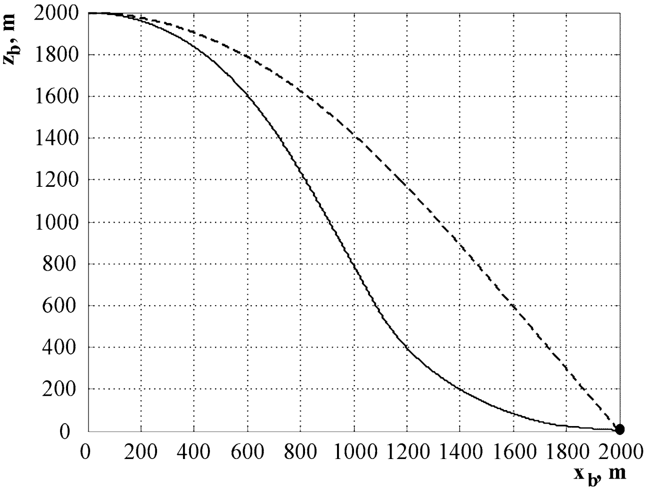

Fig. 5.18 Bomb flight trajectory in accordance with proportional navigation (dashed line) and during attack at an angle of 0° (continuous line)

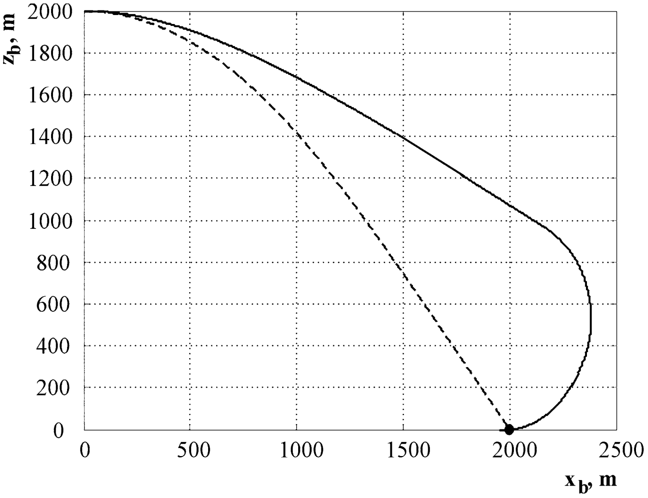

Fig. 5.19 Bomb flight trajectory in accordance with proportional navigation (dashed line) and during attack at an angle of 180° (continuous line)

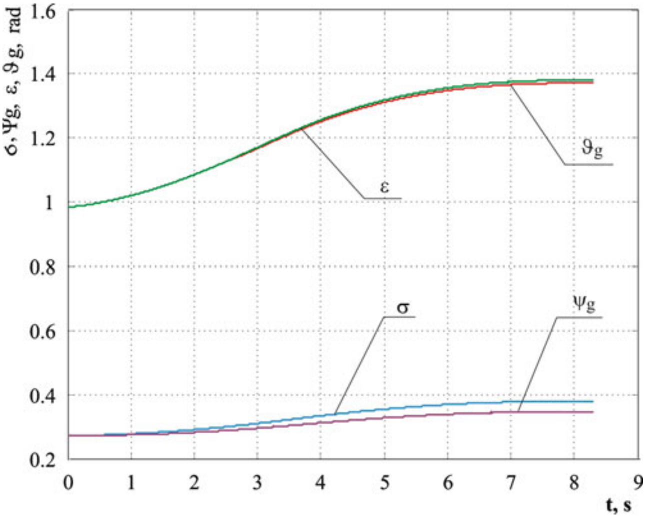

Fig. 5.20 Change in time of angles ϵ, σ of TOL position (prescribed) and angles ϑ_g, Ψ_g of gyroscope axle position, without correcting moments

Fig. 5.21 Motion paths of TOL and gyroscope axis, without correcting moments

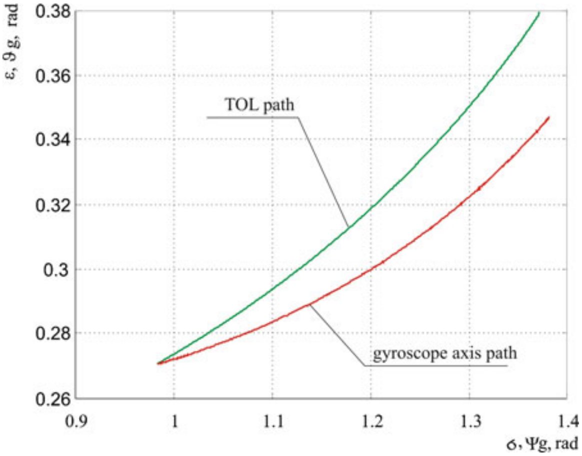

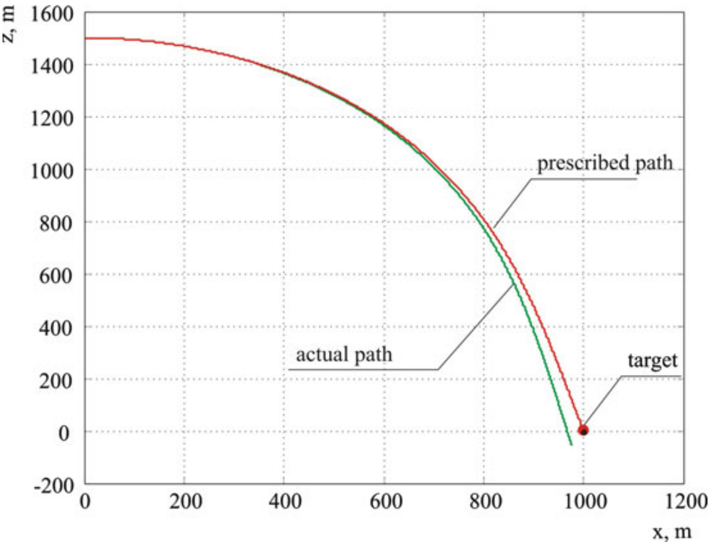

Fig. 5.22 Prescribed and actual paths of bomb flight, without correcting moments

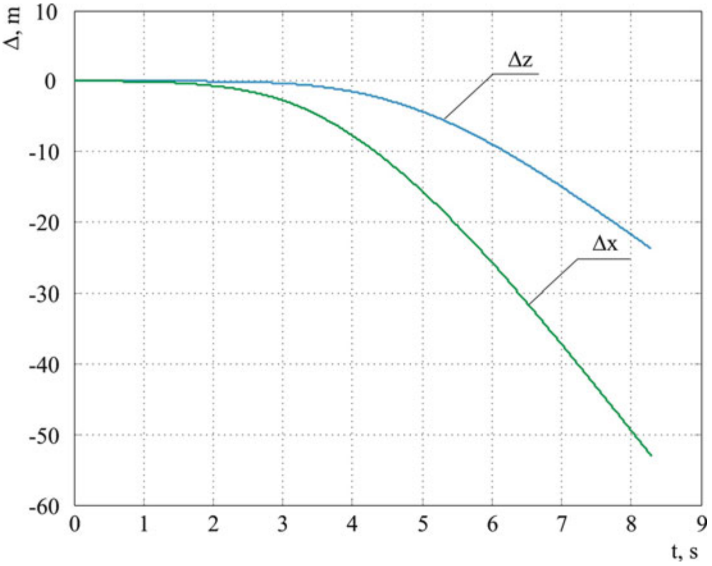

Fig. 5.23 Errors of self-guidance of a bomb without correcting moments

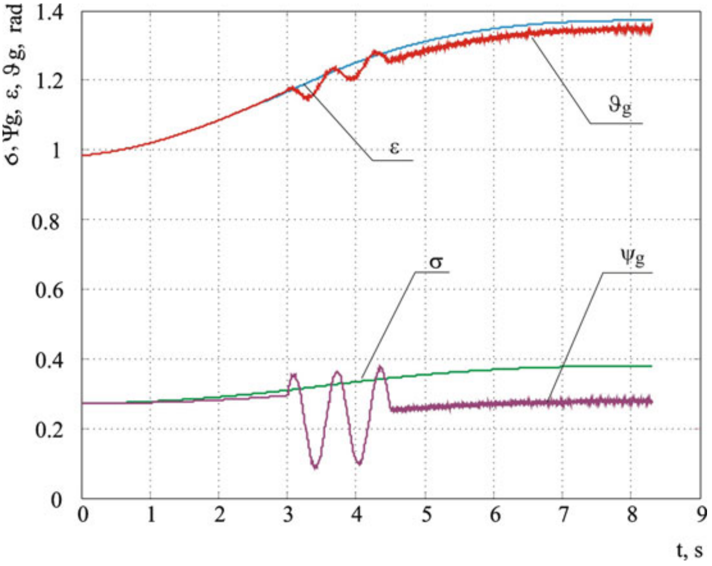

Fig. 5.24 Change in time of angles ϵ, σ of TOL position (prescribed) and angles ϑ_g, ψ_g of gyroscope axis position during appearance of disturbances, without correcting moments

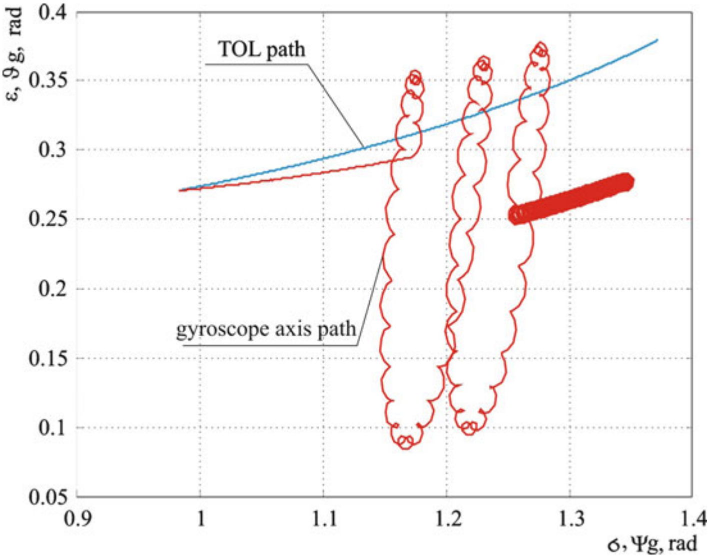

Fig. 5.25 Motion paths of TOL (prescribed) and gyroscope axis (actual) during appearance of disturbance, without correcting moments

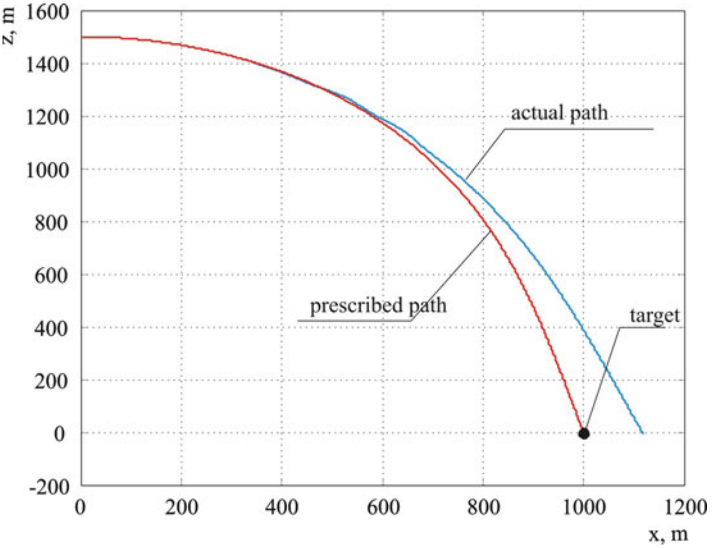

Fig. 5.26 Prescribed and actual flight paths of bomb during appearance of disturbance, without correcting moments

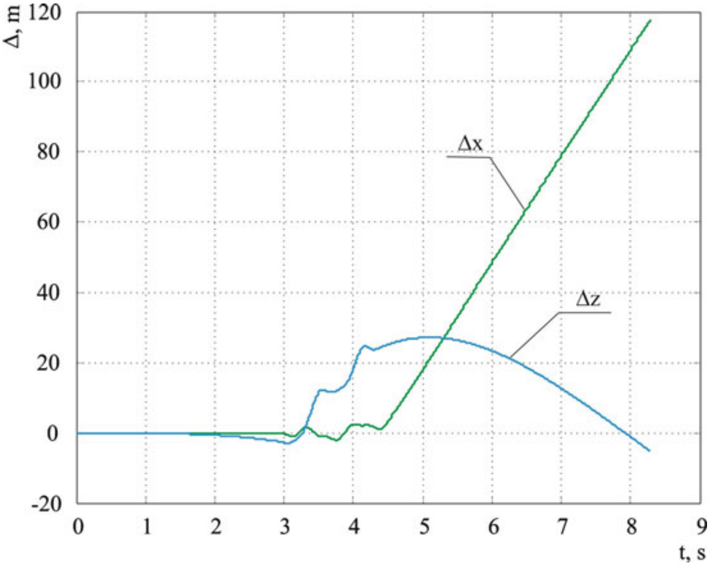

Fig. 5.27 Errors of self-guidance of bomb during appearance of disturbance, without correcting moments

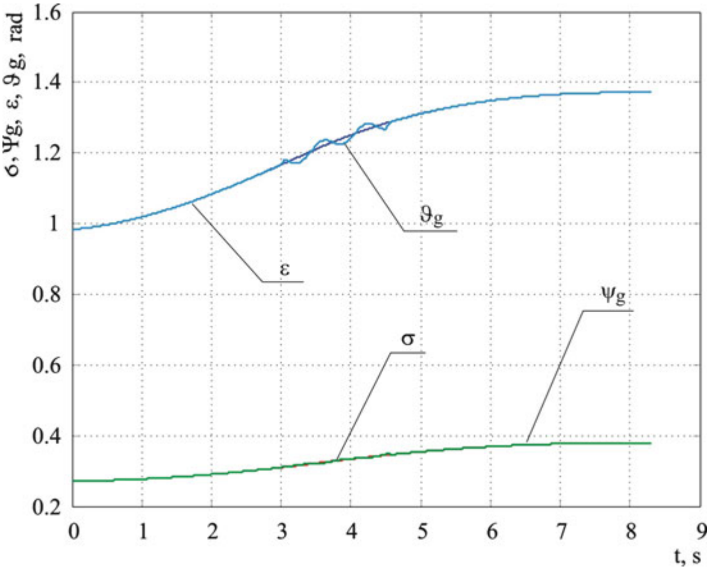

Fig. 5.28 Change in time of angles ϵ, σ of TOL position (prescribed) and angles ϑ_g, ψ_g of gyroscope axis position during appearance of disturbances, with application of correcting moments

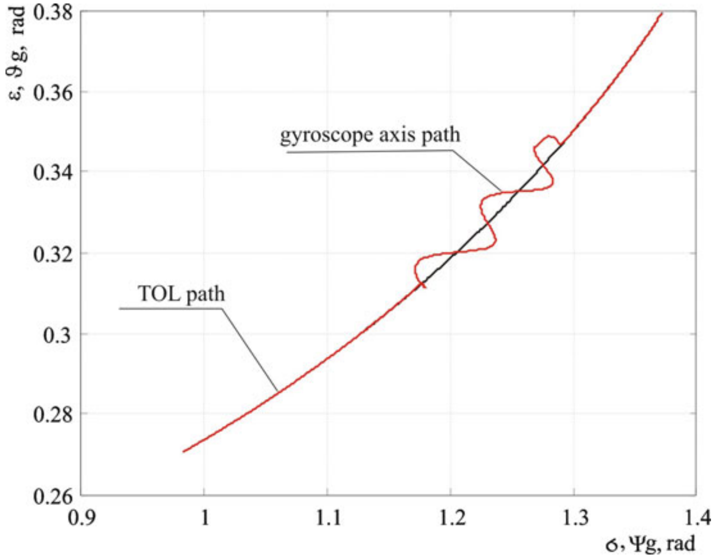

Fig. 5.29 Motion paths of TOL (prescribed) and gyroscope axis (actual) during appearance of disturbance, with application of correcting moments

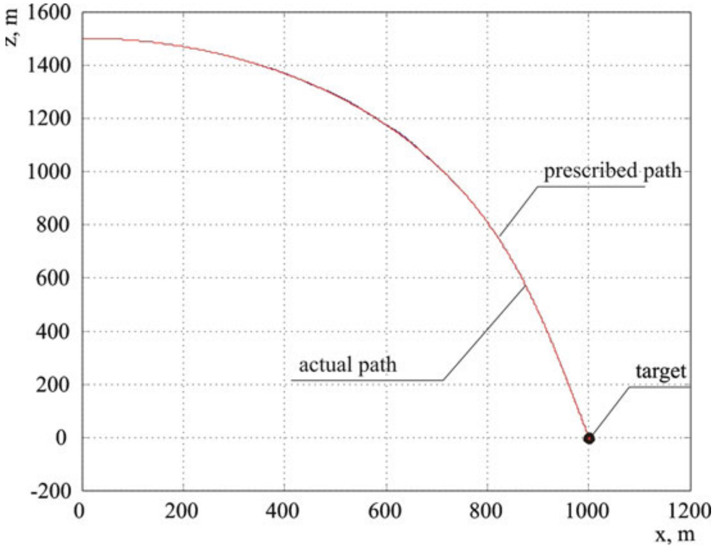

Fig. 5.30 Prescribed and actual flight paths of bomb during appearance of disturbance, with application of correcting moments

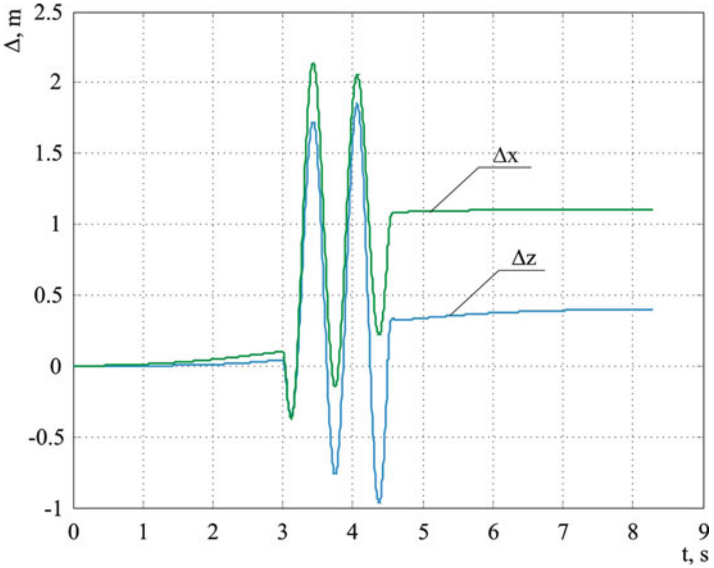

Fig. 5.31 Bomb self-guidance errors during appearance of disturbance, with application of correcting moments

The application of additional feedback in a system of automatic control of motion of the axis of a gyroscope with optimally selected parameters [12] substantially improves the accuracy of the TOL (the alignment of the TOL with the axis of the gyroscope) and consequently the minimization of errors between prescribed and actual motions of both gyroscope and guided bomb. This is clearly illustrated in Figs. 5.28–5.31.

To sum up, it may be stated that preliminary investigations confirm the possibility of application of a gyroscopic system in a guided bomb self-guidance to a ground target. However, in further research the influence of the following factors should be subjected to a more detailed analysis: (a) dry and viscous friction in frame bearings; (b) frame inertia; (c) unbalance (static and dynamic) of a rotor with respect to the intersection of frame axes, that is, the center of rotation; (d) the linear and angular acceleration of the base; (e) the elasticity of structural elements; (f) the errors of a Cardan suspension; (g) the instability of the rotor drive; (h) the intersection of the frames at angles other than 90°; (i) large angles and angular velocities of deviation of the main axis of the gyroscope from the prescribed direction; and (j) the Earth's rotational motion about its axis. Those factors have ultimate influence on the accuracy of the bomb. Moreover, various methods of self-guidance should be investigated with respect to the time to reach targets and the minimization of a gravity load acting on a bomb when approaching a target.

References

1. Z. Koruba, A mathematical model of the dynamics and control of a gyroscopic platform mounted on board of an aerial vehicle. J. Tech. Phys. **46**(1), 37–50 (2005)
2. Z. Koruba, A process of gyroscope motion control in an autonomous system, target detection and tracking. J. Theor. Appl. Mech. **37**(4), 908–927 (1999)
3. Z. Koruba, Adaptive correction of controlled gyroscope on the deck of aerial object. J. Tech. Phys. **42**(2), 203–222 (2001)
4. T.S. Taylor, *Introduction to Rocket Science and Engineering* U.S. Army Space and Missile Defense Command. (Huntsville, AL, 2009)
5. Z. Koruba, Model of final navigation segment for combat unmanned aerial vehicle. J. Tech. Phys. **44**(1), 99–115 (2003)
6. R. Yanushevsky, *Modern Missile Guidance* (CRC Press, Boca Raton, FL, 2007)
7. Z. Koruba, J. Osiecki, *Construction, Dynamics and Navigation of Close-Range Missiles, Part 1*. University Course Book No. 348 (Kielce University of Technology Press, Kielce, 1999), in Polish
8. J.H. Blakelock, *Automatic Control of Aircraft and Missiles* (Wiley, New York, 1991)
9. Z. Koruba, in *The Model of the Control of Aerial Robot with Autonomous System of Ground Object Seeking and Tracking*. Proceedings of the First Workshop on Robot Motion and Control (1999), pp. 41–44
10. Z. Koruba, Unmanned aerial vehicle flight programme, ground surface scanning and laser target illumination. J. Tech. Phys. **40**(4), 421–434 (1999)
11. G.M. Siouris, *Missile Guidance and Control Systems* (Springer, New York, 2004)
12. Z. Koruba, Optimisation of construction parameters of gyroscope system on elastic suspension. Comput. Assist. Mech. Eng. Sci. **4**(7), 595–606 (2000)
13. Z. Koruba, in *Dynamics and control model of gyroscope located on deck unmanned aerial vehicle.* North Atlantic Treaty Organization Unmanned Vehicles for Aerial, Ground and Naval Military Operations – a Symposium organised by the Applied Vehicle Technology Panel, Ankara, Turkey, 9–13 October 2000
14. Z. Koruba, J. Osiecki, *Construction, Dynamics and Navigation of Selected Arms of Precision Strike* (Kielce University of Technology Press, Kielce, 2006), in Polish
15. K. Ogata, *Matlab for Control Engineers* (Prentice-Hall, Engewood Cliffs, NJ, 2007)
16. P. De Larminat, Y. Thomas, *Automatics of Linear Systems*, vol. 3 (Flammarion Sciences, Paris, 1977), in French
17. B. Kisacanin, *Linear Control Systems: with Solved Problems and MATLAB Examples* (Kluwer/Plenum, New York, 2002)
18. Da-Wei Gu, P.H. Petkov, M.M. Konstantinov, *Robust Control Design with MATLAB* (Springer, London, 2005)
19. Z. Koruba, K. Ogonowski, The analysis of a gyroscopic system in the process of guiding an aerial bomb to a water target. Polish J. Environ. Stud. **16**(4A), 92–95 (2007)